Establishing the Viability of Drying Wet and Corroded Magnox Spent Fuel for Interim Dry Storage

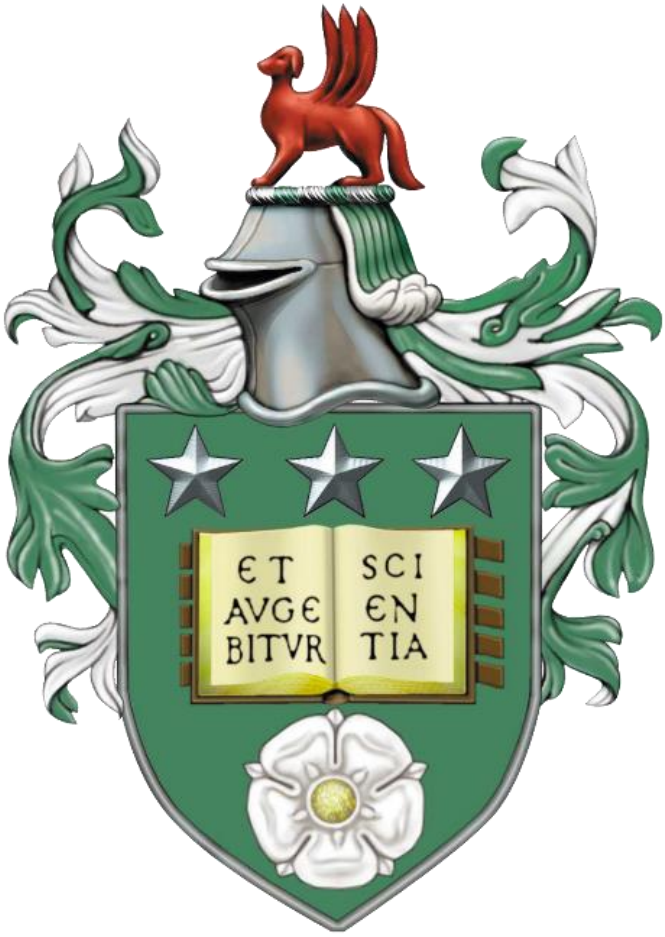

Matthew James Jackson

The University of Leeds
School of Chemical and Process Engineering

Submitted in accordance with the requirements for the degree of
Doctor of Philosophy

December 2022

The candidate confirms that the work submitted is his/her own, except where work which has formed part of jointly-authored publications has been included. The contribution of the candidate and the other authors to this work has been explicitly indicated below. The candidate confirms that appropriate credit has been given within the thesis where reference has been made to the work of others.

This thesis includes data from the following jointly authored publication:

Waste Management 2020 Conference proceedings:

Drying Wet Stored and Corroded Magnox Fuel for Interim Dry Storage, Matthew Jackson, Timothy Hunter, James Goode and Bruce Hanson, WM2020 Conference, March 8 – 12, 2020, Phoenix, Arizona, USA.

All experiments and analysis were conducted by the candidate, the data of which feature in Chapter 4 and Chapter 5.

Acknowledgements

This research has been carried out with assistance gratefully received from individuals and organisations listed here, without whom this work would not have been possible.

I would first like to thank the Engineering and Physical Sciences Research Council (EPSRC) and Nuclear Decommissioning Authority (NDA) for funding this research through Next Generation Nuclear Centre for Doctoral Training (NGN-CDT) through grant EP/L015390/1. Thanks also to the University of Leeds for accommodating me and this PhD.

Next I would like to express my gratitude to my academic supervisors from the University of Leeds School of Chemical and Process Engineering, Professor Bruce Hanson and Dr Tim Hunter, whose guidance and expertise have been vital over the past five years.

Thanks to my industrial supervisor Dr James Goode from National Nuclear Laboratory who has provided me with valuable information, particularly spent nuclear fuel activity data. Additional thanks to David Hambley from NNL and to Martyn Barnes from Sellafield Ltd.

Huge thanks to University of Leeds technicians Chris Bulman and Bob Harris who can always be relied on to bail us out when things aren't working properly.

Further thanks to TRANSCEND and the NDA for providing additional funding to allow me to carry out the active irradiation aspect of this investigation, and to the National Nuclear Users Facility. Many thanks to the staff at the Dalton Cumbrian Facility who helped and supported me during the many weeks I spent working there. Particularly I would like to acknowledge the time and effort from a number of people. Thanks to Professor Fred Currell for accommodating my work during an especially challenging period. Huge thanks to Dr Mel O'Leary for his technical advice and knowledge leading up to, during and after the experimental. Thanks to Chris Anderson for helping me get up and running with the experimental work, training me on the equipment and offering a much needed helping hand. Thanks to Dr Aliaksandr Baidak for his guidance in using the SRIM/TRIM software. Finally I would like to thank Kevin Warren and Dr Andrew Smith for their assistance in operating the γ-irradiator and ion beam.

There are many others at the University of Leeds who have provided valuable services for which I am very grateful; Dr Faith Bamiduro, Dr Faye Esat and Mo Javed for providing XRD, Karine Alves Thorne, Dr Adrian Cunliffe and Lucy Leonard for carrying out TGA analyses, Dr Toby Lord and Les Arkless for providing

CT data, Rob Simpson for assistance and training in microscopy/EDX, Dr Ben Douglas for most of the particle analysis (PSD, BET specific surface area and pycnometry), and to Dr Jabbar Gardy for provision of powder and tapped density data.

Most importantly this project would not have been possible without encouragement and support from my friends and family. Thanks to my parents David and Caroline and Grandmas Sylvia and Margaret who were always keen to ask how things were going, and provided many words of encouragement. My brothers and sisters Katy, Mark, Sarah and Thomas who also always provide words, and though not always as encouraging they do help to raise spirits. Finally I owe a huge gratitude to Hayleigh, who has made many sacrifices of her own to enable me to pursue this work. It has taken us over five years and a pandemic. Thank you so much.

Abstract

This project aims to develop and test a process which will convert wet and corroded Magnox fuel to a stable physical form which allows interim extended storage in dry conditions, prior to disposal and consider how it may behave in dry storage.

Magnox reactors were the first commercial nuclear power reactors to be operated in the UK, and the fuel elements consisted of a uranium metal fuel bar clad in a Magnox outer can. The spent fuel from these reactors is typically stored underwater for shielding and cooling purposes then reprocessed at Sellafield, but a quantity of Magnox fuel remains unprocessed after the reprocessing plant closure in July 2022. Additionally there are large quantities of spent Magnox fuel which have been held in underwater storage ponds for several decades, and the material in these ponds has corroded significantly producing secondary wastes in the form of sludges, and hazardous sites for expensive remediation. Therefore there is a risk that any outstanding inventory of wet stored Magnox fuel could develop with no available disposal route as reprocessing will be incompatible or unavailable. Therefore an alternative solution is required for storage of Magnox fuel between reactor discharge and final geological disposal. One possible solution is to dry the wet fuel and hold in a dry store.

To initially investigate the feasibility of drying corroded Magnox, the corrosion products of inactive and unirradiated Magnox simulant have been characterised by X-ray diffraction, thermogravimetric analysis and computed tomography. Published data from these analyses are not widely available for both real and simulant materials, and in regard to computed tomography are novel in this context. From this analysis mechanisms for potential physical and chemical means for water hold up have been identified. Further to this, water removal has been performed by heating corroded Magnox under vacuum. The process is monitored by observing pressure, dew point, temperature and gas flow changes supported by measuring the sample mass loss as water is removed. Temperature during drying has been tested from 40-120 °C to observe the optimum temperature with respect to drying rate and level of dryness achieved by measuring the mass loss from water removal over time. From these tests it was observed that several hours vacuum/heat exposure is required before no further water is removed, and increasing temperature was seen to enable greater extent of dryness to be achieved over all temperatures investigated. It is beneficial to minimise water carryover into dry storage to reduce fuel/cladding corrosion but also to reduce the amount of hydrogen generated via water radiolysis. Despite the industrial interest in implementing vacuum drying, there are no externally published technical reports or

papers that detail the Magnox fuel drying process or conditions. This work provides some important and relevant technical basis for realistic vacuum drying conditions and material behaviour observations.

Given the requirements for elevated temperature and extended drying times, some residual water is almost guaranteed to be present during storage. To investigate the impacts of small quantities of water carryover, gamma and alpha radiolysis experiments were undertaken at the Dalton Cumbrian Facility to observe the hydrogen generation yields of low water content/vacuum dried magnesium hydroxide and hydromagnesite. These tests showed that at water content <25% the hydrogen formation rate is higher than that for bulk water, which is an important consideration if estimating radiolytic hydrogen generation for low water content corroded Magnox fuel. Additionally, irradiation of vacuum dried powders still yielded measurable hydrogen, with decreasing yields at increasing drying temperature up to 120 °C. Radiolysis of adsorbed water on metal oxides/hydroxides is important to various areas of the nuclear fuel cycle, but surprisingly little is published surrounding Magnox spent fuel/corrosion products when compared to the scale of the challenges faced by the industry. This work builds on the existing knowledge and provides further data to understand this interesting physical effect, and also states evidence for occurrence in a new and industrially important context.

Table of Contents

List of Tables

List of Figures

Glossary

Acronyms		Terms	
AL80	0.8 wt% Al Magnox alloy	μ	Absorption coefficient, cm^{-1}
AGR	Advanced Gas-cooled Reactor	D	Diffusion Coefficient, $m^2\ s^{-1}$
AVDS	Advanced Vacuum Drying System	f	Characteristic drying rate, mass $t^{-1}\ m^2$
ASTM	American Society for Testing and Materials	G	molecules $100eV^{-1}$
BET	Brunauer-Emmett-Teller	Gy	Gray, $J\ kg^{-1}$
CVD	Cold Vacuum Drying	H	enthalpy, J
CT	Computed Tomography	I	Intensity, W/m^2
DCF	Dalton Cumbrian Facility	L	Litre
DSC	Differential Scanning Calorimetry	m/M	mass, kg
DVS	Dynamic Vapour Sorption	N	Rate of drying, mass $t^{-1}\ m^2$
EDX	Energy Dispersive X-Ray	n	Amount, moles
ESEM	Environmental Scanning Electron Microscope	P	Pressure, bar/Pa
FGMPS	First Generation Magnox Storage Pond	R	Universal Gas Constant, $J\ K^{-1}\ mol^{-1}$
FIB	Focused Ion Beam	R_H	Hydrodynamic Radius, m
FT-IR	Fourier Transform-Infra Red	T	Temperature, °C/K
FHP	Fuel Handling Plant	u	internal energy, J
GC	Gas Chromatograph	V	Volume, m^3
ICDD	International Centre for Diffraction Data	X	Moisture content, w/w
LWR	Light Water Reactor	η	Viscosity, $kg\ m^{-1}\ s^{-1}$
LET	Linear Energy Transfer	ϕ	Characteristic moisture content, g/g
Magnox	Magnesium Non-OXidising alloy	ψ	Relative humidity, %
MSSS	Magnox Swarf Storage Silo		
MS	Mass Spectrometry		
MCO	Multi-Canister Overpack		
NNL	National Nuclear Laboratory		
NDA	Nuclear Decommissioning Authority		
PSD	Particle Size Distribution		
PWR	Pressurised Water Reactor		
SEM	Scanning Electron Microscope		
SE	Secondary Electron		
SIMS	Secondary ion Mass Spectrometry		
SSA	Specific Surface Area, $m^2\ g^{-1}$		
SNF	Spent Nuclear Fuel		
SRIM	Stopping and Range of Ions in Matter		
TCD	Thermal Conductivity Detector		
TGA	Thermogravimetric Analysis		
tHM	Tonnes Heavy Metal		
TORVIS	Toroidal Volume Ion Source		
TRIM	Transport of Ions in Matter		
XRD	X-Ray Diffraction		
ZR55	0.45-0.65 wt% Zr Magnox alloy		

Chapter 1 Overview, Aim and Objectives

1.1 Project Overview

Nuclear fission has been used a source of electricity generation since 1956[1] and in 2017 accounted for 20.8% of electricity produced in the UK.[2] Currently all UK nuclear energy is produced by four CO_2 cooled graphite moderated Advanced Gas-Cooled Reactor (AGRs) stations - the fuel for which consists of UO_2 pellets clad in stainless steel - and one water cooled and moderated Pressurised Water Reactor (PWR) station - using UO_2 pellets held in zirconium alloy cladding.[3] These reactors were preceded by a fleet of another type of gas cooled reactor known as Magnox reactors - the first commercial nuclear energy reactors built in the UK. The name "Magnox" is derived from the Magnesium Non-OXidising alloy which clad the uranium metal fuel rod. Energy has been produced by Magnox reactors since the first reactor Calder Hall was opened in 1956[1] up until the closure of the final UK Magnox reactor at Wylfa in 2015.[4] Spent Nuclear Fuel (SNF) is commonly stored under water in ponds following reactor operation to provide cooling and shielding while short lived fission products decay. A significant drawback to underwater storage of Magnox fuel is that both the Magnox cladding and the uranium metal fuel will react with the pondwater. Over time this corrosion causes issues for several reasons; it complicates the handling of the fuel, the pond water becomes contaminated with radioactive material, the corrosion products produce secondary wastes which must be managed, and some corrosion products (particularly magnesium hydroxide) form a sludge which affects visibility when disturbed.[5] Long term storage of Magnox spent fuel has resulted in hazardous areas at Sellafield, particularly the First Generation Magnox Storage Pond (FGMSP) and Magnox Swarf Storage Silo (MSSS) which are now priority remediation projects in UK nuclear decommissioning.

Wet storage is also common practice for AGR and Light Water Reactor (LWR) spent fuel, and the cladding of these fuel types is largely resistant to corrosion during wet storage, but alternative storage in dry conditions has also been employed. The IAEA reported that in 2008 there were 24500 tHM in dry storage, mostly used for zirconium alloy clad fuel.[5] In the UK there is demonstrated experience in dry storage of irradiated Magnox fuel at Wylfa station, where spent fuel is discharged directly from reactor into CO_2 filled tubes for storage pending reprocessing. Whilst dry storage is common practice, the drying of previously wetted and/or corroded Magnox fuel has been considered but not industrially practiced.[6] Removal of Magnox from underwater storage and performing drying could prevent unwanted further corrosion, enabling less hazardous and more

manageable storage conditions. In order to demonstrate the feasibility of transitioning Magnox spent fuel from wet to dry storage, investigations should be undertaken to test how Magnox cladding and corrosion may interact with or retain water. Water may be held physically or chemically and the extent of these interactions must be understood if a drying regime is to be adopted industrially. Also the presence of water during storage can lead to further chemical reactions with fuel and cladding, as well as radiolysis during storage.

The current state of experience is based on drying research on similar materials such as work performed at Hanford in 2000-2004 where vacuum drying was enlisted to process 2100 tonnes of corroded spent nuclear fuel consisting of uranium metal clad in zirconium alloy.[7] Similar technology is being considered and developed for UK management of AGR fuel.[8–10] When Magnox fuel is in contact with water for extended periods it will corrode to form magnesium hydroxide, so it is as important (if not more so) to understand how these corrosion products will behave under a drying regime. Literature of magnesium hydroxide drying is limited, with some relevant work that has investigated and compared drying differences between $Mg(OH)_2$ morphologies and nanostructures, and their variance under different drying parameters such as temperature.[11] Therefore research is required in this area to inform these approaches and understand any potential technical or safety implications. If the strategy of fuel drying is to be employed it is important to get a good understanding of how these materials will behave during and after a drying process.

As mentioned, radiolysis of any water carryover must also be taken into consideration to ensure hydrogen generation is under control and will not lead to pressurisation or flammable/explosive hazards. Hydrogen generation from water radiolysis is a well-studied area. Interestingly there is an area of work of relevance to this particular application that reports that adsorbed water in heterogeneous metal oxide-water systems can cause the surface water to generate hydrogen at a greater rate through an energy transfer mechanism.[12,13] Some work has been carried out which has observed this effect in magnesium hydroxide-water systems, but the amount of data on the subject is limited.[14] Additionally, further literature has proposed that γ-radiation can cause $Mg(OH)_2$ decomposition and liberate water/generate hydrogen, which must also be taken into consideration.[15,16] In order to support the industrial application of Magnox spent fuel drying it must be proven that Magnox fuel can be dried to adequately control these reactions occurring in interim storage.

1.2 Project Aim and Objectives

The aim of this project is to investigate and evidence whether wetted Magnox spent fuel cladding can be dried adequately to prevent corrosion/degradation during dry interim storage pending eventual disposal.

The objectives required to achieve this have been identified as follows:

1. Physical and chemical characterisation of (unirradiated) Magnox cladding fragment samples and corrosion products to predict avenues for water retention and carryover
2. Perform drying tests on simulant materials (initially inactive Magnox cladding) to identify optimal drying conditions
3. Identify implications of water carryover from drying with respect to radiolytic hydrogen generation in a radioactive storage environment

This thesis describes the progress that has been made towards completing these objectives and project aims as part of this work.

Chapter 2 Literature Review

2.1 Introduction

This section presents a brief review of relevant and existing published work in the research area, of which the primary topics are:

- An introduction to the history of UK Magnox reactors and the basis for this study
- Magnox cladding and fuel corrosion reactions with water and expected behaviours during dry storage
- Previous and established drying practices performed on nuclear material
- Introduction to relevant radiochemical information and discussion

2.2 History of UK Magnox Reactor Operations and Project Context

As mentioned, the first nuclear reactors operated in the UK were known as Magnox reactors. An illustration of a Magnox fuel can shown in Figure 2-1a taken from an IAEA (International Atomic Energy Authority) 2012 report.[5] The reactors were cooled by carbon dioxide, graphite moderated, and typically operated at temperatures up to ~410 °C. The Calder Hall reactors were the first in the UK to supply energy, consisted of 4 × 46 MWe reactors and had the lowest electrical power output of any UK civil Magnox stations. The last and greatest power output reactors were the 2 × 590 MWe reactors situated at Wylfa in Anglesey.[17]

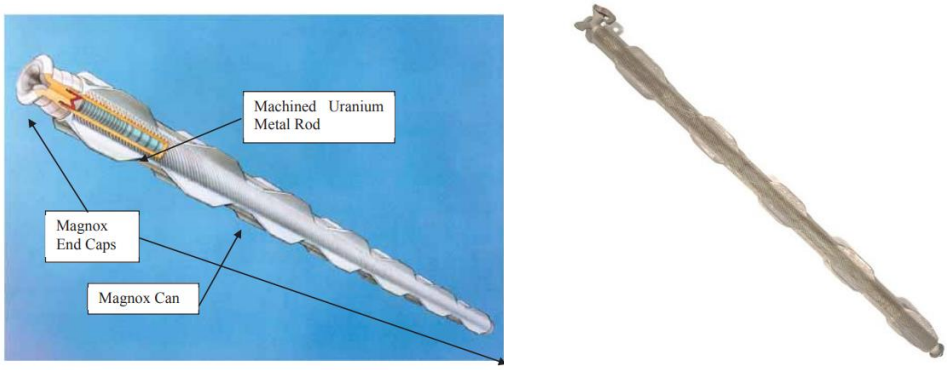

a) b)

Figure 2-1. a) Schematic diagram with cross section of typical Magnox can,[5] b) photo of typical Magnox fuel can

In the UK, significant quantities of corroded Magnox waste are held in ponds at Sellafield from first generation Magnox reactors, prior to decanning and reprocessing in the Magnox Reprocessing Plant. Extended storage in these pools has caused the fuel to degrade, generating significant volumes of additional wastes

which must be handled and disposed of. From this it is clear that underwater storage of Magnox is not viable for periods greater than a few years - historically up to 7 years has been considered "tolerable."[18] The Magnox Operating Programme (MOP9) was produced in 2012 and stated that reprocessing operations were expected to be completed in 2020. An announcement was released on World Nuclear News that the Magnox Reprocessing Plant was undergoing a controlled shutdown due to COVID-19.[19] In August 2020 a government update was released, stating Magnox Reprocessing Plant was to resume reprocessing operations with a view for completion in 2021, however this had remained ongoing with final completion in July 2022.[20,21] The latest announcement in the NDA Business Plan 2022-2025 (released March 2022) stated that 270 tonnes of fuel remain outstanding after closure.[3]

A 2015 Office for Nuclear Regulation (ONR) review[22] discusses the strategic importance of completing the Magnox reprocessing campaign, as it is fundamental to other high priority operations. The Magnox spent fuel is stored and decanned at Sellafield Fuel Handling Plant (FHP). Failure for the reprocessing plant to accept this fuel will increase the residence times and limit FHPs availability for other operations which will directly impact other important programmes, one of which being the high priority remediation of FGMSP. FHP is due to accept skips of fuel to mitigate risks from FGMSP and it is essential that the capacity is available. Remnant fuel is planned to remain in FHP, but as stated there are other needs for FHP so alternative interim options could be valuable.[3] One such option for interim management is dry storage.

2.3 SNF Wet Storage and Corrosion

The complications from wet storage most significantly arise from fuel corrosion, and the chemical/radiochemical production of hydrogen. Therefore the primary benefits from removal from underwater storage are to reduce chemical corrosion, reduce hydrogen generation from chemical reaction/radiolysis and to prevent further wet storage facility management costs whilst freeing current facilities to be repurposed or decommissioned. This section will focus on the Magnox cladding/uranium fuel corrosion aspects and potential Magnox corrosion products, but it should be acknowledged it is not within the scope of this work to study detailed corrosion information or mechanisms. Corrosion of Magnox fuel is complex, and the primary area of interest in this work is the surface and its interactions with/ability to retain water but some introductory information is included here.

2.3.1 Magnox cladding wet storage and corrosion chemistry

It is important during wet storage of all types of nuclear fuel that water chemistry is controlled such that; metal surface corrosion is minimised, the concentration of radionuclides in the storage pond is kept as low as possible, and the water clarity is maintained to enable ease of inspection and operations. The corrosion of steel clad AGR fuel, and zirconium alloy clad LWR fuel is manageable with corrosion rates reported as low as 1×10^{-6} µm/a for zirconium alloy and 0.1 µm/a for AGR cladding.[5] In order to reduce the corrosion of Magnox cladding during storage the ponds are maintained by dosing with sodium hydroxide to pH 11.5, and the presence of aggressive corrosion ions like Cl^- must be avoided as they can induce pitting corrosion. Aqueous storage of magnesium in pH 11.5 sodium hydroxide is known to form magnesium hydroxide and hydrogen according to Equation 2-1:[23]

$$Mg + 2H_2O \rightarrow Mg(OH)_2 + H_2 \qquad \text{Equation 2-1}$$

The magnesium hydroxide produced from this reaction forms a protective layer which can slow further corrosion, but the protective film can also be dissolved by the presence of acidic species - hence the desire to store the spent fuel in alkaline conditions to preserve the protective hydroxide as shown in Equation 2-2:

$$Mg(OH)_2 + 2H^+ \rightarrow Mg^{2+} + 2H_2O \qquad \text{Equation 2-2}$$

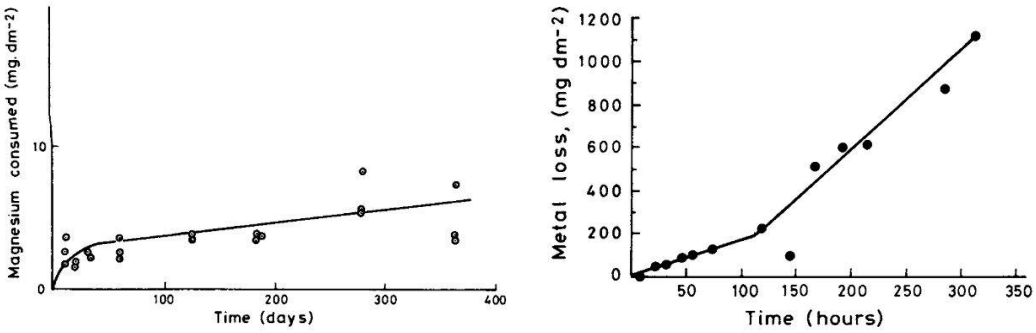

a) b)

Figure 2-2. Corrosion of etched Magnox AL80; a) at room temperature, b) in pH 11.5 sodium hydroxide solution at 100 °C (from Friskney et al.[24])

Safe storage of Magnox fuel in water has been demonstrated for 5 years at pH ≥11.4 (dosed with sodium hydroxide) and maintaining chloride and sulphate ion content <1 ppm.[5] Friskney et al.[24] state that thermodynamically magnesium oxide must exist between the metal and the hydroxide. They quote that in their work etched Magnox at ambient temperature initially corroded at a relatively high rate, which decreased over a period of days to the 'constant' rate of ~0.01 mg dm^{-2} d^{-1} (shown in Figure 2-2a, but note this precise rate is unclear from the diagram and is mentioned in the article). At higher temperatures this initial period of increased

corrosion rate is not as easy to observe as the rate transitions more swiftly to the 'constant' rate, as shown at 100 °C in Figure 2-2b. After a period of time at the 'constant' rate, the magnesium reaches a point referred to as 'breakaway,' and the rate switches to a new constant but elevated 'post-breakaway' rate. The time for the sample to achieve 'breakaway' decreases with increasing temperature, and is shown as ~120 hours at 100 °C. Friskney et al. reported that corrosion of etched Magnox AL-80 in steam at 10^5 Pa at temperatures of 100-300 °C formed various corrosion products. At lower temperatures up to ~225 °C magnesium hydroxide forms. Between ~160-225 °C magnesium hydride was observed to form and at temperatures >~200 °C magnesium oxide can form. Figure 2-2 shows how the corrosion rate in pH 11.5 sodium hydroxide solution increases significantly with increasing temperature up to 100 °C. This relationship is further described in Figure 2-3, which includes NaF doped solutions as the presence of fluoride has also been shown to inhibit Magnox corrosion. On this basis it is clear that increasing the temperature significantly increases the pre- and post-breakaway Magnox corrosion rates. As mentioned, the principle corrosion product from the reaction between Magnox and pond water during storage is $Mg(OH)_2$ (commonly known as brucite),[25] but other corrosion products have also been reported such as magnesium carbonates.[26]

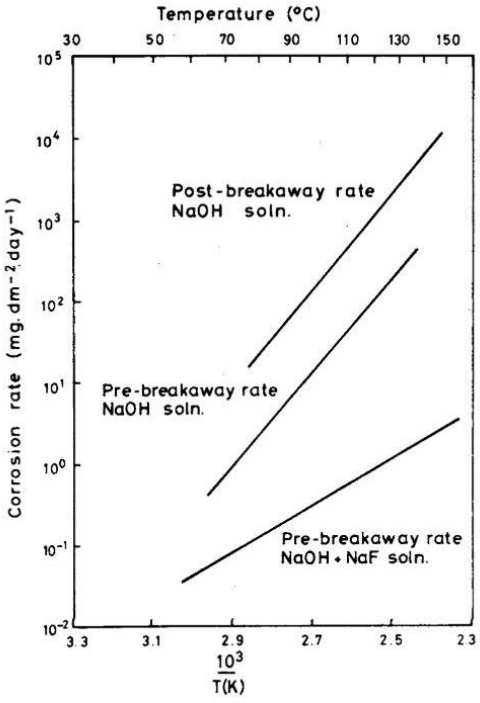

Figure 2-3. Relationship between Magnox AL-80 corrosion rate with temperature in pH 11.5 sodium hydroxide solution and fluoride dosed solutions (taken from Friskney et al.[24])

Gregson et al.[27] performed characterisation on sludge samples collected from legacy storage ponds at Sellafield by Environmental Scanning Electron Microscopy

(ESEM) with Energy Dispersive X-Ray (EDX) analysis, micro-Raman spectroscopy and Fourier transform infra-red spectroscopy (FT-IR). Some of their SEM images are included below in Figure 2-4, where they report several observable morphologies, predominantly that of interlocking hexagonal platelets, but also 1-10 µm rods as shown in Figure 2-5. Their analysis is consistent with brucite, but suggest the storage ponds may also contain species such as hydrotalcite ($Mg_6Al_2(CO_3)(OH)_{16}.4H_2O$) and some other Mg-hydroxycarbonate species such as artinite, $Mg_2CO_3(OH)_2 \cdot 3H_2O$. It is not surprising that hydroxycarbonates and similar compounds may form in the storage ponds as they are open to the air, allowing them to take in airborne particulates, organic matter from seabirds and CO_2. The formation of hydrotalcite given the relatively high magnesium : aluminium ratio of 6:2 compared to the 0.8 wt% aluminium in Magnox AL80 alloy suggests there may be a presence of an external source of aluminium in the storage ponds. Aluminium is a reactive metal but passivates by forming a thin (50-100 Å) oxide layer at the surface which is stable between pH 4-8. As the storage ponds are at pH ≥11.4 any metallic aluminium will quickly undergo alkaline dissolution and form $Al(OH)_4$ ions.[28]

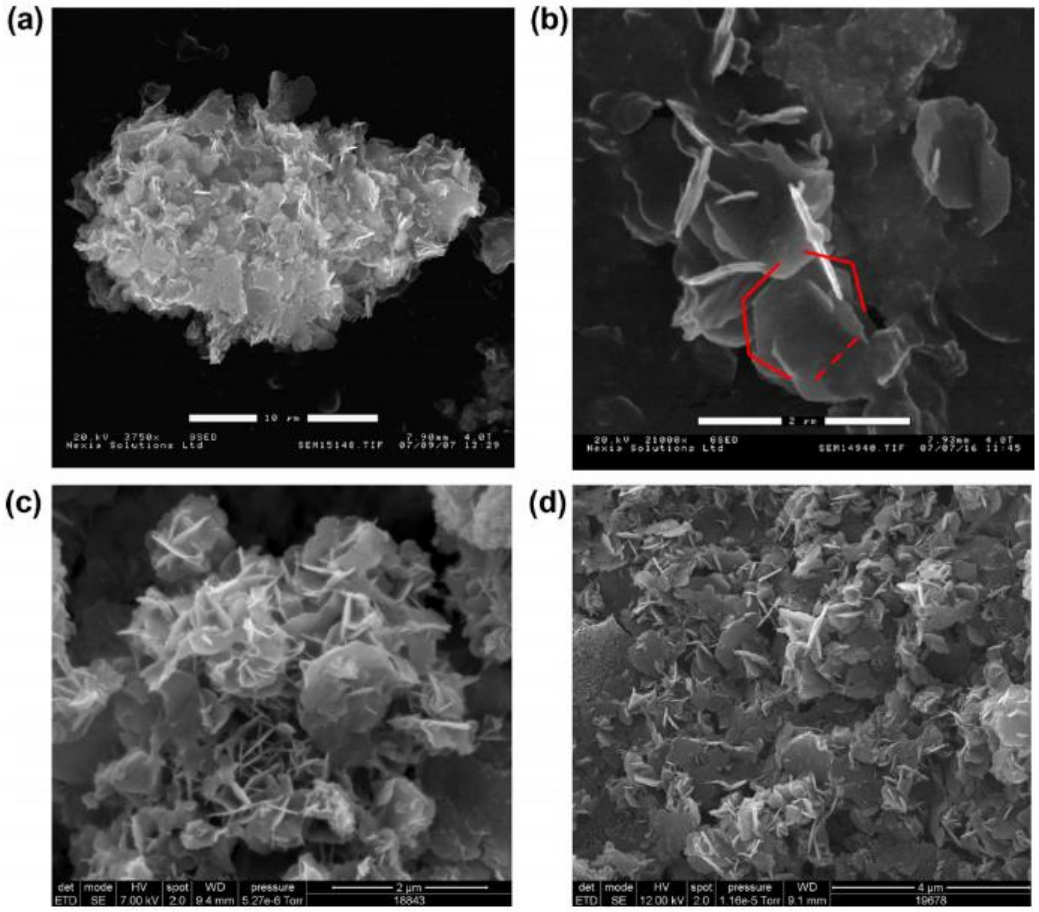

Figure 2-4. SEM images showing predominant platelet morphology; a) colloidal particle, b) expanded from (a) showing interlocking platelets, c) interlocking platelet morphology, d) corroded Magnox sludge simulant showing similar morphology (taken from Gregson et al.)[27].

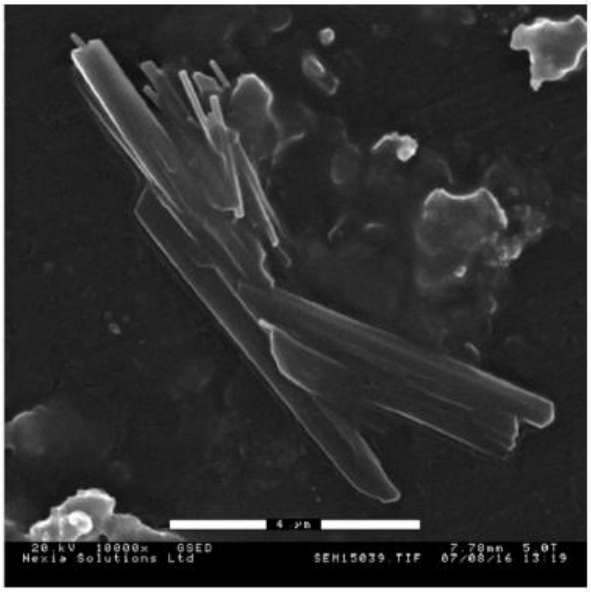

Figure 2-5. SEM of rod-like crystallites from suspended solids recovered from legacy spent fuel nuclear storage ponds (taken from Gregson et al.[27])

Hallam et al. performed corrosion tests on magnesium, Magnox AL80 and Magnox ZR55 (a similar alloy containing 0.45-0.65 wt% zirconium used to manufacture "splitter blades" which were employed to strengthen some cans in-reactor against distortion) in air at varying dryness from 200-80000 vppm, as well as with/without CO_2.[30] They performed tests where Magnox AL80, ZR55, and magnesium discs were exposed to observe and compare corrosion rates in different conditions:

- Flowing moist air with CO_2
- Static moist air with CO_2
- Flowing moist air without CO_2
- Static moist air without CO_2
- Static dry air without CO_2
- Flowing moist argon without CO_2
- Static dry argon without CO_2

Their data is extensive so a brief overview is included here. Figure 2-6 and Figure 2-7 show the corrosion rates for the Magnox AL80 and Magnox ZR55 respectively observed over time at 86-92 °C under the different conditions listed above. Magnox AL80 initially demonstrated no measurable corrosion rate in flowing air containing water vapour. Flowing air without CO_2 showed a detectable rate of corrosion which was greater during the second period of exposure. On changing the gas from air to argon with no CO_2, a further increase in corrosion rate was observed. Exposure of Magnox AL80 to moist air without CO_2 demonstrated a significant corrosion rate, higher than that seen in argon (although it is acknowledged the water vapour concentration was greater in air), and when changed to normal air containing CO_2

the corrosion rate reduced. The tests on Magnox ZR55 showed different trends to that of Magnox AL80. Initially in moist air there was no observable mass increase, which was sustained during the initial period of exposure to moist air with no CO_2, followed by a corrosion rate increase comparable to that of AL80. The following rate of corrosion in argon without CO_2 was greater than that observed in moist air, but less than the corresponding conditions for AL80. The most significant difference was that almost no corrosion was observed in moist air with no CO_2 present, where notable corrosion was observed in AL80. Interestingly on subsequent exposure to moist air with CO_2 present the corrosion rate went on to increase to a comparable rate to AL80.[30]

The most consistent trend of the corrosion data is that the presence of moisture is the governing condition that most affects Magnox corrosion. In dry conditions even in the absence of CO_2 and in air the observed corrosion was little to none. With moisture present, CO_2 is able to inhibit corrosion and removal of CO_2 was almost always accompanied by an increase in corrosion except for the example with Magnox ZR55 in Figure 2-7ii.

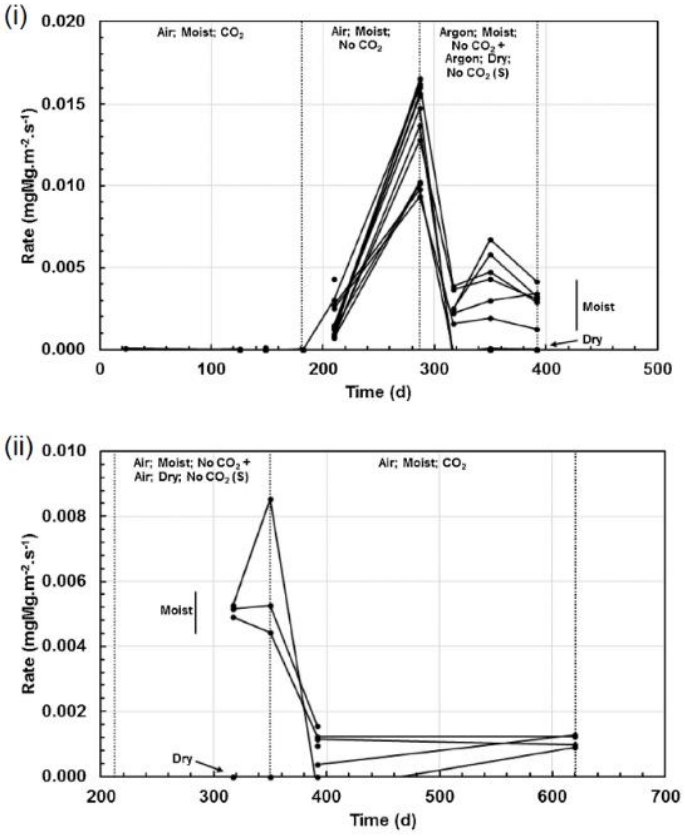

Figure 2-6. Measured corrosion rates for Magnox AL80 under conditions as specified – n.b. different X-axis scales on (i) and (ii) (Figure from Hallam et al.[30])

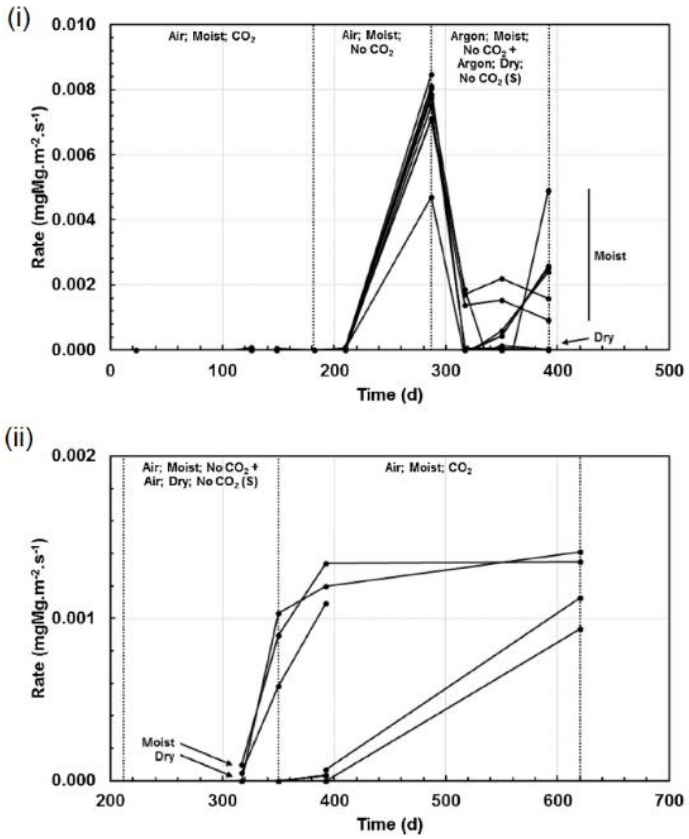

Figure 2-7. Measured corrosion rates for; Magnox ZR55 under conditions as specified – n.b. different X-axis scales on (i) and (ii) (Figure from Hallam et al.[30])

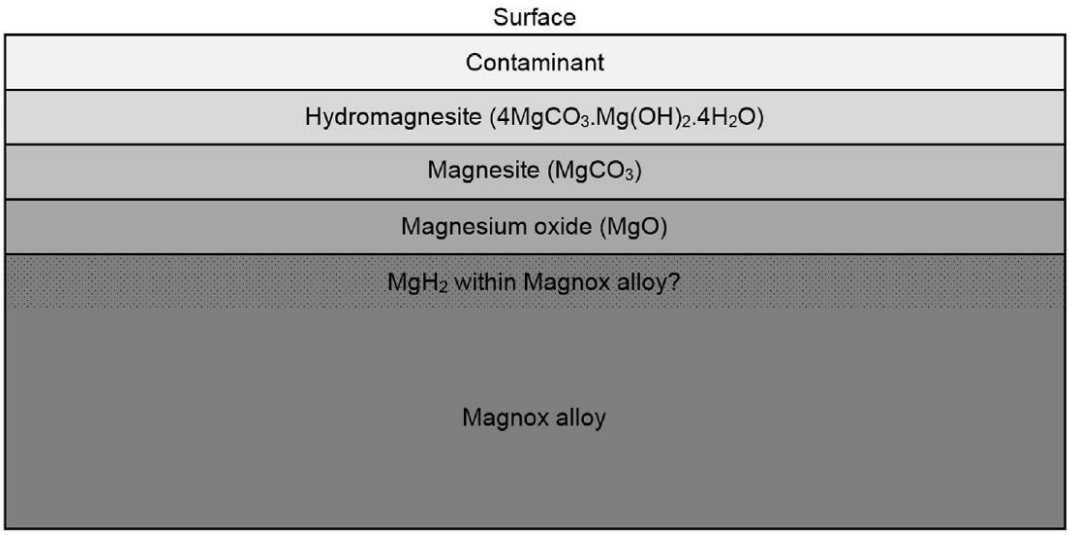

Figure 2-8. Proposed multi-layer corrosion product structure – layer thickness not representative (from Hallam et al.[30])

CO_2 inhibition has been discussed in the literature[31,32] and some discussion of this mechanism is included later. Given that the cladding of the fuel is made from Magnox AL80, the ZR55 data is of some interest but is less relevant. Also notable is that corrosion occurs in the presence of moisture whether in air or argon, although these rates are reduced in argon. Hallam Et. Al. also performed characterisation on

the corrosion products formed by X-Ray Diffraction (XRD), Scanning Electron Microscopy (SEM) and Energy Dispersive X-Ray (EDX) microanalysis, Focused Ion Beam (FIB)-SEM and Secondary Ion Mass Spectrometry (SIMS) in an attempt to identify the different corrosion products formed at the Magnox surface. Figure 2-8 shows a proposed Magnox corrosion product structure. Using SIMS the surface was sputtered away, allowing the species found at various depths to be monitored. The depth profiles suggested that several corrosion product layers were present but the signal resolution was not clear enough to definitively resolve all thin corrosion product layers, however it was possible to estimate the order of layers. From this work they speculate the formation of a corrosion product structure as shown in Figure 2-8. They go on to discuss a possible mechanism for the CO_2 corrosion inhibition. In a paper by White[33] an isothermal phase diagram is included (Figure 2-9) which predicts that at the solid-vapour region, at 400 ppm CO_2 (roughly atmospheric conditions)[34] and at water concentrations >3000 ppm the expected magnesium corrosion product is hydromagnesite, at ≤3000 ppm it is magnesite ($MgCO_3$), and at CO_2 concentrations less than 10 ppm and water concentration >1500 ppm the expected product is brucite, $Mg(OH)_2$. This suggests that magnesite or hydromagnesite forms in the presence of CO_2, and is more protective and prevents breakaway corrosion, unlike brucite which forms in the absence of CO_2. The three dimensional magnesite structures are held by ionic bonds and are better able to resist compressive stresses from corrosion, as opposed to the brucite layered structure which is held by weaker hydrogen bonds and spalls away more readily.[30]

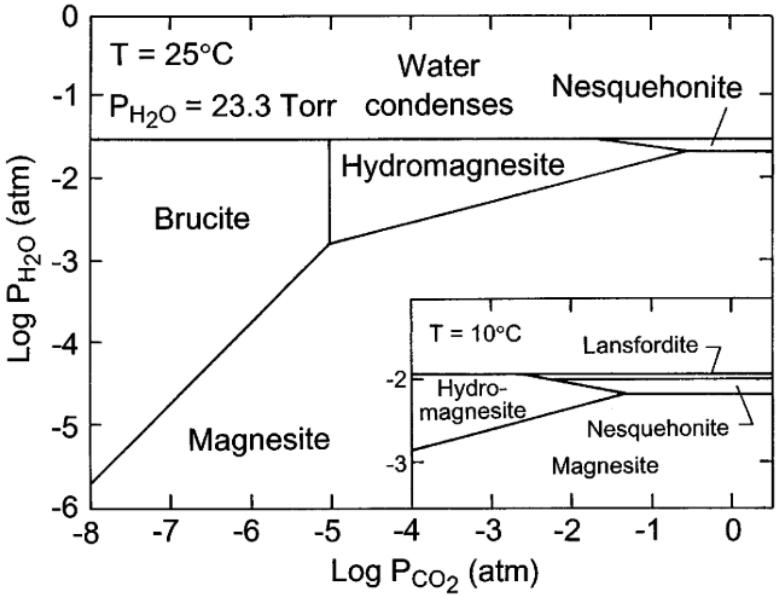

Figure 2-9. Phase diagram for MgO-CO_2-H_2O in solid-vapour region – main diagram for 25 °C with insert at 10 °C (taken from White[33])

2.3.2 Magnox uranium wet storage and corrosion

In addition to the susceptibility of the Magnox cladding to corrosion during wet storage, the same must be considered for the fuel bar itself. Magnox fuel contains a solid bar of uranium metal, which is also known to react with anoxic (without dissolved oxygen) liquid water below ~350 °C to form UO_2 and hydrogen as shown in Equation 2-3:[35]

$$U + 2H_2O \rightarrow UO_2 + 2H_2 \qquad \text{Equation 2-3}$$

The presence of hydrogen, especially during sealed storage over an extended period of time has the potential to react with uranium metal to form pyrophoric uranium hydride (Equation 2-4), which can go on to react with further water to form more UO_2 as described by Equation 2-5:[35]

$$U + 1.5H_2 \rightarrow UH_3 \qquad \text{Equation 2-4}$$

$$UH_3 + 2H_2O \rightarrow UO_2 + 3.5H_2 \qquad \text{Equation 2-5}$$

The potential for uranium hydride formation during interim storage is of concern due to the pyrophoric nature of the compound and its potential ignition risk. Uranium hydride has been formed in lab conditions with 2.5% H_2 in argon at temperatures as low as 30 °C.[36,37] The reaction between uranium hydride and air can be very rapid, and so it is important to ensure that conditions where UH_3 may form are avoided during interim storage by ensuring adequate drying is performed, thus removing the opportunity for water and uranium to react and liberate hydrogen if held in sealed storage.

Thermodynamically the most stable uranium oxide is U_3O_8 (ΔG_f -3369.5 kJ/mol at 298.15 K) compared to UO_2 (ΔGf -1031.8 kJ/mol at 298.15 K), but UO_2 is the most reported oxidation product in studies performed at <300 °C as it is more kinetically favourable.[38] Therefore it would be expected that UO_2 will be the most prevalent uranium oxidation product in wet storage conditions.

2.3.3 Simulating spent Magnox fuel

During irradiation in a reactor, the fuel cladding interacts with the carbon dioxide coolant and a surface layer consisting of mainly magnesium oxide and carbon is formed.[24] The formation of a magnesium oxide/carbon surface layer can be simulated in a laboratory by heating samples in Magnox reactor conditions. During operation the fuel cans in Magnox reactors can achieve temperatures of 250-450 °C in carbon dioxide.[30] Heating Magnox samples to these temperatures in the presence of carbon dioxide should produce a comparable surface to that of spent fuel if allowed representative exposure time. Friskney et al. state that despite these differences the final corrosion rates in sodium hydroxide solution for etched

and pre-oxidised Magnox are very similar.[24] They also note that at higher temperatures, the preoxidised Magnox exhibits an induction period which is attributed to the hydration of the magnesium oxide, but that this hydration does not progress to completion before the magnesium corrosion initiates, so any preformed magnesium oxide is not completely protective. Given that the drying process if introduced would be following several years of wet storage it would be expected that any effects of this incubation period from a semi-protective oxide layer would no longer be effective and would not need to be considered.

2.4 Characteristics of material drying processes

2.4.1 Industrial drying introduction

Drying usually relates to the application of a procedure to remove moisture to create a solid dry product. Moisture can be held in a number of ways on the surface or within pores. If a liquid in a system exerts a vapour pressure less than that of the same pure liquid, it can be considered as *bound* moisture, with any excess to this considered *unbound* moisture.[39] The vapour pressure of a substance corresponds to the pressure exerted by a vapour in a closed system where a vapour and liquid are both present together in thermodynamic equilibrium at a given temperature. This is dependent on temperature such that an increase in the system temperature will encourage more water to vaporise and exert a greater vapour pressure. Increasing the temperature of a liquid/vapour beyond the *critical temperature* will cause that phase to become by definition a gas.[40]

Thermal drying is governed by two processes. The transfer of heat to evaporate surface water, and internal mass transfer from moisture migration to the surface, and then through evaporation by the first process. The rate at which this is achieved depends on how heat is transferred from the environment to the material by conduction, convection and/or radiation, and in almost all cases heat is supplied at material boundaries and must conduct within. The evaporation is dependent on the conditions such as temperature, pressure, air flow/humidity and available surface area. The internal moisture migration is determined by the temperature, moisture content and the physical nature of the solid. Any of these factors can be the rate determining step in a drying operation. Moisture can be transported within a solid by several mechanisms such as liquid diffusion, vapour diffusion, Knudsen diffusion (e.g. under low temperature and pressure such as freeze drying conditions) and through hydrostatic pressure differences where internal vaporisation exceeds vapour transport through material to the environment.[39]

2.4.2 Water vaporisation

Evaporation of surface water occurs as a liquid comes in to contact with a dry gas, where the liquid forms a vapour which then exerts a partial pressure over the liquid. The partial pressure, P_w (assuming ideal behaviour) is equal to:

$$P_w V = \frac{m_w}{M_w} RT \;\; or \;\; P_w V_w = RT \qquad \text{Equation 2-6}$$

Where m_w is mass of water in the gaseous phase, M_w is total mass of water, V is volume, T is temperature and R is molar gas constant. The upper limit to P_w at a set of conditions defines the saturated vapor pressure, P^0_W. Plotting saturated vapor pressure on a pressure-temperature phase diagram produces liquid-vapor line *TC* (shown in Figure 2-10, taken from Mujumdar[39]) and at all positions on this line the liquid and vapour can be found together in equilibrium in saturated liquid/saturated vapour states. Point *T* is the triple point where all phases solid, liquid and vapour can coexist. Point *C* shows the critical point where no distinction between phases can be observed and all characteristics are equivalent to that of vapour.

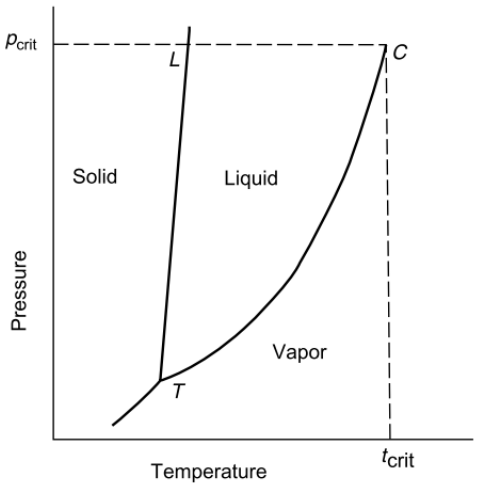

Figure 2-10. Pressure-temperature phase diagram (from Mujumdar[39])

At constant pressure the Clausius-Clapeyron equation describes the vapour pressure-temperature curve to the latent heat of vaporisation:

$$\frac{dP^0_W}{dT} = \frac{\Delta H_W}{T(V_W - V_L)} \qquad \text{Equation 2-7}$$

Where V_w and V_L are specific molar volumes of saturated vapour and saturated liquid, and ΔH_W is molar latent heat of vaporisation.

The enthalpy, *H* of a system is equal to its internal energy, *u* plus the product of the pressure, *P* and specific volume, *V*. Absolute enthalpies are not known but can be considered relative to each other. Figure 2-11 is taken from Mujumdar and shows a typical enthalpy-temperature relationship of a substance.[39] The diagram shows

example lines of constant pressure, and below critical temperature T_c a line of saturated vapour/saturated liquid is visible. The distance between these two lines, for example between points *L* and *V* at constant temperature corresponds to the latent heat of vaporisation at that temperature, and this value decreases with increasing temperature up to the critical point.

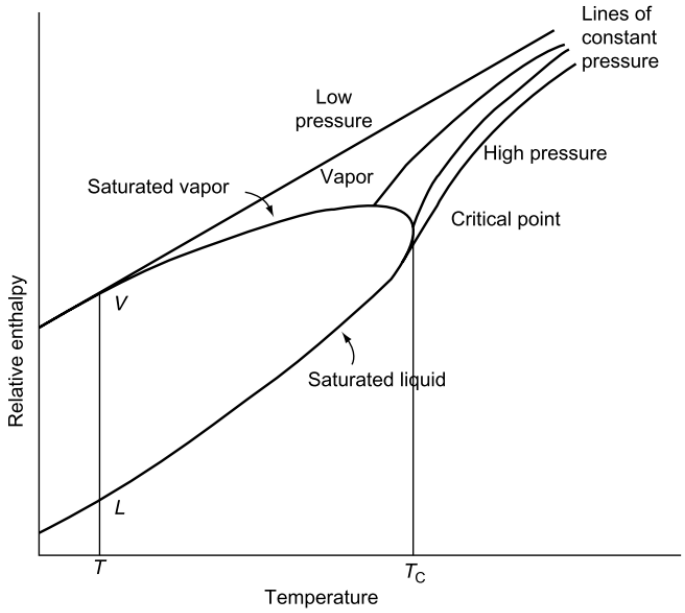

Figure 2-11. Example of enthalpy-temperature diagram

The heat capacity of a substance is defined as the heat required to raise the temperature of a unit mass of the substance by a given temperature, and the slopes of the isobars in Figure 2-11 yield the heat capacity under those conditions.

As a gas comes in to contact with a liquid, vapour will evolve from the liquid phase until the partial pressure reaches the vapour pressure at that temperature. In the context of moisture in a gas (e.g. air) this can be discussed as an absolute humidity from the ratio of mass of water to mass of gas (air). The relative humidity, ψ of a vapour-gas mixture is the ratio of the partial pressure to the saturated pressure at the same temperature (Equation 2-8):

$$\psi = \frac{P_W}{P_W^0} \qquad \text{Equation 2-8}$$

If the partial pressure of the vapour in the mixture is less than the vapour pressure of the liquid at that temperature, then the mixture is unsaturated.

2.4.3 Psychrometry and dew point

Psychrometry can be described as the study, measurement and determination of atmospheric conditions,[41] particularly in relation to moisture in air. The area has a great depth of understanding for thermodynamics of vapour/gas systems, and some

basic terms of relevance to this work are introduced here. One such term is the dew point – the temperature that a gas-vapour mixture will become saturated under cooling at constant pressure. Figure 2-12 is taken from Mujumdar[39] and displays the concept of a dew point. If an unsaturated mixture at point *F* is cooled, it will continue to saturate until it reaches the saturation point *G*, which corresponds to the dew point T_D. Any further cooling beyond this point will result in liquid condensation.

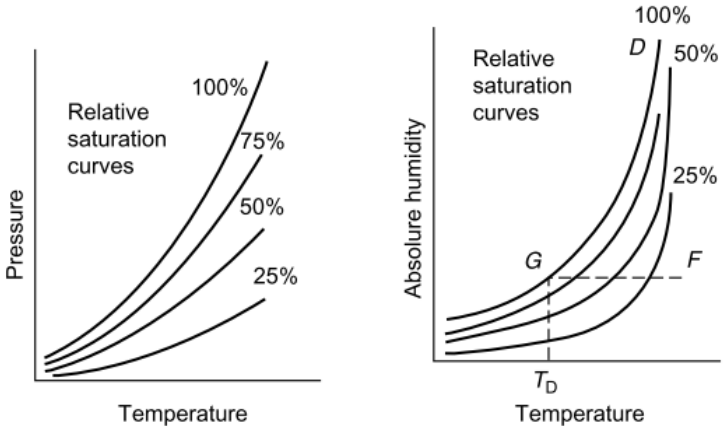

a) b)

Figure 2-12. Two psychrometric charts; a) relative saturation curves with respect to pressure and temperature, b) relative saturation curves with respect to absolute humidity and temperature

This has defined some terms and conditions relevant to discussion of the surrounding gas volume and water vapour from drying, but additionally it is important to consider what processes are occurring in the mass transfer within the wet material.

2.4.4 Conditions within wet solids during drying

During heat transfer to a solid, an internal temperature gradient is present and moisture can migrate towards the solid surface by mechanisms such as diffusion, capillary flow, pressure changes from material shrinkage and vaporisation/condensation cycles. This internal movement of water can be the determining factor in a drying process, and longer residence times/higher temperatures become increasingly important in these contexts. Solids can be classified under the following properties:[39]

- Nonhygroscopic capillary-porous media – e.g. sand/crushed minerals, where there is recognisable pore space, which is filled with liquid if saturated and air if dry, the amount of physically bound moisture is negligible and it does not experience shrinkage during drying.

- Hygroscopic-porous media – which can be subdivided into a) hygroscopic capillary porous media with macropores and micropores, e.g. clay and wood, and b) strictly hygroscopic media with only micropores e.g. zeolites. In these materials there is recognisable pore space, large amount of physically bound liquid and shrinkage often occurs during drying.
- Colloidal (nonporous) media – e.g. soap, glue some food products, where there is no pore space so evaporation takes place at the surface and all liquid is physically bound only.

The moisture content of a solid is usually expressed as the moisture content by weight per unit weight of wet or dry solid. The wet-weight basis of moisture content is defined as the moisture in a material as a percentage of the weight of wet solid. The dry-weight basis of moisture content considers moisture as a percentage of bone-dry material. Therefore a 50% moisture on wet-weight (w/w) basis denotes 50 parts by weight of water per 100 parts by weight of wet material. Conversely 50% moisture by bone-dry (b/d) weight constitutes 50 parts of water by weight per 100 parts of bone-dry material. Therefore if the 50% wet-weight example were converted to dry-weight basis, it would account for 100% moisture content (b/d), but the 50% bone-dry weight example would only represent 33% wet-weight water content.[42]

A dry material is described as hygroscopic if it will take up water whilst also reducing the vapour pressure. This is a product of molecular structure, solubility and extent of available surface. Figure 2-13 is an example from Mujumdar[39] which displays an isotherm of moisture content variation with increasing relative humidity. In section A the first monolayer of water coverage forms, then into section B double and multiple additional layers will form, and capillary condensation can also occur. In section C the increasing slope gradient is from further capillary condensation, which continues to the maximum hygroscopicity, X_{max} at equilibrium when relative humidity is at 100%.

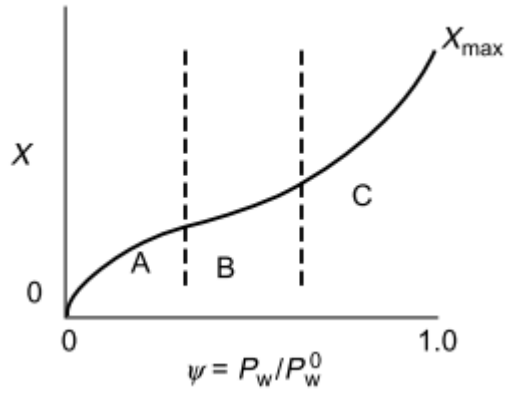

Figure 2-13. An example isotherm of moisture content, X against air saturation, ψ

2.4.5 Forms of residual water and retention

Water can be retained in a solid within capillaries, in solution within cellular structures/solid, or chemical/physical adsorption on the surface. *Free moisture* content is the amount of moisture that can be removed at a given temperature and includes both bound and unbound moisture components.[39] An American Society for Testing and Materials (ASTM) Standard has been prepared to outline best drying practices for drying SNF,[43] and it describes the various forms of water which are likely to be encountered in the drying of SNF and should be treated appropriately during drying and may persist after treatment:

- Unbound water - potential sources include surface water, trapped water or water in capillaries
- Ice - during vacuum drying the energy removed from the liquid by evaporation may be adequate to cause remaining water to freeze
- Physisorbed water - weakly bound to all surfaces (internal and external) of SNF and can be removed at relatively low temperatures by vacuum drying or forced gas dehydration
- Chemisorbed water - can be held in hydroxides and hydrates of oxidised materials, which may release the water when exposed to enough thermal energy or ionizing radiation

The most important forms of water to be considered in the drying of spent nuclear fuel/corrosion products are physisorbed/adsorbed and chemisorbed.

2.4.5.1 Adsorbed and condensed water layers

In gas/solid systems, adsorption takes place at the surface outside of the solid structure. The adsorbed species are known as the *adsorbate*, and the *adsorptive* describes the unadsorbed fluid phase. As mentioned, adsorption can be as physical (physisorbed) or chemical (chemisorbed). Physisorption is a very common occurrence that arises when any adsorbable gas is in contact with a suitable solid (*adsorbent*). The overall process summarised as physisorption can be broken down by contributions from electrostatic, dispersion, induction, repulsion and hydrogen bonding interactions between the water and the substrate.[44] For instance, Ewing calculates the electrostatic binding energy for a water molecule in the first monolayer at the surface of an NaCl crystal is comparable to the energy of a hydrogen bond, but the binding energy in higher layers has negligible electrostatic binding energy. Electrostatic binding of Mg^{2+} ions would be greater than that for NaCl due to the +2 ionic charge (c.f. Na^{+}) coupled with smaller ionic radius. Therefore the first water layer on the surface of some materials can be bound relatively strongly and this energy must be overcome to remove it. The same also

applies to dispersion, repulsion and induction energies. Water molecules within each layer will participate in hydrogen bonding, and higher layers will be able to interact with the layer directly below. If the substrate is hydrophilic (for example with the presence of hydroxyl groups in $Mg(OH)_2$) hydrogen bonding may also be available between the adlayer and substrate and provide additional binding energy.[45] The extent of surface covered by the adsorbate is commonly described in terms of fractional coverage, Θ:[40]

$$\theta = \frac{Number\ of\ occupied\ adsorption\ sites}{Number\ of\ available\ adsorption\ sites} \qquad \text{Equation 2-9}$$

Chemisorbed species are more firmly bound than physisorbed through formation of chemical (e.g. covalent) bonds. If the gas molecules penetrate the surface layer into the bulk phase of the solid then the species is deemed to have been absorbed within the medium, and it can be difficult to distinguish between these states from external measurement. Conventionally the term adsorption describes the process of molecules forming bonds with the surface of the adsorbate, where the opposite is known as desorption. This system can be described in three zones; solid, gas and adsorption space/layer. If an adsorbent is porous, the available surface for adsorption can be divided by external and internal (within pore and including all pore wall) surfaces.[46]

Mineral surfaces can support water films of various thicknesses and structures by several processes, as demonstrated in Figure 2-14 (taken from Yeşilbaş and Boily).[47] Water vapour binding on a hydrophilic low-solubility minerals occurs by two stages. The first is through adsorption where water molecules attach to the mineral surface through intermolecular interactions and hydrogen bonding. Water film thickness is dependent on the nature of the substrate, water vapour pressure/relative humidity and temperature. In the case where films are of the order of 1 nm, both the liquid-substrate and liquid-vapour interfaces affect the water properties. This film is found on effectively all surfaces under ambient conditions and can have a significant effect on the properties of the substrate material, and the chemistry of such films can vary significantly from that seen in bulk water. Despite the more ordered entropic opposition to monolayer formation, these water monolayers are driven by the enthalpic gains.[45,48] The second stage of deposition through condensation relies predominantly on water-water interactions where water nanodroplets can grow and coalesce into multiple layers with more liquid water-like behaviour. It can occur on open surfaces and within capillaries, in the interlayers between sheets or in spaces between aggregated particles. This effect is largely independent of the mineral composition.[47]

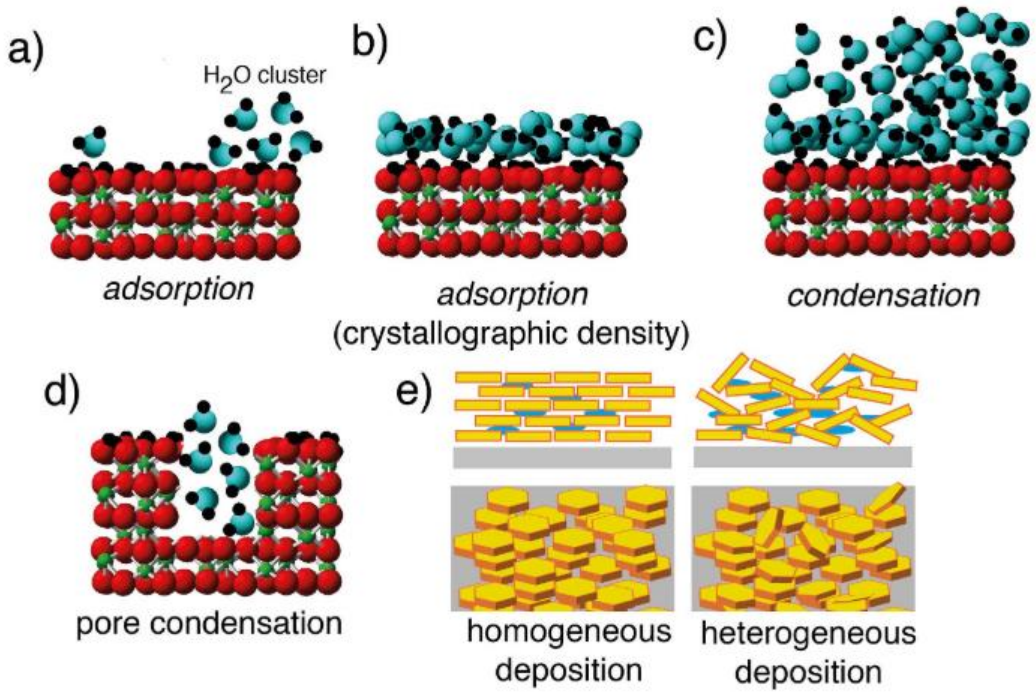

Figure 2-14. Representation of water vapour binding to mineral surfaces; a) adsorption and formation of water clusters, b) adsorption completion and monolayer formation, c) condensation regime where water-water interactions are dominant, d) capillary/pore condensation, e) interparticle condensation in homogenous and heterogeneous particles

Yeşilbaş and Boily observed water vapour deposition on a range of mineral samples.[47] In their work they observed how particle size affected the amount of adsorbed and condensed water the particles could support under ambient (25 °C) conditions by Dynamic Vapour Sorption (DVS). They report that water loadings from vapour condensation are strongly affected by particle size, where micron-sized particles with specific surface area ~10 m^2/g promote water condensation (with reported coverage of 120-2300 monolayers H_2O). Sub-micron particles were reported to support lower water loadings by condensation, of up to ~5 monolayers H_2O. This difference is put down to lack of availability of surface regions or interparticle spaces between sub-micron particles to promote condensation reactions.

Some work has been performed on magnesium oxides and surface water adsorption, and the majority of published work focuses on MgO rather than magnesium hydroxide. Foster, Furse and Passno were investigating water adsorption on MgO and the resulting FTIR spectrum showed a sharp feature at 3700 cm^{-1}. They attributed this to hydroxyls that had formed on the crystallite faces over the course of the several days experimentation, despite the roughly ambient temperatures of up to 40 °C and low pressure at ≤25 mbarA.[49] The formation of $Mg(OH)_2$ from MgO is thermodynamically favourable[45] and it is interesting to note this was observed under these relatively mild conditions. They were able to detect

islands of ~0.1 µm in height forming from adsorbed water dissolution/reaction over the course of the process. The surface before exposure is shown in Atomic Force Microscopy (AFM) images in Figure 2-15a (clean MgO surface, taken from Foster[50]) and the islands of corrosion post-exposure are visible in Figure 2-15b (after ~100 h, 25 mbarA water vapour, taken from Foster[50]).

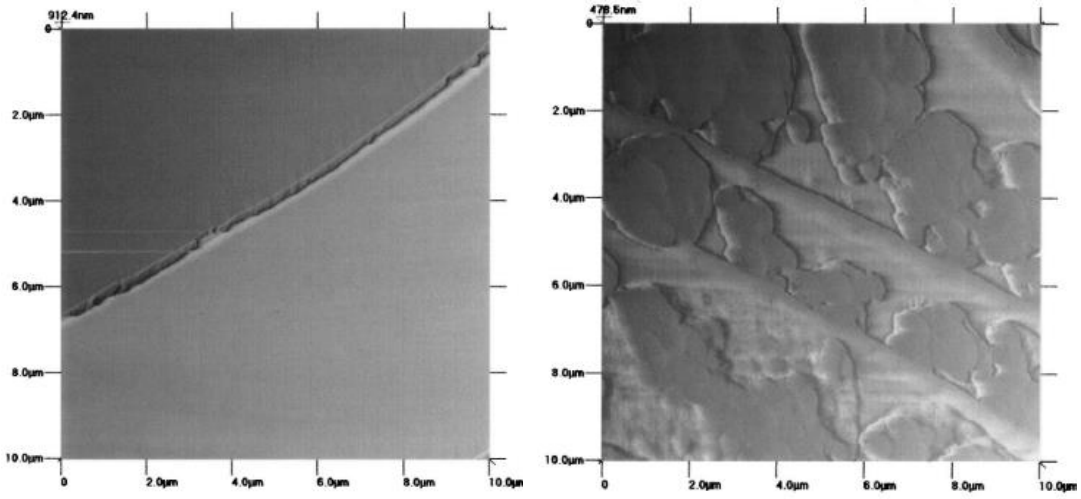

a) b)

Figure 2-15. AFM images of MgO; a) clean as-cleaved, b) MgO following 100 h exposure to H_2O vapour at 25 mbar (taken from Foster[50])

From this we can see the processes by which water becomes bound to and retained on the surfaces of potential spent fuel materials. Now it is important to consider how this may affect the drying process.

2.4.6 Drying mechanisms

Drying can occur through evaporation, where temperature is raised to the liquid boiling point, or by vaporisation where heat transfer comes from convection of warm gas/air which picks up moisture from the material and removes it. Things that must be considered for drying are the solid physical characteristics and temperature sensitivity. Drying behaviour is often measured as a function of reduction in moisture content over time, which may be monitored by humidity changes and continuous or intermittent weighing. Figure 2-16 is from Mujumdar[39] and shows a typical relationship between drying rate and time for a hygroscopic material under constant conditions. During the initial stage vaporisation occurs from the free surface water and the rate is determined by diffusion of water vapour over the air-moisture interface. As this surface water is removed, further drying requires water to be drawn to the surface through capillary forces. Over time the surface will develop dry spots where drying rates are reduced, and whilst some areas will remain wet and will continue to dry at the initial rate, the overall rate is seen to drop

as in the second drying stage – unsaturated surface drying period at the critical moisture content, X_{cr}. The second stage will continue until the surface liquid has completely evaporated and can constitute the majority of the period of falling rate, or can equally be unobservable depending on the material in question.

As further drying is applied and the process enters the third stage, the rate is defined by moisture movement through the solid from concentration gradients from within to the surface. Here the drying rate for many materials is increasingly influenced by the capacity for heat transfer into the deeper material structure, and the ability for moisture to diffuse to the surface. In some cases such as for denser materials with narrow pores/capillaries, the resistance to diffusion here can be an additional factor. During this stage, some water held by sorption is also removed. As the moisture content further lowers, the drying rate also falls, until the moisture content reaches an equilibrium value for the drying conditions. In materials where high levels of dryness are necessary, the final stage is important and drying times can be long. If diffusion through the material is a significant factor, drying times will vary with the square of the material thickness, hence thin or small material geometries are preferred.[39]

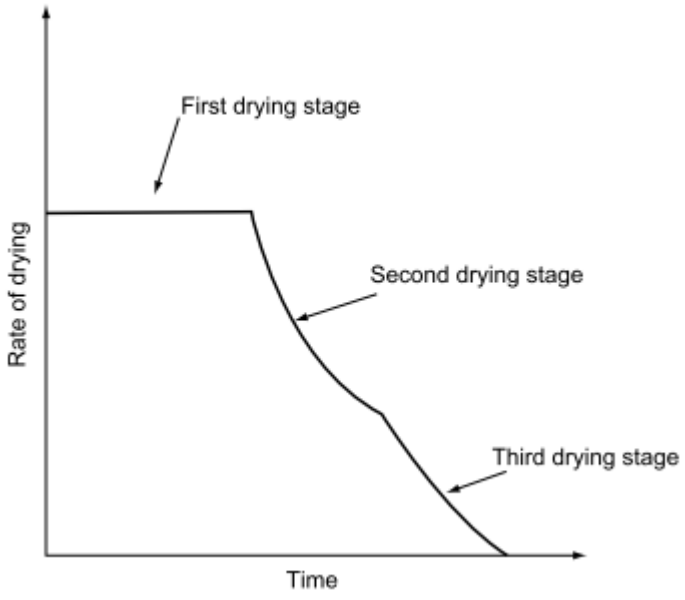

Figure 2-16. Drying rate under constant conditions over time

Considering drying rate curves as a function of drying extent can give similar geometric relationships and allows different systems/materials to be directly compared. Through normalising these curves by initial drying rate and average moisture content, the curves can be treated as characteristic of each material – thus producing a “characteristic drying curve.” The characteristic drying rate, *f* is given as:

$$f = \frac{N_V}{N_W}$$ Equation 2-10

Where N_v is rate of drying for a unit surface, and N_W is rate when the body is saturated/initial drying rate. Characteristic moisture content, ϕ can be calculated from Equation 2-11 or Equation 2-12 if the material is non-hygroscopic or hygroscopic respectively[51]:

$$\phi = \frac{\bar{X}}{\bar{X}_{cr}}$$ Equation 2-11

$$\phi = \frac{\bar{X} - X^*}{\bar{X}_{cr} - X^*}$$ Equation 2-12

Where $\bar{X}$ is average moisture content, $\bar{X}_{cr}$ is the critical moisture content (moisture content at which below this point the drying rate falls noticeably, as drying process becomes determined more by mass transfer within solid than surface vaporisation[52]) and X^* is the equilibrium moisture content (moisture content at which the material is neither gaining nor losing moisture). Plotting characteristic drying rate, f against characteristic moisture content, ϕ yields a characteristic drying curve, two examples of which are shown in Figure 2-17 (from Mujumdar[39]):

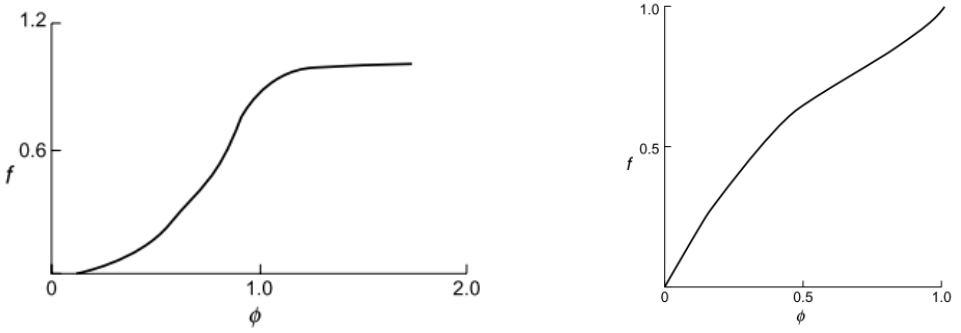

a) b)

Figure 2-17. Characteristic drying curve of a) molecular sieves, b) silica gel

In order to use the above characterisation curve to describe a materials behaviour, the process must have a consistent critical moisture content which is independent of initial moisture content and external conditions, and all drying curves for that material must be similar in shape under all conditions and invariant to any process changes. In reality it is not common for materials to meet these criteria under a significant range of such conditions but this practice is commonly used to predict drying performance.

2.4.7 Spent nuclear fuel drying and dry storage

In the context of this work, drying spent Magnox fuel has been considered to mitigate the unwanted corrosion of spent Magnox fuel following the initial period of wet storage before the Magnox undergoes extensive corrosion. The dried fuel can then potentially be stored for longer periods without further degredation in dry conditions prior to disposal in a geological facility. Dry storage of Magnox has been implemented in the UK at Wylfa power station in Wales, where the spent Magnox fuel is discharged from the reactor straight into CO_2 filled dry storage pending transport to Sellafield for reprocessing, not in a water cooled pond like at most other sites.[53] As the cladding was designed for operation in the presence of CO_2, it is well suited for dry storage as Magnox corrosion rates in CO_2 are negligible at temperatures <350 °C and feasible in dry air at <150 °C, however restrictions in the safety case describe the risks of the formation of uranium hydride if bare uranium metal is present. Magnox fuel stored in dry air will undergo pitting if the relative humidity exceeds 50% or if water ingress occurs.[5] This shows there is demonstrated viability for dry storage of Magnox spent fuel, but the drying process and dry storage of corroded fuel has not been proven. The 2015 ONR review considers drying the fuel as a contingency, estimating 4.5-6.5 years for deployment, followed by 1-4 years of operations depending on the outstanding Magnox inventory. This has the potential to result in fuel ageing for an additional 5.5-10.5 years underwater in FHP.[22]

2.4.8 Drying methods

Heating methods vary primarily by the method of heat application, temperature/pressure conditions and the manner of handling of the material in question. Heating methods employ convection, conduction or radiation (or a combination). Convection is a particularly common method of material drying via passing heated air or gas over a material, and moisture is removed by the flowed gas. Convective dryers are commonly referred to as “direct” dryers. Conductive (or “indirect”) dryers are best suited to thin and/or very wet materials, where heat is provided via contact with surfaces and moisture is removed by vacuum or a stream of gas. Dryers can benefit from incorporating a combination of direct and indirect drying methods for effective heat transfer to the material and moisture removal. Drying through heating by radiation is practiced such as by infrared radiation for drying thin films and sheets. Radiofrequency drying at 50-60 Hz is also possible, and despite being a poor conductor at these frequencies, it has the benefit of being able to heat a large volume of material evenly and target water molecules specifically.[39]

The pressure at which drying is carried out is commonly at approximately atmospheric pressure, where slightly increased pressure can help to protect the process from air ingress, but slightly below can improve drying rates. Vacuum drying operations are relatively expensive but allow drying to be performed at lower temperatures and/or in the absence of oxygen.[39]

Selection of drying techniques and conditions is complicated due to the wide range of material physical and chemical properties, thermal/chemical sensitivities, environmental and safety aspects, dryer emissions as well as final product specifications. Also the base mechanics of water removal and fundamental operation of many dryers is not well understood. Dryer selection will usually be based on balancing equipment and operating costs, product quality, safety and convenience of installation. Dryer design can be informed by a number of factors such as those just described, previous experience on other similar materials, bench-scale and pilot-scale testing and modelling. Theory can be calculated from estimations and heat/mass transfer, and further design/scale-up based on drying conditions informed by smaller scale experimental tests.[39] Previous work on development and design of the apparatus used in this work demonstrated that vacuum drying proved more effective than direct flowed gas drying.[9]

2.4.9 Vacuum drying spent nuclear fuel

As mentioned previously, drying under reduced pressure is a predominantly indirect conductive method, where drying is achieved by lowering the gas pressure to below that of the vapour pressure, thus encouraging evaporation of residual water. ASTM C1553-16 International Standard Guide for Drying Behaviour of Spent Nuclear Fuel[43] describes a general process used for drying commercial SNF for cask storage which is summarised here:

1. Seal the SNF within a container and drain excess water
2. Attach vacuum system and evacuate to evaporate water/dry the contents until the container pressure is $<4 \times 10^{-4}$ MPa (4 mbar, 3 torr) - this process is improved by additional external heating
3. Isolate the system and perform a pressure test to ensure that the reduced pressure remains stable, demonstrable by maintaining a constant pressure for 30 minutes (known as a pressure "rebound test")
4. If the pressure is observed to rise above a given limit (indicating liberation of water vapour), continue to evacuate the container via the vacuum system
5. Once a stable vacuum is established, backfill the container with an inert gas to a predetermined positive pressure to prevent further cladding corrosion inside the container

Figure 3.7 is taken from the Dry Storage Handbook by Patterson and Garzarolli[54] and it indicates the water phases that would be encountered during a vacuum drying cycle. Initially at atmospheric pressure (~0.1 MPa, 1 bar) and 50 °C the water will be a liquid at point A. The water can be converted to vapour either by increasing the temperature to 100 °C (point B) or reducing the pressure to ~0.01 MPa (0.1 bar) at point B'. During evacuation, the resultant position on the phase diagram between point C and C' is dependent on the heat input (either actively produced from vessel heaters, or passively generated from decay heat of spent nuclear fuel) and the quantity of water being removed - note that this line is at a slightly lower pressure of 3 mbar in Figure 3.7, rather than the 4 mbar stated by the ASTM standard. Water at point C will be liberated as superheated steam, whereas at point C' it will be as cold water vapour. If the heat input is less than the heat required for evaporation, the temperature will decrease. Evacuating to pressures below the triple point of water (6 mbar, 0.01 °C) increases the chance of ice formation which will have to be avoided to allow successful vacuum drying. Unwanted freezing and temperature drops can be minimised by avoiding rapid pressure drops, providing additional external heating and allowing the system to reach thermal equilibrium.

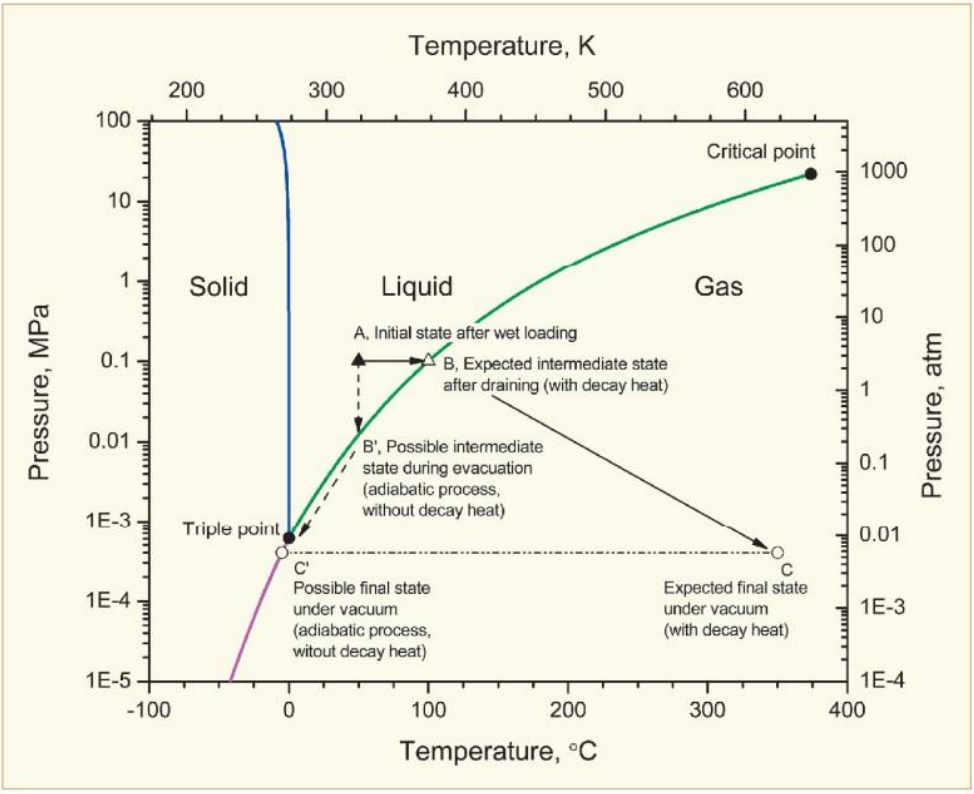

Figure 2-18. Water phase diagram displaying expected pressures and temperatures during SNF drying (Figure from Patterson et. al.)

Vacuum drying of nuclear fuel with a metallic uranium fuel bar has been performed at the Hanford site in Washington, U.S.A.[55] Hanford's history and legacy issues are

comparable to that of Sellafield, where a quantity of reactive metallic uranium metal fuel had been held underwater for several decades causing corrosion during storage, which resulted in sludge formation in the Hanford Basins - the worst of which being the East basin where the fuel canisters were unsealed. The East basin had experienced a number of leaks of contaminated water between 1974 and 1979, and again in 1993 which presented environmental and public safety concerns given the close proximity to the Columbia River. In 1995 the strategy to convert the wet SNF and associated debris to a more stable dry form for interim storage was identified and accepted. A total of 2100 tons of fuel from 105,000 assemblies were recovered between 2000-2004.[56] The process for recovery first required de-capping the canisters and the fuel contents washed, retaining any sludge within the basin. Next the fuel outer elements were separated from the inners, and the fuel elements remotely placed into stainless steel baskets for storage. Once the baskets were full the fuel was loaded into Multi-Canister Overpacks (MCOs) and taken to a Cold Vacuum Drying Facility (CVDF) where the water was removed to prepare the SNF for storage under an inert helium atmosphere. As the fuel dried at Hanford was based on metallic uranium, the challenges presented are different to that of uranium dioxide pellet fuels in that uranium can react with water during storage and generate explosive hydrogen and cause pressurization.[57,58] An instruction from Hanford CVDF describes that drying was undertaken at typically 50 °C and describes the drying procedures employed. The "Normal Vacuum Drying Cycle" involved operating a vacuum pump with condenser and additional helium purge for eight hours, followed by a helium recycle or purge for four hours, then operation using only the vacuum pump (without condenser) and helium purge for a further four hours. Once the pressure decreased below 0.1 torr (0.13 mbar) for 15 mins a pressure rebound test was performed by first observing a pressure rise <0.5 torr (0.67 mbar) over 10 mins, then a pressure rise <3 torr over 1 hour. On meeting these criteria the MCO was demonstrated as dry. The MCO was repressurised under helium to 1-5 psig (69-345 mbarG), cooled to 25 °C and pressurised to 7.3 psig (503 mbarG).[59]

The drying process and rebound test described in the procedure from Hanford works on the same principle to the one described in ASTM C1553-1625 but has lower required pressures and stricter expectations in dryness and performance. It also states that containers are backfilled with helium for storage. It is promising that corroded uranium metal drying has been demonstrated by this method, but a key difference is the SNF dried at Hanford was clad in zirconium alloy, and any sludge or corrosion was predominantly uranium based. Therefore this does not represent the behaviour of drying the potentially significant volume of corroded Magnox cladding that will be prevalent and largely unique to this project.

2.4.10 End point determination

During the performance of vacuum drying operations it is desirable to be able to determine the point of dryness or end point non-intrusively. Close-up observations are not practical for highly radioactive materials, especially when the materials are held within containers following drying and held under reduced pressure or inert atmospheres. In Section 2.4.9 the rebound tests performed at Hanford and in ASTM C1553 are discussed. These tests rely on indirectly observing water through increased pressure of an isolated system by generation of water vapour under reduced pressure. The additional time and steps required to demonstrate this dryness could potentially be reduced or avoided altogether by directly measuring water vapour *in situ* during operation.

Goode, Hambley and Hanson were able to achieve online measurements of drying progress and moisture content using mass flow, dew point, pressure and temperature data.[8–10] In their work they report the observation of a sudden drop in pressure, mass flow and dew point once the water has been removed from the system as visible in Figure 2-19. They also observe that it is possible for a rebound test to be performed and erroneously passed if the pressure were reduced low enough that slow vaporisation of any water could give rise to a slow enough pressure increase that it remained within the pressure tolerances during the rebound test period. The rebound test also relies on a system which can maintain a vacuum seal for the required period, but this is not inherently necessary for removal of water. Removal of water can be performed in a variety of conditions - not limited to pressures <4 mbar - and a test for dryness outside of these conditions is of value.

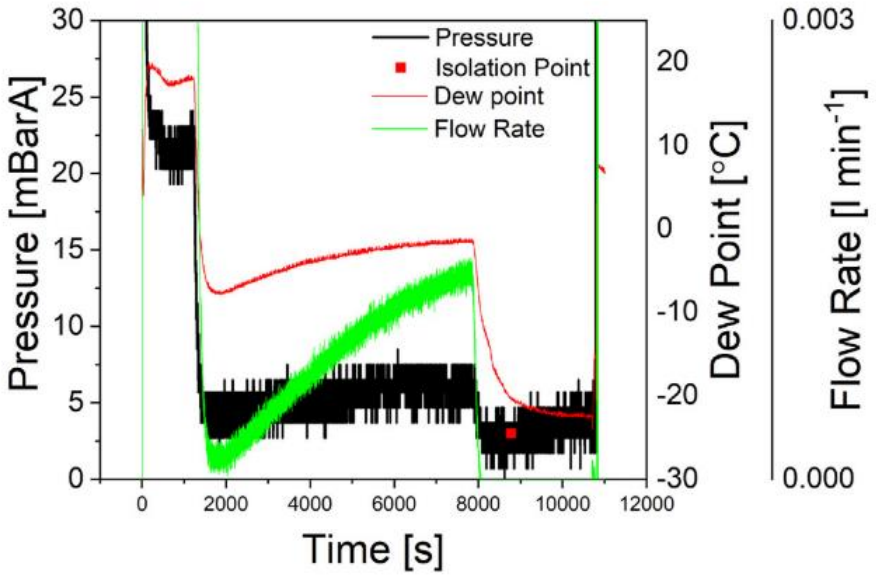

Figure 2-19. Determination of drying end point (taken from Goode et al.[10])

2.4.11 Drying Magnox spent fuel/magnesium hydroxide

Vacuum drying in the UK has been considered for some time as a contingency for spent Magnox fuel, and was listed in the 2014 NDA Magnox Fuel Strategy Contingency Options.[60] Research has been undertaken to look at vacuum drying intact fuel elements in batches of 26 based on the previous experience from Hanford, with drying times in the range of 2-4 hours, but there is little publicly available detailed information on the process.[61] Magnox Ltd have enlisted Mechatech Advanced Vacuum Drying Systems (AVDS) in remediation of facilities to assist in handling sludges, resins and other waste. They were first deployed at Berkeley in 2013, and have since been operated at Bradwell and Chapelcross, but relevant information is largely limited to NDA announcements and web articles, with no widely available technical literature.[62,63]

Despite the commonality of magnesium hydroxide, there are not many reports available on its drying. One publication on drying of magnesium hydroxide nanosheets and microparticles has been published by Yun, Mujumdar et al. and describes drying of three different morphologies of magnesium hydroxide.[11] They oven dried the samples in air at temperatures 80-140 °C, and observed that drying rate and equilibrium moisture content decreased with increasing drying temperature (example shown in Figure 2-20a). They observe that the drying rate curves (Figure 2-20b and Figure 2-21) exhibit three stages (as described in Figure 2-16) of constant rate, first falling rate and then second falling rate period. An observation made in the paper is that the moisture in the nanosheets is more difficult to remove than for microparticles, likely to be due to smaller pores in nanosheets and hence greater capillary pressure. Another observation was that the amount of water removed during the constant rate period decreases with increasing drying temperature, but the amount removed during the falling rate period increases with increasing temperature. Also the time spent during each rate period decreased with increasing temperature. They also reported a variation between hygroscopic ability of the three morphologies, where microparticles were the least hygroscopic and the nanosheets were the most, indicating that this is affected by the morphology as well as the chemical composition, but no explanation is provided.

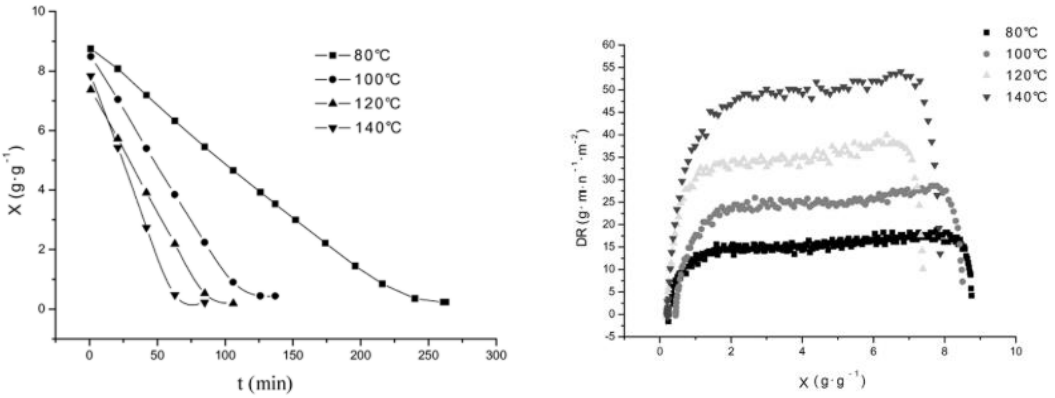

a) b)

Figure 2-20. Data for drying of $Mg(OH)_2$ nanosheets at 80-140 °C; a) drying curve of moisture content (X, g g^{-1}) over time, b) drying rate (DR, g min^{-1} m^{-2}) curve over moisture content (from Yun et al.[11])

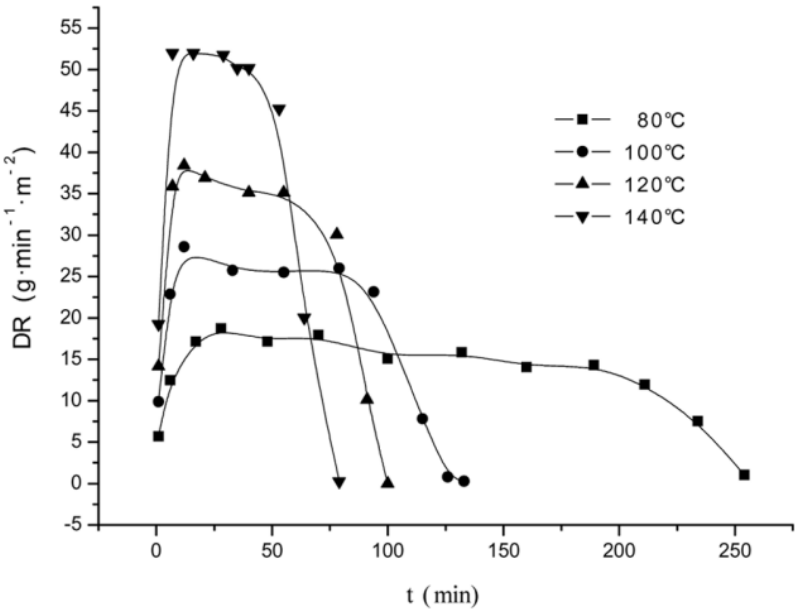

Figure 2-21. Drying rate curves against time from drying at 80-140 °C for $Mg(OH)_2$ nanosheets (taken from Yun[11])

Dry storage in the UK is proven for spent Magnox fuel direct from reactor discharge but is unproven for SNF recovered from wet storage. Some drying experience for other nuclear materials exists in the UK for AGR fuel and Magnox at a research scale to inform contingency options.[8–10,53,61] As it stands any widely available information is scarce, and limited to the small amount of published work on drying rates of similar materials or brief industrial releases with little technical detail. Given the relevance of the program with the recent closure of the Magnox Reprocessing Plant there is real interest and urgency to develop this area of technical

understanding. The literature presented so far provides an overview of existing and relevant drying practices and drying of relevant materials. The next section looks at the implications for water carryover into a radioactive dry storage environment.

2.5 Materials/Spent Nuclear Fuel Behaviour in Radioactive Environments

2.5.1 Introduction to radiation chemistry

The fundamental characteristics of radioactive materials are both what make them so valuable as fuel and so hazardous to handle, particularly following their use in reactor. Radioactive materials spontaneously undergo radioactive decay, a process by which the elemental composition changes and ionising radiation is emitted. This section will introduce some of the main concepts that are of relevance to this work, and in relation to spent fuel behaviour and water radiochemistry during storage in a radioactive environment.

2.5.2 Types of ionising radiation and interactions with matter

The predominant types of ionising radiation are; alpha particles, beta particles (electrons, β^- or positrons, β^+), gamma rays and also the emission of nucleons such as neutrons/protons. The different radiation types vary with respect to mass, charge and energy transmission, which causes the interactions with other matter to vary too. Uncharged particles like neutrons can penetrate on the order of a metre through a solid or liquid, whereas charged particles like electrons and protons will only travel up to a few millimetres.[64]

Alpha particles consist of two protons and two neutrons, equivalent to a He^{2+} ion. The process of emission results in the atomic mass reducing by four and proton number reducing by two, as shown in Equation 2-13:

$$^{238}U \rightarrow {}^{234}Th + {}^{4}He^{2+} \qquad \text{Equation 2-13}$$

Alpha activity is predominantly found in heavier nuclei where proton number >83.[65] During beta decay, the atomic mass does not change. Emission of a β^- causes the atomic number to increase by one unit with conversion of a neutron to a proton.[65] Gamma rays are electromagnetic radiation which are emitted during nuclear transmutations from radioactive nuclei. An emission from a given species will have a discrete characteristic energy, such as the gamma emission of ^{60}Co. Absorption of gamma radiation by a target material is dependent on the energy of the incoming γ-photon as well as the density and atomic number of the receiving material. Nomenclature for energies in nuclear processes are often expressed in terms of

electron volts (eV), which is the equivalent energy an electron gains when passing a potential of 1 V (or 1.602×10^{-19} J).[65]

Activity is discussed in terms of decays per second (Bq), and is calculated by multiplying the half-life, $t_{1/2}$ by the number of atoms, so species with shorter half-lives will therefore have greater specific activities. As a result, some radioactive species may be more problematic in the near term, but given the half-life is relatively short it is practical to store such materials in a well shielded location (such as an underwater storage pond) to allow the most radioactive species to decay. The need for long term management of radioactive materials is necessary where materials are sufficiently radioactive that human and environmental contact could have harmful effects, but the half-life of the material is so long that the radioactivity cannot be outwaited, for example irradiated nuclear fuels. This is illustrated in Figure 2-22 which was taken from a report published by Swedish nuclear fuel and waste management company Svensk Kärnbränslehantering AB[66] based on information published by Hedin.[67] The figure shows how radiotoxicity (from ingestion) of the spent nuclear fuel components following discharge (at time = 0.1 years) are many orders of magnitude greater than that of natural uranium (shown by the blue line), and that in order for the radiotoxicity to decay to that found naturally takes >200,000 years. Clearly it is not possible to wait for all the material to decay, and the activity is too high to be released in any significant volume, so it is necessary to store such materials in a controlled manner until a more permanent method for disposal is established.

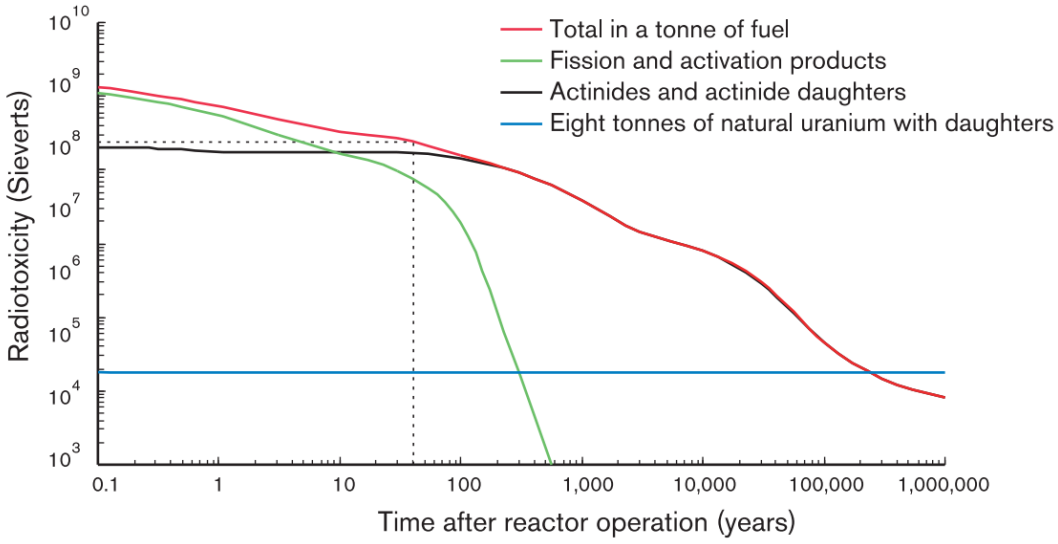

Figure 2-22. Toxicity of the waste for Swedish BWR fuel (burnup of 38 MWd/t U) as a function of time – dotted line indicates 30 to 40 years of interim storage when fuel will be deposited in the final repository (taken from Svensk Kärnbränslehantering AB Report[66])

2.5.3 Radiation interactions and effects on materials

2.5.3.1 Ionising radiation interactions with materials

The average penetrative range of an incoming α-particle in a solid will depend on the energy of the ion and the density/atomic number of the material. For reference, a 7.69 MeV α-particle (from ^{214}Po) will penetrate 6.95 cm in air, but only 18.7 μm in iron. Multiplying the average penetrative (or extrapolated) range by the material density allows the range to be expressed in units of g/cm^2. The absorption properties of a material is known as the stopping power, and defined as the energy lost per unit distance a particle has travelled (Equation 2-14), which is dependent on the particle energy.[65] This is closely related to the linear energy transfer (LET) which is energy absorbed in matter per unit length the particle has travelled (Equation 2-15). The stopping power is equal to the LET value plus E_x, energy loss to the environment by radiative electromagnetic losses e.g. through bremsstrahlung (Equation 2-16). Stopping power and LET work on the basis of continuous slowing down and therefore provide quantitative average energy losses and qualitative information on the density of reactive species.[68]

$$\frac{dE_{loss}}{dx}$$ Stopping Power Equation 2-14

$$\frac{dE_{abs}}{dx}$$ LET Equation 2-15

$$\frac{dE_{loss}}{dx} = \frac{dE_{abs}}{dx} + E_x$$ Equation 2-16

Beta particles have much greater ranges and are strongly affected by electron density of the media through which they travel, giving rise to a zig-zag trajectory. Beta radiation interacts with matter in three main ways:

1. Electron interaction causing electron shell excitation and ionisation, a process which is dependent on the electron density of the absorber
2. As β^- radiation interacts with atomic nuclei, the electrons lose energy in steps and emit photons as X-rays (Bremsstrahlung)
3. Backscattering of electrons, where a β particle is reflected back towards the direction of the source

Additionally a positron can produce two γ-rays of energy 0.51 MeV by annihilation with its antiparticle the electron (the sum of the energies of both photons being equivalent to that of two electron masses).[65] For the reasons described, it is best practice to use materials of relatively low atomic number (e.g. aluminium or Perspex) to shield beta radiation to minimise the generation of bremsstrahlung.

Whilst α- and β-radiation interact with matter by essentially undergoing collisions with the absorber, γ-radiation energy transfer and interaction with matter is minimal as the photons are uncharged. Absorption of γ-photons obeys the exponential decay equation in Equation 2-17:

$$I = I_0 e^{-\mu d} \qquad \text{Equation 2-17}$$

Where I = Intensity, μ = absorption coefficient, and d = thickness of absorber.

These are the main absorption mechanisms for γ-radiation as described below and in Figure 2-23 (taken from Choppin[68]):

1. Coherent (Bragg or Rayleigh) scattering – γ-ray is absorbed and re-emitted with the same energy but a change in direction, the probability for which increases with the square of proton number, but decreases with γ-energy.[68]
2. Photoelectric effect – whereby an incoming γ-photon transfers its energy to an electron which is ejected at the energy of the incoming γ-photon minus the (relatively small) electron binding energy.[65]
3. Compton effect – a γ-ray photon partially transfers some energy to an electron which is emitted, and the incoming γ-photon changes frequency and direction proportional to the scattering angle.[65]
4. Pair Formation – observed at energies ≥ 1.02 MeV (equivalent to two electronic masses) where the γ-ray photon interacts with a nucleus and creates an electron and a positron (effectively the reverse of annihilation). This process increases in probability with increasing photon energy and dominates at γ-photon energies > 10 MeV, and also increases with absorber atomic number squared.[65]

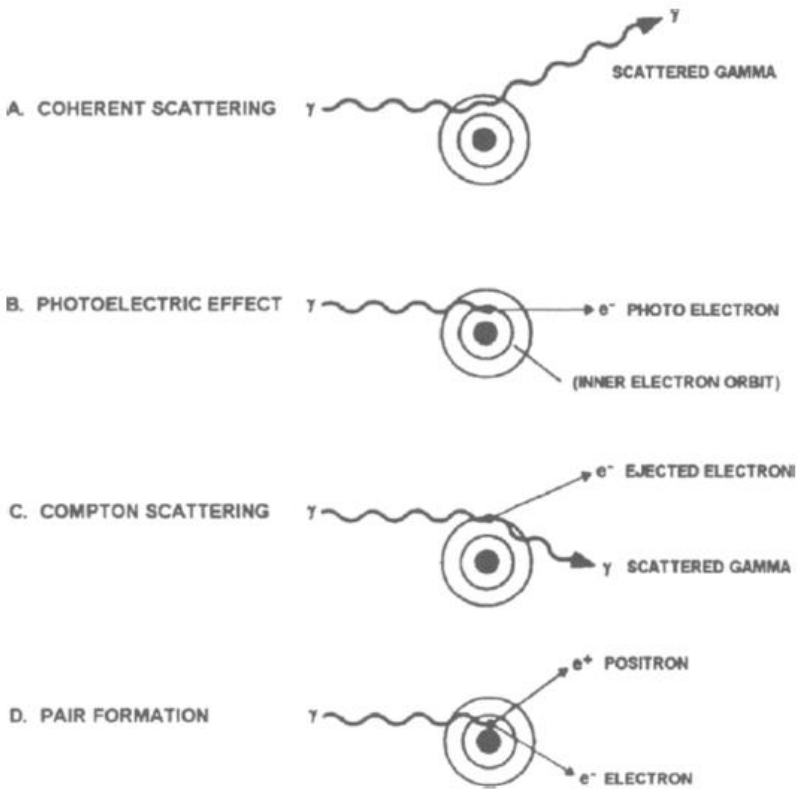

Figure 2-23. Processes for γ-radiation interaction and absorption (from Choppin[68])

The total absorption of a material is found from the sum of the absorption coefficient of the combined mechanisms. Some additional minor processes for energy absorption are induced nuclear reactions from high energy γ-radiation and small scale Thomson/Compton scattering at the nuclei.[65] The main energy transfer mechanism for ~1 MeV γ-photons is Compton scattering, where the photon energy ejects an orbital electron, transferring some kinetic energy to it whilst the incident photon retains the remaining kinetic energy. As the photon energy drops to approximately 60 keV, the photoelectric effect dominates, whereby all of the photons energy is transferred to an (often inner orbital) electron.[64] The difference in binding energy of the higher and lower orbital causes emission of X-rays and low energy *Auger electrons* as an outer electron moves to fill the inner vacancy. The process of electron cascade with X-ray and Auger electron transmission continues until the atom reaches its ground state.

Neutrons are produced from spontaneous fission reactions, but due to the lack of charge display very little interaction with electrons. The primary observation from neutron interactions are with nuclei via elastic and inelastic scattering and nuclear reactions. During elastic scattering the total kinetic energy is unchanged from the reaction, whereas inelastic collisions transform some kinetic energy to excitation energy. Types of neutrons are distinguished by their energies, where 0-0.1 eV are classed as thermal neutrons, 0.1-100 eV as slow neutrons, 0.1-100 keV as

intermediate neutrons, and 0.1-10 MeV as fast neutrons.[65] As neutrons are uncharged they are not impacted by coulombic repulsion and can be absorbed by nuclei of elements such as boron.

From this we can see the energy is absorbed mainly through ionisation and atomic excitations. The chemical effects from this depend on the composition of the matter and the amount of energy deposited. As energy is lost by a high energy charged particle moving through matter it produces a *track* of ionised and excited particles along the travelled path. Most of the interactions involve the electrons of the media rather than the nuclei. Secondary electrons produced from ionisation events can have varied energies and therefore give rise to different effects. If the energy is low (<100 eV) then the range in liquids and solids is short, so the ionisations and excitations caused by them occur near to the site of primary ionisation, leading to a relatively high local concentration of these reactive species/events known as a *spur*. Secondary electrons with high energy can go on to form new tracks and can be referred to as δ-rays. For high energy electrons, spurs form at separated intervals along the track, but with more ionising heavier species like α-particles and protons, the spurs can overlap as columns of excited/ionised species. Tracks from X-rays and γ-rays produce tracks of fast electrons, the energy of which go into forming spurs (6-100 eV), blobs (100-500 eV) and short tracks (500-5000 eV).[68]

2.5.3.2 Ionising radiation reactions

High energy particles or photons initiate an ionization process in solids liquids and gases, where the radiation gives rise to a primary reaction that can produce species like ions in Equation 2-18 or excited atoms/molecules in Equation 2-19:[65]

$M \rightsquigarrow M^+ + e^-$	Ionisation	Equation 2-18
$M \rightsquigarrow M^*$	Excitation	Equation 2-19

The products from the primary reactions are then able to undergo further secondary reactions such as those in Table 2-1:

Table 2-1. Secondary reactions from ionising radiation (from Lieser[65])

Reaction	Description
$M^+ \rightarrow R^+ + R\cdot$	Dissociation
$M^+ + e^- \rightarrow M^*$	Recombination
$M^+ + X \rightarrow Y^+$	Chemical reaction
$M^+ + X \rightarrow M + X^+$	Charge transfer
$M^+ \rightarrow M^{n+} + (n-1)e^-$	Auger electron emission
$M^* \rightarrow M + h\nu$	Fluorescence
$M^* \rightarrow 2R\cdot$	Dissociation to radicals
$M^* \rightarrow R^+ + R^-$	Dissociation to ions
$M^* + X \rightarrow Y$	Chemical reaction
$M^* + X \rightarrow M + X^*$	Transfer of excitation energy

The most common of these reactions are recombination, fluorescence and dissociation to radicals. Recombination is particularly favoured in liquids and gases. The products of the primary reactions are formed in the track of the high energy ion or photon, and in the highest concentration for heavier ions such as alpha particles and protons. The primary products then give rise to the secondary reactions which typically occur in 10^{-7} to 10^{-10} seconds.[65]

The concentration of the products is proportional to the energy lost by the incoming ion/photon per unit distance, LET. If particles have sufficiently high energy it is possible for them to undergo nuclear reactions. As an electron interacts with nuclei they can emit photons by bremsstrahlung.[65] Ionising radiation (except for neutrons) predominantly interact with orbital electrons, so energy deposition is dependent mostly on electron density which also approximates to mass density.[64] Neutrons can lose their energy in steps as they undergo multiple collisions with particles, or they can induce nuclear reactions. Photons tend to give off all their energy in a single step.[65]

2.5.4 Radiation dose and yield

It is of necessity to be able to consistently quantify the amount of ionising radiation an object has been exposed to or absorbed. There have been various standard units for this over time, but the most commonly used in modern times is the SI unit of the *Gray*, which is defined as 1 joule energy absorbed per kilogram. Here the energy absorption is independent of whether the incident radiation was a charged particle, uncharged particle or a photon.

Decomposition of matter from exposure to ionising radiation is known as radiolysis. The radiation chemical yield is described as a *G-value*¸ and is used to standardise and describe the molecular yield of a process or reaction related to ionising radiation absorbed. The SI definition for this is in terms of mol/joule, but it has been (and still remains in many cases) common practice for G-values to be discussed in units of molecules product/100 eV energy absorbed. This work will use the latter units for G-value for better consistency and direct comparison with similar literature. The conversion is simple as 1 mol/J = 9.649 x 10^6 molecules/100 eV.[68]

2.5.5 Radiolysis of water

As water interacts with ionising radiation a chain of reactions occur, and the timescales for these can be very short, an overview of which (taken from Choppin et al.[68]) is shown in Figure 2-24a. Within 10^{-16} seconds the ionisation event can occur with formation of H_2O^+, which can go on to react with a water molecule within 10^{-14} seconds and form H_3O^+ and an ·OH radical. The electron can then go on to ionise further water molecules as long as its energy remains above the water ionisation threshold of 12.61 eV. It will then lose its remaining energy by causing vibrational and rotational excitation of water molecules before eventually becoming solvated, e_{aq}^- (in <10^{-12} seconds), which is a powerful reducing agent. The excited state H_2O^* dissociates within 10^{-14}-10^{-13} seconds. Therefore these initial physical processes are complete within 10^{-12} seconds where the species can equilibrate with the water.[68]

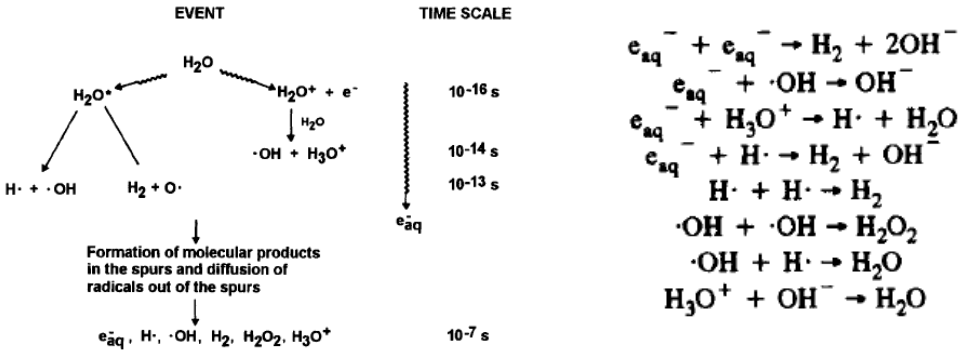

a) b)

Figure 2-24. a) Radiolysis of water events and timescales, b) spur reactions in water (from Choppin et al.[68])

As previously described, the radiolysis products cluster in spurs, from which they can diffuse away. Within the spurs a wide range of recombination reactions can occur, forming molecular or secondary radical products such as those listed in Figure 2-24b. This occurs within 10^{-7} seconds and gives the radiolysis products e^-_{aq}, H·,·OH, H_2, H_2O_2, and H_3O^+. G-values for irradiation of liquid water are given in

Table 2-2, and it can be seen that as LET increases (i.e. for He^{2+} ions), G-values for molecular products increase and those for radicals decrease as tracks are formed.

Table 2-2. G-values (in molecules/100 eV) of radiolysis products from liquid water[68]

Radiation Source	$G(-H_2O)$	$G(H_2)$	$G(H_2O_2)$	$G(e^-_{aq})$	$G(H\cdot)$	$G(\cdot OH)$	$G(\cdot HO_2)$
γ and fast electrons	4.1	0.45	0.70	2.7	0.60	2.70	0.026
12 MeV He^{2+}	2.8	1.1	1.1	0.042	0.27	0.54	0.068

Within the nuclear industry, recommendations have been made with respect to application of G-values, as they can vary based on aspects such as temperature, pressure, atmosphere (and presence of oxygen), dose rate and total absorbed dose. With respect to pH it is generally agreed that there is no strong dependence of primary yields of radiolytic products on pH, although the situation at extreme pH's (i.e. <3 or >12) is not fully determined. The variation with pH is mostly seen in radical formation and has little effect on yields of molecular hydrogen or hydrogen peroxide.[69–71,72] Radiolytic hydrogen generation is reported to be predominantly produced by reactions involving hydrated electrons, nonhydrated electrons and/or hydrated electron precursors.[73,74] In a paper reviewing radiolytic G-values for various materials with relevance to industrial application produced by Hunter, Adeogun, Dawson, LaVerne and Watson, they recommend using $G(H_2)$ from β- and γ-irradiation of water of 0.45 molecules/100 eV, with an upper bound of 0.5 molecules/100 eV for temperature fluctuations up to 100 °C.[69] They also recommend the $G(H_2)$ for 5 MeV helium ions from pure water is 1.2 molecules/100eV with an upper bound of 1.7 molecules/100 eV, which is close to the value described in Choppin et al. (for 12 MeV He^{2+}) in Table 2-2.[68,69] These G-values are widely accepted as accurate for pure water, but as discussed the G-value can be affected by the environment and system.

2.5.5.1 Interactions of water with oxide surfaces during radiolysis

Water radiolysis has been reported to display different behaviours in the presence of solid/liquid interfaces. This is significant in the context of nuclear waste storage and disposal due to the variety of heterogeneous systems in which water is often found, such as with concretes and waste materials. Such systems can modify the behaviour and yields of species generated by the interactions with radiation from that observed in bulk water. Previous work has looked at hydrogen generation from radiolytic decomposition of water adsorbed on the surface of metal oxides, and how it can differ from that seen in bulk water, much of which is discussed in a review by Le Caer.[13] Early work by Allen et al. discussed "radiolysis and energy transfer in the adsorbed state," and that excitation through irradiation of a solid can move to the

surface and cause the adsorbate to react or decompose.[75,76] In some of their work they observed radiolytic decomposition of azoethane on the surface of some insulating metal oxides, and proposed this was a result of migration of energy in the form of electrons, holes or excitons (electron and positive hole pair which can move together as a unit[77]) from within the solid to the surface and then transfer this energy to the adsorbed molecules. This effect was dependent on the energy gap between the ground state and conduction band in the solid (band gap) which they identified through variation in behaviour between insulators and semiconductors. They also observed a correlation whereby more perfect solid lattices gave increased adsorbate radiolysis (presumably through more effective energy transfer). It was proposed that over time, the radiation induced defects and imperfections in the solid lattice can accumulate and hinder energy transfer, or that decompositions occur at preferred sites and that once the preferential sites are occupied, there may be delays for migration of new species for reaction.

This increase in reaction rate/energy transfer can be considered as “radiation catalysis” whereby the adsorbed species receive a higher effective radiation dose than would otherwise be directly absorbed.[13] Further work has been carried out to investigate the relationship between band gap and radiolytic hydrogen yield from adsorbed water molecules on metal oxides, such as that by Petrik, Alexandrov and Vall.[12] They produced a study on energy transfer during gamma radiolysis of metal oxides (particularly ZrO_2), and again saw that energy absorbed by one phase of a heterogeneous mixture can be redistributed and induce effects in the other phase. This consists of two stages, where the energy migrates from the bulk to the interface, and then transfers through the interface between the phases. Following interaction with ionizing radiation, the energy is dispersed by secondary electrons (10^2-10^5 eV), intermediate energy electrons (0.1-100 eV) and thermalized particles of excitations (<0.1 eV). At an interface between two media of different density or composition, secondary electron flux can occur to different extents in each direction, which in some cases can give rise to adsorbed molecules receiving a higher dose than would otherwise be seen in bulk single phase. Additionally intermediate energy electrons and “hot” carriers (electrons or holes with high kinetic energy) can contribute to surface reactions from a few atomic layers to 50-250 nm.

Table 2-3. Selection of data adapted and selected from Petrik et al.[12] displaying effect of $G(H_2)$ via energy transfer from metal oxide to adsorbed water

Group 1 Decrease $G(H_2)$		Group 2 Little Effect $G(H_2)$		Group 3 Increase $G(H_2)$	
Compound	G-value	Compound	G-value	Compound	G-value
MnO_2	0.002-0.04	MgO	1.3-1.9	ZrO_2	10-80
Co_3O_4	0.001-0.06	CeO_2	2.6	Ga_2O_3	30
CuO	0.001-0.08	TiO_2	0.3-0.5	Eu_2O_3	6-40
Fe_2O_3	0.09	Cr_2O_3	0.1-2.0	Yb_2O_3	6-10

In their work they observed radiolytic yields from γ-radiation of water adsorbed on the surface of a range of metal oxides, and noted that the radiolytic behaviour of the tested materials could be categorised in three ways; those that decrease the hydrogen yield, those where the yield is roughly equivalent to bulk water, and those that increase the yield (Table 2-3), where the chemically closest tested oxide to this work is MgO, which falls into Group 2. The $G(H_2)$ for MgO was measured to be 1.3-1.9 which despite being assigned as having little effect, is still 2.9-4.2 times greater than the literature bulk value. Figure 2-25a shows the amount of hydrogen produced vs absorbed gamma dose for 20 µmol water vapour compared to equivalent quantity adsorbed on ZrO_2, and it is clear the hydrogen generation rate is approximately two orders of magnitude greater when adsorbed. Figure 2-25b shows the data from Petrik et al where hydrogen yields are shown against oxide band gap, and all oxides that promote radiolytic hydrogen generation fall in the range 4.5-6 eV, which is close to the H-OH dissociation energy of 5.1 eV[78]. In their work they propose that the mechanism for radiolysis of adsorbed water is through migration of excitons to the surface and resonant coupling with the adsorbed water molecules.[12,79] The proposed range for this migration is ~5 nm.[12] Magnesium hydroxide is considered a wide gap insulator, with experimental band gaps reported in the range of 5.17-5.70 eV.[80,81] This fits within the resonant range discussed so may suggest greater radiolysis to be expected for adsorbed water than on MgO (band gap 7.6 eV[82]).

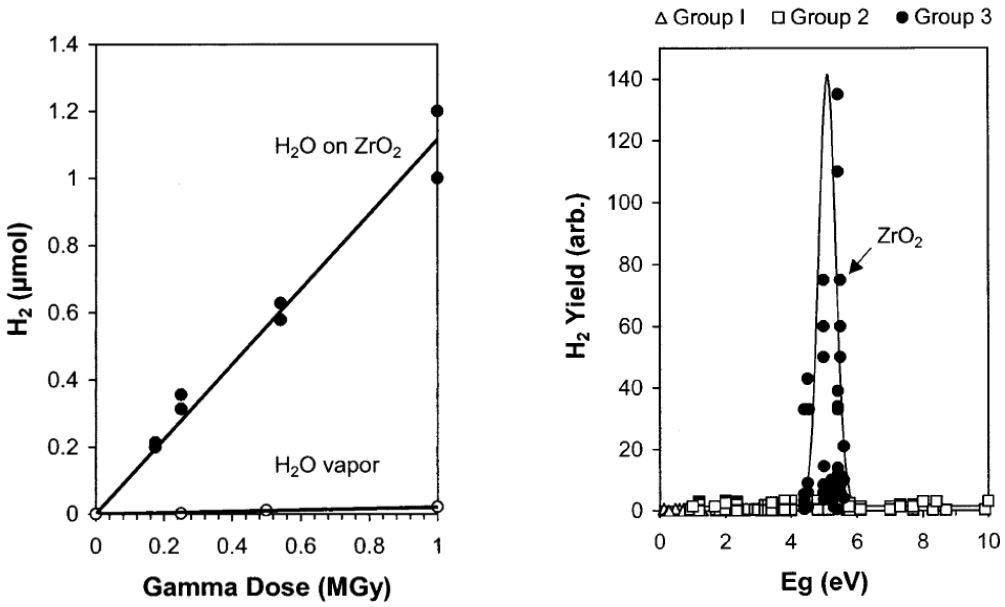

a) b)

Figure 2-25. a) amount of H_2 produced against absorbed γ-energy absorbed for radiolysis of 20 µmol water vapor and 20 µmol adsorbed on ZrO_2 surface, b) H_2 radiation chemical yield vs oxide band gap for radiolysis of adsorbed water grouped by effect on radiolytic G(H_2) where; Group 1 – reduced rate, Group 2 – little effect on rate, Group 3 – increased rate (taken from Petrik et al.).

Additional factors may also affect the H_2 yield. Particle size/specific surface area, as decreasing the particle size generally correlates with increasing H_2 yield.[13,83] The form of water is also important, where physisorbed water is more susceptible to reaction than chemisorbed water/hydroxyl groups, therefore more efficient at generating hydrogen.[84] Hydroxyl groups can also act as charge carrier trapping sites, which allows more efficient energy transfer, but hydroxyl groups with strong hydrogen bonds are inefficient for trapping. Also, interestingly the dose rate plays a factor as high dose rates can give rise to lower G-values than lower dose rates, as energy may be used for alternative reactions which result in exciton consumption, and are therefore not available for water decomposition/H_2 generation.[85]

As already discussed, in the context of water in the presence of nuclear materials in a heterogeneous system, it is going to be necessary from a safety perspective to understand the nature of flammable gas (i.e. hydrogen) generation. If a given estimate were based on a G-value scaled from that observed in bulk water, it may not be accurate for materials with low water contents.

2.5.6 Reported literature of Magnox corrosion products/brucite irradiation

The work so far has discussed irradiation of metal oxides which is more commonly published than work on hydroxides, and such issues that relate to magnesium hydroxide are quite unique to the UKs Magnox legacy. Some work has been carried out in a thesis by Donoclift which looked at quantifying G-values for $Mg(OH)_2$, where mixtures of $Mg(OH)_2$ with varying water content from 4-100%.[14] This work observed G-values <0.6 (close to literature value of 0.45) for all mixtures except for the sample at 4% water where a greater $G(H_2)$ of 1.3 was measured.

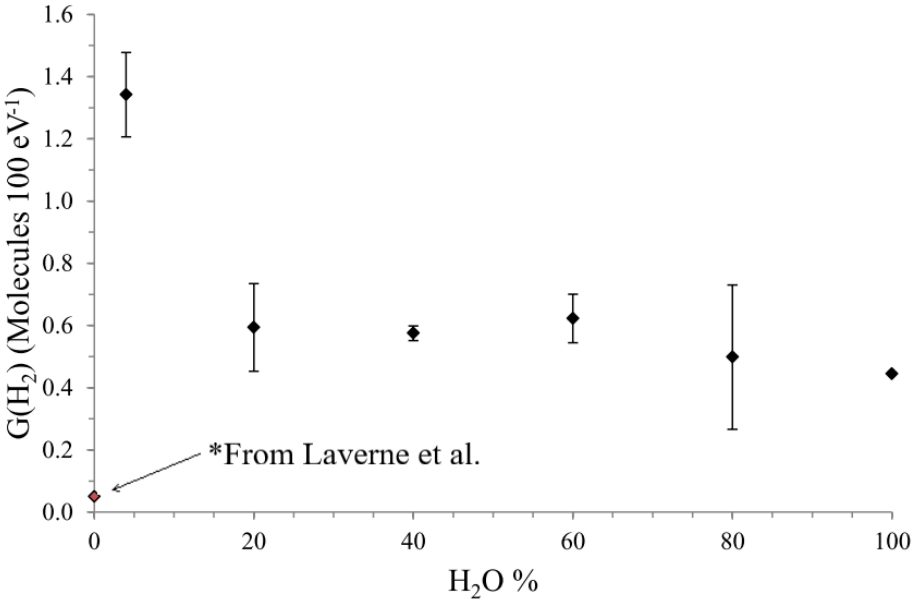

Figure 2-26. G-value of $Mg(OH)_2$ at varying water content 4-100% (taken from Donoclift[14] with *additional data from Laverne[16])

Laverne et al. observed H_2 production from magnesium hydroxides amongst other compounds irradiated with γ-radiation and 5 MeV He ions.[16] This was performed using a ^{60}Co gamma irradiator and tandem Van De Graaff accelerator. They report G-values for 24 h 100 °C dried (to remove surface/adsorbed water) magnesium hydroxide of 0.051 (γ-irradiation) and 0.038 (He^{2+} irradiation). This suggests irradiation of the solid itself is capable of producing hydrogen, in addition to the potential for radiolytic breakdown of adsorbed water. It is worth noting that other literature reports that $Mg(OH)_2$ thermal dehydration of adsorbed water can still persist up to 200-280 °C,[86,87] so there is a possibility the samples were less dehydrated than anticipated. If this is the case there is likely to be some hydrogen generation attributable to any remaining adsorbed water.

Comparable observations are described in work by Shpak et al,[15] where $Mg(OH)_2$ crystallites were exposed to a ^{60}Co γ-radiation source at room temperature in air at ~10^4-9.75 x 10^7 Gy doses. They also report that irradiation can alter the onset of

thermal decomposition, and has been reported in some cases to accelerate it as structural defects are formed which act as nucleation centres. The product from the irradiation was $MgCO_3 \cdot Mg(OH)_2$, and radiolysis extent was ~5% from a dose of 97.5 MGy. They propose this occurs by dehydration of $Mg(OH)_2$ to MgO, then by carbonation from the atmosphere to $Mg(CO)_3$. This mechanism clearly requires the presence of CO_2 to proceed to the carbonate product, but could be a source for radiolytic water production (and thus further hydrogen) from the magnesium hydroxide solid. If this does proceed in accordance to the G-value of 0.051 molecules/100 eV, the effect is approximately an order of magnitude less than $G(H_2)$ for water.

2.6 Literature Review Summary

This chapter has covered a number of important topics to provide context to the project, as well as introduce theoretical concepts which are important to understanding the research that follows.

This work is of interest to inform future strategy for spent Magnox fuel storage, and minimise the potential for further facilities (specifically Fuel Handling Plant) to have issues with future Magnox corrosion. As mentioned, spent Magnox cladding and fuel bars will react with storage water in ambient conditions over long periods of time, and removing the material from underwater storage is a potentially simple and effective means to reduce this risk. Some experience exists of dry storage in CO_2 atmospheres from Wylfa, and research has been performed on Magnox corrosion in a range of atmospheres to understand how these transitions can affect corrosion rates going forward.

A review of drying technology and water interactions with solid surfaces/drying atmospheres was included to provide a basis of understanding of the processes at work during drying. The main forms of water retention are through unbound water, physisorbed/adsorbed water and chemisorbed water. The way in which solids dry was covered, with discussion of typical drying rate curves as a function of time/moisture content. Then a brief section on current drying technologies practiced in the nuclear industry. For the purposes of this investigation, the focus is on vacuum drying based on the desire to provide further understanding for existing technologies and practices. Vacuum drying has been implemented in the industry previously at locations such as Hanford in the USA, as well as in the UK with Magnox Ltd and Mechatech Systems. Finally some literature on $Mg(OH)_2$ drying introduced, where variation of drying rates with temperature from 80-140 °C were covered.

The final section of the review covered some radiochemical concepts to provide background to the important factors that affect spent fuel in radioactive environments. Firstly types of ionising radiation and their basic interactions with matter and primary/secondary species were summarised. From there the basis of radiation dose, yield and the radiation chemical yield “G-value” (molecules produced per 100 eV energy absorbed), and the effect of radiolysis of water (particularly hydrogen generation) was discussed – in particular literature on the topic of radiolysis of water adsorbed on metal oxide surfaces and energy transfer effects on relative G-values. This is an important topic for one of the later results chapters in this work. Finally a review of the literature on magnesium hydroxide irradiation studies was included, where some work has been carried out to look at radiolytic degradation of $Mg(OH)_2$, but little work has been done to look at its energy transfer to surface water which will be a large focus of this investigation later.

This concludes the literature review of this section, but aspects of this will be referred to throughout the thesis.

Chapter 3 Experimental Apparatus, Preparations and Methods

3.1 Introduction

This chapter will introduce and describe the experimental techniques and methodologies that have been employed during this investigation.

3.2 Experimental and Characterisation Methods

The experimental methods and applications covered are:

- Removal of Magnox corrosion product by ultrasonic bath, and XRD characterisation of corroded Magnox/dried sludge
- Thermogravimetric analysis of corroded Magnox to observe thermal decomposition of products
- Computerised tomography and optical/electron microscopy of corroded Magnox to identify structural features
- Particle analysis techniques; surface area, density, and particle size distribution
- Vacuum drying tests using bespoke drying rig on Magnox corrosion products and samples of simulant corroded Magnox cladding

3.2.1 Preparation of simulant Magnox

Magnesium hydroxide was sourced under the trade name Versamag® from Martin Marietta Magnesia Specialties, and is prepared by precipitation from magnesium-rich brine and dolomitic lime and provided as a white powder.[88] Hydromagnesite (magnesium carbonate hydroxide hydrate) was provided by Honeywell Fluka. The National Nuclear Laboratory have a large stock of various types of inactive and unirradiated Magnox cladding corroded to different extents used to simulate different states of corroded Magnox waste, and two samples of Magnox cladding have been received for testing and analysis. These materials are accepted as best corroded Magnox simulant as used for industrial research purposes. Samples were prepared by extended storage in drums under water. For the received samples the majority of the material has dried and the hydroxide/corrosion product is firmly adhered to the metal surface. Initial observations of the corroded Magnox show that the corrosion product is present over the whole surface of the Magnox, with very little bare metal visible. This is shown in Figure 3-1a and Figure 3-2. For all samples the corrosion product is well adhered onto the surface, requiring mechanical

intervention to remove. Four corroded Magnox samples were used/prepared for testing. At times the corrosion product was removed using pliers and other tools which proved difficult as the corrosion product was crystalline and hard (such as Sample 3 recovered from the piece shown in Figure 3-1a). In order to assess the physical features produced by the corrosion process and consider how this may affect water retention, it is beneficial to observe the metal surface with any features free from the corrosion product without damaging them. Removing the corrosion product mechanically could scratch or damage the surface and may affect further testing so a method for removing the corrosion by ultrasonic bath was employed. Various types of corroded Magnox samples e.g. shards and can fragments were placed under deionised water or pH 11.5 sodium hydroxide SNF storage water simulant solution in an ultrasonic bath at 30-40 °C at 120 kHz. The temperature was set slightly above ambient as to limit further corrosion with higher temperatures, but also to observe if increasing the temperature slightly in water/sodium hydroxide alone was able to remove surface corrosion. After 4-9 hours exposure to sonication some corrosion product was removed from the surface and settled as a sludge, whilst some remained adhered to the metal surface. All metal samples were removed from the liquor and dried in ambient atmospheric conditions.

a) b) c)

Figure 3-1 Corroded Magnox samples; a) corroded Magnox metal, b) sludge from sonication

3.2.2 Observing Magnox surface and removing corrosion product

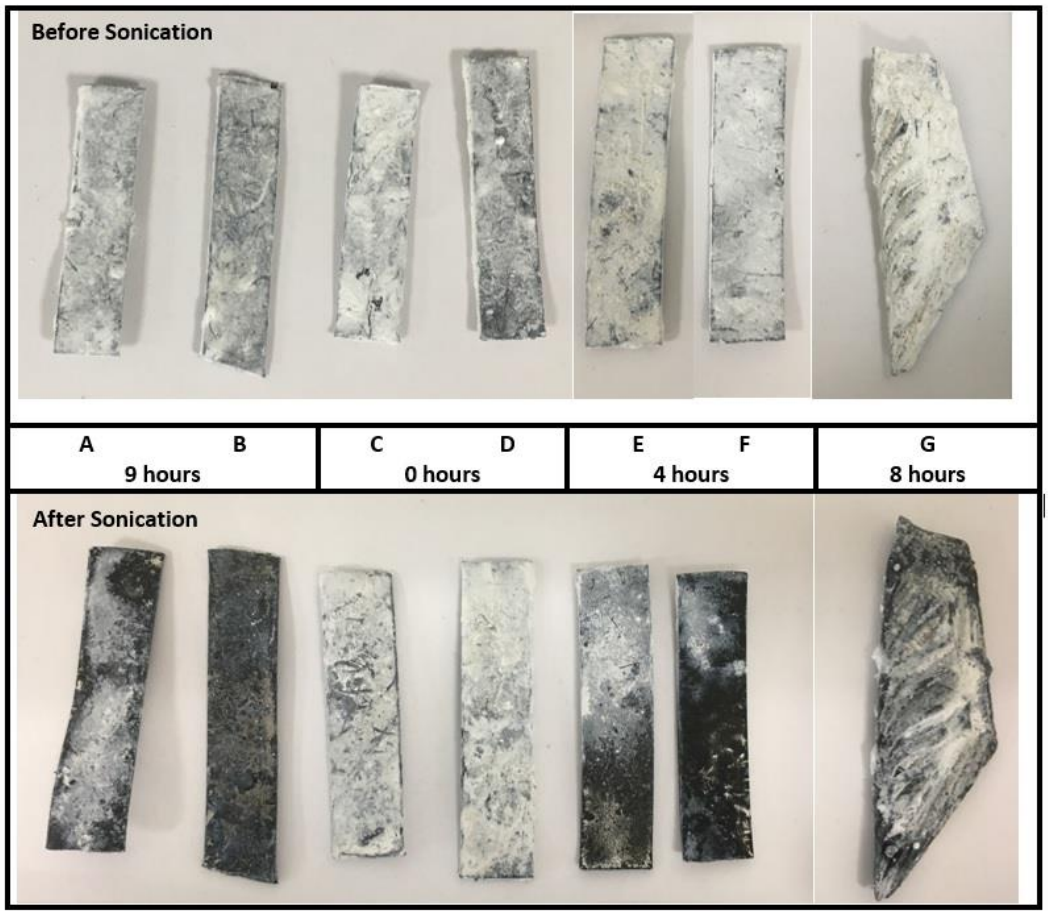

Figure 3-2. Corroded Magnox samples surface corrosion removal with sonication

The corroded Magnox samples (A-G) were stored individually under deionised water within a plastic bottle in a 40 °C water bath and sonicated for varying lengths of time. The sonication proved to be effective at removing large amounts of surface corrosion and exposing the Magnox metal surface beneath. The samples are displayed in Figure 3-2 and it can clearly be seen that the samples exposed to sonication (A,B,E,F and G) have large areas of bare metal visible, whereas there is no visible change in samples C and D which were held in deionised water without sonication. Most samples which were sonicated still had some visible corrosion product adhered to the surface in patches

The corrosion product removed by sonication produced a white sludge that settled at the bottom of the bottles but appeared milky and opaque when disturbed. An example of this is shown in Figure 3-1b which was gathered from sonication of a number of Magnox can shards/fragments together. The sludge was collected by pipette and water removed by evaporation in an oven at 40 °C overnight, isolating a very fine grey dried sludge powder, “Sample 4” (visible in Figure 3-1c).

3.2.3 X-ray diffraction

X-Ray Diffraction (XRD) is a powerful analytical technique for identifying chemical compounds based on their crystallographic structure, primarily used for single crystals and powders. An X-ray diffractometer provides a monochromatic X-ray which is targeted at a sample at a range of incident angles, and a detector counts the intensity of scattered/reflected radiation. As the X-ray wavelength is of the same order of magnitude as the distance between atoms in molecules (10^{-10} m), different incident X-rays can be diffracted from two different atoms/planes of a molecule and remain in phase, giving rise to a greater observed intensity at the detector. Once these angles are identified, the inter-plane spacing, *d* can be calculated trigonometrically using Braggs law (Equation 3-1):[40]

$$n\lambda = 2d \sin\theta \qquad \text{Equation 3-1}$$

Where *n* = diffraction order (in terms of relative path length differences), λ = X-ray wavelength, *d* = inter-place spacing and θ = angle between incident X-ray and lattice plane.[89] XRD data are well documented and a reference database is maintained by the International Centre for Diffraction Data (ICDD) which allows users access to material information such as d-spacings and relative peak intensities.

For this investigation XRD has been used to characterise unknown solid samples by comparison with known powder samples. All XRD data was recorded on a Malvern PAnalytical X'Pert Pro MPD X-ray diffractometer from a Cu K-α x-ray source (45 kV, 40 mA). Powdered or loose samples were loaded directly on to the XRD, and any samples too large or misshapen to fit on a sample holder were placed in the X-ray line intact.

3.2.4 Thermogravimetric analysis with FT-IR/Mass spectrometry

Thermogravimetric analysis (TGA) is a valuable technique that enables quantification of mass changes from chemical/thermal reactions. The technique monitors sample mass with changes in temperature, so as a compound undergoes a process at a certain temperature e.g. an oxidation reaction from heating in air, the associated mass change can be accurately measured which can be used to infer details such as the chemical stoichiometry. TGA can be used to study effects from heating, cooling and prolonged isothermal activity in air, chosen gas (e.g. N_2) or under vacuum to control which reactions are available to the sample. Supportive analysis of the reaction/decomposition products from techniques such as mass spectrometry (MS) or Fourier Transform Infrared (FT-IR) can be very valuable. This additional data gives better confidence of the process that is responsible for a given

sample mass change, for example detection of molecular water during a mass loss will be indicative of a dehydration step.

For this investigation, TGA/FT-IR analysis was undertaken on a Mettler Toledo TA/DSC1 with a Nicolet Thermo iS10 FT-IR spectrometer, under a 50 mL/min nitrogen flow, at 10 °C/min temperature ramp from 30 to 800 °C. TGA-MS was performed on a Netzsch STA 449 F5 Jupiter ASC DSC-TGA coupled with Aeolos QMA 403 D mass spectrometer. Testing was carried out under nitrogen from 30 to 800 °C ramping at 10 °C/min.

3.2.5 Computed tomography

X-ray microscopy and Computed Tomography (CT) techniques are able to provide non-destructive information about the internal structure and composition of a given material. Common with medical/dental and wider scientific applications, the process works by irradiating with x-rays to provide projections through the sample from a large range of angles. It is then possible to assemble the projections to mathematically construct cross sectional images which can be arranged to create a three-dimensional structure of the internal volume of the target.[90] The generated images can then be used to quantitatively observe and identify characteristics or features of interest based on differing density e.g. cracks or voids.

The CT analysis here was captured on a Zeiss Xradia 410 Versa instrument on an intact corroded Magnox sample. Imaging conditions were 40 kV at 0.4x optical magnification with voxel size of 5300 μm^3, at an exposure of 20 sec per projection, and a total of 1601 projections. Image analysis was performed using the software FIJI. Firstly the images were threshold adjusted such that only the component of interest (i.e. the metal and/or corrosion) was visible, and then the image sequence converted to binary. Then the images were inverted such that internal corrosion product voids could appear as objects which were filled so internal voids were integrated into the solid structure. The filled image was then subtracted from corresponding unfilled metal/corrosion image to leave only the void area visible. At this point the pixels of the metal, corrosion and the now visible void volumes could be quantified to account for a relative volume ratio of each, providing quantitative structural information about the corroded Magnox sample.

3.2.6 Microscopy; optical and scanning electron microscopy

Optical microscopy was used to observe and measure surface features of corroded Magnox samples following corrosion product removal. Optical and confocal microscopy was performed using a Zeiss LSM 800 microscope. Scanning Electron Microscopy (SEM) with Energy Dispersive X-ray (EDX) analysis was carried out on a Hitachi TM3030Plus Table top SEM.

3.2.7 Surface area

Surface area measurements are commonly performed in accordance with Brunauer-Emmett-Teller (BET) theory, which relates to adsorption of gaseous molecules onto a solid surface.[91] The BET interpretation takes account of the ability for multilayer adsorption by permitting the first adsorbed layer to support further adsorbed layers which can continue effectively indefinitely (which is not accounted for in more simplistic approaches like the Langmuir Isotherm).[40]

The amount of gas that can adsorb to a surface is directly dependent on the exposed and accessible surface area, as well as other conditions such as pressure and temperature. Typically for BET surface area analysis nitrogen gas is used, and the environment is cooled by liquid nitrogen. The process requires addition of a known quantity of nitrogen gas sequentially into the sample chamber, and the chamber pressure from each addition is precisely monitored. With pressurisation the number of adsorbed N_2 monolayers will increase until saturation is achieved, at which point no further N_2 will adsorb with any additional pressurisation. At this point the sample is removed from the N_2 atmosphere and heated, which causes the adsorbed nitrogen to desorb, enabling quantification. The process results in a BET isotherm which displays gas adsorbed as a function of relative pressure, and from this relationship it is possible to discern structural information about a material. The isotherm matches experimental observation well over certain pressure ranges, but can underestimate extent of adsorption at low pressure and overestimate at high pressure.[40]

BET surface area analysis was carried out on as-received magnesium hydroxide and hydromagnesite on a Micromeritics Tristar 3000 and FlowPrep 060. The samples were degassed on the FlowPrep at 150 °C under flowing nitrogen for 5 hours. A full isotherm of nitrogen adsorption data was collected at 77 K on the Tristar, with BET analysis carried out at relative pressures 0.05-0.2.

3.2.8 Density

A method for precisely defining the volume and density of a material is by Pycnometry. The basis for this method is in accordance with Boyle-Marioette's law of the relationship between pressure and volume. Pycnometry is usually carried out with small and inert gases, most commonly helium or nitrogen and assumes the gases behave ideally.[92] Density was assessed for as-received magnesium hydroxide (4.8043 g) and hydromagnesite (2.2979 g) on a Thermo Fisher Scientific Pycnomatic ATC helium pycnometer, calibrated at 20 °C using a 20 ml sample holder and steel calibration sphere. Measurements were made automatically until three were obtained with a standard deviation of <0.5%.

3.2.9 Particle size

PSD for magnesium hydroxide and hydromagnesite was measured on a Malvern Panalytical Mastersizer 3000 laser diffraction particle size analyser with Hydro MV wet dispersion unit. The samples were dispersed in deionised water for the measurement. Data from both samples was analysed using the same optical properties (for $Mg(OH)_2$; refractive index 1.570, absorption coefficient 0.010). After a 30 second background measurement, five consecutive 30 second runs were carried out with stirrer speed 3500 rpm and these averaged.

3.3 Vacuum Drying Apparatus and Methods

3.3.1 Drying rig design and operation

Vacuum drying was performed using a rig as shown in the schematic in Figure 3-3 and image in Figure 3-4. It consists of various components which allow control and monitoring of the drying conditions. The assembly and development of the apparatus is described in previous work by Goode et al.[8,9] The apparatus has been adapted for this work as will be discussed later.

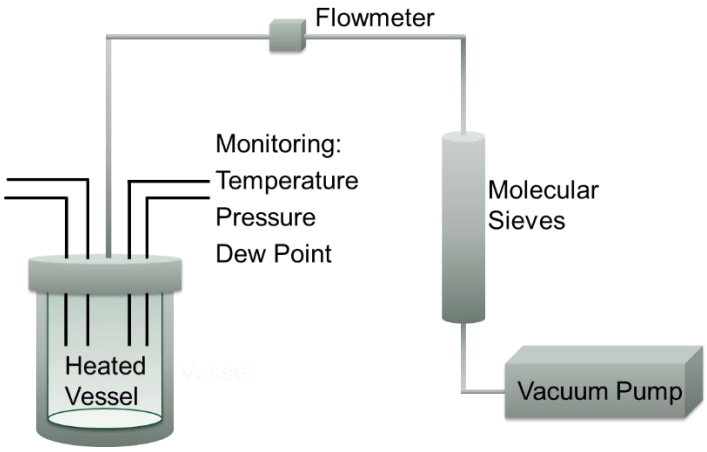

Figure 3-3. Schematic of drying rig

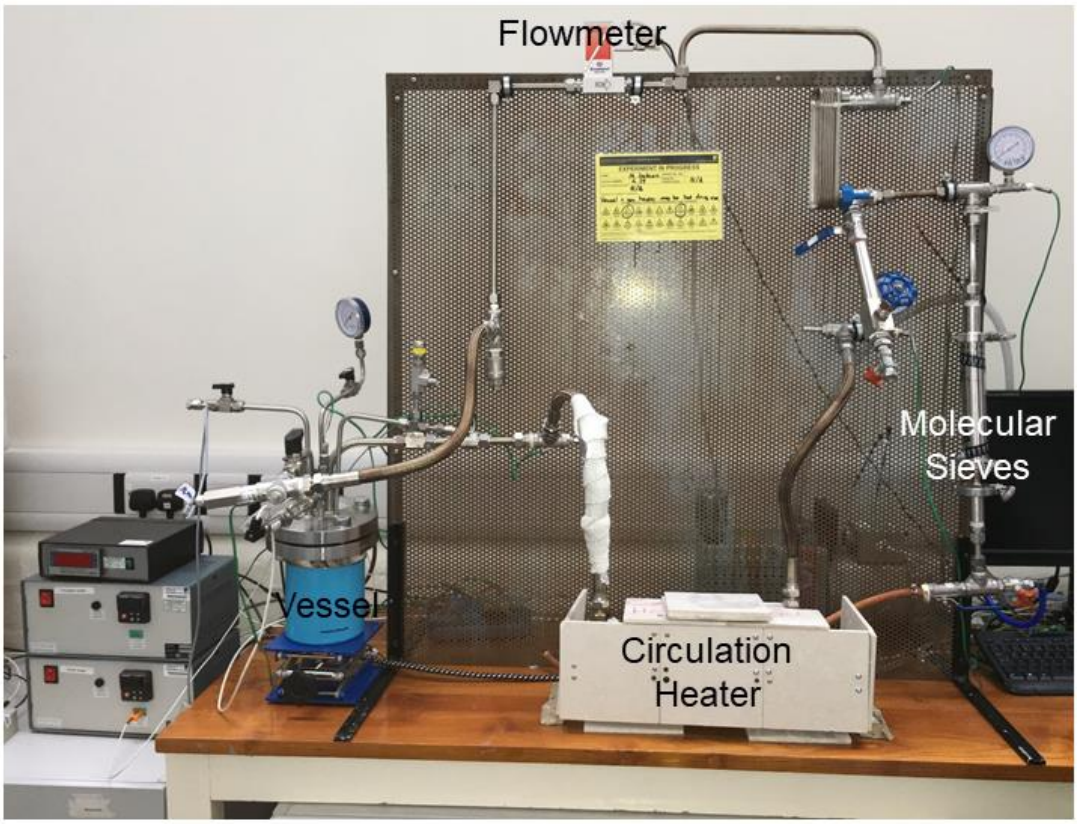

Figure 3-4. Image of drying rig

The rig consists of a vessel with a bolt mounted flange, sealed with various ports for gas flow and monitoring of vessel conditions. A band heater is installed around the vessel which allows elevated temperatures to be achieved and is controlled externally. Instrumentation to monitor the vessel pressure, temperature and dew point are inserted via sealed inlets to reduce leakages. The rig also has a mass flow meter to observe the flow velocity during vacuum and flowed gas drying operations. The instrument specifications are:

1. Pressure - measured by an OMEGA PXM319-002A10V 0-2 barA pressure transducer, with voltage logged by TracerDAQ and converted using manufacturer supplied three point calibration data.
2. Dew Point - measured by a MICHELL Instruments SF52 Dew-Point transmitter and read by MICHELL Instruments Easidew Hygrometer, with voltage logged by TracerDAQ and converted using calibration line from hygrometer readout.
3. Flow - measured using a Bronkhorst High-Tech B.V. series mass flow meter with thermal conductivity method of detection, and logged using the manufacturer supplied software which is displayed as a percentage of a defined maximum flow for a given gas (here 1.997 g/min air mass flow) and cannot be directly used to measure flow for unspecified components. On

this basis it is not used to directly determine water vapour mass flow but it does give a good indication of the relative flow between test conditions.

4. Temperature - measured using Welded Tip Gas and Water Tight PTFE K-type thermocouples fed into the vessel with a Spectite sealed feedthrough supplied by tc.co.uk and logged using a Pico TC-08 datalogger read by Picolog software.
5. Vessel Band Heater Controller - Watlow EZ Zone Controller.

A Molecular sieve is present to capture evaporated water, allowing for water mass balance to be achieved as well as protecting the vacuum pump from taking in moisture.

The vacuum pump is essential to reduce the rig pressure for vacuum drying, and pressures of 3-4 mbar are achievable in the current rig arrangement via an Edwards E2M5 rotary vane pump. Thermocouples are in place at sample surface/vessel internal, vessel base (outside) and vessel gas in/out. A rope heater was enlisted for some later tests to heat the rig steel tube at ~40 ˚C from the vessel lid to the molecular sieve column to prevent water condensation during drying. In addition to this some redundant parts were removed (such as heat exchanger and unnecessary tube length) to reduce the internal surfaces for potential water condensation, shown in Figure 3-5.

Figure 3-5. Image of drying rig following addition of rope heater (beneath lagging) and removal of unnecessary parts

Before undertaking drying tests the operational capabilities of the rig were assessed to ensure it could operate and perform consistently by achieving and holding suitably reduced pressure, maintaining constant temperature and providing appropriate data for analysis. Through operational experience some limitations of the rig have been identified. Firstly the vessel temperature moderation has some restriction, as the large amount of steel is relatively slow to conduct heat from the band heater, making the temperature moderation insensitive. Also the narrow tube bore limits the gas flow, restricting the effectiveness of flowed gas drying. As mentioned in Section 2.4.9 a recognised test for dryness is to hold the pressure of an isolated vessel at <4 mbar for ~30 mins. To assess the viability of assessing dryness by this method using the drying rig, a test to measure how gas-tight the vessel and rig was undertaken. The vessel was evacuated until no further pressure loss was observable - reaching 3.25 mbar - at which point the vessel was isolated and evacuation stopped to observe the pressure increase over a 30 minutes period. Once the time was over the vessel pressure had increased by 1.95 mbar to 5.20 mbar (shown in Figure 3-6). From this test it appears that the current vessel/rig setup is not adequately airtight to enable a test which relies on holding <4 mbar for any length of time. This should not have a significant impact on performing vacuum drying as the rig is capable of reaching adequately low pressures for evaporation of water.

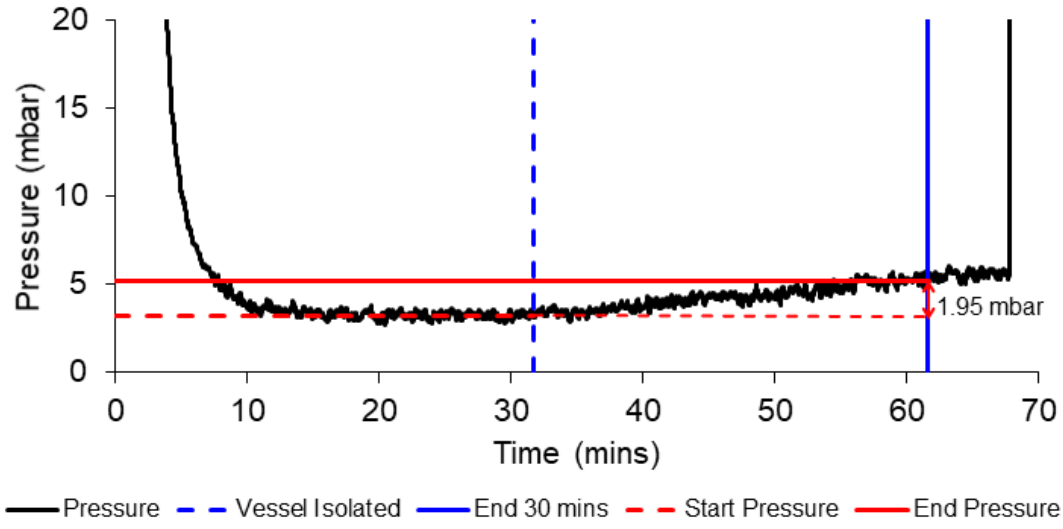

Figure 3-6. Vessel pressure performance

3.3.2 Drying test sample preparation and drying procedure

For the purposes of wetting in preparation for vacuum drying tests, corroded Magnox samples 1 and 2 (shown in Figure 3-7) were stored for a period of ≥12 hours in deionised water at ambient temperature. The wet samples were removed from storage water and towel dried to a consistent start (wet) mass of ≈14.85 g for

Sample 1 and ≈56.05 g for Sample 2. For “unbound water” drying tests (where a measured volume of liquid water was dried with no Magnox sample present) the desired mass of water was weighed into a steel open topped dipper. The dipper was freely able to be placed inside the rig for drying and removed at intervals for weighing to track water removal. Prior to this, the vessel heater was set to the desired test temperature, and when applicable rig steel tube rope heater was turned on and all dataloggers started. Once the vessel internal thermocouple displayed the intended test temperature, the sample was loaded and promptly sealed inside. Then the vessel was evacuated to dry the sample for the intended time, after which the sample was removed for mass measurement. For most tests this was performed at 10 minute intervals for the first hour, and then 30 or 60 minute intervals following the first hour. As the sample removal and mass measurement interrupted the data, an additional uninterrupted test without mass measurements was carried out at each temperature for comparison, onto which the mass measurements were overlaid for visualisation and interpretation.

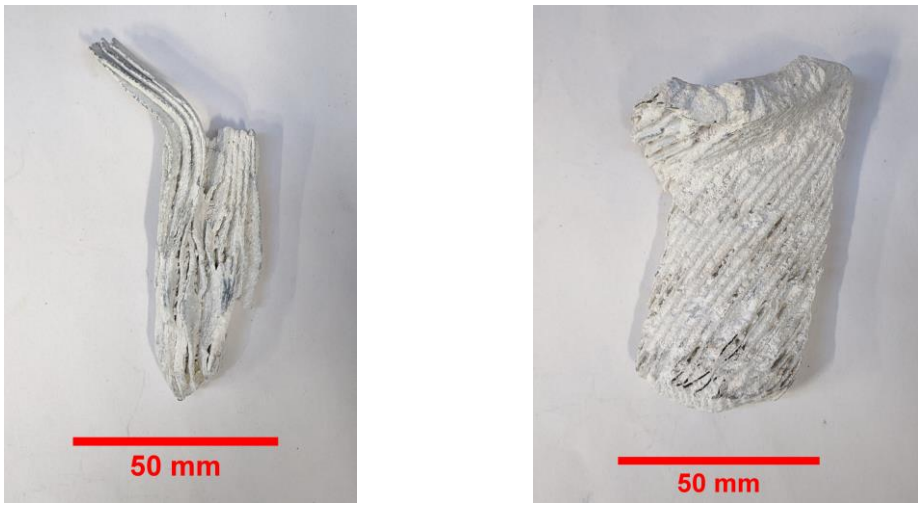

a) Sample 1 b) Sample 2

Figure 3-7. Corroded Magnox drying samples

Initially experimental length was undefined and was undertaken until no significant mass loss (typically <20 mg for Sample 1) was observed over 30 mins of drying. Over time and from practical experience based on drying temperature and water content, Sample 1 was dried for 3-4 hours total per test. For Sample 2 the drying time was set at 5 hours for all test conditions, which mostly produced mass loss <100 mg for the final 30 min drying period.

3.3.2.1 Error and variation analysis of method

A complication that arises from discussion of this process is the determination of how “wet” or “dry” a sample actually is. As a sample is removed from a container of

water, the majority of the water is unbound. Removal of this water has no real bearing on the experimental data but given the primary method of drying progress quantification is by mass loss it can have significant effect on the results. Therefore it was necessary to identify a “wet” start mass for each sample and keep this consistent, which was achieved by initially towel drying off excess unbound water. After this was performed for several drying tests a consistent starting “wet” mass for each sample was identified, and any following tests were kept close to this value whilst ensuring not to alter the preparation method. This method works on the assumption that the sample itself remains consistent over the course of the experimental investigation, although this assumption has proven to have its own limitations.

The starting mass over the 17 tests for Sample 1 that are included in this investigation had an average of 14.85 g with a standard error of the mean of ±0.013 g. The average starting mass over the 16 tests for Sample 2 was 56.05 g with a standard error of the mean of ±0.015 g. Tests at a given temperature were mostly undertaken sequentially for Sample 1 i.e. all data was gathered at 40 °C, then all data at 60 °C, then at 90 °C and finally at 120 °C. Given that the basis of this investigation shows that these samples do react readily with water, and the process requires the sample to be assumed consistent throughout, considerations were then given to how the test process could affect the sample itself. On this basis, for Sample 2 tests were scheduled to vary the temperature incrementally between each individual test such that no block of temperature data is going to cause the sample to change and unknowingly impact the following dataset. This approach proved to give a more balanced dataset which will be discussed further in the results later in this thesis.

The primary variable for this investigation was the drying temperature, with additional variables of time and the test sample. It also transpired that the temperature control of the vessel introduced the most significant variation between tests. Due to the relatively large volume of steel in the main vessel, the band heater had a tendency to overheat the vessel which required attention to manage the sample temperature and ensure experimental consistency. This heating variation is believed to give rise to the largest variation between drying tests under the same nominal conditions, particularly during tests at 40 °C where the variation is highest. As a result, the variation in temperature during testing was the most common reason for anomalous results and experimental repeats, so this was minimised by carrying out 3 repeats plus one uninterrupted test for each set of conditions.

Chapter 4 Characterisation of Magnox Corrosion Products

4.1 Introduction

One of the limitations to recreating real world conditions and materials in a research environment is ensuring the simulant materials are representative of those which they look to imitate. This is especially true of nuclear materials and wastes, for which access to real materials is very restricted, requires specialist facilities and not widely published due to sensitivity. This investigation employs corroded Magnox metal that was produced by the National Nuclear Laboratory, as well as chemically pure potential corrosion products from commercial manufacturers. This chapter aims to perform various analyses on these materials for comparison to real materials to assess representability, as well as gain additional knowledge on the chemical and physical attributes. Chemical analysis was performed to identify the compounds and species in the corroded Magnox samples by techniques such as X-ray diffraction and to quantify the amount of water present in test samples by thermogravimetric analysis. Physical analysis was performed to non-destructively attempt to quantify the extent of corrosion and potential routes for water trapping within Magnox samples by computed tomography, optical and scanning electron microscopy and energy dispersive X-ray analysis. Finally particle analysis was performed to identify particle size distribution in water, surface area and density.

4.2 Results and Discussion

4.2.1 Chemical analysis

4.2.1.1 X-ray diffraction

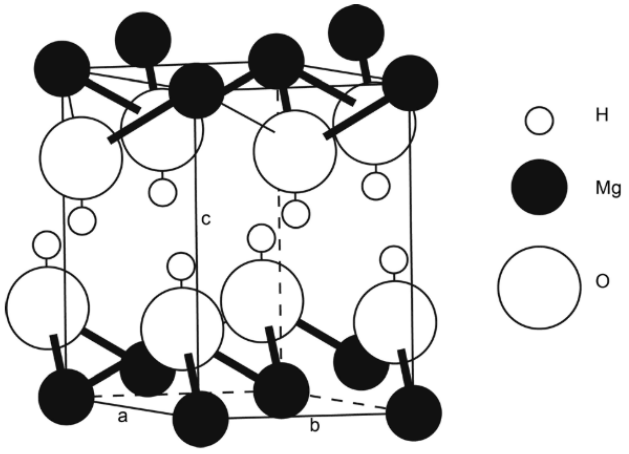

Figure 4-1. Crystal structure of $Mg(OH)_2$ (taken from Guo[93])

From review of literature and corrosion of magnesium in water, it is expected for wet stored Magnox cladding to predominantly contain magnesium hydroxide, commonly known as the mineral brucite. It has a hexagonal structure of trigonal symmetry, that consists of MgO_6 octahedra, with hydrogen atoms at each apex. The layers stack such that the hydrogen atoms are opposite the space between the three nearest hydrogen atoms in the facing layer, with no significant hydrogen bonding, as illustrated in Figure 4-1 (taken from Guo[93]).[94,95] Preliminary characterisation of samples was performed by XRD, which is shown in Figure 4-2:

1. Sample 1 – corroded Magnox sample used in drying (shown in Figure 3-7a),
2. Sample 2 – corroded Magnox sample used in drying (shown in Figure 3-7b),
3. Sample 3 – harvested by mechanical scraping dry material from a corroded Magnox sample shown in Figure 3-1a
4. Sample 4 – Produced from dried sludge generated by ultrasonic treatment of corroded Magnox (shown in Figure 3-1 in Methodology Section 3.2.1)

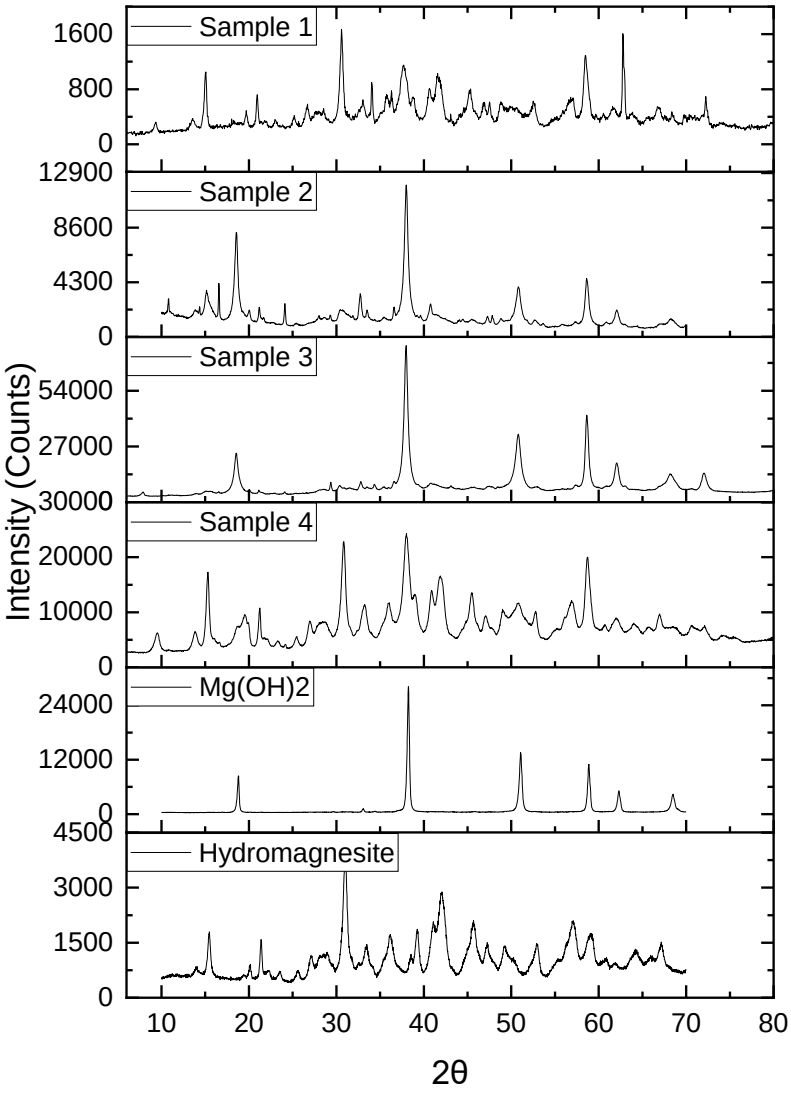

Figure 4-2. X-Ray diffraction of corroded Magnox Sample 1-4, magnesium hydroxide and hydromagnesite

As can be seen from the XRD, Sample 2 and 3 contain predominantly magnesium hydroxide, and Sample 4 a mixture of magnesium hydroxide and hydromagnesite. The diffraction pattern of Sample 1 was taken on the surface of the Magnox sample and not from a powdered sample to avoid damaging the sample, thus the amount of corrosion product for analysis was limited by the quantity at the sample surface, hence the low signal intensity.

XRD of Magnesium hydroxide produced diffraction peaks at 2Θ; 18.8°, 33.1°, 38.2°, 51.1°, 58.9°, 62.3° and 68.5°. The most distinctive hydromagnesite diffraction peaks are at 2Θ; 15.4°, 21.4°, 31.0°, 39.2° and 42.1°, consistent with those reported in literature.[96] From the XRD, Sample 1 appears different to the others in that the $Mg(OH)_2$ signal is harder to discern, with absence of the characteristic strong signal at 2Θ 38.2°. Some aspects of the diffraction pattern do match well with that of hydromagnesite (also shown), with particular correspondence to the signal at 2Θ 30.6°. XRD of Sample 4 also suggests a mixture of magnesium hydroxide and hydromagnesite. XRD patterns of Sample 2 and 3 consist predominantly of magnesium hydroxide, where Sample 2 appears to have other impurities present which are difficult to assign from the pattern but may be consistent with artinite,[97] $Mg_2(CO_3)(OH)_2{\cdot}3H_2O$ (as shown in Figure 4-3) which would be consistent with findings from Gregson et. al.[27]

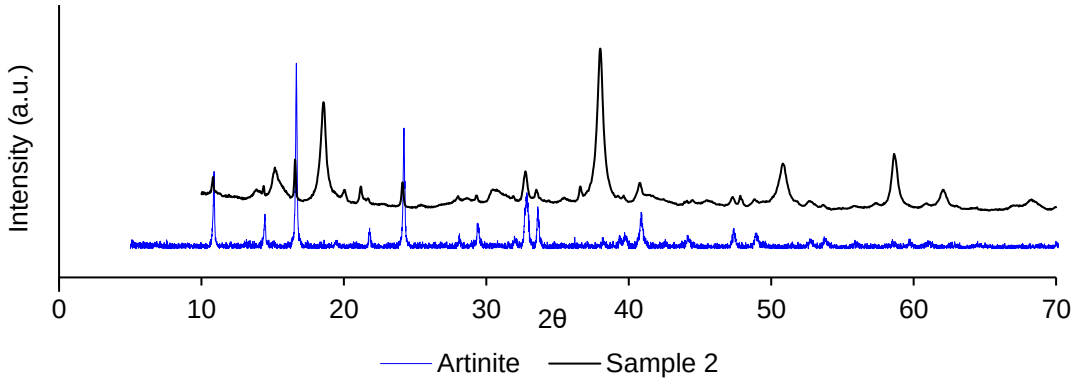

Figure 4-3. XRD of Sample 2 with diffraction pattern of artinite overlaid

4.2.1.2 Thermogravimetric analysis

Thermal decomposition was performed on as-received magnesium hydroxide, as-received hydromagnesite, Sample 3 and Sample 4 under nitrogen, which is shown in Figure 4-4. Decomposition of magnesium hydroxide occurs in one step through dehydroxylation to magnesium hydroxide (Equation 2-3) which occurs at 285-475 °C in Figure 4-4a, consistent with literature.[98,99,100,101]

$$Mg(OH)_2 \rightarrow MgO + H_2O \qquad \text{Equation 4-1}$$

The TGA decomposition was also undertaken with mass spectrometer analysis of off-gas products.

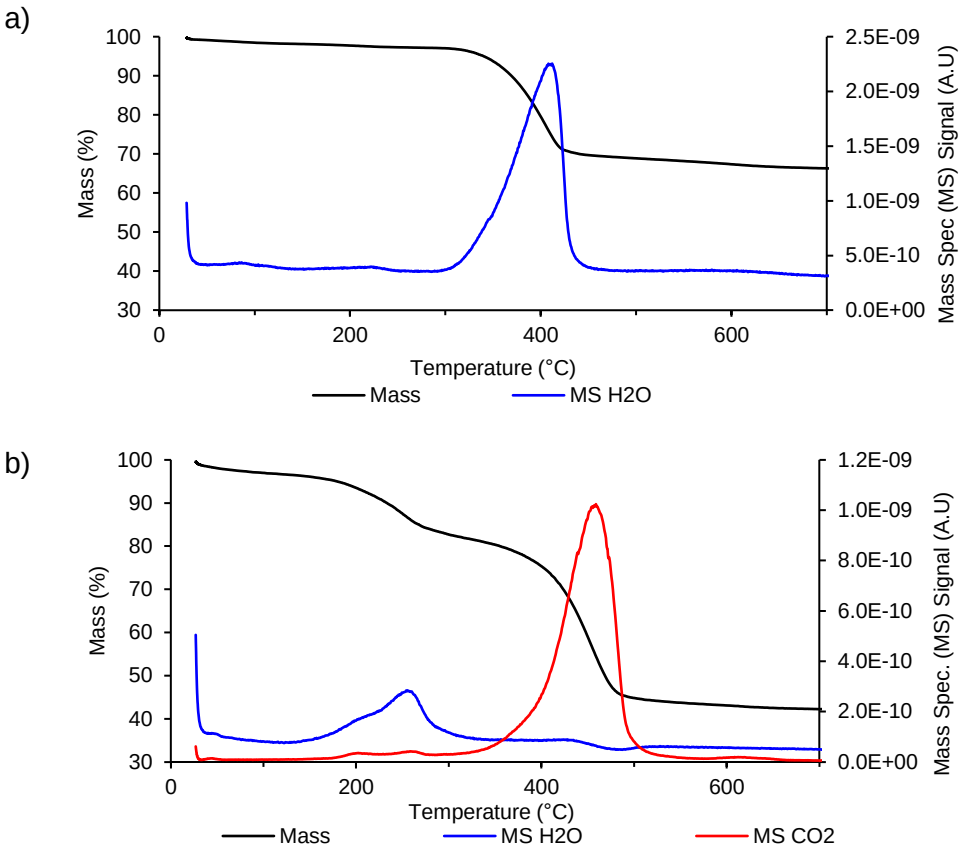

Figure 4-4. Thermal decomposition of samples; a) as-received magnesium hydroxide (with mass spectrometry), b) as-received hydromagnesite (with mass spectrometry)

As expected the decomposition is associated with loss of water from dehydroxylation, but also of interest to this work is the presence of physisorbed water on the sample material. This water is removed prior to the main decomposition step and is attributed to the mass loss in the first 285 °C of heating for $Mg(OH)_2$, measured here as 2.84% by mass. It appears to occur in two distinct but small responses from the mass spectrometer, the first up to 140 °C, then the second up to 285 °C.[87] Some literature vary as to what temperatures the removal of adsorbed water occurs, although some agree that it is up to 200 °C and the dehydroxylation reaction does not commence until ~280-300 °C.[86,87,102–104] Liu et al. report that the temperature of decomposition onset increases with increasing heating rate.[105] Given the clear point of decomposition here and the mass spectrometer water signals (which were consistently visible for multiple samples), the water content is attributed as such. For all other compounds, mass loss attributable to that of physisorbed water is negated when considering chemical

changes and decomposition at temperatures beyond this point, effectively considering this mass as the “dry” sample mass).

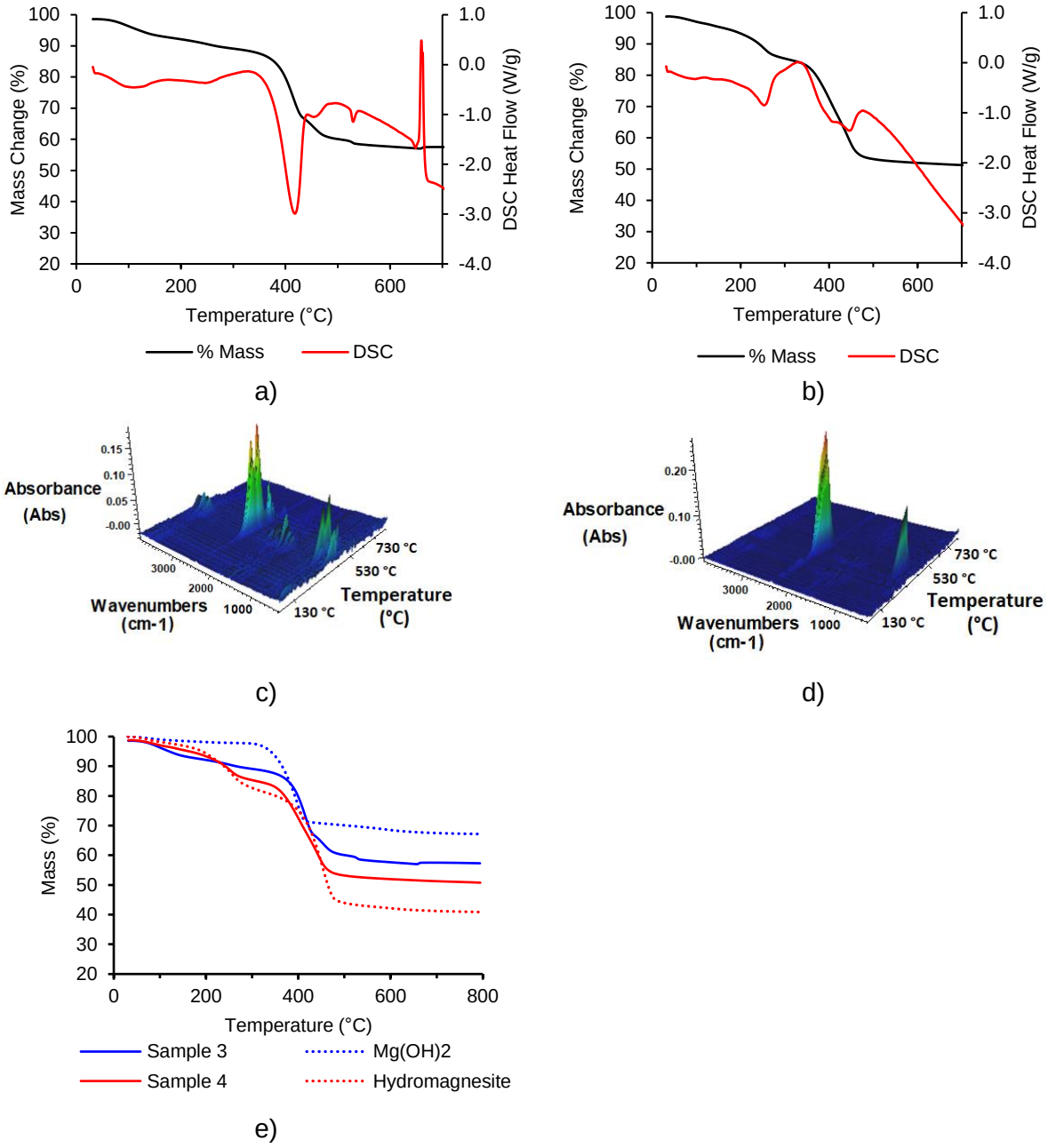

Figure 4-5. Thermal Decomposition of samples; a) Sample 3 (with DSC), b) Sample 4 (with DSC), c) FT-IR for Sample 3 TGA, d) FT-IR for Sample 4 TGA, e) all samples displayed together with magnesium hydroxide + hydromagnesite

The decomposition through dehydroxylation of magnesium hydroxide measures a mass loss of 30.3% (measuring from the sample mass at 285 °C to the final mass at 800 °C and negating any mass lost from physisorbed water), which is close to the theoretical value of 30.9%.

Decomposition of hydromagnesite occurs in three main steps; dehydration of four water of crystallisation molecules, dehydroxylation and decarbonation as outlined in Table 4-1. The dehydration step occurs between 120-315 °C giving rise to the water response in the mass spectrometer signal, with measured associated loss of 15.2% mass – which is close to the theoretical stoichiometric mass loss of 15.4%. The dehydroxylation and decarbonation steps occur together over the same temperature range which initiates after dehydration at 315 °C, with the sharpest mass loss observable up to 500 °C and stabilising at 700 °C and a strong response in the mass spectrometer CO_2 signal. This step had an observed mass loss of 41.4% from 315-800 °C which is close to the theoretical mass loss of 41.5% and consistent with literature values.[106] In addition to the thermal decomposition process it was of interest to establish the amount of physisorbed water on the as-received solids by looking at mass loss from vaporisation of surface water prior to loss of water of crystallisation, which was measured as 3.36%.

Table 4-1. Thermal decomposition steps of as-received hydromagnesite

Reaction	Step	Temp. (°C)	Mass Loss (%)	Theoretical Mass Loss (%)
$Mg_5(CO_3)_4(OH)_2.4H_2O \rightarrow Mg_5(CO_3)_4(OH)_2 + 4H_2O$	Dehydration	120-315	15.2	15.4
$Mg_5(CO_3)_4(OH)_2 \rightarrow Mg_4(CO_3)_4MgO + H_2O$	Dehydroxylation	315-800	41.4	3.9
$Mg_4(CO_3)_4MgO \rightarrow 5MgO + 4CO_2$	Decarbonation			37.6

TGA of corroded Magnox samples 3 and 4 data are summarised in Table 4-2 and displayed in Figure 4-5a-e. Sample 3 mass loss was gradual during the initial heating phase, losing 2.33% mass up to 100 °C. The sample mass continued to drop gradually from 100-330 °C by 8.24% of the “dry” mass. At 330 °C the main decomposition step initiates which is visible as an initially large and consistent drop with associated endothermic DSC response until the temperature reaches 430 °C, at which point the line reaches a small shoulder and decomposition slows slightly, with the DSC rising from -3.0 to -1.0 W/g. The 330-800 °C decomposition displayed a mass loss of 32.3%, giving rise to a total mass loss from decomposition of “dry” sample of 40.5%. After 500 °C the sample mass remained fairly consistent with a small endothermic event visible at 520-545 °C, and a more notable exothermic event at 650-675 °C. Inflexions similar to that at 530 °C have been reported in the literature for hydromagnesite decomposition, which is attributable to crystallisation of magnesium carbonate which also coincides with a carbonate response on the FT-IR, but the small magnitude of the signal here suggests this crystallisation is not occurring to a significant degree which is consistent with the observations at similar heat rates in nitrogen and air.[106,107] In some reports this is present as a sharp exotherm, specifically at greater heat rates (20 °C/min) and affected by

atmosphere.[108] Sawada reports that packing density of the sample can affect the decomposition, and the exotherm is more likely to be visible for densely packed samples, which would apply here as the material was crystalline and firm, having been scraped from the corroded Magnox surface.[109–111] Whilst the exotherm present here at 660 °C does initially look comparable to that seen in literature for carbonate crystallisation, the temperature difference at which it occurs suggests it is unrelated. It happens to coincide with the melting point of magnesium (650 °C) and also aluminium (660 °C), which could be present in metallic form (particularly magnesium) due to the method of sample harvesting, but the process of melting is endothermic so does not explain this observation.

Table 4-2. Thermal decomposition data of corroded Magnox samples

Sample	Temperature	Temperature (°C)	Mass Loss (%)
Sample 3	Dehydration (physisorbed)	0-100	2.33
	Dehydration (chemisorbed)	100-330	8.24
	Dehydroxylation/ Decarbonation	330-700	32.3
	Total (dry)	100-700	40.5
Sample 4	Dehydration (physisorbed)	0-100	1.71
	Dehydration (chemisorbed)	100-315	12.7
	Dehydroxylation/ Decarbonation	315-700	34.5
	Total (dry)	100-700	47.2

It is interesting that the decomposition of Sample 3 displayed character of hydromagnesite/magnesium carbonate decomposition (particularly detection of CO_2 in IR – strong signal at wavenumbers 600-700 cm^{-1}, 2300-2400 cm^{-1} and weak signal at 3600-3700 cm^{-1} – and mass loss of 32.3% c.f. 30.9% for $Mg(OH)_2$) when considering the XRD suggested the sample comprised predominantly of magnesium hydroxide.

Thermal decomposition of Sample 4 was similar to that of Sample 3, occurring in two main steps following initial drying and shown in Figure 4-5b+d. During the removal of physisorbed water up to 100 °C a mass loss of 1.71% was observed, producing the “dry” sample solid. This value is affected by the preparation method, and since the solid was isolated by oven drying at ~40°C it is unsurprising this value is less than that of other samples. From there gradual dehydration of chemically bound water gave rise to a further 12.67% (slightly less than the theoretical 15.4% for hydromagnesite) up to 315 °C. During this phase a faint IR signal corresponding to water (1500-1800 cm^{-1} and 2900-3600 cm^{-1}) is visible, likely due to the relatively

slow evolution of water during this step. During the decarbonation and dehydroxylation step from 315 °C to the end of testing the mass loss was a further 34.5%, again slightly less than the theoretical 37.6% for hydromagnesite. This step was associated with strong CO_2 and faint water signals by infrared spectroscopy. The TGA is consistent with the XRD data which suggests that Sample 4 contains a mixture of predominantly Mg-hydroxycarbonate (hydromagnesite) with presence of some magnesium hydroxide.

4.2.1.3 Using TGA to quantify composition

If it is known that a mixture contains purely two compounds (such as magnesium hydroxide and hydromagnesite), it would be possible to estimate the relative composition based on the mass of decomposition. It is known that the theoretical mass loss on decomposition of magnesium hydroxide is 30.9%, and for hydromagnesite is 56.9%, so therefore thermal decomposition of a mixed sample will vary linearly between these two values by the following relationship (Equation 4-2):

$$\%\, Hydromagnesite = \left[\frac{56.9 - 30.9}{100}\right]^{-1} \times Mass\ Loss\ \% - 118.74 \qquad \text{Equation 4-2}$$

From this relationship, the composition of Sample 3 is estimated at 36.9% hydromagnesite and Sample 4 at 62.7%. This estimation does work on assumptions that there are no other impurities/components and that no adsorbed water is present. These factors will introduce uncertainty, particularly for hydromagnesite where the dehydration is very gradual and less well defined than magnesium hydroxide, but the majority of adsorbed water will be removed at 100 °C so uncertainty from adsorbed water should be insignificant.

4.2.2 Physical characterisation

4.2.2.1 X-ray µ-computed tomography (CT)

X-ray µ-CT has been reported in recent literature for quantitative monitoring of corrosion of nuclear materials in simulated storage scenarios by Paraskevoulakos, Hallam, Adamska and Scott,[112] and for Mg alloy corrosion monitoring by Davenport et al.[113] The work by Paraskevoulakos et al. was able to non-invasively and non-destructively track the corrosion of uranium and subsequent formation of the uranium corrosion products UO_2 and UH_3, demonstrating the efficacy of these techniques for corrosion analysis. Here a three-dimensional CT scan of Sample 1 was compiled which allows interrogation of physical structure and composition which wouldn't be achievable otherwise. The process yields a stack of slices, such as the one in Figure 4-6a which can be manipulated to highlight specific aspects of

the sample/image. Due to the difference in density, the corrosion product and metal substrate are differentiable by the lighter shade on a grayscale image of the denser metal. From this the image threshold can be adjusted until the metal and/or corrosion are highlighted, which enables further analysis. In Figure 4-6b the metal and corrosion have been coloured in grey and black respectively, and within the gaps between corrosion certain voids can be seen. These are of interest to this investigation as they provide a viable route for trapping of liquid water. Through software manipulation these holes can be filled to produce the binary image in Figure 4-6c, with the voids/holes filled. By addition/subtraction of these images of Figure 4-6b+c, the holes/voids can be highlighted without the solid, as shown in Figure 4-6d.

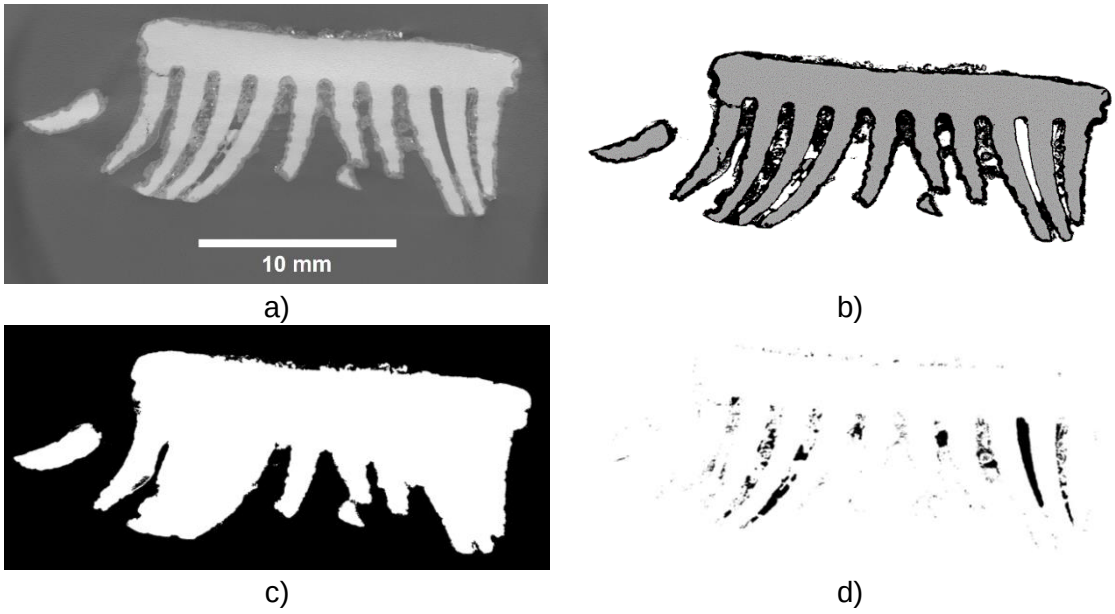

Figure 4-6. Analysis process of CT scan slices; a) raw scan image, b) threshold selection showing metal (grey) and corrosion (black), c) selection of image metal and corrosion with “holes filled”, d) image showing only voids/holes

Table 4-3. Component area/ratio as shown in Figure 4-6

Component	Shade	Pixels	Ratio
Black (corrosion)	0	133793	0.30
Grey (metal)	170	296282	0.66
Filled Volume (inc voids)	255	451985	1.00
Voids	0	22273	0.05

By comparing the pixel numbers of the individual components (as listed in Table 4-3), a relative volume of each can be quantified. This method has been applied to each projection to quantify the whole sample, and visualised in three dimensions. Figure 4-7 shows; a) volume of raw scan images (metal+corrosion), b) metal only, c) corrosion only, and d) shows the void space as estimated by the method described. Figure 4-7e+f show the void space coloured in blue overlaid on the corrosion as a visual representation of the potential for water trapping in such voids.

By calculation over the whole volume this has been estimated at an additional 3% of the metal/corrosion volume for Sample 1 (Table 4-4). From the pixel size of 17.4 µm, and a voxel volume of 5.3 x 10^{-9} cm^3 the volume of each component can be calculated, which shows the void volume of the scan at 0.12 cm^3.

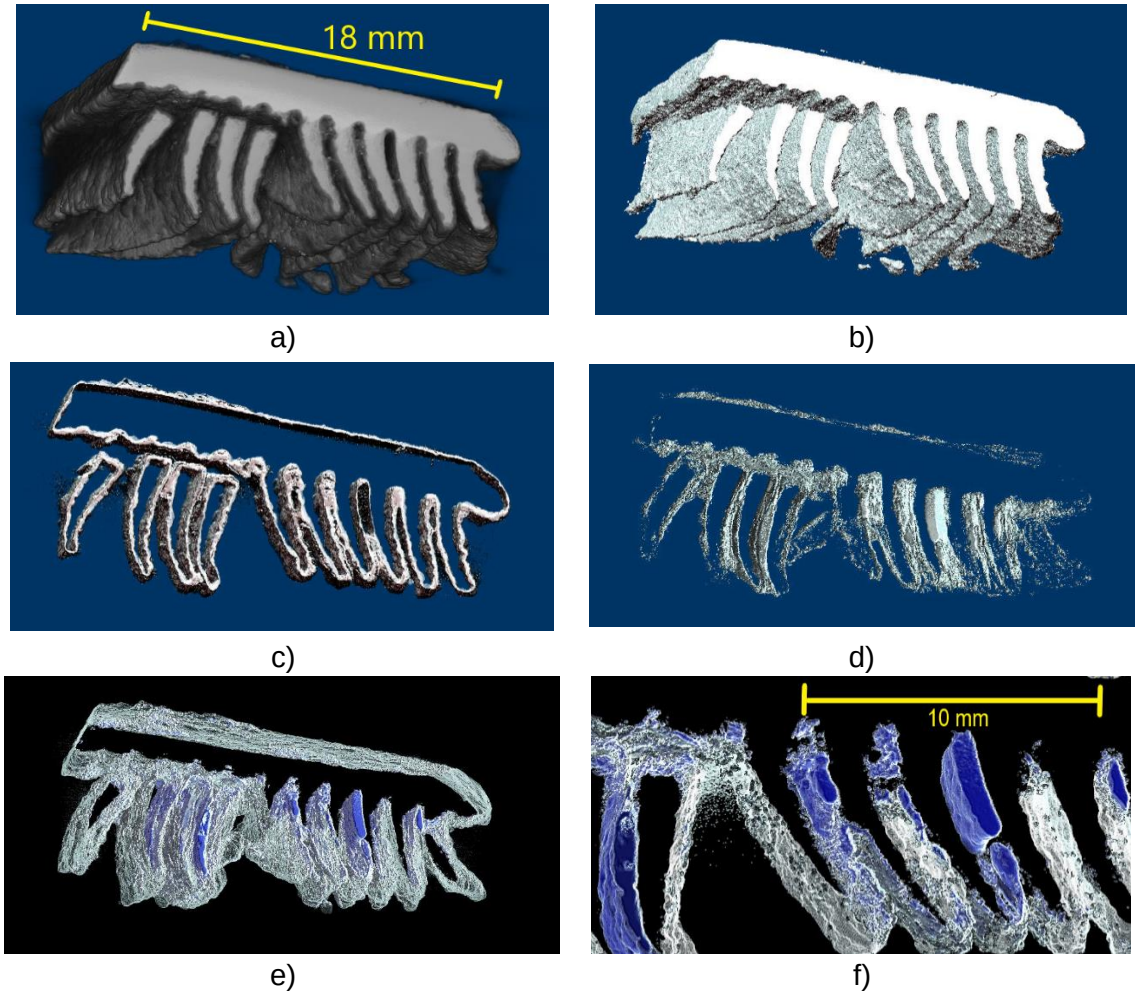

Figure 4-7. Image analysis of CT scan of Sample 1; a) whole sample (1400 slices/23.8 mm depth), b) metal only (1400 slices/23.8 mm depth), c) corrosion only (100 slices/1.7 mm depth), d) voids (600 slices/10.2 mm depth), e) corrosion surface with voids filled in blue (600 slices/10.2 mm depth), f) closeup of corrosion surface with voids filled in blue (600 slices/10.2 mm depth)

Table 4-4. Component area/ratio for Sample 1 as measured from Figure 4-7

Component	Volume (cm^3)	Ratio
Metal	2.33	0.63
Metal + Corrosion	3.57	0.97
Corrosion	1.24	0.34
Voids	0.12	0.03
Total (Metal+Corrosion+Voids)	3.69	

This scan demonstrates that with significantly corroded Magnox, voids can be found within the structure which may provide opportunity for volumes of water to be trapped. In addition to the extensive corrosion, this particular sample is largely distorted and deformed, likely from a simulated decanning process. Figure 4-7 shows that many of the sample fins are bent, and some have become detached from the cladding. The corrosion between some adjacent fins meet to form pockets of internal volume, sealed by the corrosion products. It is acknowledged that such analysis by this method is limited to the volume contained within the scan range. Therefore other routes or channels for water escape beyond this range are not captured by a single scan.

It is hard to estimate precisely how representative this corroded and misshapen sample is when simulating an intact fuel can of undetermined storage time, but the fundamental can geometries and chemical processes/products should still be valid. Looking at CT scans in this way is a versatile and powerful tool to assess both qualitatively and quantitatively for corrosion extents and potential for water trapping in such materials.

4.2.2.2 Ultrasonic treatment of corroded Magnox

The corrosion on the surface of the Magnox samples covers the majority of most individual pieces with a layer of white material, identified as predominantly magnesium hydroxide. In order to analyse the underlying substrate and metal surface, it was necessary to remove the corrosion whilst minimising mechanical interference and damage, whilst achieving a good standard of metal visibility. Sonication of the samples for 4-9 hours was able to achieve this as shown in Experimental Methods Section 3.2.1. As described corroded Magnox samples were prepared by sonication in water, such that surface corrosion products could be removed without exposing the samples to significant mechanical damage (shown previously in Figure 3-2).

4.2.2.3 Microscopy

Two of the sonicated samples were observed and compared by optical/electron microscope, one selected on the basis of the most surface corrosion removed

(Figure 3-2B), and a control with no corrosion removed Figure 3-2C. The images are displayed in Figure 4-8 to Figure 4-13. Figure 4-8a shows Sample C, the control sample with no corrosion product removed. Figure 4-8b shows Sample B, with corrosion removed by sonication. Figure 4-9 shows images of surface corrosion of the control sample. Figure 4-9a shows a close-up optical image of the corrosion surface at Site 1, which shows the thick layer of corrosion product and holes through which dark patches of metal can be seen. Figure 4-9b is close-up image of another location on the sample surface, where the corrosion product has formed needle-like structures, and another hole through which the metal surface is visible. Figure 4-9c+d shows confocal microscopy topographical images of the optical position from Site 1. Figure 4-9e+f shows confocal microscopy topographical images of the optical position from Site 2. These figures are able to display the relative heights/depths of the features shown and provide quantitative information on the dimensions. The data indicate that the range in height from the lowest to highest point is approximately 100 µm in Figure 4-9c, and that the diameter of the hole is approximately 170 µm. It cannot be inferred from the image whether the hole leads to a corrosion pit of the surface of the metal, so the depth of the surface corrosion here is uncertain.

a) b)

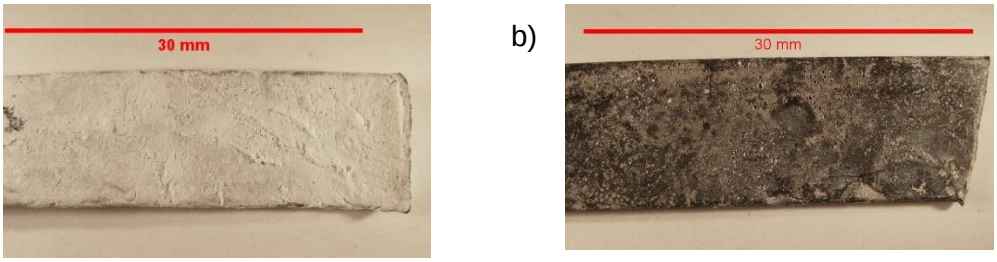

Figure 4-8. a) Image of Sample C (control), b) Image of Sample B (sonicated)

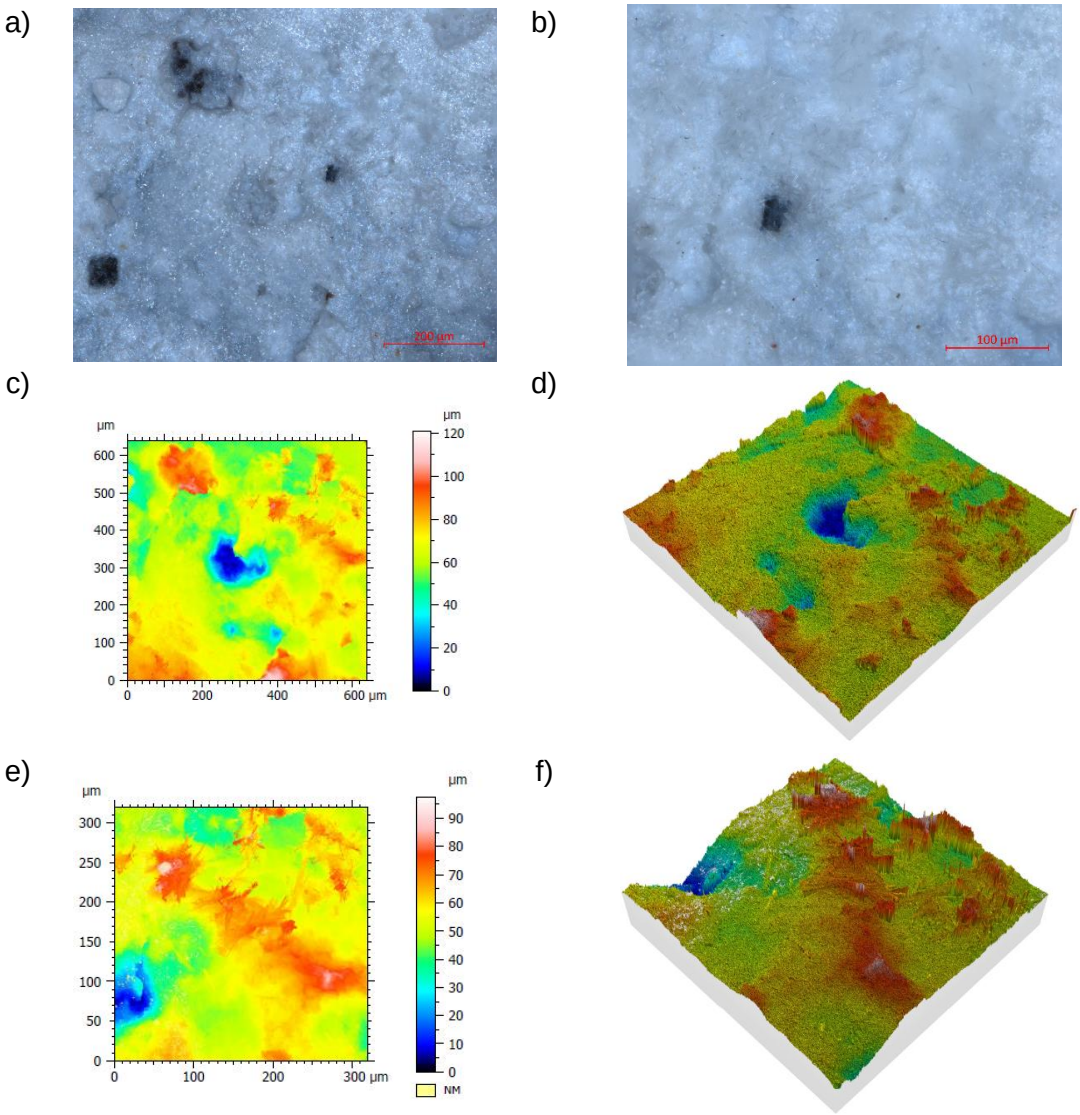

Figure 4-9. Microscopy images of sample C (control); a) microscope image of corrosion Site 1, b) microscope image of corrosion Site 2, c) d) 500x magnification SE SEM image, e) 1kx magnification SE SEM, f) 2.5kx magnification SE SEM, g) 5kx magnification SE SEM, h) 10kx magnification SE SEM

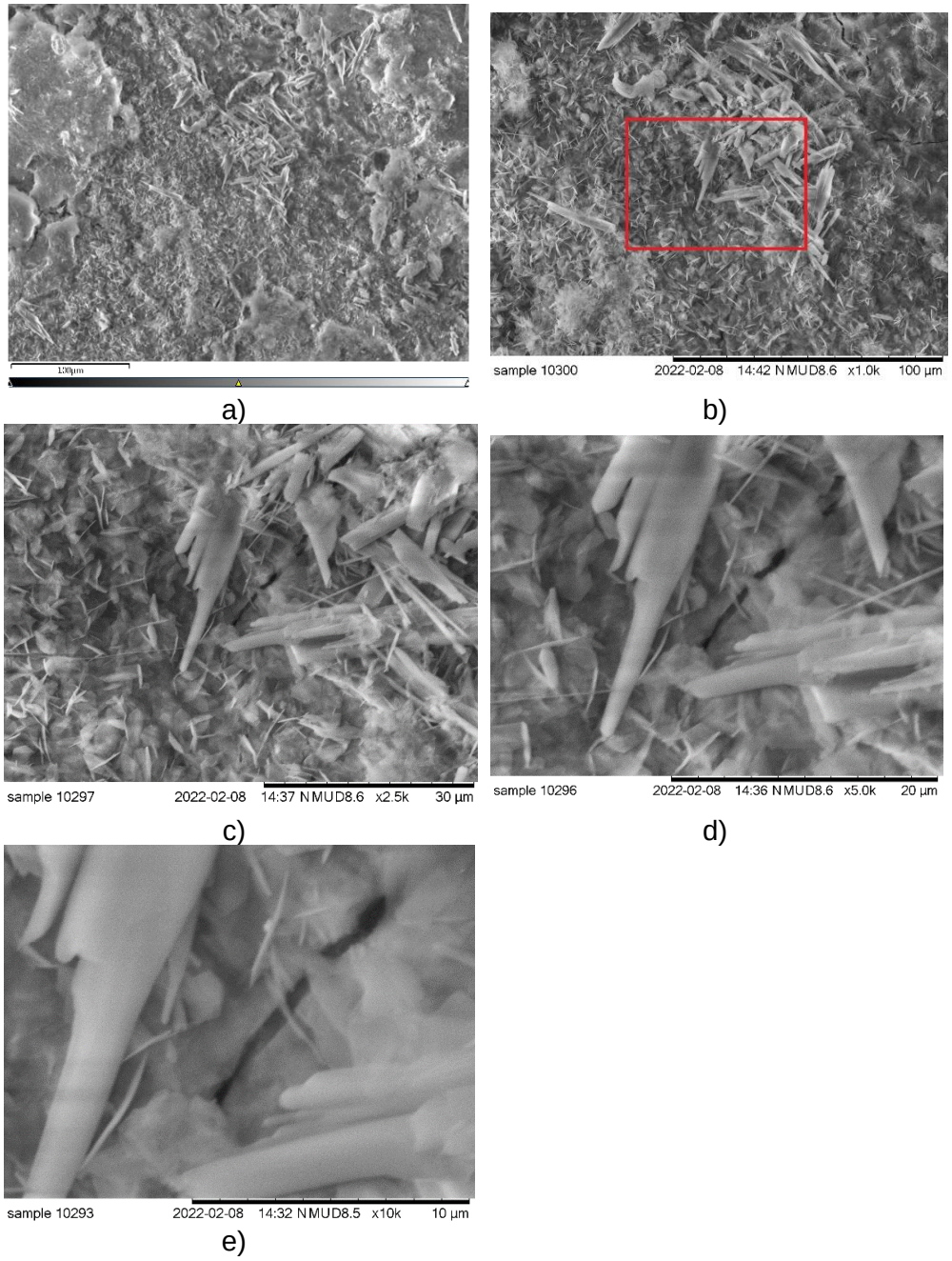

Figure 4-10 Images of Corroded Magnox Sample C; a) 500x magnification SE SEM image, b) 1000x magnification SE SEM image, c) 2.5kx magnification SE SEM image, d) 5000x magnification SE SEM image, e) 10kx magnification SE SEM image,

Topographical images from Figure 4-9e+f show part of the hole and needle-like structures similar to those seen in Figure 4-10. The height range varies by 90 µm from the bottom of the hole to the top of the needles. As with the previous sample it is not clear if the hole is a pit and penetrates the metal surface, or is a hole in the corrosion product to the metal surface so the corrosion product depth cannot be measured here. The hole has an approximate diameter of 120 µm, and depth of 55 µm. Figure 4-10a-e show secondary electron (SE) SEM images of the same position at a range of magnifications from 500-10,000x magnification. The images

show a variety of morphologies in proximity, with a large crust of material present covering a significant portion of the surface, along with interlocking platelet morphology and needles/rods (similar to that reported by Gregson at al. in Section 2.3.1 as brucite and potentially artinite/nesquehonite)[27]. At magnifications 2500x and higher, hexagonal platelet morphologies of approximately 1-2 µm in diameter are visible. The rods vary in size and length, and those pictured are up to 30 µm long and 2-3 µm thick. Gregson et al do report the presence of rod-like crystallites protruding from aggregates. The dimensions described by Gregson et al. are generally smaller (1-10 µm in length and 75-500 nm wide) and appear different in the images, so it cannot be said if these morphologies are the same but equally they were recovered from sludges and suspensions, not from the surface of corroded metal so the smaller size is unsurprising.

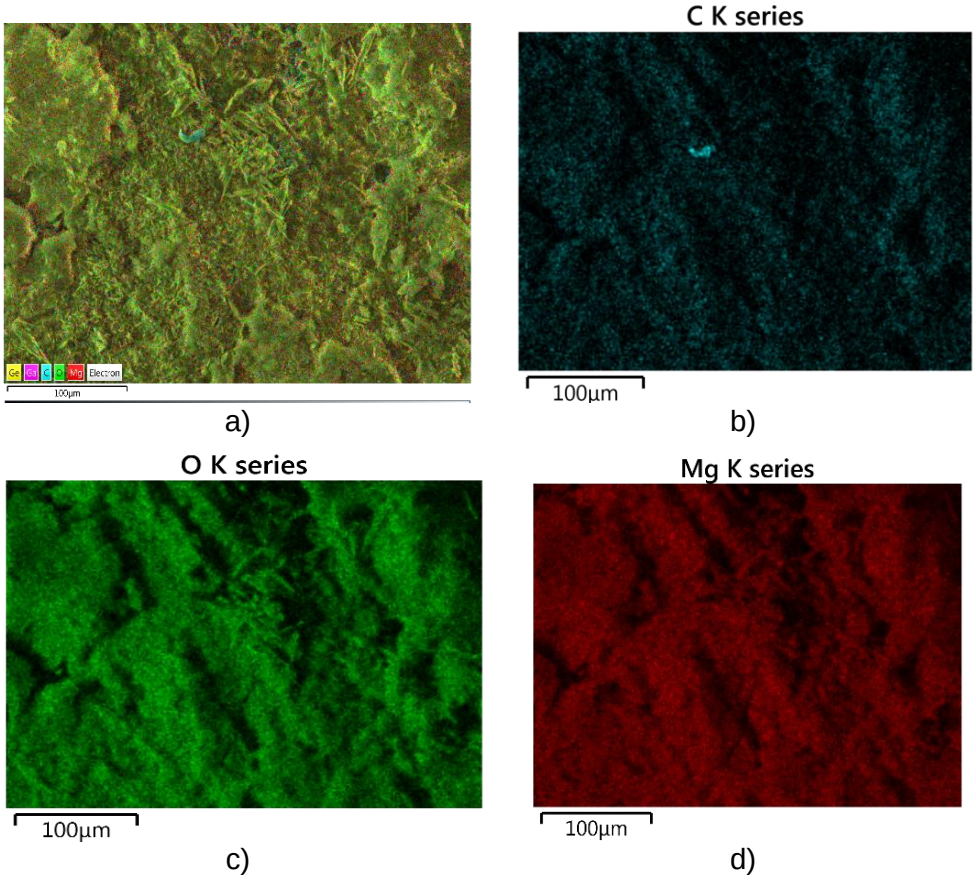

Figure 4-11 EDX of corroded Magnox Sample C; a) all components, b) carbon, c) oxygen, d) magnesium

EDX of Sample C (Figure 4-11) indicate the strong presence of magnesium and oxygen, with lesser carbon coverage, consistent with composition of magnesium hydroxide and/or magnesium hydroxycarbonates (e.g. hydromagnesite). In Figure 4-11b an area of high carbon content is visible, which is believed to be surface contamination and not an alternate phase or compound. Dark patches are visible in

the EDX due to shadow from the surface topography cast by the angle of X-ray source within the microscope, and is not representative of variations in composition.

The optical images of Sample B in Figure 4-8b and in Figure 4-12a+b show the surface is dark grey/black, with visible corrosion pits across the whole area. Some small patches of white corrosion are still adhered to the surface but most of the area is clear. Figure 4-12c-f show topographical confocal microscope image of the surface of Sample B from Site 1 and Site 2. The images highlight the corrosion pits and indicate the depth of the pit at both Sites are approximately 70-80 µm (on the basis that highest levels in red/white are corrosion built up from the surface, and are not considered here with respect to pit depth). The diameter of the pits are 125-200 µm.

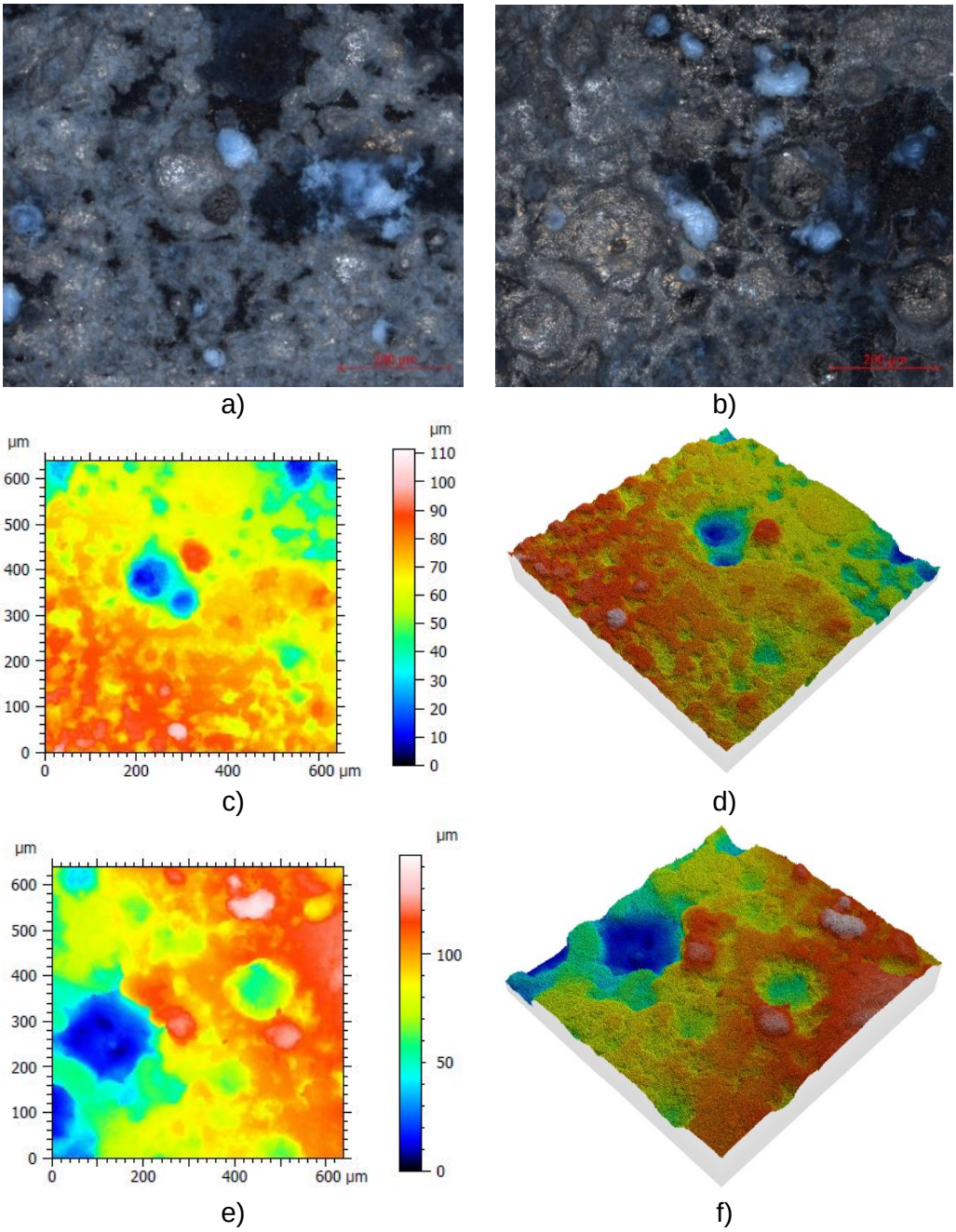

Figure 4-12. Microscopy images of sample B; a) microscope image of Sample B (Site 1), b) microscope image of Sample B (Site 2), c,d) topography of Magnox Sample B Site 1, e,f) topography of position in Sample B Site 2

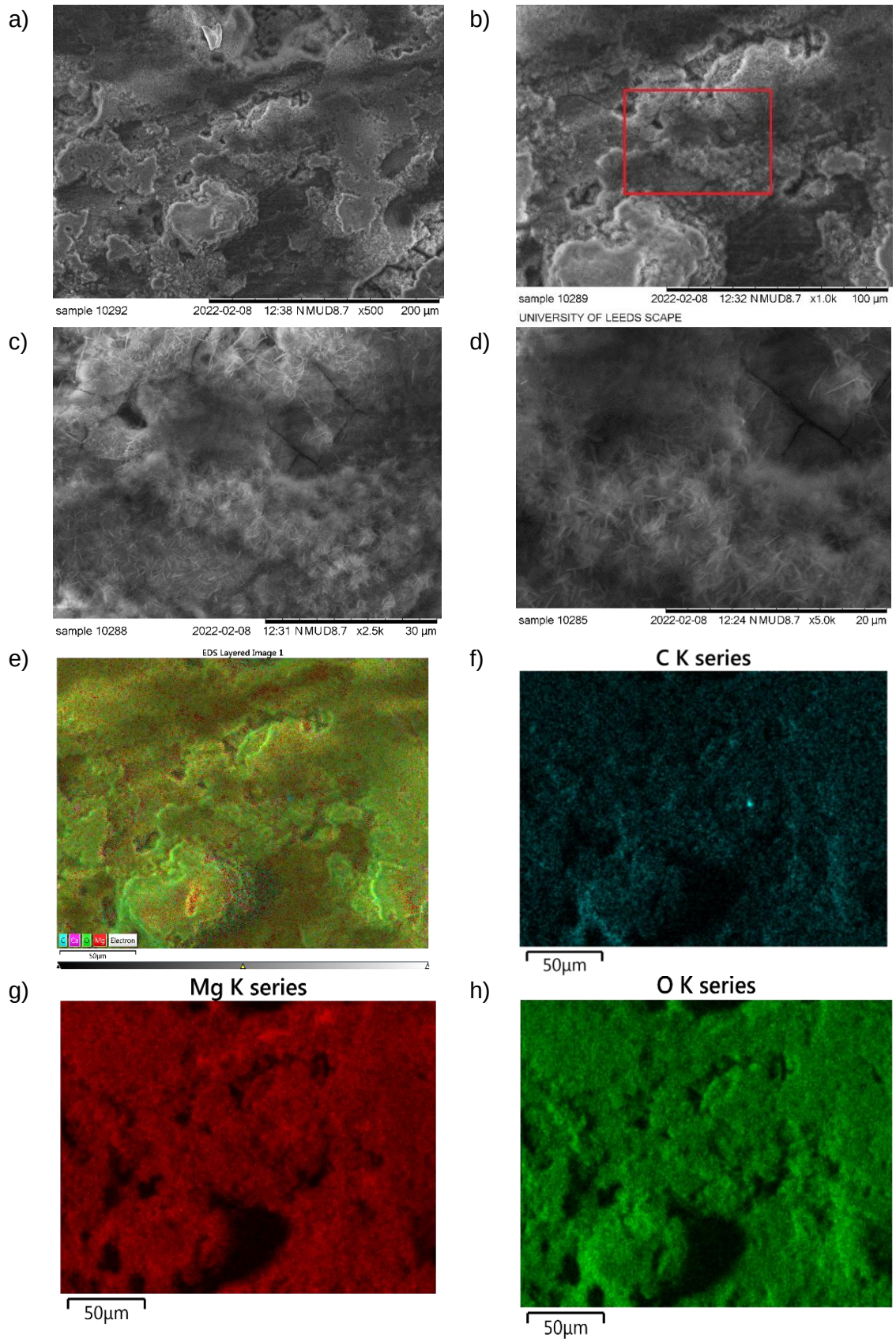

Figure 4-13 SEM/EDX of surface of Sample B showing; a) 500x magnification SE SEM, b) 1kx magnification SE SEM, c) 2.5kx magnification SE SEM, d) 5kx magnification SE SEM, e) EDX of all elements overlaid, f) SEM image for EDX of carbon coverage, g) EDX of magnesium coverage, h) EDX of oxygen coverage

Figure 4-13a-d show SE SEM images at 500-5000x magnification. In Figure 4-13a+b at 500 and 1000x magnification respectively the surface topography is visible, where individual layers of surface corrosion can be seen above the underlying metal. At 1000x magnification the structure of these layers becomes apparent, where interlocking platelet-like “webs” are first observed, and at 2500-5000x (Figure 4-13c+d) magnification these individual particles are seen more clearly, at 1-2 µm in size. Microscopy of Sample B showed an absence of the bulk crust or rod morphology corrosion seen in Sample C, which evidently must be less firmly bound than the dark coloured interlocking platelets.

As with the control sample, EDX (Figure 4-13e-h) detected consistent strong coverage of magnesium and oxygen with lesser carbon coverage over the whole sample surface. The oxygen coverage appeared consistent across the whole area, including within the pits despite them being more metallic in appearance.

SEM of magnesium hydroxide/hydromagnesite powders and of dried Sample 4 are shown in Figure 4-14. SEM of $Mg(OH)_2$ is shown at 100x and focused on one particle at 2500x magnification in Figure 4-14a+b. The SEM shows a large number of particles, the vast majority of which are of the order of several microns to sub-micron in size. Some larger particles are visible, such as the one focused in Figure 4-14b which measures approximately 30 µm in diameter to some larger particles up to 100 µm. Figure 4-14c+d show SEM of hydromagnesite powder at 100x and 2500x magnification. The figures show similarly to $Mg(OH)_2$ the majority of particles are of the order of a few microns or smaller, with the larger particles measuring 20-30 µm. The SEM figures here did not show particles as large as 100 µm as seen for $Mg(OH)_2$.

SEM for corroded Magnox Sample 4 is shown at 100x and 2500x magnification in Figure 4-14e+f. Some >80-100 µm particles are visible in Figure 4-14e with other particles measuring in the range of <50 µm and many small particles on the order of <10 µm. Many dry particles are of the order of micron or greater diameter, so in accordance with the work by Yeşilbaş and Boily will most likely be able to support many (10^2-10^3) condensed monolayers of water on the surface and between particles.[47] EDX analysis for the SEM image in Figure 4-14f is shown in Figure 4-15a-e. The images show the elemental distribution across the particle surface and it is predominantly made up of magnesium and oxygen, and also carbon. The dark area on the right of the EDX images is due to the EDX detector being obscured from the sample by the slightly raised topography of the left side of the particle, and is not due to an absence of the presence or difference of elemental composition. The carbon visible behind the particle is attributable to the stub. An SEM and EDX overlay of hydromagnesite is shown in Figure 4-16a-e for

comparison, where a similar elemental composition and coverage of magnesium, oxygen and carbon can be seen.

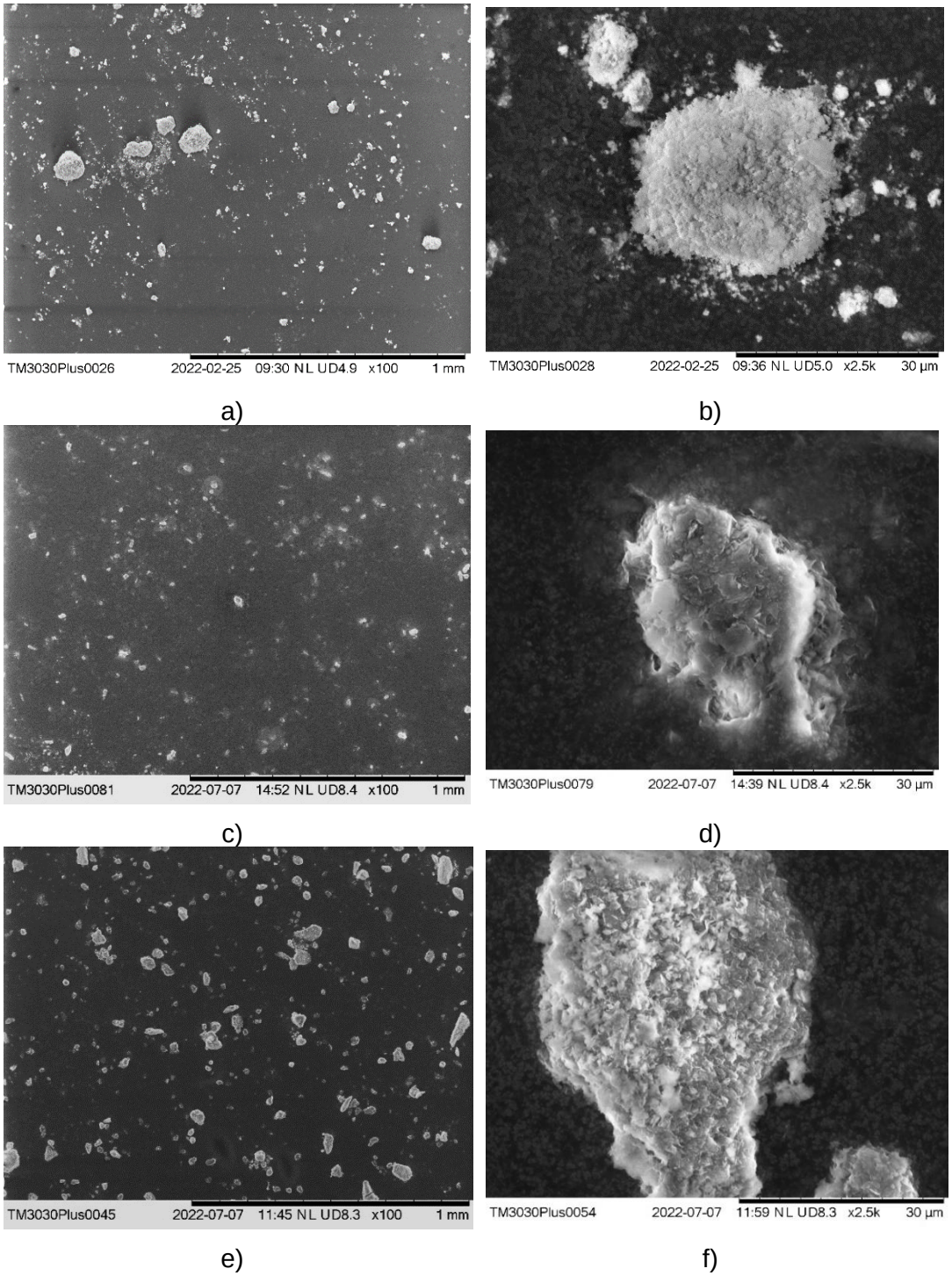

Figure 4-14. SEM images of powders; a) magnesium hydroxide 100x magnification SE, b) magnesium hydroxide 2.5kx magnification SE, c) hydromagnesite 100x magnification SE, d) hydromagnesite 2.5kx magnification SE, e) Sample 4 100x magnification SE, f) Sample 4 2.5kx magnification

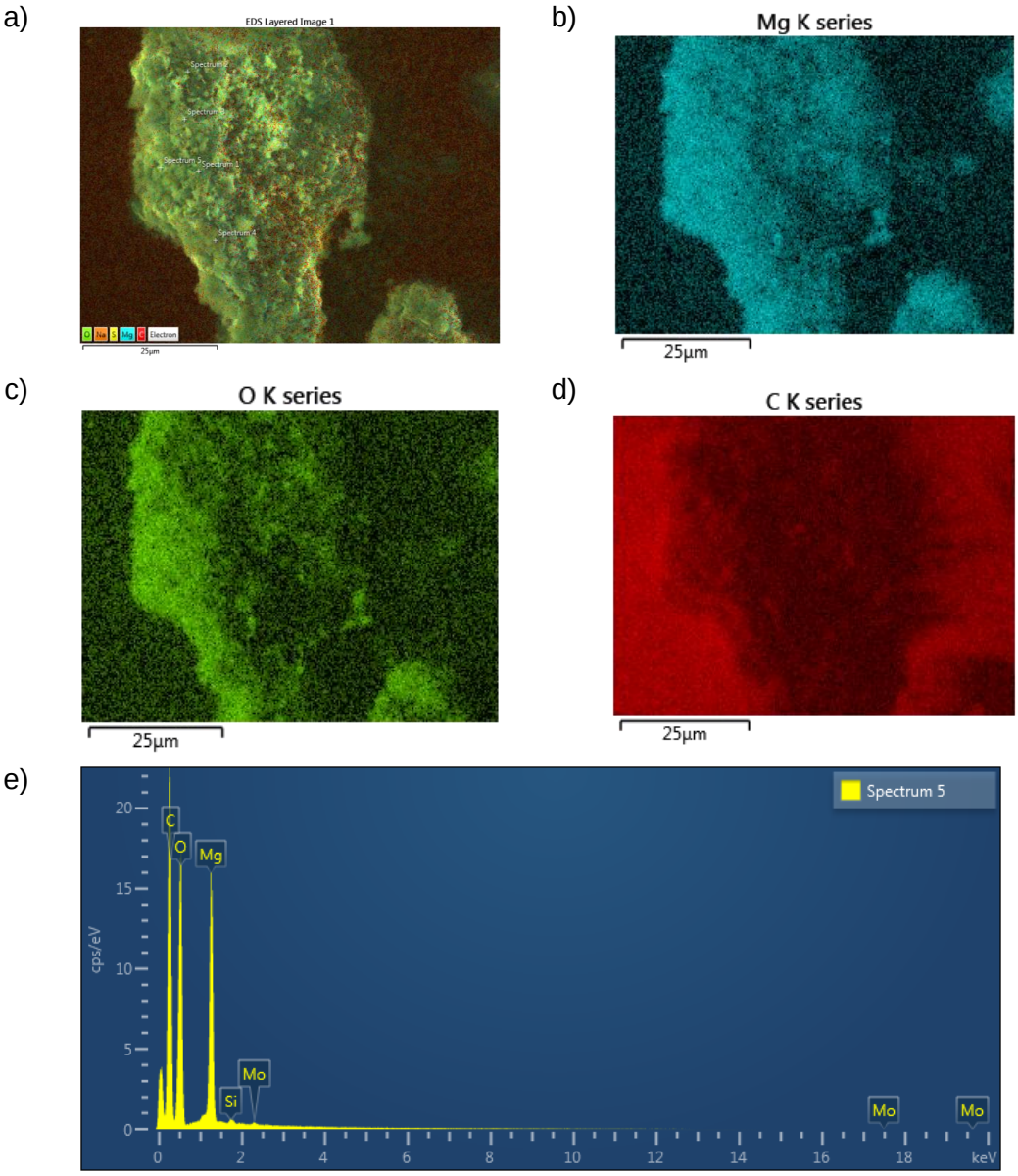

Figure 4-15 SEM/EDX of surface of dried sludge Sample 4 showing; a) SEM of surface with overlaid EDX, b) EDX showing magnesium coverage, c) EDX showing oxygen coverage, d) EDX showing carbon coverage, e) EDX spectrum

The image in Figure 4-17a shows a piece of corroded Magnox fin trimmed from Sample 1. Figure 4-17b-f show SEM images taken of the cutting. At lower magnification as in Figure 4-17b a thick coverage of corrosion is visible across the whole surface, at a range of topographies from the underlying material. Most the coverage is in the form of a thick solid “crust” but amongst this at lower coverages and in gaps between these regions are areas covered by thinner “webs” of finer structures (Figure 4-17d-e, “Site 1” (similar to that shown in Figure 4-13d)). Figure 4-17f (Site 2) focuses on the “crust” that covers most of the surface. A hairline crack is visible across the length of the images, which shows a possible route for water ingress and demonstrates the poor protective qualities of Magnox corrosion,[114] and provides a possible avenue for water surface access or trapping. Overall the

corrosion surface is very uneven, with a presence of a variety of corrosion features and structures.

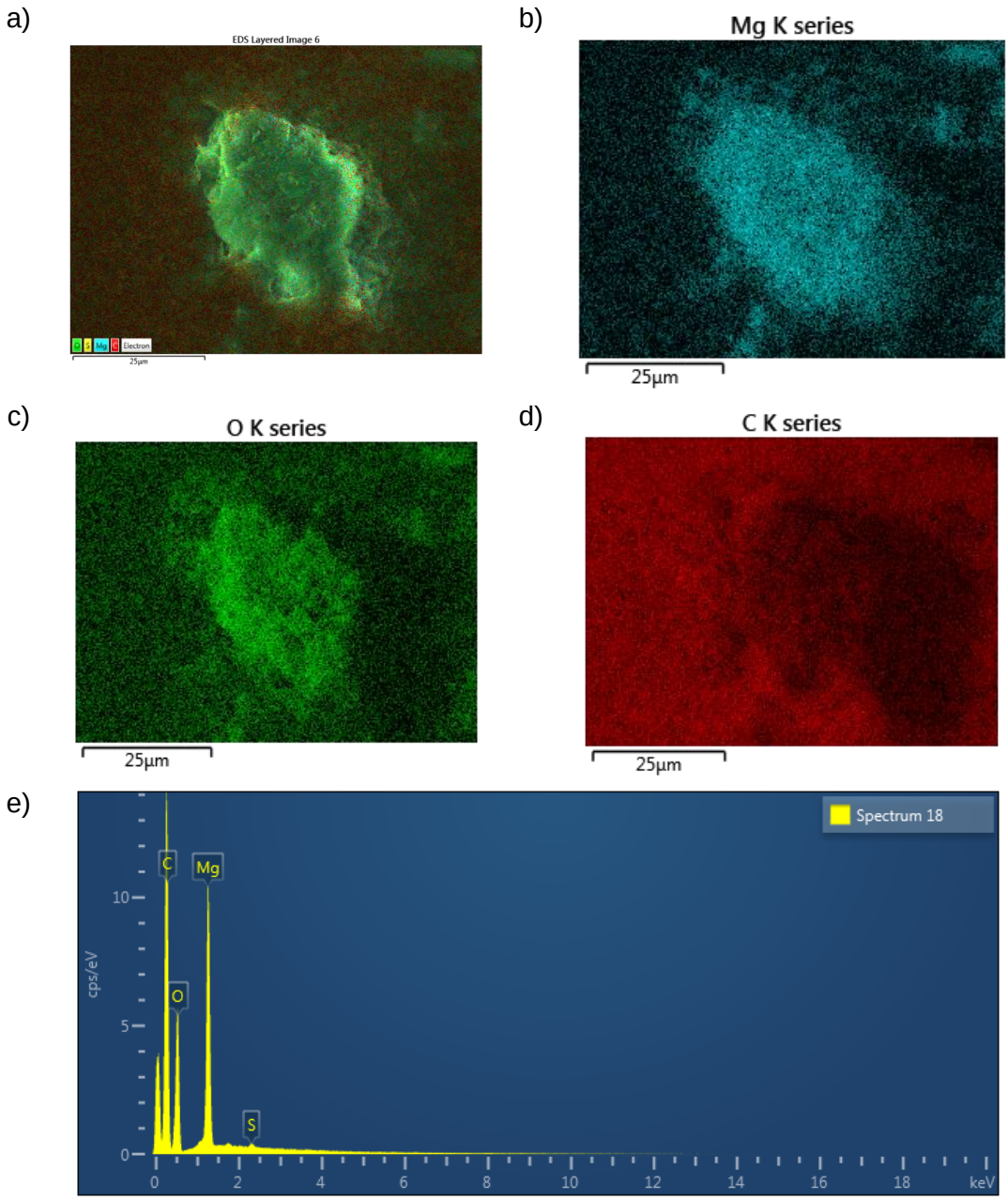

Figure 4-16 SEM/EDX of surface of hydromagnesite showing; a) SEM of surface with EDX of various elements overlaid, b) EDX of magnesium coverage, c) EDX of oxygen coverage d) EDX of carbon coverage, e) EDX spectrum

Figure 4-18a-d shows EDX of trimmed Sample 1 fin at Site 1. The EDX showed only the presence of magnesium and oxygen (no carbon). It should be noted that the darkness in the centre of the image is not due to an absence of magnesium or oxygen, but an artefact of shadow due to the angle of the EDX detector being obscured by the raised coverage from corrosion to either side. The same elements can be seen in Figure 4-18e-h. The lack of carbon present suggests the species

here are magnesium hydroxide (or oxide) and no presence of carbonate or hydromagnesite in either surface deposit.

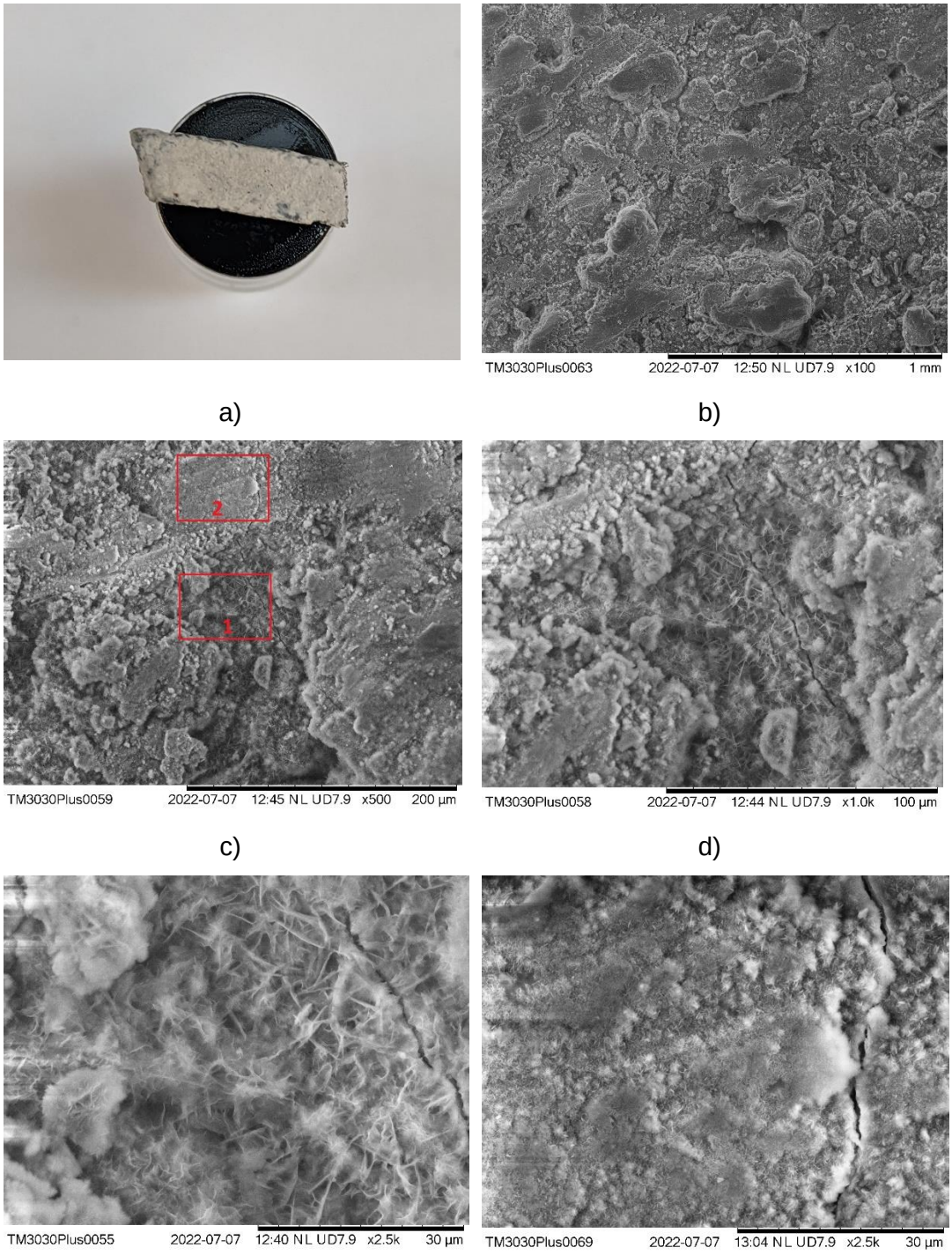

Figure 4-17. Optical and SEM images of Sample 1; a) image of Sample 1 trimming, b) 100x magnification SE, c) 500x magnification SE, d) 1kx microscope image (Site 1), e) 2.5kx magnification SE (Site 1), f) 2.5kx magnification SE SEM (Site 2)

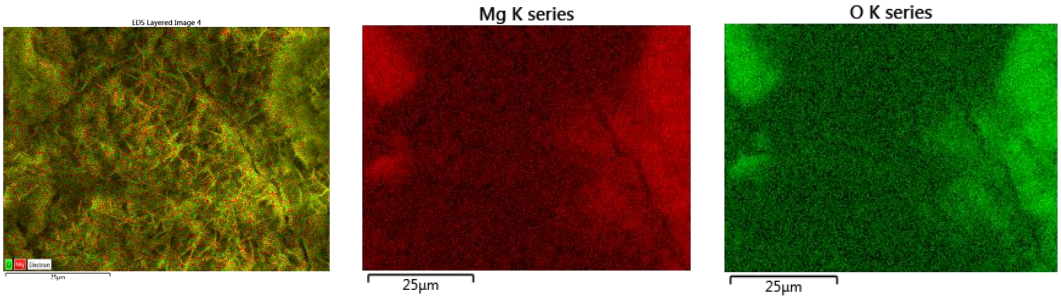

a) b) c)

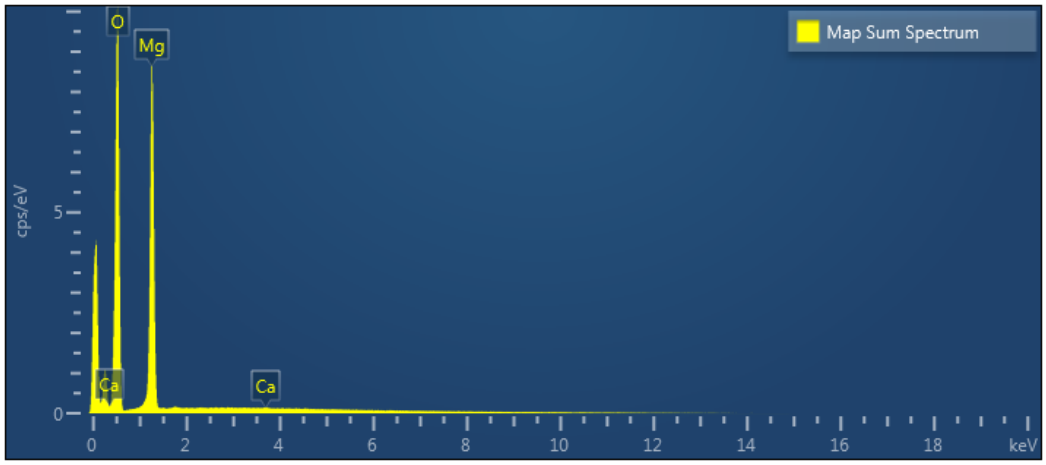

d)

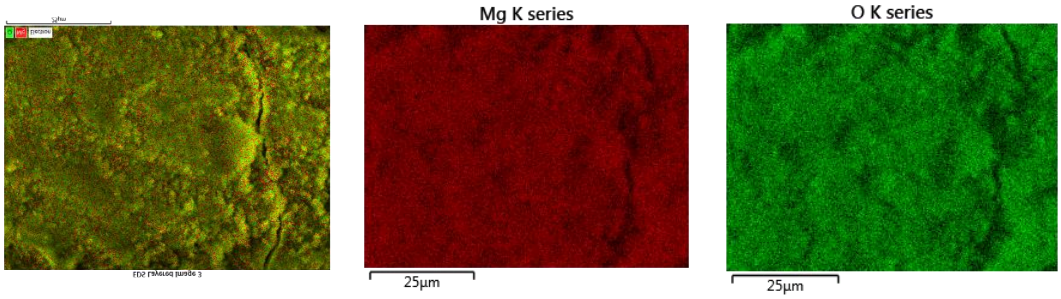

e) f) g)

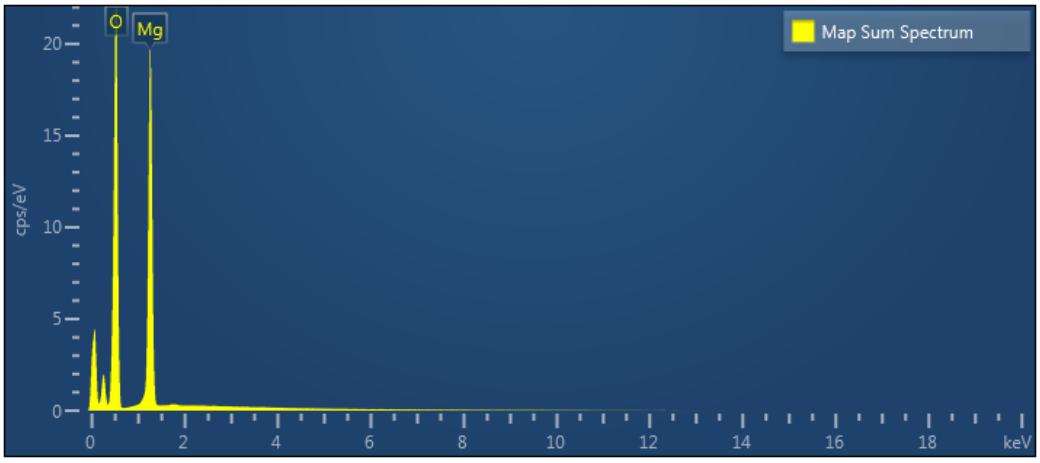

h

Figure 4-18. EDX of Sample 1; a) SEM image with EDX Mg and O overlaid (Site 1), b) EDX showing magnesium coverage (Site 1), c) EDX showing oxygen coverage (site 1), d) EDX Spectrum (Site 1), e) SEM image with EDX Mg and O overlaid (Site 2), f) EDX showing magnesium coverage (Site 2), g) EDX showing oxygen coverage (Site 2), h) EDX Spectrum (Site 2)

4.2.3 Particle characterisation

For certain aspects of this investigation, as-received powders were used, as well as lab prepared simulants to give insight for comparison to potential real-world examples, and inform aspects such as particle dimensions and surface area. The data here compare manufacturer powders with prepared simulant samples, and this information will be also applicable to later aspects of this investigation (particularly Chapter 6).

4.2.3.1 Particle size analysis

Consideration of particle size is of interest to compare test powders to materials found *in situ* and also for relevance to interaction with radiation as will be discussed later. The particle size distributions for magnesium hydroxide and hydromagnesite are shown in Figure 4-19. The size distribution for magnesium hydroxide was measured at 1-198 µm, peaking at 5.2% volume density in the range 15.4-17.5 µm. The size distribution for hydromagnesite was measured from 2.0-255.6 µm, peaking at 7.78% volume density at 10.5 µm, with a shoulder at 81.0-118.8 µm of 0.80-0.90% volume density.

During PSD analysis of Corroded Magnox Sample 4 the powder produced a suspension which was unstable to the instrument conditions, as between individual measurements the volume % of the particles of diameter >100 µm reduced over time, and the volume % at <100 µm increased. The data plotted in Figure 4-19 is an average of the five tests shown in Figure 4-20, which shows how the particle size distribution varied over the course of five measurements.

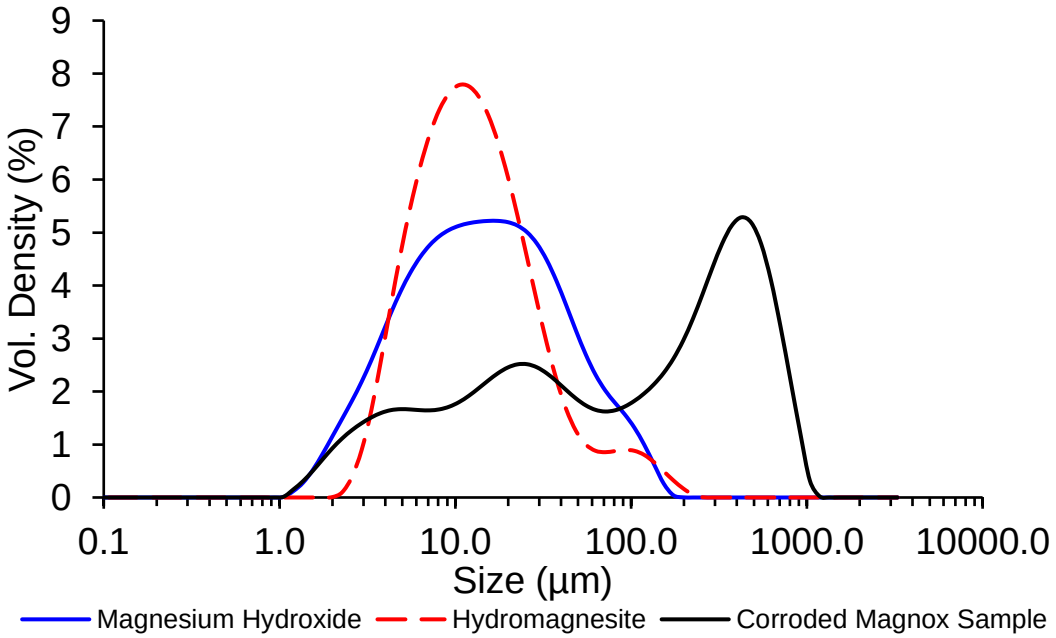

Figure 4-19. Particle size distribution of magnesium hydroxide and hydromagnesite powders

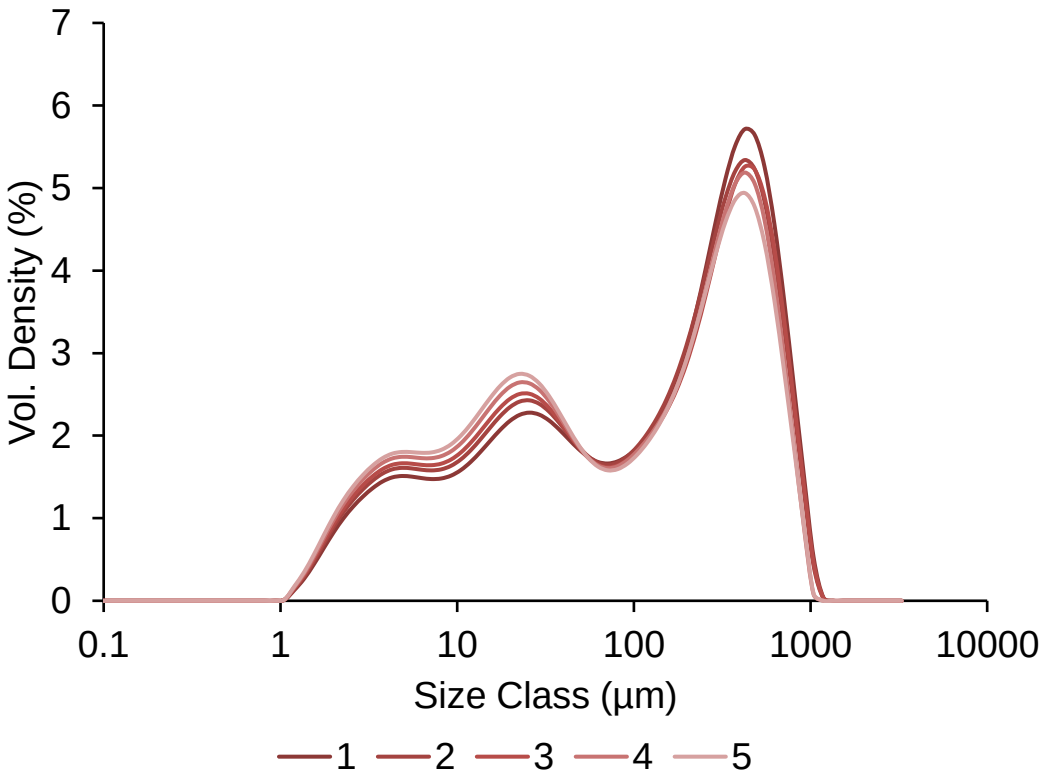

Figure 4-20. Individual PSD experiments 1-5 of Sample 4

The PSD of the manufacturer supplied magnesium hydroxide and hydromagnesite powders in suspension is overall smaller than that of the isolated sludge from Sample 4. Given that the SEM images show dried particles of diameter up to ~100 µm as a fine powder, but that the sludge is visibly thick, it appears the particles can agglomerate up to 100-1000 µm in diameter, in a manner that is not observed in the magnesium hydroxide and hydromagnesite powders. This is consistent with the visible differences between the compounds when suspended in water. The magnesium hydroxide and hydromagnesite powders do produce a milky white mixture which begins to settle within <10 mins of disturbance (Figure 4-21) which differs notably from the slow settling sludge-like suspensions of Sample 4 and other corroded Magnox sludges in Figure 3-1.

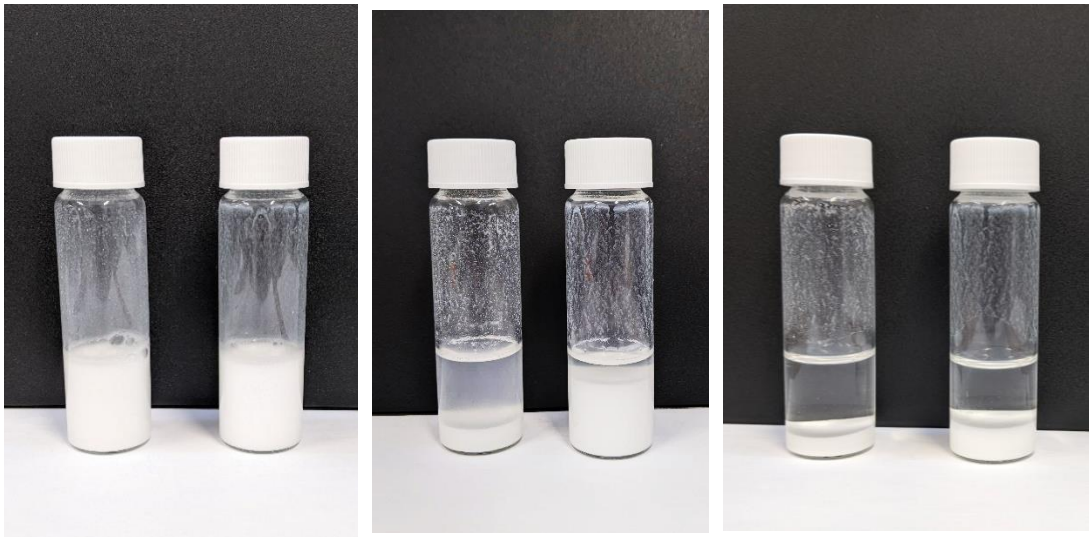

a) b) c)

Figure 4-21. Settling of shaken Magnesium hydroxide (left) and hydromagnesite (right) in water after; a) 0 mins, b) 10 mins, c) fully settled

4.2.3.2 BET Surface Area

The surface area data for magnesium hydroxide and hydromagnesite is shown in Figure 4-22. For magnesium hydroxide the BET surface area was measured at 13.907 m^2/g, and BET constant, C of 151.1, with a correlation coefficient of 1.000. The surface area of hydromagnesite was measured higher than that of magnesium hydroxide at 22.542 m^2/g, and BET constant, C of 160.7, with a correlation coefficient of 1.000. It is logical that the specific surface area of hydromagnesite was larger than for magnesium hydroxide from the lower volume average particle size shown in 4.2.3.1. As expected for both compounds the BET isotherm shows little porosity from the particulate (0.0469 cm^3/g for magnesium hydroxide and 0.0713 cm^3/g for hydromagnesite).

BET surface area analysis was measured for Sample 4 at 25.571 m^2/g and BET constant, C of 105.1 with a correlation coeficient of 1.000. Sample 4 had a higher measured surface area than both magnesium hydroxide and hydromagnesite powders, despite the larger measured particle size. The total pore volume measured for Sample 4 was 0.0990 cm^3/g. It is interesting to note the magnitude of adsorbed N_2 on Sample 4 was much greater than for the magnesium hydroxide and hydromagnesite solids (90 $cm^3\ g^{-1}$ c.f. 1.5-2.5 $cm^3\ g^{-1}$) despite a similar surface area to hydrogmagnesite and approximately double that of the magnesium hydroxide. Perhaps this could pertain to a greater affinity for adsorption and hence introduce a greater potential for water retention on more representative simulant sludges and corrosion products than commercial powders.

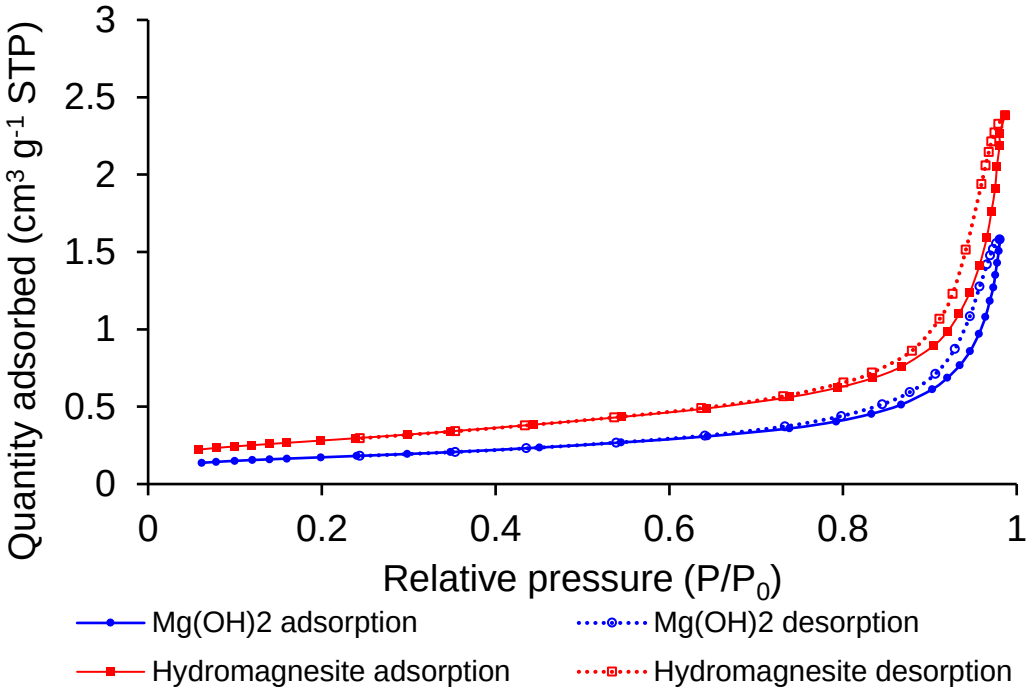

Figure 4-22. N_2 gas adsorption/desorption on magnesium hydroxide and hydromagnesite

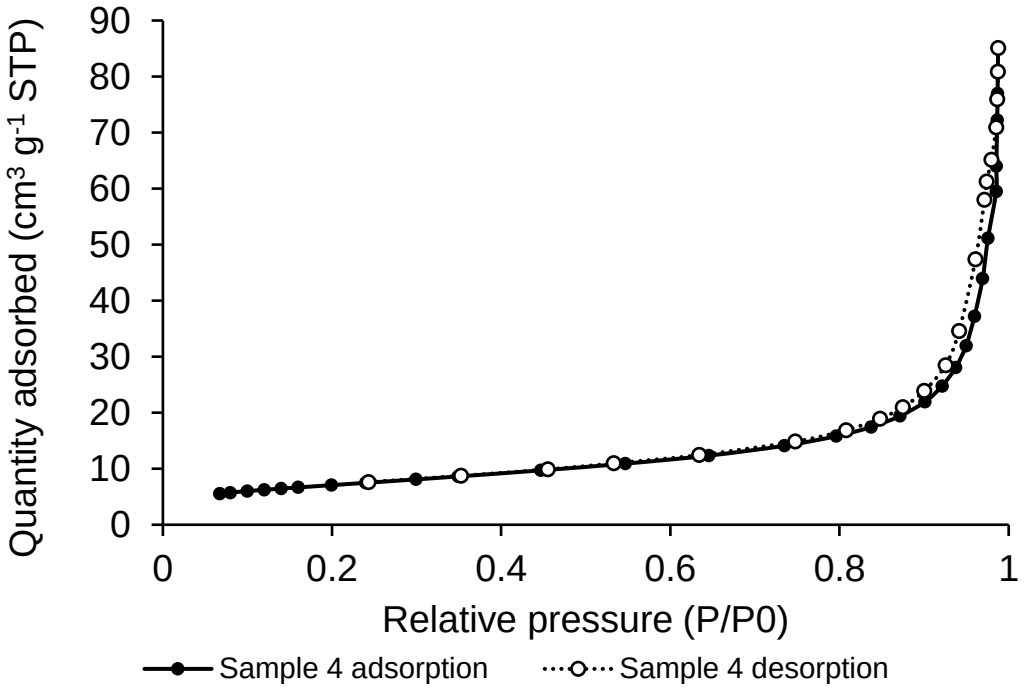

Figure 4-23. N_2 gas adsorption/desorption on corroded Magnox Sample 4

4.2.3.3 He Pycnometer and powder tapped Density

It was evident from handling the powders that despite the similar literature density, the powder density was particularly light and fluffy for hydromagnesite. Density was measured by helium pycnometry as 2.35 g/cm^3 for magnesium hydroxide and 2.22 g/cm^3 for hydromagnesite. Powder densities were measured at 0.43 g/cm^3

(bulk) and 0.53 (tapped) for magnesium hydroxide and 0.16 g/cm^3 (bulk) and 0.20 (tapped) for hydromagnesite. Both powders clearly pack much less densely than their measured or literature solid densities.

4.3 Conclusions

Characterisation of corroded Magnox products has been performed to identify chemical and physical characteristics of potential wet stored spent Magnox fuel. Simulant corrosion products were isolated by sonication, and XRD identified the primary product as magnesium hydroxide, but also observed the presence of hydromagnesite in some samples, and also potential for artinite, $Mg_2(CO_3)(OH)_2{\cdot}3H_2O$ in Sample 2. It is interesting that Mg-hydroxycarbonates have been detected as they contain bound water within the chemical structure, which may prove difficult to remove by a drying process and could potentially provide another avenue for water carryover into dry storage if it can be thermally or radiolytically liberated. Thermogravimetric analysis estimated hydromagnesite composition as 36.9% and 62.7% in two of the samples that were analysed, and was also used to quantify water content of as-received $Mg(OH)_2$ as 2.84% and 3.36% for hydromagnesite.

Non-destructive structural information was achieved by computed tomography and image analysis of a piece of simulant corroded Magnox, where the sample was measured to consist of 63% (by volume) metal, 34% corrosion and 3% internal voids with the potential to trap liquid water within. Optical and electron microscopy were employed to observe corrosion products and features, such as pits which were measured at 125-200 µm in diameter and 55-80 µm in depth. SEM of corroded materials showed corrosion covering most of the surfaces in “crust,” with areas of protruding rods ~30 µm in length, as well as finer needles. Some areas at lower layers closer to the substrate had smaller flower-like morphology, as well as rods/needles and thin platelets which could be artinite or nesquehonite[27] but are not definitively identified here. EDX of Sample 1 showed the presence of magnesium and oxygen but no carbon suggesting the corrosion product is magnesium hydroxide (or magnesium oxide). The lack of carbon in Sample 1 is inconsistent with XRD, but the XRD signal of that sample was unreliable due to the small sample thickness and weak signal. EDX of corroded Magnox Sample B+C and of isolated sludge Sample 4 indicated some carbon content, so the sludge is likely to contain Mg-hydroxycarbonate such as hydromagnesite as identified by XRD, which was supported by CO_2 detection during TGA. The lower penetration of electrons from SEM/EDX means that elemental information is limited only to the surfaces of analysed samples. Higher penetration of X-rays during XRD will enable detection of compounds that may not be observable by SEM so the absence of carbon in

Sample 1 cannot be ruled out by EDX alone. SEM of Magnox with corrosion removed by sonication showed adherence of some remaining corrosion to the surface as topographies of several layers above pits into the substrate surface. EDX showed oxygen coverage across the whole surface showing the metallic surfaces must still be oxidised to an extent. In all corroded Magnox samples, cracks of ~1 µm width could be seen that ran long distances across the surfaces. This was compared to commercially available powders of $Mg(OH)_2$ and hydromagnesite, and the Sample 4 simulated sludge particles were observed to be generally larger, up to the order of ~100 µm in size.

Further particle characterisation was carried out to compare chemically pure powders to simulant corroded Magnox material Sample 4. Particle size distribution of magnesium hydroxide and hydromagnesite powders measured particle diameter range from 1-1000 µm, with peaks at 4.9 µm at 1.8% volume density, 2.6% volume density at 29 µm and 5.2% volume density at 425 µm diameter. The corroded Magnox particles appear to agglomerate in water as no particles greater than 100 µm were observed by SEM, and the volume density >100 µm decayed with subsequent measurements. PSD of magnesium hydroxide was measured at 1-198 µm, peaking at 5.2% volume density in the range 15-19 µm. The size distribution for hydromagnesite was measured from 2.0-255.6 µm, peaking at 7.78% volume density at 10.5 µm, with a shoulder at 81-119 µm of 0.90% volume density. Surface area of Sample 4 was measured at 25.571 m^2/g with porosity of 0.099 cm^3/g. As-received magnesium hydroxide had surface area of 13.907 m^2/g with porosity of 0.0469 cm^3/g, and hydromagnesite had a surface area of 22.542 m^2/g with porosity of 0.0713 cm^3/g. Visible observations with regard to settling, coupled with particle size data do suggest that there are behavioural differences between the commercially available magnesium hydroxide/hydromagnesite and real/simulant Magnox corrosion products.

Characterisation has provided useful information to quantify water content of the materials used in this investigation, and to identify the chemical components present in Magnox corrosion products. Physical characterisation and application of CT has provided a quantitative estimation of the extent of corrosion and potential for trapped liquid water on one of the corroded Magnox samples used in this investigation as 3% by volume. Techniques have also been applied to assess how representative commercial chemicals are when compared to simulant corroded Magnox and real-world materials. The particle and physical characterisation data are also applied in later parts of this investigation.

4.4 Recommendations and Further Work

It is acknowledged that some of the simulant test materials employed here are heavily corroded and may be more representative of spent nuclear fuel from legacy facilities such as FGMSP. Spent nuclear fuel from more controlled storage facilities such as Fuel Handling Plant are likely to be less corroded, but accurate fuel condition is not openly available so direct comparison is difficult. This information should be applied as preliminary quantitative data, and proof of concept for CT as a non-destructive technique for assessing corroded material internal structure and void volume. The test materials are physically small and from a limited sample size, so considerations should be made for application to full fuel cans and scale-up.

This work has provided useful data to compare and assess commercially available and lab prepared simulant materials. Further comparison to analyses from real corroded fuel materials would provide further validation to how representative this data is. One such set of experimental data could be to investigate water sorption of corroded Magnox products to assess the hygroscopicity and compare to commercially available powders.

4.5 Characterisation Appendix

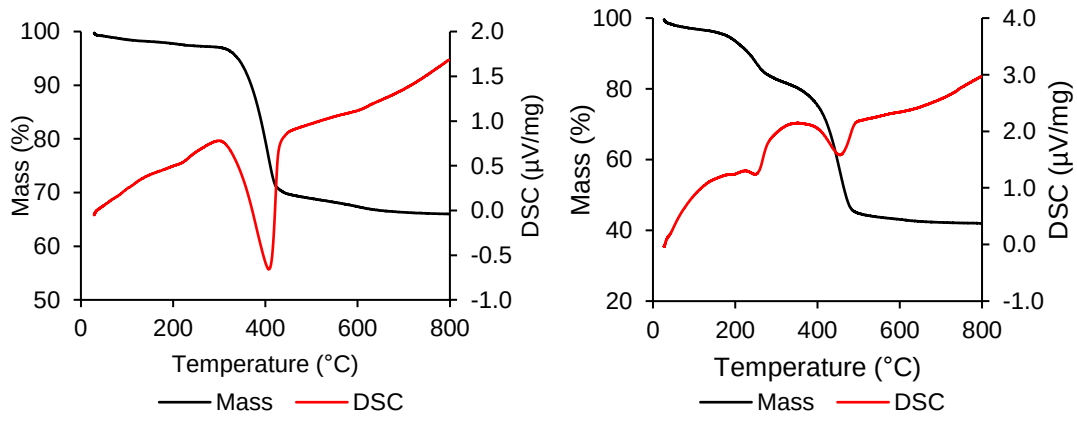

Figure 4-24. TGA and DSC thermal decomposition data for; a) Magnesium hydroxide, b) hydromagnesite

Chapter 5 Vacuum Drying Corroded Magnox Spent Fuel

5.1 Introduction

Chapter 4 has introduced the nature of material that may be encountered when removing Magnox spent fuel from an extended period in storage ponds. This chapter aims to build on this and investigate what potential drying conditions could be suitable and viable for this material. As mentioned in Section 2.4.9 vacuum drying of comparable materials has been successfully applied. Of particular relevance is the remediation of Hanford Basins through recovery and “Cold Vacuum Drying” (CVD) at 50 °C of wet and corroded metallic uranium spent fuel.[59] Whilst this technology and application has been demonstrated industrially, there are key differences between Hanford and Magnox at Sellafield, most notably the cladding. The fuel at Hanford enlisted a zirconium clad, which is very inert to reaction with water but Magnox cladding can undergo extensive corrosion in contact with water over long timescales, which has given rise to some of the biggest challenges the UK nuclear industry currently faces. Therefore with Magnox wet stored fuel both the fuel bar and cladding have opportunity to react with storage water and produce corrosion products, sludges and avenues for interaction with water which must be understood in order to inform industrial practices.

This chapter aims to investigate how vacuum drying techniques can be applied to corroded Magnox cladding, by testing and comparing a range of drying conditions, and considering how these processes may require adaptation to suit these specific materials. Corroded Magnox samples were vacuum dried following storage in water, with the primary variable being the process temperature. Initial testing was undertaken to scope and identify the primary observations. A second set of tests on a larger corroded Magnox sample were designed based on the learning from the first set, which provided further knowledge and underpinned some concepts from the first test. Following both these investigations, some inconsistencies remained unanswered so a final set of tests were undertaken in which unbound liquid water was vacuum dried to give further knowledge surrounding the pressure, flow and dew point behaviour during vacuum drying.

These results have provided the groundwork for expected drying behaviour of corroded Magnox, particularly in identification of achievable levels of dryness whilst drying at temperatures of 40-120 °C.

5.2 Results and Discussion

5.2.1 Vacuum drying corroded Magnox samples

5.2.1.1 Corroded Magnox Sample 1

An overview of the data collected from vacuum drying of corroded Magnox Sample 1 is shown in Figure 5-1. Each plot shows the pressure, dew point, flow, temperature and sample mass displayed together. During testing it is necessary to open the vessel to remove the sample for experimental setup and inspection, and during these instances the data appear disrupted. These disruptions are identified in the figures by the dashed lines marked “2” and do not need to be considered. It is important to remember (as mentioned in Methodology Section 3.3.2) that this data disruption effect is seen at every mass inspection point due to the necessity to interrupt the test for sample weighing. Therefore the drying overview in Figure 5-1 (and for all other drying overview figures) is compiled by overlaying the average mass data for all tests (which is tabulated in chapter appendix Table 5-8) onto the pressure, dew point, flow and temperature of a single uninterrupted extended test, such that the data shows a continuous and readable trace. This data is repeated with a focus on the first 90 mins (where the majority of drying activity is observed) in Figure 5-2. All data between tests with and without mass inspections have been compared and this approach is the clearest way of displaying this information. An expansion of the interruption at 180 mins from Figure 5-1b undertaken at 60 °C is shown in Figure 5-3.

For this set of experiments the overall process at each temperature show the same general trends for all readings except sample mass. Pressure, flow and dew point data under each test condition are directly compared in Figure 5-4. During the initial evacuation at time = 0 mins there is a drop in temperature resulting from evaporative cooling. The pressure drops from atmospheric pressure to ~25-30 mbar within the space of 1.5 mins at 40 °C, and progressively quicker with increasing temperature to 0.9 mins at 120 °C, and this is associated by a large spike in the flow as the mass of air passes the flow meter. This data exceeds the scale of the figures as displayed (peaking at 125-132%, equivalent to 2.50-2.64 g/min air) as this period does not provide meaningful information with respect to drying. Similar to the pressure, the flow reached a minimum of 1.88% at 1.5 mins at 40 °C, which occurred sooner with increasing temperature up to 0.75 mins at 120 °C where the minimum was 1.81%. Following this minimum, at all temperatures the flow increased at ~0.2 min after the minimum to a generally consistent flow of 2.2-2.4%. The dew point in this period for all tests climbed at the point of evacuation from starting point of 0-7.5 °C up to 20-23 °C after 1.0 mins. The 90 °C data shows

a sharp jump to 60 °C from 1.0-1.9 mins which is attributed to an instrument fault, as the data resumes the expected state following this, so is not included in the figures or discussed further. No mass measurements are taken before 10 minutes of evacuated drying so no mass data is available for this period.

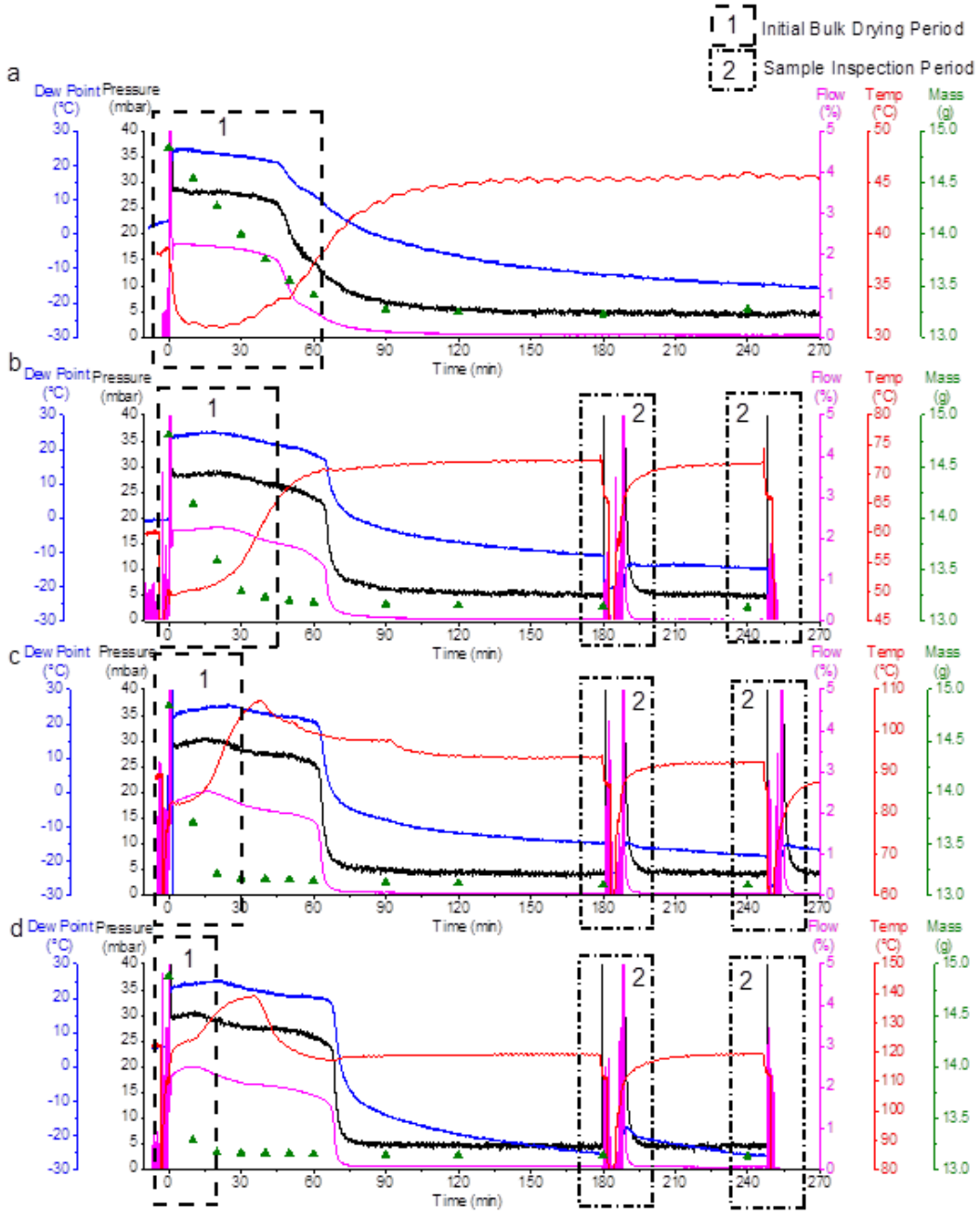

Figure 5-1. Vacuum drying overview of corroded Magnox Sample 1 at; a) 40 °C, b) 60 °C, c) 90 °C and d) 120 °C

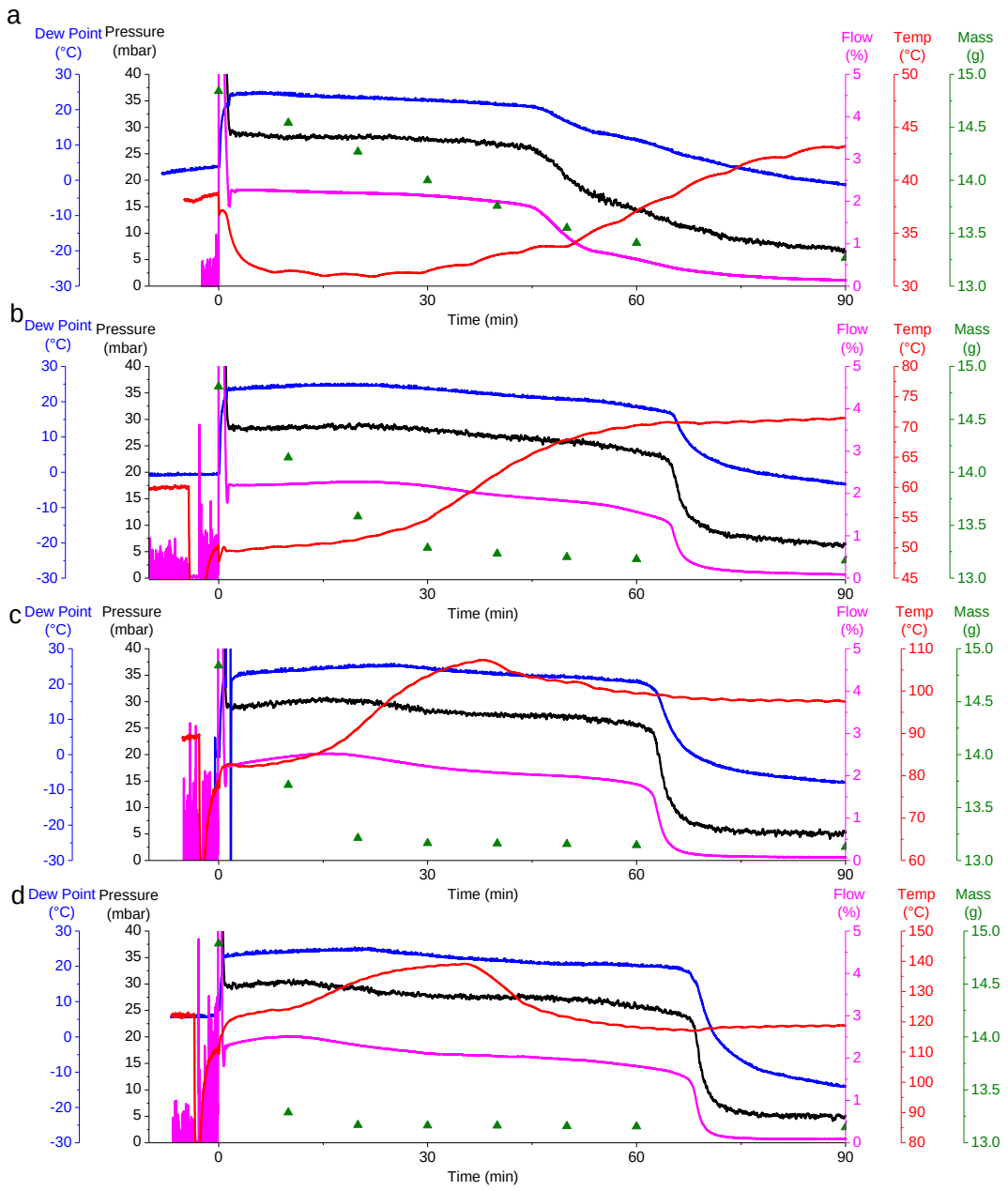

Figure 5-2. Focus on first 90 mins of vacuum drying overview from Figure 5-1 at; a) 40 °C, b) 60 °C, c) 90 °C and d) 120 °C

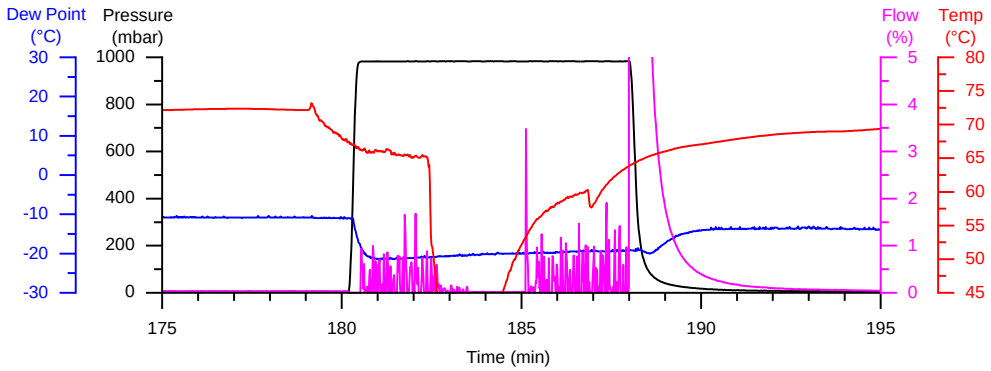

Figure 5-3. Expansion of Sample 1 60 °C drying overview displaying mass observation interruption at 180 mins drying (from Figure 5-1b)

In the 45 mins following initial evacuation, each metric remains stable with the pressure at 28-29 mbar, flow at 2-2.5% and dew point at 23-26 °C. In the initial 30 mins the 90 °C and 120 °C measurements showed slightly elevated readings at 29-31 mbar pressure/2.5% flow, but this did not produce a visible change in the dew point. This steady behaviour was seen up to 62-67 mins for 60-120 °C at which point a sharp drop to a baseline of 4-6 mbar pressure and 0.1% flow was seen, which was sustained for the remainder of the experiment. Dew point showed a very similar trend but without a consistent baseline for all temperatures, which appeared to continually decrease as the test went on, reaching -0.8 °C, -3.3 °C, -7.9 °C and -14.2 °C for 40, 60, 90 and 120 °C drying respectively. At 40 °C the pressure and flow drop was observed earlier after 45 mins, and was more steady and prolonged – occurring gradually over a 40 minute period. In Figure 5-3 the increase in pressure up to atmospheric (~1000 mbar) from 180-188 mins shows the period in which the test is interrupted by the mass measurement whilst the vessel is open. As can be seen the vessel temperature returns to the desired test temperature promptly. The pressure and flow both drop rapidly on evacuation within one minute, and are stable within 3-4 mins.

From this data there was no obvious variation or trend with change in temperature, but the mass change showed a distinct correlation with drying temperature. Mass loss is intuitively related to drying, and the period where the majority of mass loss is observed is marked by the dashed area labelled “1” – the “bulk drying period” (assigned as the point that the rate is <0.015 g/min) on Figure 5-1. Mass loss and drying rates are displayed in Figure 5-5. It is clear that according to the mass loss, increasing temperature gives rise to significantly increased samples mass loss rates. Mass loss at 40 °C is steady with the bulk drying occurring over 60 mins. Bulk mass loss at 60 °C occurred in 30 mins, 20 mins at 90 °C and 10 mins at 120 °C. Following this period of bulk mass loss, drying continued for up to 180-240 mins total, where continued gradual mass loss was observed as summarised in Table 5-1. The 49 mg increase in the 40 °C amount dried from 13.224 g at 180 mins to 13.273 g at 240 mins is not representative of an increase in mass during drying in this period, and is an artefact of the different averages from the variation of the measurements at each point, and is not deemed of any significance or impact to the investigation.

The drying rates for the set of experiments are shown in Figure 5-5a where mass losses are plotted with initial drying rates shown. The initial rate increases with increasing temperature, measured at 0.024, 0.061, 0.081 and 0.160 g/min at 40 °C, 60 °C, 90 °C and 120 °C. In Figure 5-5b the drying rates are plotted against time for

the first 90 mins. At 40 °C the different stages of drying rate are visible as described in Section 2.4.6 drying rate stages and Figure 2-16, where an initial steady period is present up to ~30-40 mins, at which point the rate starts to slow and enters the second drying stage. From 75 mins onwards the rate is significantly slower as the drying enters the third reduced drying rate stage. At 60 °C The drying rate appears to be entering stage 2 within the first measurements within 15 mins, so the first stage seems largely complete by this point, and the final stage is seen after 30-35 mins drying. At 90 °C the ~0-25 min data points seem to show the second drying stage and the first stage appears complete before the first mass measurement is taken. At 120 °C the measured rates drop very swiftly and the final drying stage occurs within <20 mins. It is evident that the mass measurements for Sample 1 are not frequent enough to precisely identify drying rate stages due to the relatively small quantity of water/time spent at each stage. For the tests carried out at >60 °C the first stage was complete before enough mass measurements could be taken. On this scale and with this apparatus it is not practical to inspect the sample more frequently due to the uncertainty that would be introduced and additional time to removing the sample for mass measurements. Nevertheless relative drying rate data has been compiled and gives a clear indication as to drying trends with temperature and drying time.

Table 5-1. Bulk and end sample masses from vacuum drying Sample 1

Temperature (°C)	“Bulk” mass loss time (min)	Mass after “bulk” drying (g)	240 min drying mass (g)
40	60	13.408	13.273
60	40	13.231	13.132
90	30	13.163	13.101
120	20	13.167	13.132

The data show that the sample mass after 240 mins drying decreases with increased temperature from 40-90 °C, implying that increasing the temperature not only increases the drying rate, but also increases the amount of water removed and improves overall drying extent. During these tests the final mass of those dried at 120 °C were greater than those at 90 °C, which is inconsistent as it suggests the 120 °C product is less dry than that dried at 90°C, and is counterintuitive to the previous observation. On the basis that this is observation is not valid, one possible explanation could be that the sample itself has physically changed over the course of the investigation. For the data to be directly comparable as stated in Section 3.3.2.1 the corroded Magnox sample mass must be assumed to remain constant for the duration of the experimental campaign.

There are potential ways that the mass may be affected or change over the course of the investigation. Firstly the sample must be held in water prior to testing, and the basis of this investigation is that wet storing these materials causes corrosion over

extended periods. Therefore it is natural for the sample to gradually corrode whilst in storage for preparation for each test, which is likely to slowly increase the sample mass as the magnesium metal reacts with water to form magnesium hydroxide. Each data set takes 5-6 hours to acquire, so all the data was gathered over several months. Additionally the majority of the data at each temperature was collected together, meaning any changes to the sample will be most significant when collecting data later into the experimental schedule, i.e. during the 120 °C tests. An alternative possibility for sample variation over time is that the drying process itself causes the sample to react with the surface water. The testing was undertaken at elevated temperature 40-120 °C, so the sample has repeatedly had extended potential for exposure to heated water and vapour. As discussed previously the work by Foster et al. has already reported magnesium oxide reactions from prolonged exposure at <25 mbar pressure water vapour forming islands of magnesium hydroxide.[49,50] For this work a brief investigation was carried out by etching a piece of Magnox in citric acid to remove surface corrosion, and then boiling in water for several hours to observe if any measurable or visible corrosion occurred. An additional vacuum drying test was carried out for 3.5 hours at 90 °C with two pieces of etched Magnox in the drying rig, one partially submerged in a vial of liquid water and the other placed external to the vial. This was in order to see if during drying and in contact with liquid water/water vapour any visible changes to the Magnox surface were observable. For both of these investigations no optical or milligram mass scale changes to the Magnox metal were seen over the course of a single test. The work by Foster et al. observed <µm scale changes over ~100 hours exposure. Also the samples in use here have large amounts of corrosion product on the surfaces, so the metal substrate is only in minimal contact with the water vapour within the vessel. So whilst any such effects are likely to occur to a degree, it is not believed that the drying process has any significantly enhanced corrosive influence on the Magnox samples, and this observed change in sample mass is most likely to the storage conditions between tests rather than the drying process itself.

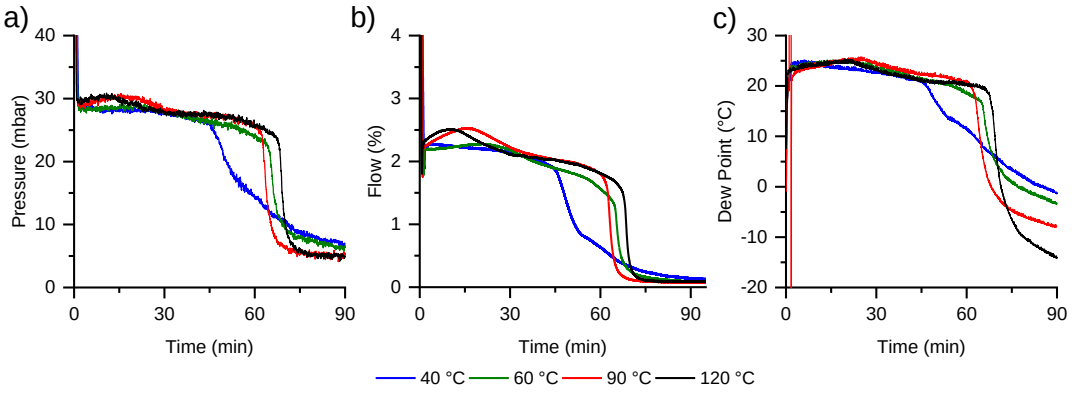

Figure 5-4. Vacuum drying sample 1 data; a) pressure, b) flow and c) dew point

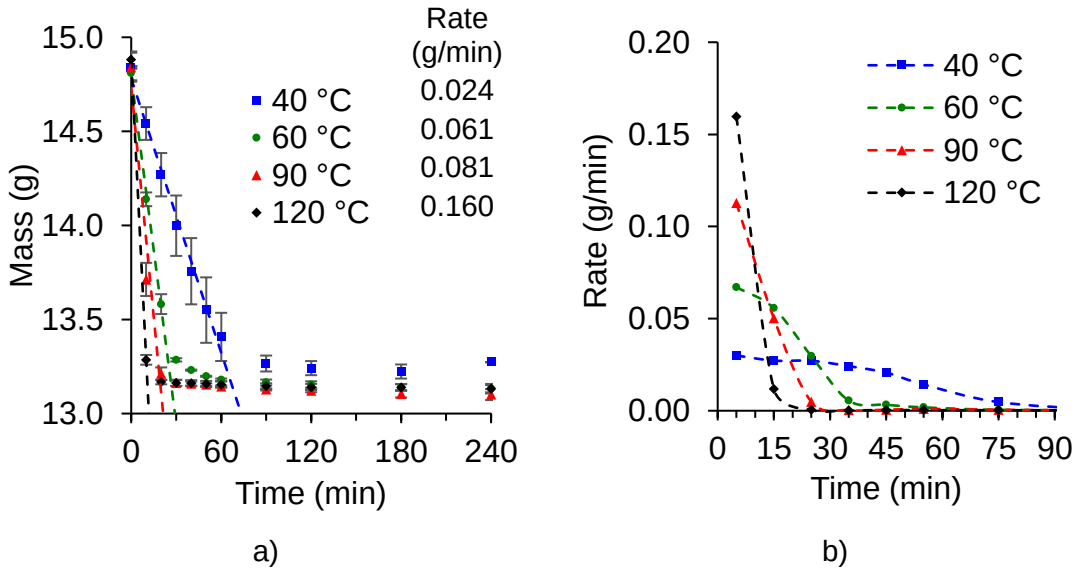

Figure 5-5. Sample 1 vacuum drying data for 40-120 °C showing; a) Mass change and initial rate, b) drying rate over time (first 90 mins)

An additional investigation was carried out to query if heating beyond 90 °C produced measurable mass losses, as opposed to the observations mentioned previously where drying at >90 °C displayed no drying benefits. Sample 1 was prepared as usual by storing in water for a minimum of 12 hours. It was then dried at 40 °C for 6 hours with mass inspections every two hours, and the final mass loss was 8 mg over two hours. The sample was removed and stored in a container with dessicant to minimise water uptake prior to the next test, but despite this some mass gain (average of 59 mg, maximum of 83 mg) was observed during storage in every instance. Then the sample was dried at the next temperature increment by the same process for another 6 hours and stored in dessicant prior to the next test. This data is displayed in Figure 5-6 (N.B the figure is scaled such that the starting 40 °C wet mass is not included, data listed in Appendix Table 5-10) which shows a clear trend that drying Sample 1 at increased temperature without external intervention such as wet storage gives rise to greater mass loss, and therefore improved drying. Thermal decomposition of the samples is not expected at this temperature range, other than removal of some water of crystallisation within the hydromagnesite structure, should any hydromagnesite be present within Sample 1 (which was not evident by EDX). Additionally mass gain between tests shows that a proportion of this mass lost is recovered from the air (presumably through atmospheric water vapour). On this basis it can be said with confidence that vacuum drying at temperatures beyond 120 °C does enhance drying. Additionally under reduced pressure at 33-42 mbar the boiling point of water is 26-30 °C, so any surface water temperature will be modest and is not equivalent to that of the vessel heater. It is true that water vapour following evaporation can be heated beyond the boiling point, but etched Magnox in the presence of water vapour during drying

showed no observable interaction with water vapour within the drying vessel over 3.5 hours exposure. On this basis it is presumed that the variation in sample mass and reduced observed efficacy of drying at above 90 °C is actually an artefact of the slow gradual corrosion of Sample 1 in storage water between tests.

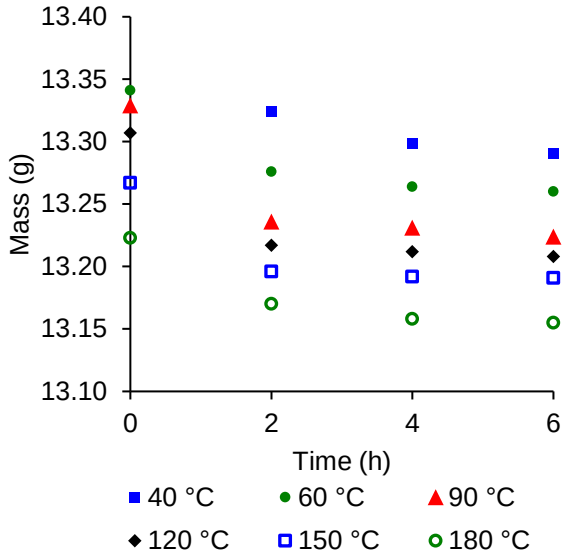

Figure 5-6. Drying Sample 1 at increasing temperature concurrently without wetting between tests

5.2.1.2 Corroded Magnox Sample 2

Based on these findings, another series of drying tests were undertaken on another test material, corroded Magnox Sample 2. This sample was larger and had a greater amount of hard surface bound corrosion, so it was expected to be more difficult to dry. To avoid some of the issues that had arisen during testing of Sample 1, the test temperature of Sample 2 was changed between each individual test. Therefore any physical change to the sample would be balanced across all datasets and not weighted towards those undertaken last.

An overview of all data is shown in Figure 5-7, and pressure, flow and dew point data under each test condition are directly compared in Figure 5-8. For the drying data for Sample 2, as with Sample 1 during evacuation at time = 0 mins there is a drop in temperature. The pressure drops from atmospheric pressure to ~25-28 mbar within 1.8 mins at 40 °C, and sooner with increasing temperature to 1.1 mins at 120 °C, which is coupled with a spike in the flow. As with Sample 1, this data exceeds the scale of the figures (peaking at 132% or 2.64 g/min air). From this the flow reached a minimum of 1.36% in 1.78 mins at 40 °C, 1.45% in 1.15 min at 60 °C and 1.7% in 1.2/1.0 mins for 90/120 °C respectively. Following this minimum, at 40 and 60 °C the flow increased to a consistent flow of 1.57-1.73%. On evacuation the

dew point in this period for all tests climbed to 18-27 °C after 1.5 mins. No mass measurements are taken before 10 minutes of evacuated drying.

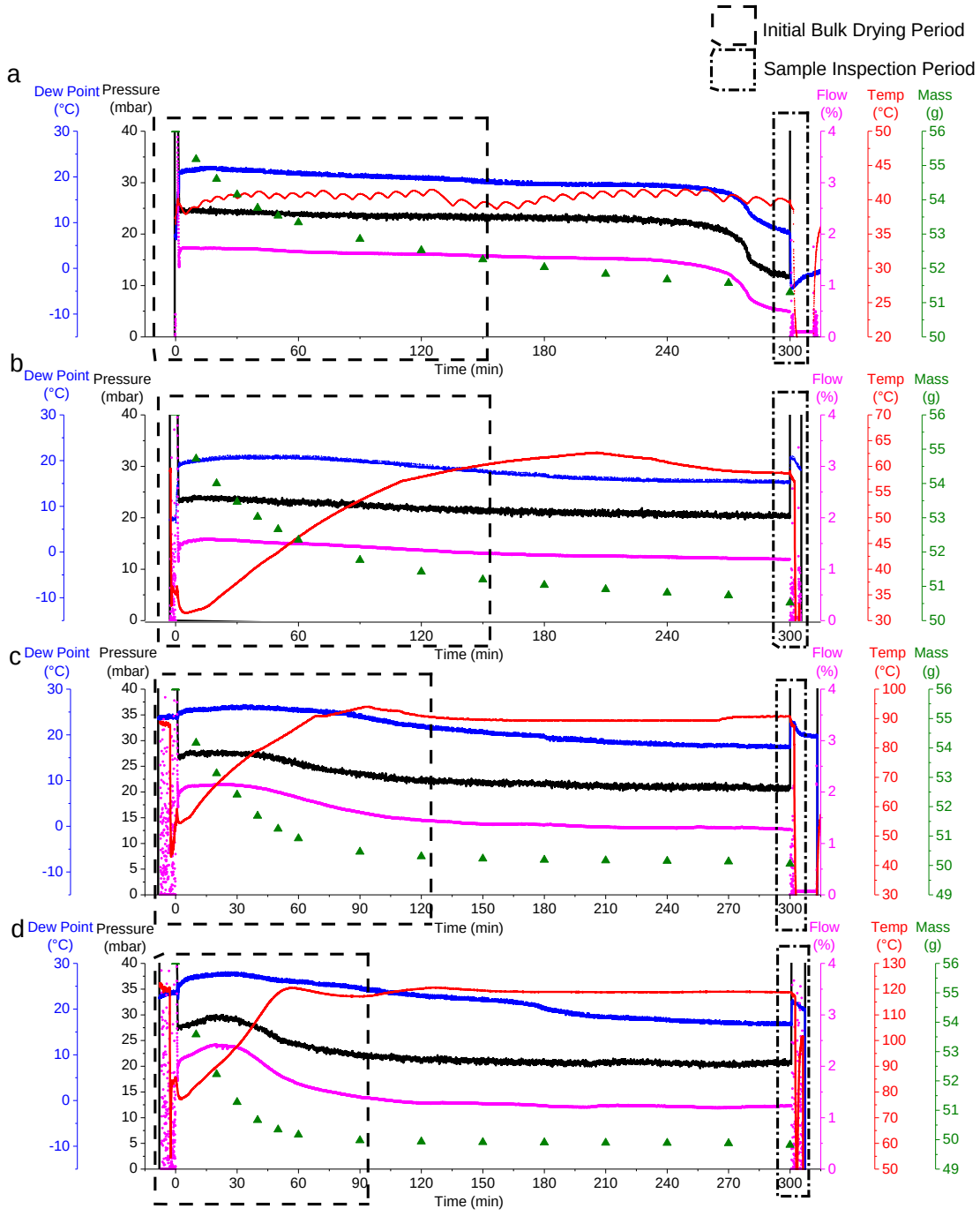

Figure 5-7. Vacuum drying overview of corroded Magnox Sample 2 at; a) 40 °C, b) 60 °C, c) 90 °C and d) 120 °C

Following initial evacuation over the course of each experiment the pressure, flow and dew point follow close relationships and are generally stable and consistent for the duration. The pressure remained at ~20-24 mbar, flow at 1.25-1.55% and dew point at 18-22 °C for the majority of the experiment at 40 and 60 °C. At 90 °C and 120 °C the initial pressure, flow and dew point rose to 27-30 mbar, 2.1%-2.4% and

25-28 °C in the initial 45 mins, and then gradually reduced into the range of the 40-60 °C temperature data after 90 mins.

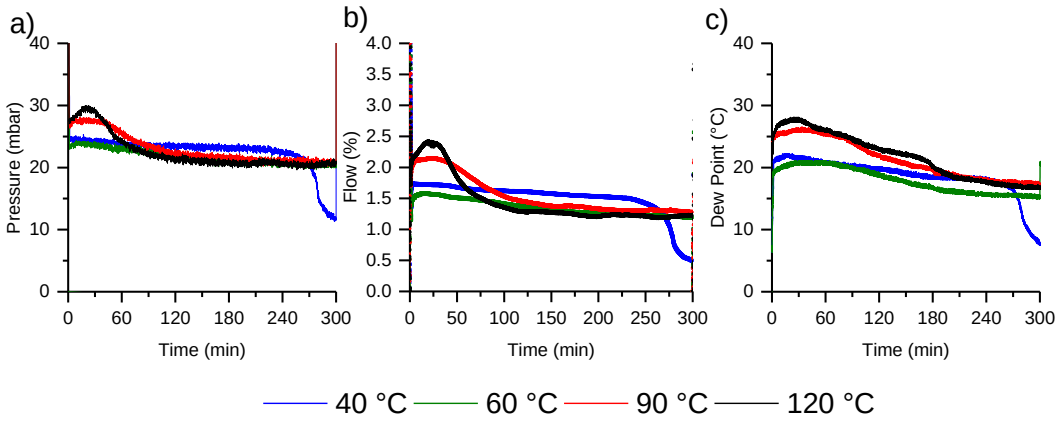

Figure 5-8. Vacuum drying Sample 2 data; a) pressure, b) flow and c) dew point

Pressure, flow and dew point remained approximately consistent within these ranges for the rest of the test period and did not demonstrate the same drop to baseline as seen in Sample 1, with the exception of the 40 °C test. Instead the 40 °C data is seen to drop, initiating at 240 mins. This is a surprising observation and will be discussed further later.

From the pressure, flow and dew point data as with Sample 1 there were no obvious variations or trends with change in temperature, but the mass change does correlate with drying temperature. Sample 2 mass loss was more gradual than Sample 1 and less clear to assign the period where the bulk drying is observed, so has been assigned as the point that the average rate is less than 0.01 g/min (Figure 5-7 and summarised in Table 5-2). Mass loss and drying rates are shown in Figure 5-9. Assigning the bulk drying by an assumed rate minima has one drawback in that it does not account for the different total amounts of water removed, so the “bulk drying” at 40 °C and 60 °C is reported to occur in the same amount of time, despite the higher temperature removing notably more water. Again, it can be seen that increasing temperature gives rise to increased mass loss rates. Mass loss at 40 °C was steady with the bulk drying occurring over 150 mins. Bulk mass loss at 60 °C occurred in 150 mins, 120 mins at 90 °C and 90 mins at 120 °C. Gradual mass loss continued over 300 mins total, as summarised in Table 5-2. A slightly larger than expected mass loss is seen from 270-300 mins drying of Sample 2, which is not representative of enhanced drying in this period. Instead, it is an artefact of the different averages from the measurements at both intervals. The average measured at 300 mins includes a fourth data point from the uninterrupted drying, rather than the three datapoints with regular inspections seen for all other inspections. On this basis, the previous interval from 230-270 mins drying will be discussed here (and

shown in Table 5-2). For Sample 2 even after 230 mins drying, steady mass loss was still observable at 40 and 60 °C of 101 and 78 mg. At 90 °C the mass loss was less at 21 mg, and much less at 120 °C where only 8 mg mass loss was seen. From this, it can be seen that the larger and more corroded Sample 2 proved more difficult to dry then Sample 1, with notable mass of water still being removed after 270 mins drying at 40-60 °C.

Table 5-2. Bulk and end sample masses from vacuum drying Sample 2

Temperature (°C)	Bulk mass loss time (min)	Mass after bulk drying (g)	300 min drying mass (g)	Mass loss 230-270 mins (g)
40	150	52.257	51.298	0.101
60	150	51.194	50.521	0.078
90	120	50.306	50.053	0.021
120	90	49.974	49.821	0.008

The increase in temperature from 40-120 °C consistently increased the sample drying rate and extent of drying for Sample 2 as displayed in Figure 5-9. The initial rates are 0.072, 0.103, 0.146 and 0.192 g/min at 40, 60, 90 and 120 °C respectively. The rates are greater than that for Sample 1 due to the larger sample size, water loading and surface area. Also due to the greater loading the rates are sustained longer than for Sample 1 which allows easier assignment of rate stages (in accordance with Mujumdar as described in Section 2.4.6[39]), although Stage 1 is still not clear to assign, presumably because of the low water loading the stage is short lived relative to the inspection frequency. Sample 2 displayed more gradual drying than Sample 1, and from the data the second drying stage appears to be visible from the second measurement point at 10-20 mins onwards to 40-50 mins. After this the drying rate is consistently slow, but sustained mass loss is seen over the duration of the test period, most notably at 40-60 °C. Mass loss at 90-120 °C is significantly reduced after 90 mins. The general trend with increased drying rate at increased temperature is consistent with that seen by Yun et al. as shown in Figure 2-21.[11]

This data further supports the theory that increasing the temperature does indeed remove more water, and that the inconsistencies seen for Sample 1 are more likely a result of sample changes over the course of the investigation. This is illustrated in Figure 5-10 in the trend of sample mass for vacuum drying Sample 1 and Sample 2 for 240 mins. Sample 2 shows consistently increased mass loss under the same drying conditions that Sample 1 was exposed to.

So far this investigation has acknowledged that there was no observable trend between temperature and vessel pressure, dew point or rig mass flow, but that there was a clear relationship with mass loss. Theoretically once all air has been removed from the rig and vessel, all mass flow and pressure should reach a

minimum close to zero, and anything measured above zero should be attributable to water vapour produced from sample water vaporisation. This water vapour should then be removed by the vacuum and captured on the molecular sieves. The mass observations on the molecular sieves were consistent with the mass loss from the sample water so this is known to be true. In this case, the pressure, flow and dew point should have some correlation to the drying process. On review of this data it was initially unclear why this was not observed so a further investigation was undertaken to investigate the rig performance when drying unbound liquid water. One possible reason for seeing elevated flow and pressure could be that the system has a leak, but from extensive testing no leak was found, and the system was able to be evacuated successfully and within normal operating parameters without a sample/water present. Therefore it was evident some interaction with the sample/water was causing these elevated pressure and flow observations.

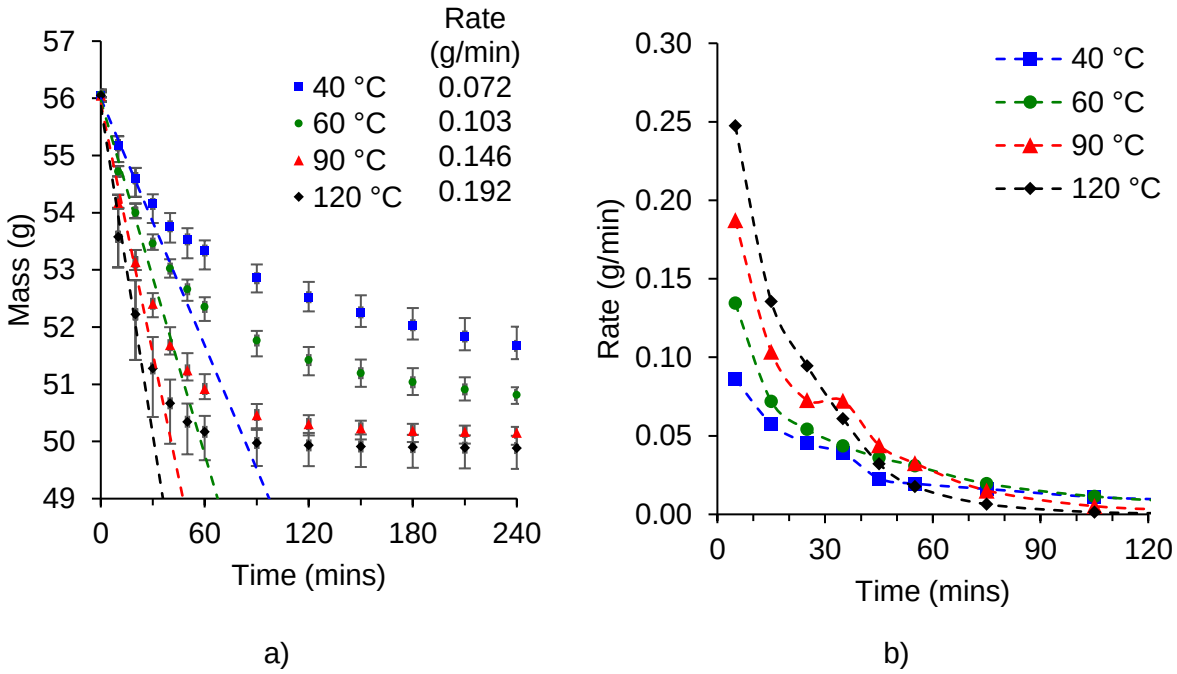

Figure 5-9. Sample 2 vacuum drying data for 40-120 °C showing; a) Mass change and initial rate, b) drying rate over time

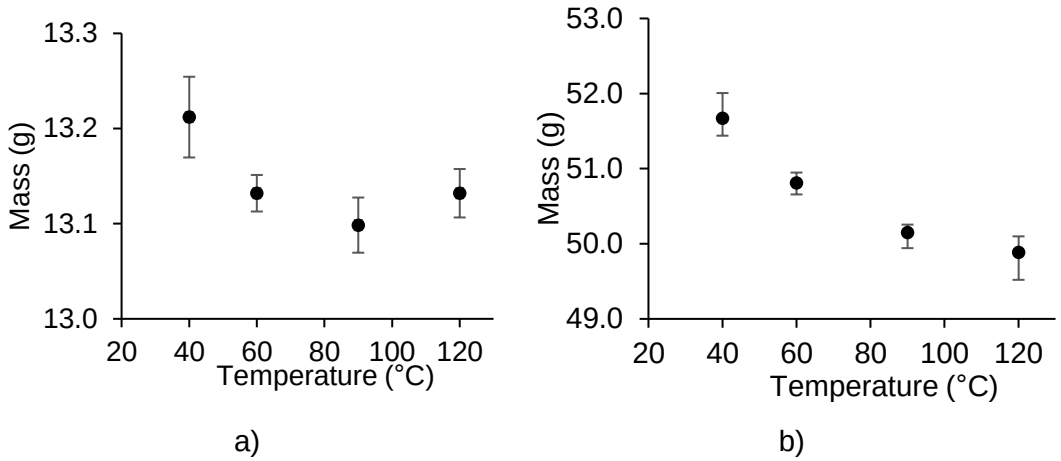

Figure 5-10. Sample mass after 240 mins drying at each temperature for a) Sample 1, b) Sample 2

5.2.2 Corroded Magnox drying rate analysis

Based on the information in Section 2.4.6[39] some characterisation of drying rates and behaviours may be performed. Treating the Magnox samples as non-hygroscopic, the characteristic moisture content, ϕ can be calculated from average moisture content, $\bar{X}$ divided by critical moisture content $\bar{X}_{cr}$. $\bar{X}$ here is calculated by assuming that the sample is bone-dry at the lowest observed average mass obtained during the testing campaign, and moisture content is assigned relative to this on dry-basis. It is difficult from the rate-time data in Figure 5-5b and Figure 5-9b to assign $\bar{X}_{cr}$. As there is no consistent and easily definable point at which a the drying rate transitions from clearly steady first stage to decreasing second stage. For both samples the most distinguishable condition where this is visible is at 40 °C and 60 °C drying, and the resulting values are listed in Table 5-3. The average of these values has then been used to calculate the characteristic moisture content, ϕ from Equation 2-11 over the range of temperatures and is plotted in Figure 5-11.

Table 5-3. Critical moisture content and temperature at point of rate change (t_{cr}) for Sample 1 and Sample 2 drying 40-120 °C

	Sample 1		Sample 2	
Temperature (°C)	t_{cr} (min)	X_{cr}	t_{cr} (min)	X_{cr}
40	35	0.069	45	0.079
60	15	0.079	15	0.098
190	-	-	-	-
120	-	-	-	-
Ave		0.074		0.089

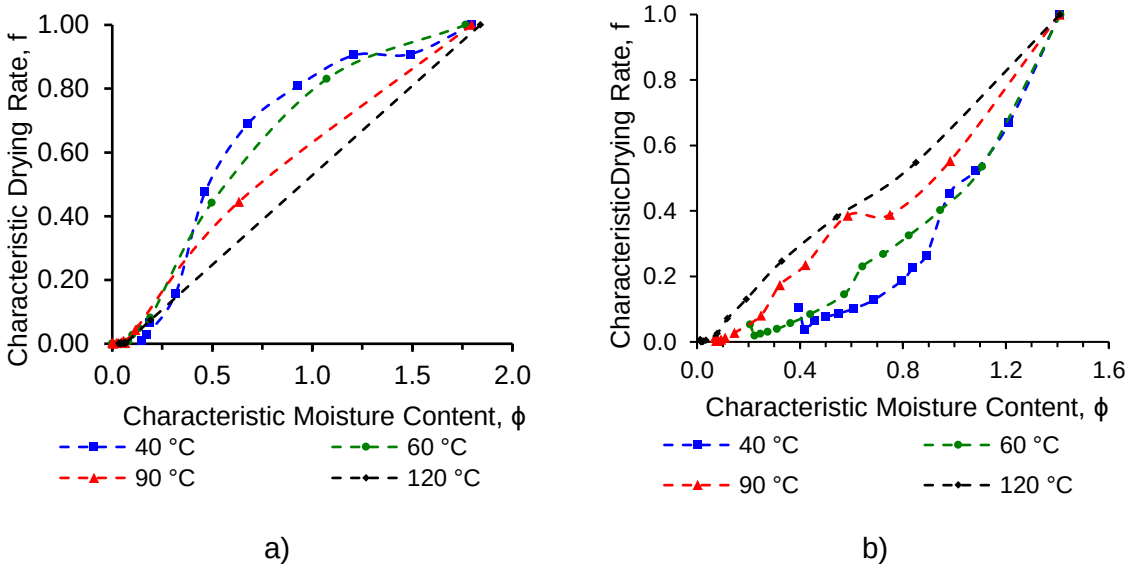

Figure 5-11. Characteristic drying curves for drying corroded Magnox Samples 1+2 at 40-120 °C

The data for 40 °C and 60 °C are most consistent, but from this data it is difficult to assign whether this characteristic drying rate/moisture content data is applicable to a wide range of conditions. It is acknowledged that one of the factors that determines whether a characteristic drying rate can be attributed to a material requires the material $\bar{X}_{cr}$ to be invariant of temperature. Unfortunately the data here could not prove this for the samples tested, mostly due to difficulty in taking frequent mass measurements, particularly at temperatures >60 °C where the early stages of mass changes were very rapid and the water volumes were small. Additionally the data/moisture content estimations are skewed by the significant proportion of the sample which is unreactive metal substrate that does not contribute to the process. The general trend between temperatures is consistent with that seen by Yun et al. where drying rates and times are significantly reduced with increasing temperature.[11] They did not make the same observation about overall extent of drying being greater at higher temperature, but they did not test at temperatures <80 °C where these observations were most significant so that is not directly comparable here. Further work in this area would benefit from more frequent mass observations, coupled with larger sample/water volumes to help improve data/trend resolution. Additionally it would be valuable to undertake a study with a greater number of samples and known sample surface areas to assign specific drying rates per unit area, which can then be directly compared and sample gross size will not be a factor.

5.2.3 Drying rig baseline testing

5.2.3.1 Vacuum drying unbound liquid water

To get a better understanding of drying liquid water under the specific conditions of this apparatus, a series of liquid water experiments were undertaken for comparison to the corroded Magnox sample data already discussed. To ensure liquid water results were directly comparable to previous data, the mass of water used was consistent with the average mass loss from drying Sample 1 from 240 mins drying at each given temperature (show in Table 5-2). Drying tests at each temperature were undertaken in the same manner as for Sample 1 and Sample 2, - an overview for which is in Figure 5-12. The benefit of drying unbound water is that the point of sample dryness can be determined with certainty as no water will remain in the container. As can be seen in Figure 5-12, total dryness was achieved in 40-45 mins at 40 °C, ~12.5 mins at 60 °C, <12.5 mins at 90 °C and <5 mins at 120 °C (best approximation due to need for inspections). Despite these known points of dryness, pressure, flow and dew point continued to be elevated for 75-90 mins after initiation, which is similar to the 60-75 mins observed for Sample 1. On this basis it is clear that another factor is giving rise to these observations. The mass loss at each temperature is listed in Figure 5-13a with the initial rate of mass loss shown by the line of best fit. As expected, the increase in temperature consistently increases the drying rate. In Figure 5-13b this data is displayed with that for Sample 1 for direct comparison, and shows the rate of mass loss for equivalent mass of free water was quicker than that associated with the Magnox sample. This is expected to be a result of more effective heat transfer from the vessel wall to the metal container through conduction, as the Magnox sample will have a larger mass of Magnox/corrosion through which the heat must conduct before the surface water will boil. The water on the Magnox sample would likely have a greater effective surface area with which to evaporate, but equally the surface has many small cracks and voids within which the water removal will be obstructed.

Table 5-4. Average mass loss on drying Sample 1 at given temperature

Temperature (°C)	Mass (g)
40	1.57
60	1.68
90	1.74
120	1.75

On further inspection of the drying rig during this aspect of the investigation, moisture was detected that suggested water was condensing within, which is consistent with the test dew point measured at approximately 35 °C (i.e. above

room temperature/rig wall temperature external to the heated vessel). Therefore it was assumed that water following vaporisation from the sample was then condensing further down the line, and essentially equilibrating between vapour/liquid on the rig walls. This is consistent with the pressure and flow data where an approximately constant reading was observed for an extended period following perceived point of sample bulk drying, until a final drop to baseline showed the final quantities of water were removed from the rig. This effect was more pronounced for the larger quantity of water loaded for Sample 2 drying, where the total mass of water seemingly was not dried out and the pressure/flow did not proceed to reach the baseline.

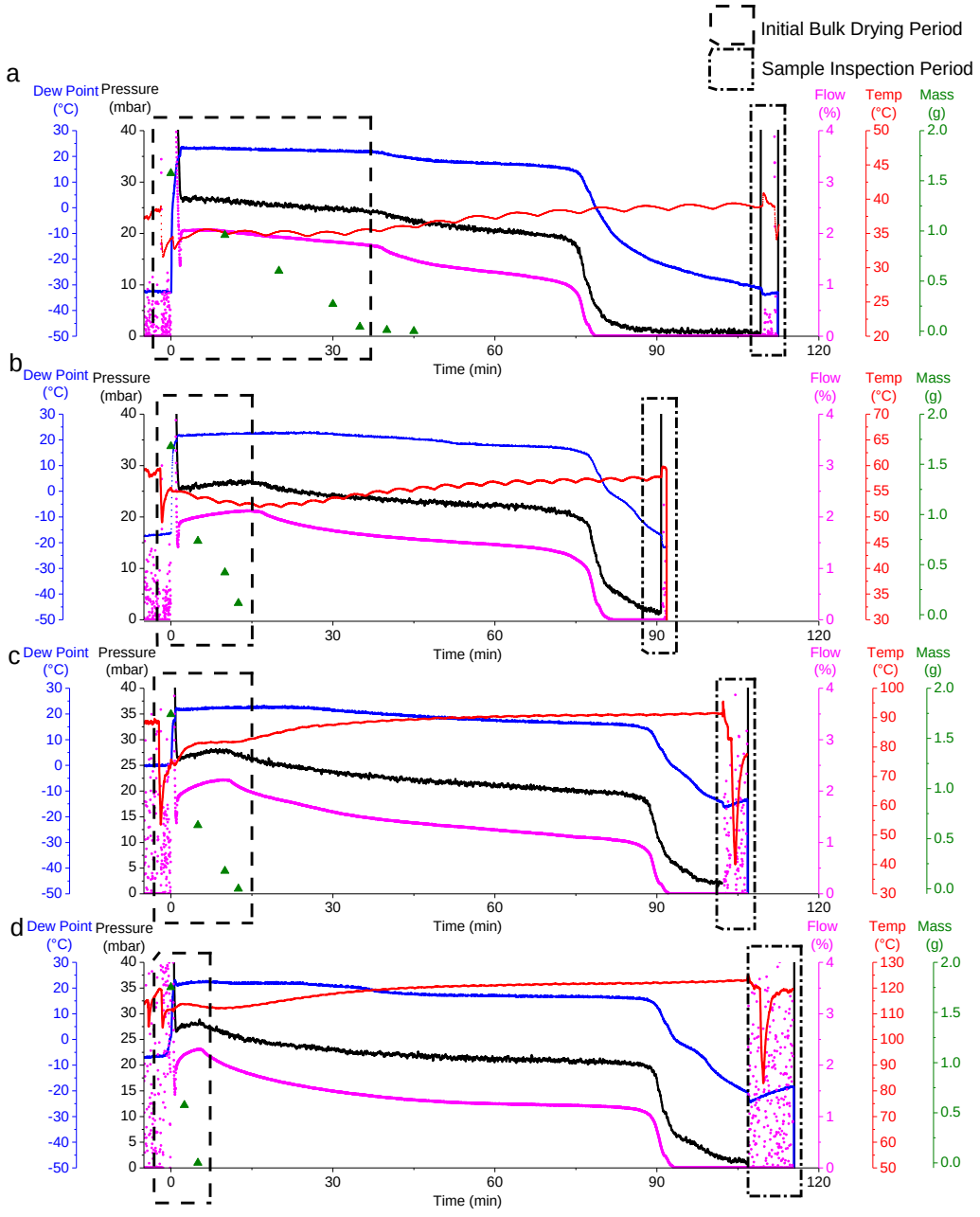

Figure 5-12. Vacuum drying unbound liquid water at given temperature; a) 40 °C, b) 60 °C, c) 90 °C and d) 120 °C

On this basis it was of interest to investigate this theory and confirm its potential effects on the drying process. This was achieved by heating the temperature of the rig walls to reduce/prevent condensation within.

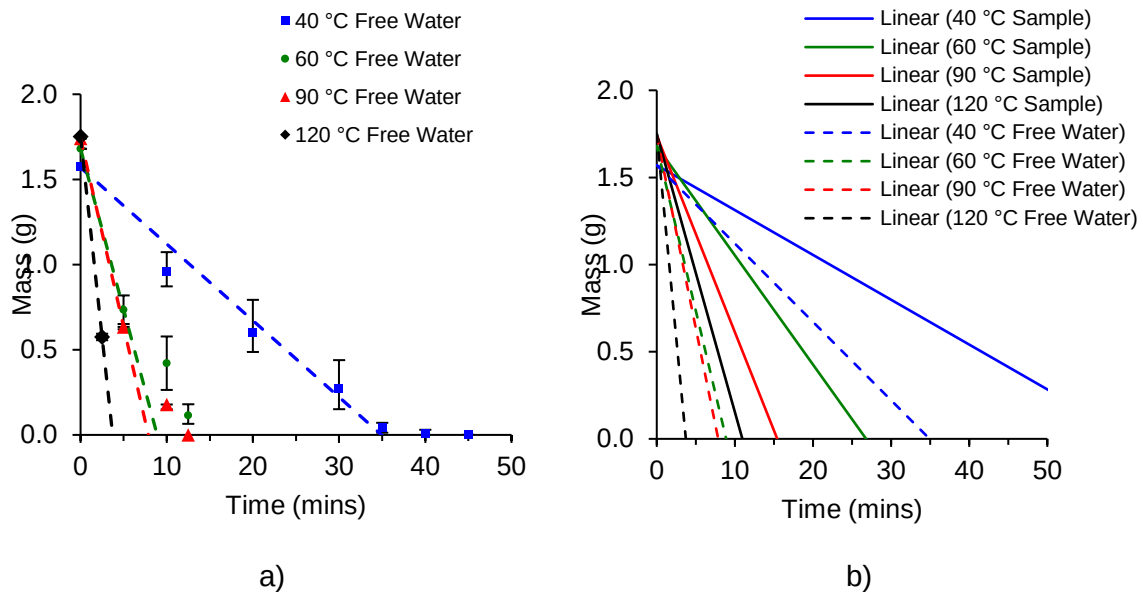

a) b)

Figure 5-13. a) Mass loss of free water (equivalent quantity from Sample 1 drying investigation), b) initial linear mass loss gradients of water from Sample 1 (solid lines) c.f. free water (dashed lines) at same temperature

5.2.3.2 Vacuum drying unbound liquid water with heated rig

To observe and identify any possible variation to the drying process that addition of a heater to the rig tube walls could have, all other parameters such as temperature and free water mass were kept constant. An overview of all data is shown in Figure 5-14, and as presented each plot shows one uninterrupted dataset overlaid onto the average mass data from several inspections. The heater was fitted to the ~2 metre rig tube, starting from the vessel lid round beyond the flow meter to the molecular sieves. The heater temperature was measured at 35-45 °C.

The free water mass loss with the heated rig data for all test temperatures are summarised in Figure 5-15, along with unheated rig data for direct comparison. The mass loss equates to an approximately linear rate, as listed in Table 5-5. The mass loss with increasing temperature gave rise to increased rate of mass loss as expected, but notably the rate of mass loss with the heater on from 40-90 °C was consistently lower than that without the heater. At 120 °C the two rates were barely separable (0.45 with heater c.f. 0.47 without heater).

The pressure, flow and dew point data also displayed very different behaviour with the heated rig tube. Figure 5-16 displays the data collected without the rig heater

(left) with the equivalent conditions with the rig heater (right) and the differences are clear to see. The pressure, flow and dew point all increase notably with increasing drying temperature, and also drop to the baseline in a consistently comparable time to the point at which the free water was removed. This shows with certainty that the previous pressure, flow and dew point behaviour was related to condensation on the rig walls.

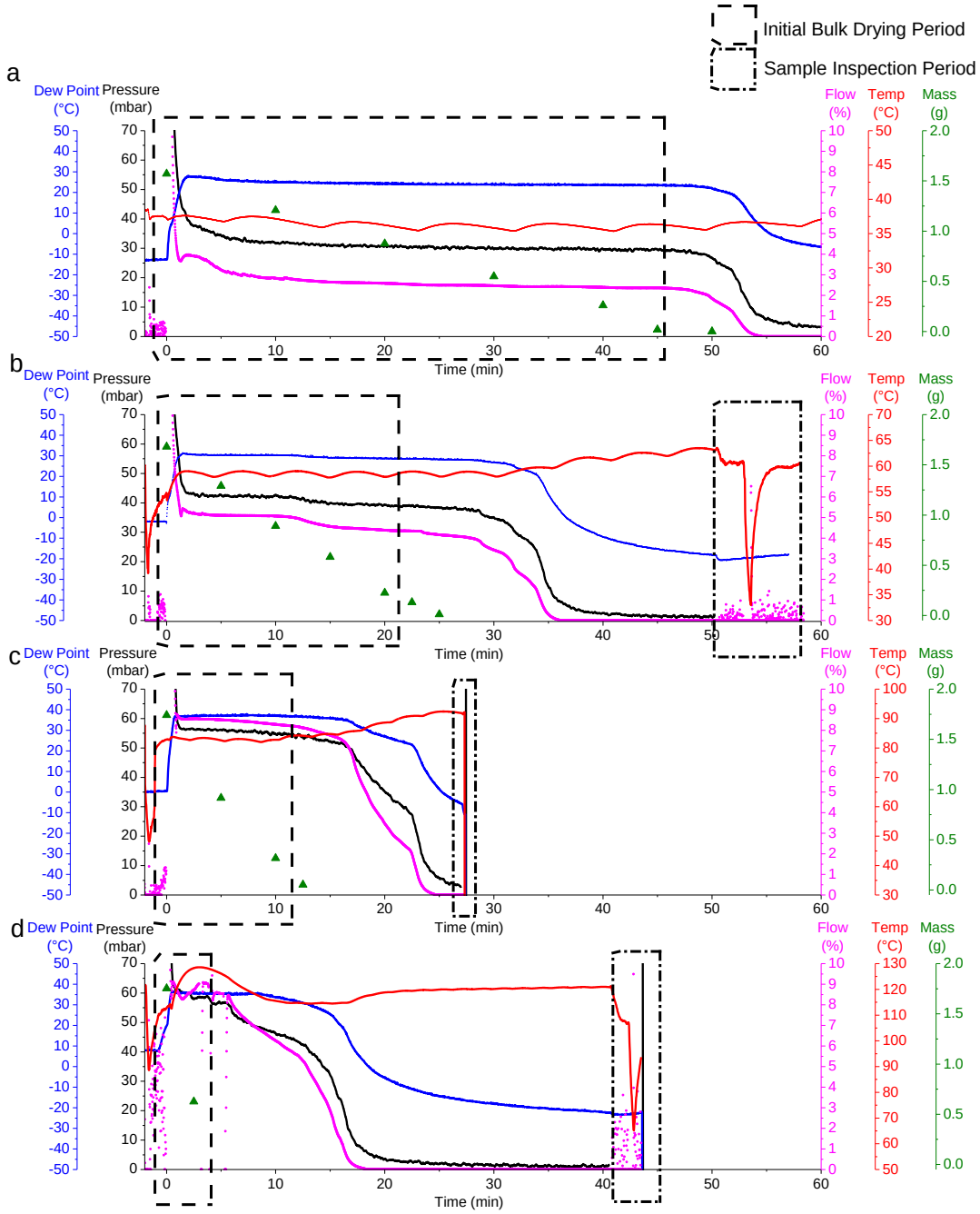

Figure 5-14 Vacuum drying free water with at given temperature with heated rig; a) 40 °C, b) 60 °C, c) 90 °C and d) 120 °C

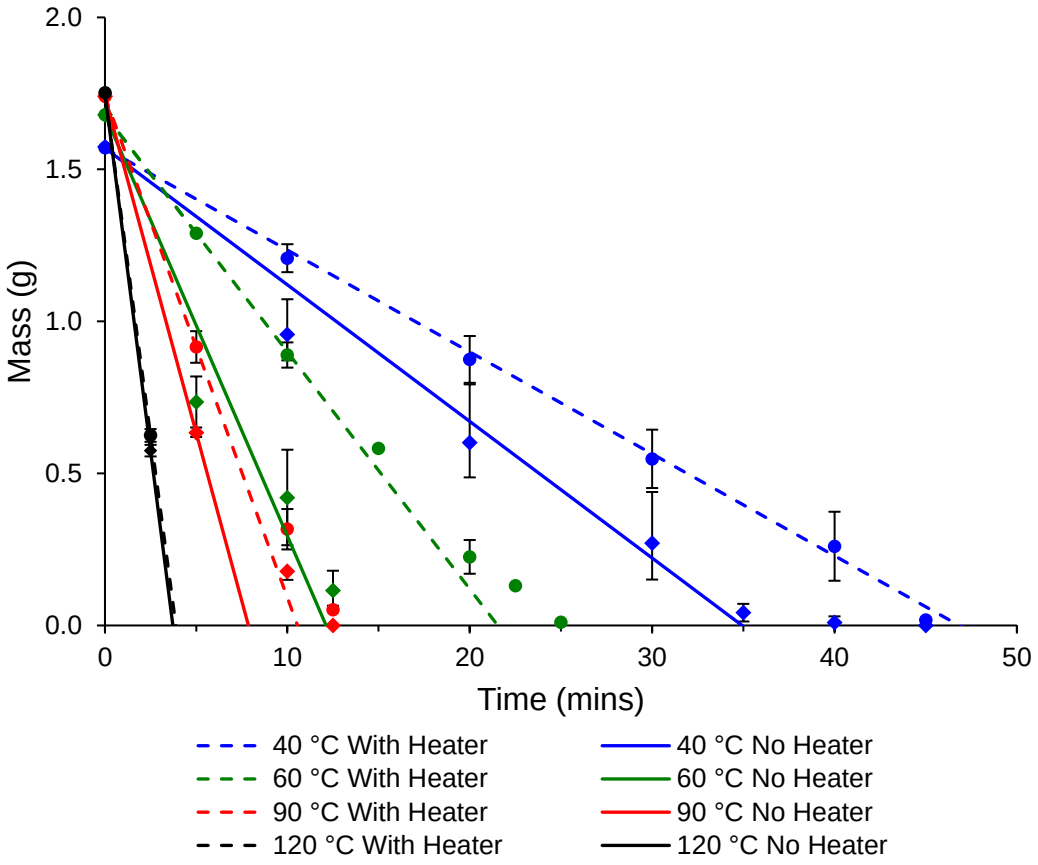

Figure 5-15. Mass loss from drying free water at given temperature with rig heater on (dashed line/circles) and off (solid line/diamonds)

Table 5-5. Mass loss rate of free water with and without rig heater

	Drying Rate (g/min)	
Temperature	No Heater	With Heater
40	0.045	0.034
60	0.14	0.078
90	0.22	0.16
120	0.47	0.45

There are still some observations here to address. Firstly it is interesting that the rate of water mass loss is lower in the presence of the rig heater. This is very likely to be a result of the increased water vapour pressure within the vessel during drying resulting in reduced vaporisation on remaining liquid water. Figure 5-16a shows that the pressure without the rig heater was at approximately 20-28 mbar at all points during the drying, at which point the boiling point of water is ~18-23 °C (Table 5-6 data from Rogers and Mayhew[115]). In Figure 5-16b it can be seen that the rig heater increases the vessel pressure to 31-59 mbar, which in turn increases the boiling point of water to ~26-36 °C. From this, the data demonstrate that employment of the rig heater resulted in reduced drying rates, but greatly improved control of condensation from drying.

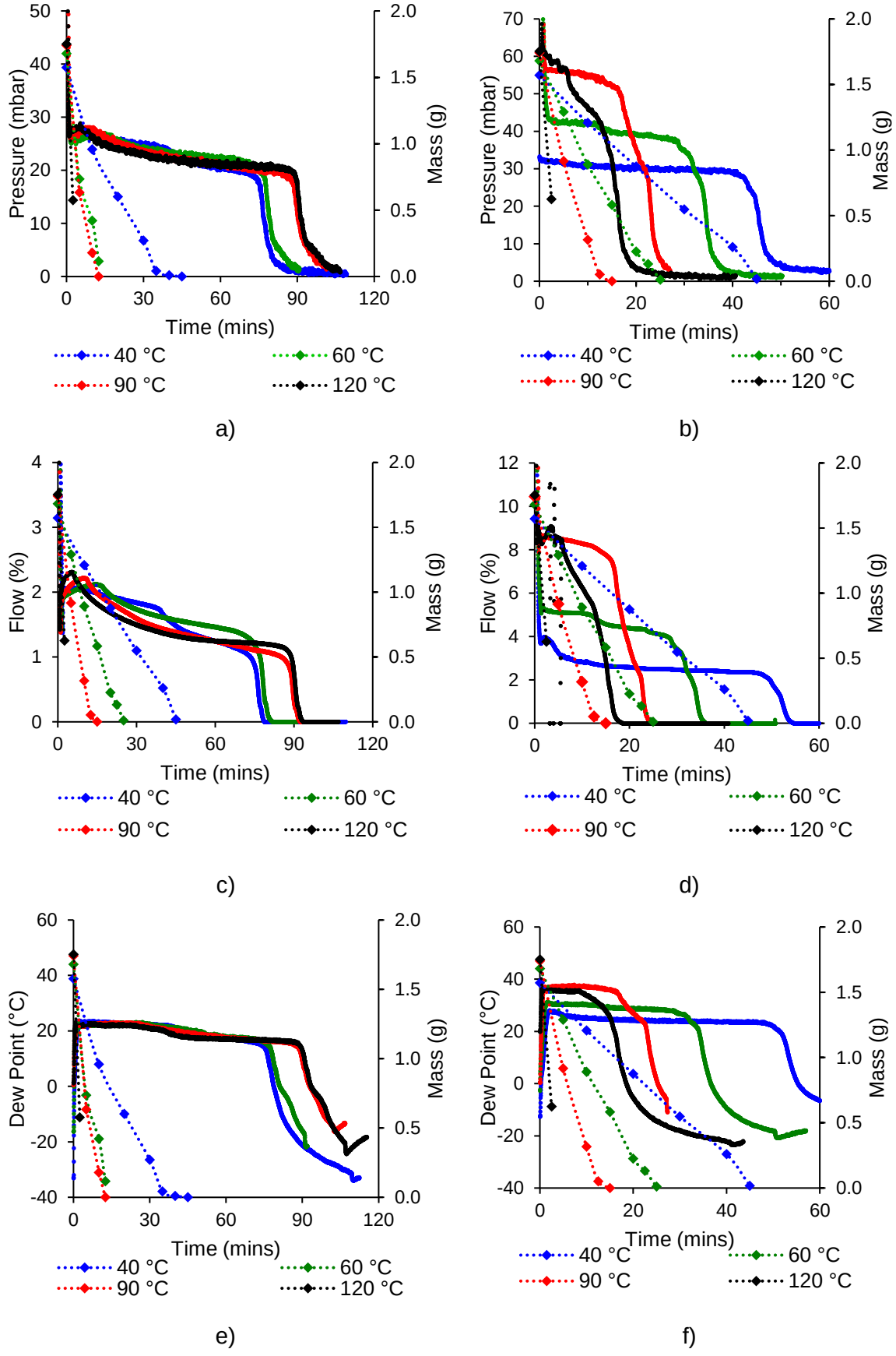

Figure 5-16. Pressure, flow and dew point from drying free water at given temperature with rig heater off; a) pressure, c) flow and e) dew point, and with heater on; b) pressure, d) flow and e) dew point

Table 5-6. Water boiling point at range of pressures

Pressure (mbar)	Boiling Point (°C)
6.11	0.01
6.57	1
20.6	18
28.1	23
33.6	26
42.4	30
59.4	36

Additionally despite introduction of the rig heater and improved correlation between free water drying and pressure/flow, there is still a delay between the point of dryness and pressure/flow baseline. This is likely to be due to some parts of the rig/vessel remaining unheated, particularly some feedthroughs into the vessel lid. Additionally, especially at 90-120 °C the dew point is close to that of the rig walls, so there may be some condensation despite the inclusion of the heater. In order to improve this in further work, it would be beneficial to minimise the amount of internal surfaces, tube walls and unnecessary fittings to reduce the available contact areas for water condensation. Water vapour capture is currently managed by the molecular sieves. In the current orientation, water vapour must travel ~1.5 metres before it can register at the flow meter, and ~2 metres before capture on the molecular sieves. This could be reduced by removing the flexible braided tube which currently allows the rig lid to be removed in favour of a short rigid inlet. Then the sample loading and unloading could instead be achieved by lowering and raising the vessel body, whilst the lid remains in place. The inlet could then feed straight into any instrumentation such as dew point meter and flow meter, then into the molecular sieves to be captured. This redesign would significantly reduce the internal surfaces and reduce potential for water condensation.

5.2.4 Ambient mass gain following drying

Following drying of corroded Magnox samples, during weighing it was observed that the sample would slowly increase in mass when exposed the open atmosphere. This has been attributed to readsorption of water vapour from air. This effect was quantified by drying Sample 1 for 5 hours at 40 and 90 °C, and the same for 2.0 g of as-received magnesium hydroxide and hydromagnesite for comparison (shown in Figure 5-17 and summarised in Table 5-7). Mass loss was observed to be greater for hydromagnesite than for magnesium hydroxide at both test temperatures which suggests the hydromagnesite powder has more physisorbed/bound water than the magnesium hydroxide. At 40 °C magnesium hydroxide mass loss was at 0.85%, and 2.0% for hydromagnesite. At 90 °C for magnesium hydroxide and hydromagnesite the mass loss was measured at 1.4%

and 3.1%. This is less than the mass loss observed by TGA, which was up to 2.84% for magnesium hydroxide heated to 285 °C and 3.36% for hydromagnesite when heated to 120 °C.

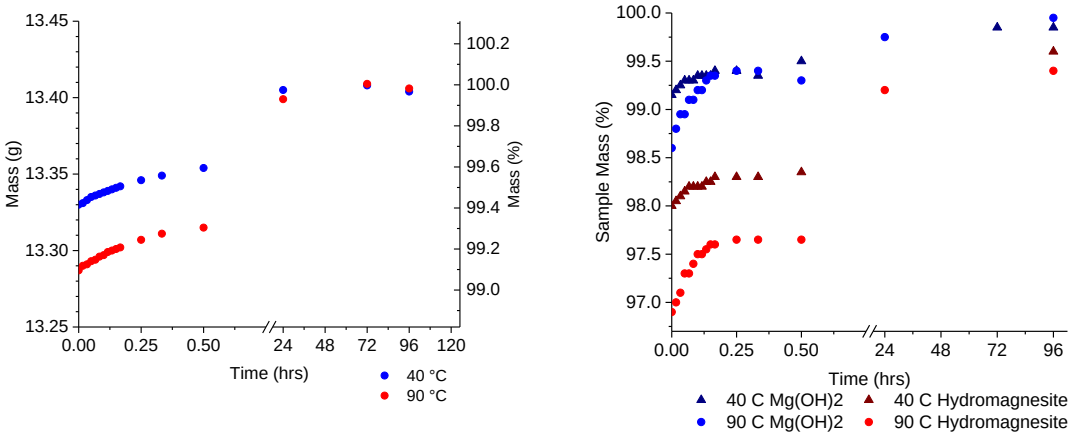

a) b)

Figure 5-17. Sample mass change in ambient atmospheric conditions following 5 hours vacuum drying at specified temperature for; a) Sample 1, b) magnesium hydroxide and hydromagnesite powders

Table 5-7. Mass change over time following 5 hours vacuum drying at given temperature

Temperature	Time	Sample 1	$Mg(OH)_2$	Hydromagnesite
40 °C	0 min	99.42%	99.15%	98.00%
	10 min	99.51%	99.40%	98.30%
	30 min	99.60%	99.50%	98.35%
	24 h	99.98%	-	-
	96 h	99.97%	99.85%	99.60%
90 °C	0 min	99.09%	98.60%	96.90%
	10 min	99.20%	99.35%	97.60%
	30 min	99.30%	99.30%	97.65%
	24 h	99.93%	99.75%	99.20%
	96 h	99.98%	99.95%	99.40%

For Sample 1, the mass change is predominantly considered in terms of mass loss rather than % mass. The secondary axis does display the mass loss as a percentage of total, relative to the highest measured mass. This is primarily as an indicative measure, as considering the total mass is not wholly meaningful given the significant quantity of sample metal is inert (i.e. the uncorroded magnesium substrate below the surface) and not involved in the process.

Mass loss from drying at 90 °C was greater than at 40 °C as expected from previous data, and hydromagnesite . For all materials, immediately after removal from the vessel the mass increased steadily for the first 10 mins, and the increase occurred at a quicker rate for the powders (but not seen for Sample 1) dried at 90 °C c.f. those dried at 40 °C. After this point mass gain slowed but still continued.

The mass at 30 mins following drying of magnesium hydroxide at 90 °C appears lower than that measured at 20 mins, which implies the mass has reduced over this period. It should be noted that in real terms this is a discrepancy of 2 mg, and over the period of 10 mins is likely to be a small drift on the mass balance over the 10 minute period and is not representative of any unexpected sample behaviour.

Following 24 hours from drying completion for Sample 1, there was little difference between the test undertaken at 40 °C and the one at 90 °C. For the magnesium hydroxide and hydromagnesite powders following 24 hours in ambient conditions after 90 °C drying (no 40 °C data available) both samples had recovered the majority of the lost mass, with magnesium hydroxide at 99.7% and hydromagnesite at 99.2%. After 96 hours the magnesium hydroxide regained almost all lost mass, at 99.85% following drying at 40 °C, and 99.95% after 90 °C drying. Hydromagnesite also recovered further mass up to 96 hours after drying, which was slightly less than magnesium hydroxide at 99.60% after 40 °C drying and 99.40% following 90 °C drying. One noteworthy observation here is the ability for both powders to regain the lost mass to almost exactly the starting mass. If the powders had quantities of “excess” water residual from any preparation or manufacturing procedure, this water would likely be more easily removed and would not be recovered by adsorption from atmosphere. This observation is of some interest to the following chapter on radiolysis of Magnox corrosion products where the importance of quantifying the surface water on these powders is of most relevance.

These observations demonstrate the importance for maintaining a moisture-free atmosphere during storage for these materials following a drying procedure. Clearly any dried Magnox corrosion products display hygroscopic behaviour as moisture is re-adsorbed onto the surface. If a drying process were to be employed industrially, this observation demonstrates the importance of ensuring dried fuel is backfilled with inert and dry storage gas. The implications for this re-adsorbtion are debatable, but the following chapter aims to research this in further detail and provide some data to inform this question.

5.3 Conclusions

Vacuum drying has been performed on Corroded Magnox Samples 1 and 2 to compare drying temperatures at 40-120 °C. Extent of drying was primarily monitored by observing mass loss, with supporting data from rig/vessel pressure, water vapour mass flow and dew point.. For Sample 1 the “bulk” drying of free water was observed to occur within 60 mins of starting at 40 °C, and increasingly quickly up to within 20 mins at 120 °C. Drying at increasing temperature was generally shown to increase both the drying rate and overall quantity of water

removed. For Sample 1, optimal drying was identified at 90 °C rather than at the higher temperature of 120 °C. This was unexpected and is likely to be related to the sample physically changing, gaining mass through corrosion over the course of the experimental program. This is supported by a test that was undertaken to dry the sample at increasing temperature without wetting between each condition, which showed that drying at temperatures greater than 90 °C (up to 180 °C) gave consistently greater overall dryness through mass loss. Therefore it is concluded that the vacuum drying process does not cause significant or excessive unwanted corrosion to the Magnox sample.

In response to this and to provide further data, a second corroded Magnox Sample 2 was vacuum dried under comparable conditions. Drying Sample 2 at 40-120 °C also demonstrated increased drying rates and greater extent of dryness through drying at higher temperatures, but conversely to Sample 1, Sample 2 measured greater mass loss at 120 °C c.f. at 90 °C, which further supports the previous conclusion regarding physical change of Sample 1 over experimental regime.

On review of all the drying data, drying rates were significantly slower, and the time to achieve sample dryness is greater at 40 °C c.f. temperatures ≥60 °C. On this basis it is recommended that any drying of these materials is undertaken at temperature >40 °C. Increasing the drying temperature will give rise to both increased drying rates and greater extent of dryness achieved, but it is acknowledged that this in turn gives rise to more engineering and potential safety challenges. The lowest temperature recommended from this work for vacuum drying corroded Magnox is 60 °C, although lower temperatures of drying at 50 °C[59] have been reported industrially elsewhere for comparable materials.

A lack of correlation between rig pressure, dew point and mass flow and the mass loss from drying were observed during drying of corroded Magnox samples. On further investigation of drying free water, it was discovered that the water vapour was condensing on the walls within the rig. An external rope heater was installed to reduce this which mad a significant difference to the pressure, flow and dew point response. Interestingly the heater also in turn reduced the rig drying rates, which is most likely a result of the increased vapour pressure within the rig during drying. From this it is clear that effective water vapour management is important to optimise drying rate and rig performance. Here it was shown that reducing water vapour condensation on rig walls provided better vapour management and cleared the rig more rapidly, but in turn lowered the drying rate of the sample. This could be improved by reducing internal surfaces available for condensation and relocating the molecular sieves (or another form of vapour management e.g. a condenser) close to the vessel outlet.

The final aspect to this investigation was observing the dried samples re-adsorb water from the atmosphere following drying. This was most rapid in the first 10-15 mins following drying but continued mass gain was seen for several days after drying. The same behaviour was observed in magnesium hydroxide and hydromagnesite powders. This demonstrates the importance of ensuring that dried materials are backfilled with inert and dry gas to prevent water re-adsorption onto materials surfaces.

5.4 Recommendations and Further Work

This chapter has introduced and investigated a number of aspects of the drying of Magnox spent fuel and corrosion products, primarily in identifying the impacts of drying temperature and time, and an attempt to quantify the relative benefits of this are investigated in the next chapter of this thesis. These drying rates are very specific to the samples used here under these specific conditions so cannot be directly applied elsewhere, but the general trends and drying temperature implications should be valid for other applications. From these experiments, it is recommended that the drying temperature for corroded Magnox must be >40 °C for effective drying extent and rates, and the recommended minimum temperature is 60 °C. Increasing benefits in drying rate and overall amount of water removed were seen at temperature ≥120 °C, but it is acknowledged other practical or safety limitations may affect this. The samples used here were of unknown surface area. Sample 1 had some internal structure/void space analysed by CT in Section 4.2.2.1. Further work in this area looking to investigate and quantify the effect of void space/volume, surface area and drying rate/temperature would be of interest.

One factor with respect to drying rig design and practical implementation that became apparent from this investigation is the effective management of the water vapour produced by the drying process. It is recommended that this is condensed or removed by other means as soon as practical, as the presence of water vapour pressure will slow the removal of remaining liquid/adsorbed water.

Further work in this area that would be valuable is considering scaling up the process to larger/intact fuel cans and multiple cans simultaneously. Water diffusion from within the corroded material volume will be dependent on effective heat conduction to the material and will most likely play a major factor in potential drying rates. As part of this process it may be valuable to consider alternative drying technologies such as direct convective methods.

Other aspects of work that have not been considered here are drying the uranium fuel bar itself, along with any fuel corrosion products that will most likely be present.

Additionally there could be considerations given to drying water that is trapped between the Magnox cladding and the fuel bar, through defects, cracks and pinholes.

5.5 Chapter Appendix

Table 5-8. Sample 1 mass from vacuum drying at specified temperature/time

	40 °C Sample						60 °C Sample				
Time (mins)	1	2	3	4	5	Ave	1	2	3	4	Ave
0	14.73	14.88	14.93	14.84	14.822	14.84	14.86	14.80	14.81	14.77	14.81
10		14.60			14.48	14.54		14.14	14.10	14.17	14.14
20		14.35			14.188	14.27		13.57	13.54	13.64	13.58
30		14.11			13.885	14.00		13.28	13.28	13.30	13.29
40		13.88			13.632	13.76		13.23	13.23	13.23	13.23
50		13.67			13.427	13.55		13.20	13.20	13.20	13.20
60		13.50			13.317	13.41		13.18	13.18	13.19	13.18
90		13.30			13.236	13.27		13.15	13.17	13.18	13.17
120		13.27			13.215	13.24		13.14	13.16	13.17	13.15
180		13.25	13.28*		13.197	13.22	13.12	13.13	13.15	13.16	13.14
240		13.24	13.28	13.30		13.27	13.11	13.12	13.14	13.15	13.13
300			13.27	13.29		13.28					
360	13.17					13.17					
Mass Loss	1.57	1.64	1.66	1.55	1.63		1.75	1.68	1.67	1.62	
Ave. Final Mass				1.61					1.68		

*Sample measured at 210 mins (not 180)

Table 5-9. Sample 1 mass from vacuum drying at specified temperature/time

	90 °C Sample					120 °C Sample					
Time (mins)	1	2	3	4	Ave	1	2	3	4	5	Ave
0	14.84	14.83	14.85	14.84	14.84	14.85	14.88	14.96	14.86	14.86	14.88
10	13.78		13.75	13.61	13.71		13.27		13.28	13.32	13.29
20	13.25		13.20	13.18	13.21		13.15		13.18	13.17	13.17
30	13.18		13.15	13.15	13.16		13.15		13.18	13.17	13.16
40	13.17		13.16	13.15	13.16		13.14		13.17	13.17	13.16
50	13.16		13.16	13.15	13.15		13.14		13.17	13.16	13.16
60	13.15		13.15	13.14	13.14		13.14		13.17	13.16	13.15
90	13.12		13.13	13.13	13.13		13.13		13.16	13.15	13.15
120	13.11		13.13	13.12	13.12		13.12		13.16	13.15	13.14
180	13.10	13.08	13.12	13.12	13.10	13.12		13.15	13.14	13.14	13.14
240	13.09	13.08	13.12	13.12	13.10	13.11		13.15			13.13
300		13.08			13.08						
Mass Loss	1.57	1.76	1.73	1.71	1.76	1.74	1.76	1.81	1.72	1.72	1.75
Ave. Final Mass			13.10						13.13		

Table 5-10. Successive drying of Sample 1 without wetting between tests

Time (h)	40 °C	60 °C	90 °C	120 °C	150 °C	180 °C
0	14.952	13.341	13.329	13.307	13.267	13.223
2	13.324	13.276	13.236	13.217	13.196	13.17
4	13.298	13.264	13.231	13.212	13.192	13.158
6	13.290	13.260	13.224	13.208	13.191	13.155

Table 5-11. Sample 2 mass from vacuum drying at specified temperature/time

	40 °C					60 °C				
Time (mins)	1	2	3	4	Ave	1	2	3	4	Ave
0	56.08	56.12	56.03	55.95	56.05	56.15	56.04	56.02	56.05	56.07
10	55.34		55.32	54.89	55.18	54.71		54.64	54.82	54.72
20	54.78		54.75	54.28	54.60	53.90		53.94	54.16	54.00
30	54.32		54.32	53.82	54.15	53.41		53.35	53.62	53.46
40	53.99		53.82	53.48	53.76	53.02		52.86	53.19	53.02
50	53.73		53.67	53.20	53.53	52.69		52.46	52.83	52.66
60	53.52		53.49	53.01	53.34	52.43		52.11	52.52	52.35
90	53.10		52.86	52.61	52.85	51.93		51.49	51.88	51.77
120	52.79		52.50	52.27	52.52	51.65		51.16	51.46	51.42
150	52.56		52.21	52.00	52.26	51.43		50.96	51.19	51.19
180	52.33		51.98	51.78	52.03	51.28		50.81	51.01	51.04
210	52.16		51.76	51.59	51.84	51.12		50.72	50.89	50.91
240	52.01		51.57	51.44	51.67	50.95		50.66	50.83	50.81
270	51.88		51.52	51.31	51.57	50.81		50.62	50.77	50.73
300	51.77	50.82	51.41	51.19	51.30	50.69	50.08	50.59	50.73	50.52
Mass Loss	4.31	5.30	4.62	4.76	4.75	5.46	5.96	5.44	5.32	5.54

Table 5-12. Sample 2 mass from vacuum drying at specified temperature/time

	90 °C					120 °C				
Time (mins)	1	2	3	4	Ave	1	2	3	4	Ave
0	56.15	56.08	55.94	56.02	56.05	56.11	56.03	56.02	56.06	56.05
10	54.08		54.31	54.12	54.17	53.04		53.62	54.07	53.58
20	53.00		53.35	53.06	53.14	51.43		52.42	52.82	52.22
30	52.17		52.59	52.46	52.41	50.43		51.58	51.83	51.28
40	51.52		52.00	51.53	51.68	49.96		50.96	51.08	50.67
50	51.07		51.54	51.12	51.24	49.78		50.60	50.66	50.34
60	50.74		51.18	50.84	50.92	49.67		50.38	50.45	50.17
90	50.23		50.66	50.50	50.46	49.57		50.15	50.20	49.97
120	50.11		50.46	50.35	50.31	49.57		50.08	50.15	49.93
150	50.04		50.36	50.29	50.23	49.55		50.06	50.12	49.91
180	49.99		50.31	50.27	50.19	49.54		50.05	50.12	49.90
210	49.96		50.28	50.26	50.17	49.53		50.04	50.11	49.89
240	49.94		50.26	50.26	50.15	49.52		50.04	50.10	49.88
270	49.90		50.24	50.25	50.13	49.51		50.03	50.09	49.88
300	49.85	49.89	50.23	50.24	50.05	49.48	49.69	50.02	50.09	49.82
Mass Loss	6.30	6.19	5.71	5.78	5.99	6.63	6.34	6.00	5.97	6.23

Table 5-13. Mass (g) from vacuum drying free water at specified temperature without heated rig

No Rig Heater

40 °C						60 °C					
Time (mins)	1	2	3	4	Average	Time (mins)	1	2	3	4	Average
0	1.574	1.574	1.575	1.574	1.574	0.0	1.679	1.680	1.681	1.68	1.680
10	1.073	0.928	0.872	-	0.958	5.0	-	0.651	0.819	-	0.735
20	0.793	0.487	0.523	-	0.601	10.0	0.578	0.264	0.420	-	0.421
30	0.439	0.151	0.221	-	0.270	12.5	0.100	0.065	0.180	-	0.115
35	0.000	0.013	0.071	-	0.028						
40	0.030	0.000	0.000	-	0.010						
45	0.000	0.000	0.000	-	0.000						
90 °C						120 °C					
Time (mins)	1	2	3	-	Average	Time (mins)	1	2	3	-	Average
0	1.74	1.741	1.742	-	1.741	0	1.75	1.752	1.75	-	1.751
5	-	0.648	0.62	-	0.634	2.5	-	0.556	0.594	-	0.575
10	-	0.150	0.207	-	0.1785	5	-	0.00	0.00	-	0.000
12.5	-	0.000	0.000	-	0.000						

Table 5-14. Mass (g) from vacuum drying free water at specified temperature with heated rig

With Rig Heater

40 °C					60 °C				
Time (mins)	1	2	3	Average	Time (mins)	1	2	3	Average
0	1.572	1.571	1.570	1.571	0.0	1.679	1.681	1.680	1.680
10	1.254	-	1.162	1.208	5.0	0.000	-	1.290	
20	0.952	-	0.798	0.875	10.0	0.848	-	0.931	
30	0.644	-	0.452	0.548	15.0	0.000	-	0.582	
40	0.374	-	0.147	0.261	20.0	0.170	-	0.281	
45	0.000	-	0.018	0.009	22.5	0.000	-	0.131	
50	0.120	-	0.000	0.060	25.0	-	-	0.011	
90 °C					120 °C				
Time (mins)	1	2	3	Average	Time (mins)	1	2	3	Average
0	1.741	1.741	1.74	1.741	0	1.752	1.752	1.752	1.752
5	0.968	-	0.864	0.916	2.5	-	0.604	0.646	0.625
10	0.383	-	0.25	0.317	5	-	0	0	0.000
12.5	0.102	-	0.001	0.052					
15	0	-	0	0.000					

Chapter 6 Hydrogen Generation From γ- And α-Radiation Of Magnox Corrosion Products

6.1 Introduction

The previous chapters of this thesis have aimed to assess what could be present in wet stored corroded Magnox fuel and what to expect from a potential drying regime. This chapter intends to address the question of how dry is adequate, and what are the implications for water carryover into a dry radioactive environment. The findings of this investigation have suggested that the level of dryness that can be achieved is dependent on the age and condition of the material that is destined for processing, and the intensity of the drying process it is exposed to. On this basis it is important to try to probe in to how water could behave when present in the presence of corroded Magnox in a radioactive environment, and attempt to quantify how much hydrogen could potentially be generated in these conditions. As experimental radioactive testing requires access to very specialist capabilities, the data in this chapter was gathered with the use of the gamma and alpha radiation sources at the Dalton Cumbrian Facility (DCF).

6.2 Experimental Development and Methods

6.2.1 Spent fuel dose and composition estimates

For planning irradiation work it is of value to estimate a representative dose which may be found *in situ*. Radiation dose rate data following reactor discharge for spent Magnox fuel is based on information estimated from FISPIN/Microshield data (provided by NNL[116]) for an average Magnox fuel burnup of 5 GWd/teU,[117] shown for a period of 50 years in Figure 6-1. Based on these activities, from Microshield dose rate estimations over a 30 year period from 20-50 years post irradiation, 2 mm thick magnesium will absorb a γ-irradiation dose of approximately 12 kGy/cm^2. This estimation is not recommended to be used in any other applications and is only used here as an indication of a potential representative dose. Estimations vary hugely based on all assumptions such as point and length of consignment, as well as geometry and loading volume, but as shown in Figure 6-1, radiation activity and energies do not vary significantly beyond the first 10 years after discharge.

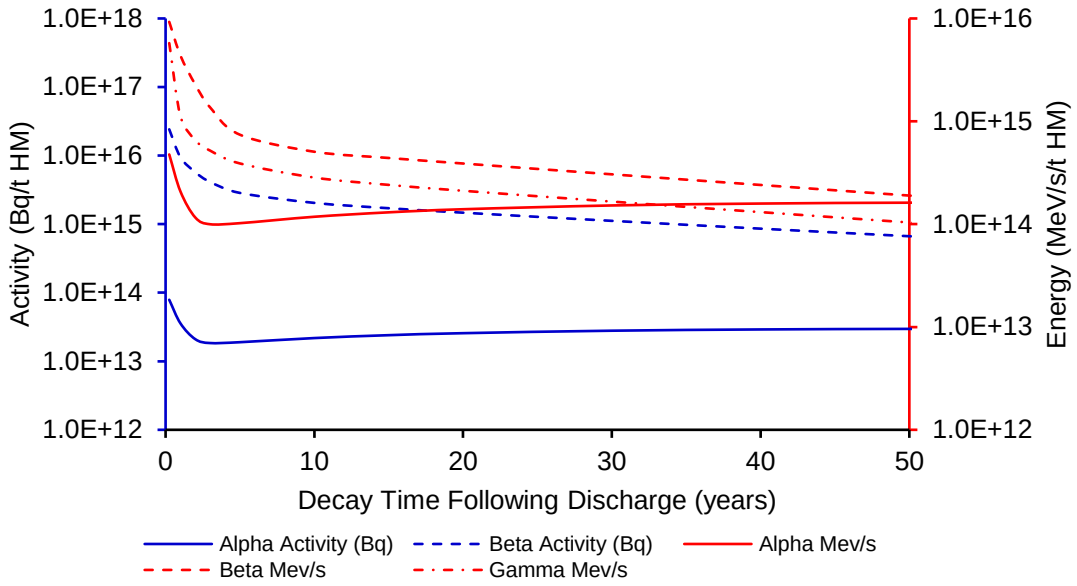

Figure 6-1. Alpha, beta and gamma radiation activity/energy for 5 GWd/te HM burnup Magnox fuel based on predicted data from FISPIN 10[116]

6.2.2 Radiolysis apparatus and analytical equipment

To undertake active γ- and α-irradiation testing of potential Magnox corrosion products, a series of experiments were planned to expose magnesium hydroxide and hydromagnesite to radiation and observe hydrogen generation. The aim of the work was to test and quantify how the variation of water content and absorbed radiation dose affected the hydrogen yield. This work was carried out using the bespoke facilities at the Dalton Cumbrian Facility (DCF) with additional funding provided by the Nuclear Decommissioning Authority via the TRANSCEND consortium.

6.2.2.1 ^{60}Co γ-Irradiator

Gamma irradiations were undertaken at the DCF on the Foss Therapy Services Model 812 ^{60}Co gamma irradiator.[118] ^{60}Co is a common source of gamma radiation for research and medical purposes. It has a half-life of 5.27 years, and principally decays by emission of a beta particle to excited ^{60}Ni, followed by emission of two gamma photons of 1173 keV and 1332 keV down to its ground state, as illustrated in Figure 6-2a so is expected to impart energy primarily through Compton scattering (as described in Section 2.5.3.1).[119,120]

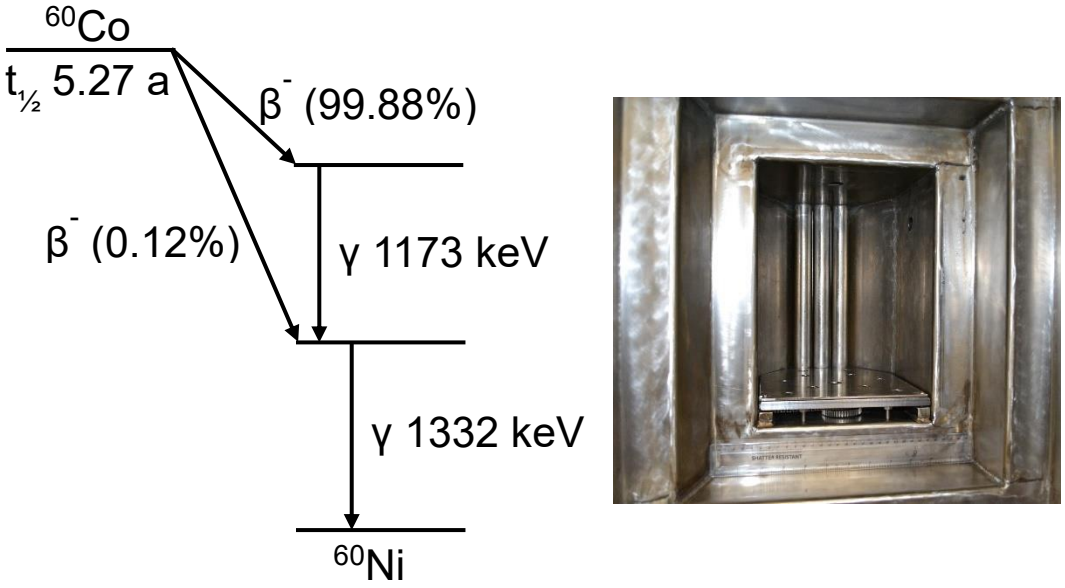

a) b)

Figure 6-2. a) Decay scheme of cobalt-60; b) γ-Irradiator chamber and cobalt-60 source guide rods

The irradiator consists of three ^{60}Co source rods, each of which contain replaceable capsules to enable refreshment of dose rates as the sources decay over the lifetime. The rods are held within the self-shielded irradiator chamber during the course of irradiations, and are lowered into the base of the irradiator to protect operators whilst the door is open to enable access for sample loading/setup. Dose rates can be controlled by varying the number of source rods in place during irradiations, managing the distance to reduce absorbed dose via inverse square law over distance or deliberately shielding samples inside the irradiator.[118] Dose rates can also vary based on position from left to right due to the orientation of the source rods. For the experiments performed here, maximum (or close to maximum) dose rates were required to achieve total absorbed doses representative of that from contact with spent nuclear fuel over many (estimated as ~30) years whilst allowing experiment times to be practical during 1-2 week access windows.

6.2.2.2 Gas chromatography

Gas chromatography was performed on a modified SRI 8610C Gas Chromatograph (pictured in Figure 6-3a) which identifies component intensity signals via a Thermal Conductivity Detector (TCD) and a 6’ MS13X column for sample component separation. The typical column length for these instruments is 3’, but the additional length allows for delayed hydrogen elution which avoids the signal appearing during an early period of baseline disturbance before stabilisation.[121]

Prior to operation, the GC column was baked out at 120 °C for 50 mins at a pressure of 1 barA argon carrier gas. It is important to opt for a carrier gas with a significant difference in thermal conductivity to maximise detection sensitivity. The most common carrier gas for such experiments is helium, but as these experiments were primarily looking to measure hydrogen, argon was used instead which also permits detection of oxygen and nitrogen. The TCD relies on measuring the difference in thermal conductivity between pure carrier gas and the carrier gas with separated components of the sample gas mixture, and if the difference is small (for example between helium and hydrogen) then sensitivity is lost. Following baking the column was cooled to 80 °C, the pressure increased to 2 bar and the TCD temperature at 140 °C.

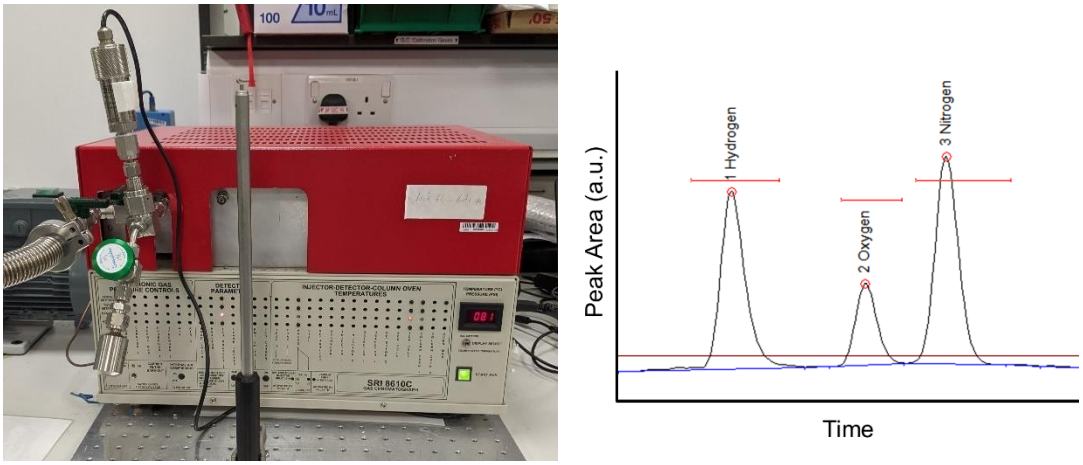

a) b)

Figure 6-3 a) SRI gas chromatograph; b) example GC spectrum showing hydrogen (peak 1), oxygen (peak 2) and nitrogen (peak 3) – n.b. arbitrary units

For analysis, sealed sample holders were attached via a Swagelok tube fitting. The GC was then evacuated, with pressure observed by a pressure transducer located at the sample inlet. This serves to both remove the previous sample gas from the GC and also ensure the new sample holder is loaded correctly and leak tight. Once the GC was evacuated, the sample holder valve was opened to allow the gas to enter the GC and the pressure was recorded. Once the pressure was stable and the sample was correctly loaded then the GC analysis was started. The elution time will vary based on the GC setup and column used, and in this configuration hydrogen eluted at 0.54-0.65 min, oxygen at 0.77-0.85 min and nitrogen at 0.85-0.99 min. The peaks appeared suitably separated and peak areas could be reliably integrated. The areas under the peaks directly relate to the volume of gas eluted, but without calibration to achieve a direct relationship between peak area and gas quantity the data cannot be interpreted accurately. For best confidence in the peak area integral, it was apparent that peak areas <1.0 (arbitrary) units had the

most uncertainty so experiments aimed to produce a detectable signal >1.0 units, but this was not always possible, particularly for tests with minimal water presence as will be discussed later.

To equate the hydrogen signal to a usable form such as a quantity of gas in molecules/moles, application of the ideal gas law can be used (Equation 6-1):[40]

$$PV = nRT \qquad \text{Equation 6-1}$$

Where P = pressure in Pascals, V = volume in m^3, n = amount of gas in moles, R = universal gas constant; 8.314 J K^{-1} mol^{-1} and T = Temperature in Kelvin. In order to apply this, it is necessary to know the internal volume of the GC plus any attached apparatus during measurement (i.e. the sample holder). To establish this, the sample holder volume was established by mass difference upon filling with water (12.6 cm^3), and then application of a rearrangement of the Boyles law enables calculation of GC internal volume from Equation 6-2 (where n and T are constant):[40]

$$P_1V_1 = P_2V_2 \qquad \text{Equation 6-2}$$

From application of this principle, the addition of a known pressure and volume from a sealed 12.6 cm^3 sample holder established the GC internal volume as 13.0 cm^3. This can now be used with known pressure and temperature from the perfect gas law in Equation 6-1 to establish amount of hydrogen gas, n in moles.

6.2.2.3 GC H_2 calibration and H_2 yield calculation

In order to get meaningful data from the GC elution peak, it is essential to perform calibration tests to observe the relationship between sample quantity and detector response. This was achieved by filling the sample holders with known mixtures of hydrogen/argon and measuring the peak area. The gas mixtures were prepared using the manifold detailed (simplified) in Figure 6-4 and shown in Figure 6-5. The mixture was prepared in the 1 L mixing chamber, initially at a nominal pressure of 1.5 bar. This was then released to the sample holders (which had been previously evacuated) to fill them with the desired gas mixture – typically at ~1.3 bar. The sample holders were sealed and attached to the GC which would first be evacuated. Following evacuation the gas mixture was released in to the GC at a typical pressure of 0.5-0.6 bar where it was analysed and the peak area recorded. This was performed multiple times at a variety of hydrogen concentrations/pressures to establish a relationship between hydrogen concentration and detector signal (shown in Figure 6-6).

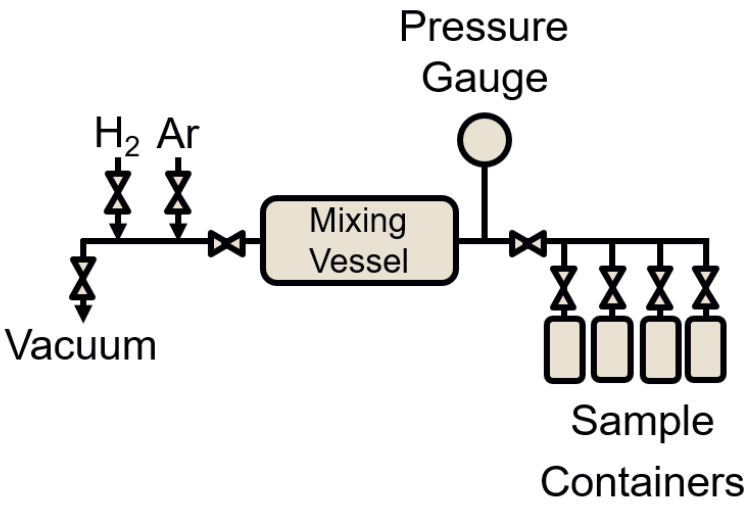

Figure 6-4. Sample preparation gas manifold schematic diagram (simplified)

In the calibration chart Figure 6-6, the black points labelled “various % H2” were prepared at the start of the investigation in accordance with the aforementioned method with nominal sample pressure of 1.3 bar. In order to gain confidence that variation of pressure did not affect detector response, and ensure that GC operation had remained consistent over the course of the investigation, at the end of the experimental period further GC response tests were performed. The blue points labelled “0.10 % H2” and the red “0.05% H2” were gathered from known mixtures of the designated H_2 concentration, but instead of releasing the entire gas volume into the GC at once, the gas was only partially released in, then the pressure was recorded along with the associated GC signal. This was performed multiple times at various pressure in the range of ~0.1-0.4 bar to gain confidence the GC could consistently produce data even when sample pressures were low. As can be seen the 0.1% H_2 and 0.05% H_2, the data is entirely consistent with the data gathered at the initial data set which gives good confidence that the GC data is reliable at this range of pressures/concentrations and the performance was consistent over the course of the investigation. One observation from the calibration line is that the variance appears greater as the peak area drops <1.0, so on this basis it is desirable to aim for experimental hydrogen yields that produce peak areas >1.0, although this was not always possible without availability to perform longer irradiations. There is still reasonable correlation at these low (<1.0) peak areas, provided the peak is clearly defined enough for a precise shape to be identified for integration.

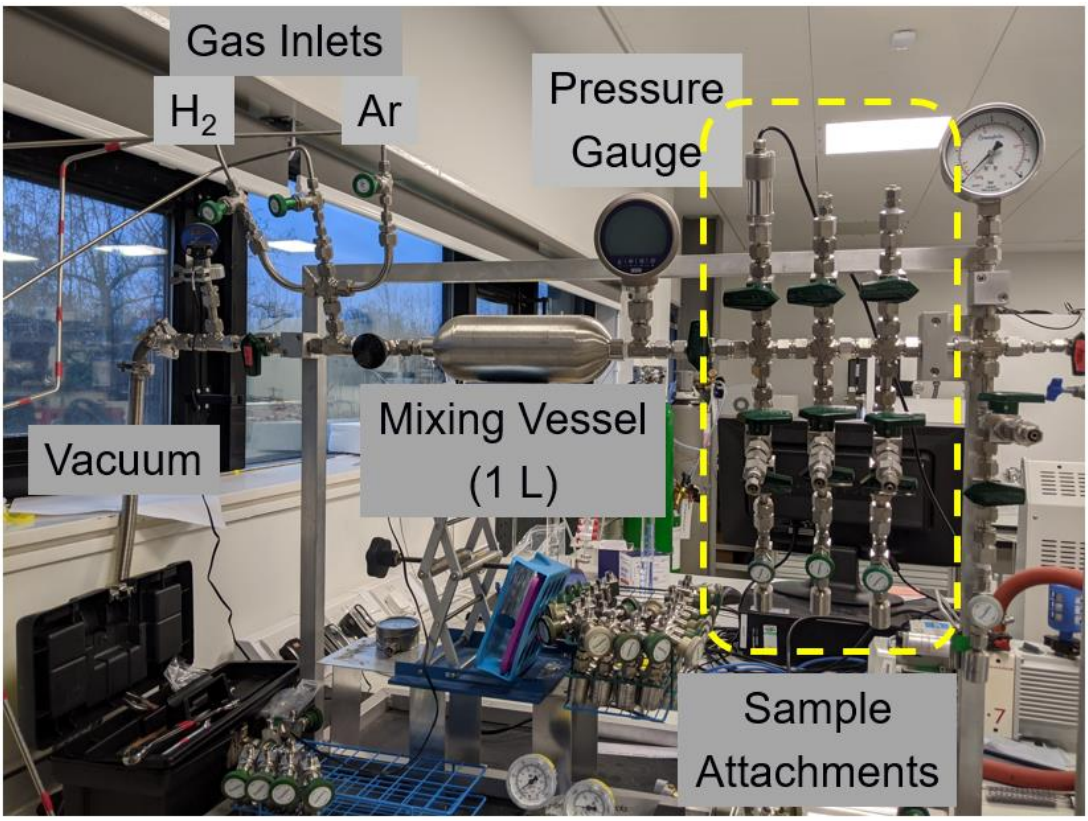

Figure 6-5. Sample preparation gas manifold

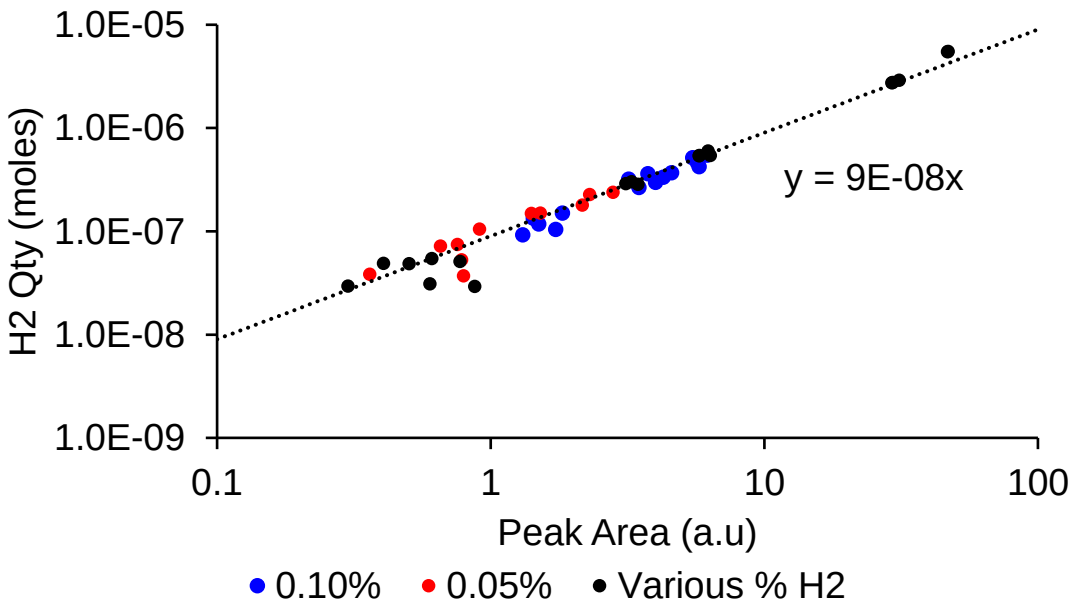

Figure 6-6. Calibration line for quantity of hydrogen (in moles) with respect to GC peak area

6.2.2.4 Sample preparation for γ-irradiation

For the purposes of irradiation experiments, material selection is very important. Any material will incur radiation damage over the course of the experiment, so it is essential that the setup uses materials that will not fail during irradiation, or compromise results by undergoing unwanted chemical/radiochemical reactions. One particular limitation is the incompatibility of plastics and rubbers within the radiation field. Suitably radiation resistant materials such as steels were used to contain the solid samples and radiolytic hydrogen, enlisting the use of valves without any plastic components. Sample holders were entirely stainless steel and consisted of a 10 cm^3 cylinder, connected to a reducer and sealed by a bellows valve.

Solid samples were prepared by pipette addition of water to a known mass of as-received chemical solid powder in the quantities listed in Table 6-1 and mixed in a beaker which yielded a fine free flowing powder, even at the >20% water content mixtures. It was considered that some evaporative losses may occur during sample preparation and evacuation, and through preliminary tests these were estimated at 0.05 g per sample, so an additional 0.05 g water was added to each to account for these losses. From practical experience and monitoring of mass losses during sample preparation, the losses from evaporation are now believed to be significantly less than the 0.05 g per sample initially identified, so the added 0.05 g water is included in further calculations and accounted for during data analysis and G-value estimations. The extra 0.05 g added accounts for ~2.2-3.8% water in the solid samples. The sample water was added based on the mass of weighed as-received powders, and does not account for any water associated with or adsorbed onto the powders as they are. Water content of the as-received magnesium hydroxide and hydromagnesite was quantified by TGA in Section 4.2.1.2 as 2.84% and 3.36% respectively, and was accounted for retrospectively in water content estimations and subsequent calculations.

The powdered solid sample was placed into the sample cylinder via a funnel, then the reducer/valve were sealed on, assembling the “holder.” Due to the relatively small amount of water present in the samples it was initially intended to maximise the amount of sample present to give the best chance of achieving measurable hydrogen yields. During sample preparation it became apparent that the low density of the powders (particularly for hydromagnesite) restricted the amount of sample that can be loaded, especially in combination with the narrow sample cylinder tube bore. For this reason the loadings of 0% and 10% water content hydromagnesite were limited to 1.80 g solid. Once filled, the holder valve was attached, then weighed, and connected to the manifold shown in Figure 6-4 and Figure 6-5, then

evacuated and backfilled with argon three times. Following backfilling the sample holder was sealed, removed and reweighed to observe any mass losses during evacuation. Any difference in mass was then recorded and accounted for in future calculations.

Table 6-1. Sample preparation data for various water content magnesium hydroxide and hydromagnesite

	Nominal Added Water (%)	Nominal Solid Mass (g)	Nominal Water Mass (g)	Actual Water Mass* (g)	Actual Water Content (%)
$Mg(OH)_2$	20%	1.00	0.30	0.328	24.7
	10%	2.25	0.30	0.364	13.9
	0%	2.25	0	0.064	2.8
Hydromagnesite	20%	1.00	0.30	0.334	25.0
	10%	1.80	0.25	0.310	14.7
	0%	1.80	0	0.060	3.3

*Including added mass accounting for evaporative losses and surface water of as-received materials as determined by TGA-mass spectrometry (2.84% magnesium hydroxide, 3.36% hydromagnesite)

For irradiation, the samples were loaded into a rack of 4 horizontal positions and 2 vertical (i.e. top and bottom), then placed in the irradiator chamber as shown in Figure 6-7. The samples would then be irradiated for the desired time to give the target absorbed dose (most commonly for 1 h at the front of the irradiator, with the exception of some which were irradiated for 2 h in the second row from the front). Once the irradiation was complete, the samples were removed and analysed on the GC in accordance with the method described in Section 6.2.2.3.

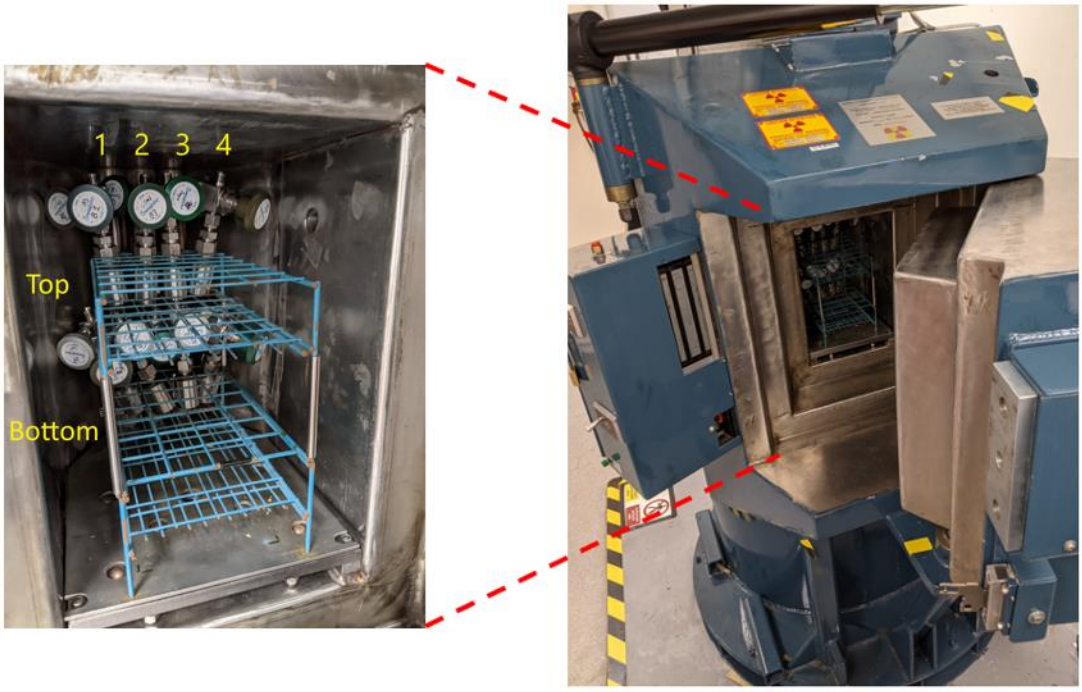

Figure 6-7. Samples loaded into the rack within the γ-irradiator chamber

6.2.2.5 Vacuum drying of samples for γ-irradiation

In addition to the varied water content samples irradiated as mentioned in Section 6.2.2.4, further work was carried out to investigate the impact of vacuum drying temperature on hydrogen yield from radiolysis of water. In order to investigate this, as-received magnesium hydroxide/hydromagnesite powders were prepared, by first weighing in to an open sample cylinder and vacuum drying in an oven at 40 °C, 60 °C, 90 °C, 120 °C or 200 °C for the times listed in Table 6-2. Due to restrictions in time and irradiation availability it was not possible to dry samples for consistent periods, but based on the vacuum drying studies undertaken as part of this thesis it is not believed that these inconsistencies in drying time will be significant as the majority of drying (particularly at temperatures >60 °C) occurs in <1 h. It was necessary to dry the samples within the container rather than in a more desirable large surface area geometry as the amount of time required to load the samples into the holders following drying would be too significant (~10 minutes per sample) and would result in readsorption of water from the atmosphere. Once samples were removed from the drying ovens they were promptly capped and weighed, and any weight loss from drying was recorded for estimation of water loss and new water content. The samples were then evacuated and backfilled with argon three times for irradiation and GC analysis in the same manner described in Section 6.2.2.4.

Table 6-2. Temperatures and times of vacuum dried samples for irradiation

Drying Temperature (°C)	Drying Time (h)
40	56
60	56
90	4.5
120	42
200	42

6.2.2.6 γ-Irradiation dosimetry

As the ^{60}Co half-life is 5.3 years, the dose rate will reduce over the course of the lifetime so it is important to quantify the dose rate for a set of experiments. Additionally the experimental setup can affect the dose that the sample received, for example the steel sample holders will absorb some radiation and shield the samples held within, and the dose rate varies based on location in the chamber. A common method to quantify a dose rate is by observing the products from known radiolytic reactions and inferring the dose rate from the reaction stoichiometry. In this instance the rate of molecular hydrogen generation from γ-radiolysis of water was used, which gives additional benefit as the study intends to focus on this reaction.

As covered in Section 2.5.5, exposing water to γ-radiation yields a wide variety of products such as H^+ ions, H· and ·OH radicals, hydrated electrons (e^-_{aq}) and molecular hydrogen (H_2). The chemical yield of molecular hydrogen has been quantified with a G-value of 0.45 molecules/100 eV at γ-energies of 0.1-20 MeV.[122] Using this known rate, a known volume of water reagent and measurable quantity of molecular hydrogen product, the dose rate can be inferred. Additionally, Spinks and Woods describe that the presence of Br^- or I^- in water can protect molecular hydrogen formed during irradiation. From extended irradiation times, H_2 products can be consumed by water radiation products, particularly ·OH. Halide anions (X^-) are unreactive towards aqueous electrons and hydrogen radicals, but Br^- in millimolar concentrations can undergo rapid electron transfer reactions with ·OH as shown in Equation 6-3:[123]

$$\cdot OH + Br^- \rightarrow BrOH^{\cdot -} \qquad \text{Equation 6-3}$$

From this, the presence of the Br^- can act as an effective scavenger for ·OH and prevent consumption of molecular hydrogen during irradiation, and the Br^- is then reformed through reaction with e^-_{aq} and H·, so can effectively protect the molecular

H_2 indefinitely without being consumed itself.[123] As such the inclusion of protective concentrations of bromide (in this case 10 mol/m^3 KBr) allows the measured G(H_2) to equate to the molecular product yield of 0.45 molecules/100 eV.[122]

On this basis, the method for establishing the dose rate for the samples was devised. A 10 mol/m^3 KBr solution was deaerated by bubbling argon for ≥15 mins, and then added to pre-weighed sample holders in 2 g aliquots. The sample holders were then sealed and inerted with argon gas and irradiated for 60 min in the allocated irradiator top/bottom level, front/2nd row and left/right (1-4) position in accordance with the method described in Section 6.2.2.4. Following the irradiation the samples were removed and analysed by GC using the method in Section 6.2.2.3.

6.2.2.7 Methodology for calculation of dose rate, hydrogen yield and G-value

Once the hydrogen yield in moles was established, the dose rate can be evaluated. From a known volume of water, at a known G(H_2) of 0.45 molecules/100 eV (equivalent to 0.047 µmol/J), irradiated for a known time the absorbed energy (in J) can be calculated. By dividing the hydrogen yield by the G-value, the total energy (in J or eV) absorbed by the 2 g sample is known. Then, given that 1 Gray = 1 J/kg, the total dose in Gy is measurable, and by dividing this by the irradiation time the dose rate is calculated. By performing this for each individual position in the irradiator chamber, it is possible to create a matrix of dose rates and positions, because as mentioned previously the dose rate is not constant across the irradiator so it is necessary to analyse each position individually.

Collation of data from irradiation of 1 mmol KBr solution provided the basis for the dose rates displayed in Table 6-3 which lists the average dose rate, and Figure 6-8, which states the experimental range over two individual tests in each position; top/bottom level, position 1-4 (left to right) and the first or second row from the front. Over the course of the investigation it became apparent that occasionally leaks or valve failures would cause some of the H_2 sample volume/pressure to be lost. In these instances the GC pressure would be measurably lower than expected, and the GC signal would appear smaller than for comparable tests. Given the linear response to hydrogen signal and hydrogen partial pressure with varied sample quantity (as shown in the calibration line in Figure 6-6) it is possible to correct the measured signal for samples known to have leaked. As the samples were produced in batches of 3-4 of equivalent starting pressure, the expected pressure can be established from the other samples from the same batch, so the signal can be corrected in accordance with the ratio of the sample batch average GC pressures to the leaked sample pressure. Multiplying the peak area by this ratio then corrects the signal (and therefore calculated hydrogen volume) rather than accepting the lower

value or rejecting as anomalous. Samples that have been corrected by this means are denoted as such in Table 6-3. The data in Table 6-3 and Figure 6-8 show the central positions on the first row generate the greatest sample dose rates due to the closest proximity to the source rods. This effect is still noticeable but less pronounced in the second row. The average dose rates listed in Table 6-3 are those primarily used for any dose estimates during this investigation.

Table 6-3. Dose rate by position in irradiator chamber

		Dose Rate (Gy/min) at position			
		1	**2**	**3**	**4**
Row 1 Top	High	163	227	218	173
	Low	149	216	216	162
	Ave	**156**	**222**	**217**	**167**
Row 1 Bottom	High	167	272	255	164
	Low	150	255	246	162*
	Ave	**159**	**264**	**250**	**163**
Row 2 Top	High	104	142	119	110
	Low	99	128	115	99
	Ave	**101**	**135**	**117**	**105**
Row 2 Bottom	High	97	126*	120*	109*
	Low	84	113	111	91
	Ave	**90.4**	**120**	**115**	**99.8**

*Some sample loss experienced during measurement of one entry, so hydrogen signal corrected based on pressure ratio

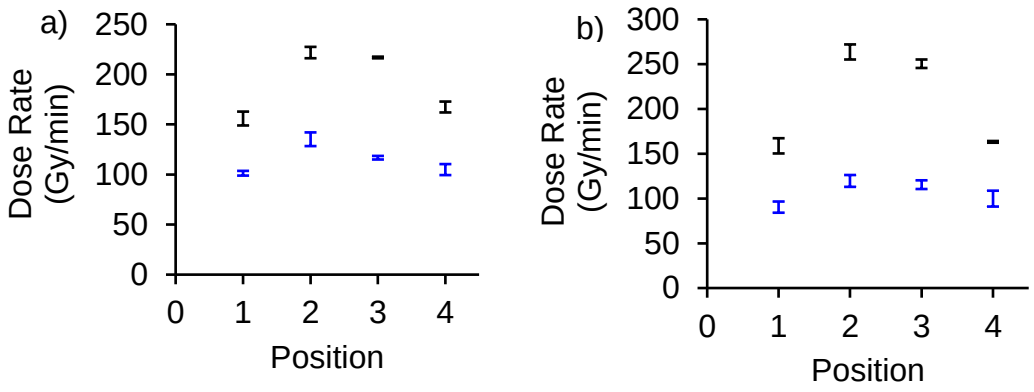

Figure 6-8. Range of measured dose rates at given position in irradiator chamber for row 1 (black, higher dose rate) and row 2 (blue, lower dose rate); a) top level, b) bottom level

With the dose rates established for each position, it is now possible to perform quantitative analysis on irradiated magnesium hydroxide and hydromagnesite samples. After a sample is irradiated by the method in Section 6.2.2.4 the hydrogen peak can be used to measure the quantity of hydrogen yielded. Given that the hydrogen is presumed to be solely from the radiolysis of the water component, it is important that the amount of water is quantified, which was assessed using TGA-MS by the method in Section 3.2.4. From an assumed starting quantity of water in the as-received material, the amount of water present in the sample material can then be assessed by observing mass change during sample preparation (either as an increase from added water, or a decrease from vacuum drying) to derive the sample water content during irradiation, as displayed in Equation 6-4. It is then possible to calculate the energy from γ-radiation absorbed by multiplying the dose rate by the time, and dividing by the sample mass. This mass is conventionally considered as only the mass of water and negates the mass of the solid, but here additional calculations which include the solid mass as the sample mass are also performed for comparison. This is due to some uncertainty surrounding some assumptions that are made when calculating the G-value for estimated small quantities of water, which can potentially have relatively significant impacts on the magnitude of the G-value and will be discussed further in Section 6.2.3.5. As this investigation refers the G-value in units of molecules/100 eV, the energy must be converted from joules to electron-volts. Once the energy is established, dividing the amount of hydrogen detected (in molecules) by the energy absorbed (in 100 eV) yields the G-value (Equation 6-5).

$$E\ (J) = \frac{dose\ rate\ (Gy/min) \times time(min)}{mass\ (kg)}$$ Equation 6-4

$$G(H_2) = \frac{H_2\ qty\ (molecules)}{E\ (100\ eV)}$$ Equation 6-5

6.2.3 Error and uncertainty associated with γ-irradiation, GC methodology and hydrogen yield analysis

6.2.3.1 Dose rate

The data in Figure 6-8 show the range of dose rates calculated over two tests in each individual position. The ranges at each position vary by the values specified, and two standard deviations from the averages is 4.6%. On this basis, dose rates are based on the average for each position +/- 4.6%, which is carried forward to assess the uncertainty in subsequent calculations.

Table 6-4. +/- Range variation % from 2-point average at each position

		1	2	3	4
Top	Row 1	4.4%	2.6%	0.4%	3.2%
	Row 2	2.3%	5.1%	1.5%	5.2%
Bottom	Row 1	6.0%	3.4%	2.0%	0.6%
	Row 2	6.9%	5.5%	4.2%	8.9%

2 standard deviations of variation: 4.6%

6.2.3.2 Sample preparation

During the sample preparation method described in Section 6.2.2.4, one avenue for uncertainty came from sample loss during the evacuation and degassing stage. It was observed that the evacuation had a tendency to sometimes remove some of the solid powder – particularly with the lighter hydromagnesite. This mass loss was accounted for by weighing before and after evacuation/argon filling. Losses were generally negligible but at times significant in the range of 0.12-0.19 g (primarily for hydromagnesite samples). In each case the mass is known and accounted for in G-value calculations so it is not expected that this will affect any findings.

6.2.3.3 Gas chromatography volume

As demonstrated by calibration line in Figure 6-6, good consistency between results was achievable, however it was desirable to achieve peak areas >1.0 (arbitrary

units) to gain confidence in peak identification and integration. With this in mind, irradiation times were planned to maximise hydrogen yield whilst also permitting manageable experiment time and data output. Interpretation of smaller peak areas down to ~0.5 units were occasionally necessary, especially for samples with very low water content (i.e. vacuum dried tests).

Some uncertainty with respect to calculation of hydrogen quantity is introduced by the volume uncertainty in manufacturing of the sample cylinders. The GC volume is constant and unchanged, but the sample cylinders come with internal volume uncertainty of ±10% (equivalent to ±1 cm^3). The combined volume of sample cylinder, valves and GC internals comes to 23.4 cm^3, which means the 1 cm^3 uncertainty is equivalent to 4.3% volume uncertainty. This is combined with the 4.6% dose rate uncertainty from Section 6.2.3.1 to give γ-irradiation uncertainty of ±8.9%.

6.2.3.4 GC peak area correction from pressure ratio

As discussed in Section 6.2.2.7 it was necessary to apply a pressure correction for certain test samples based on sample gas loss, which was evident from the lower GC pressure during analysis. As the GC response to sample is linear with increasing concentration it is reasonable to apply this correction with corroboration from equivalent samples of which confidence is assured. To demonstrate this correction, one instance will be illustrated. Two samples of the same composition (1 mmol dm^{-3} KBr in deionised water) in the same location were irradiated (bottom level, row 1, position 4) for 60 mins. The sealed sample registered a peak area of 10.4 units with a GC pressure of 0.551 bar. The leaked sample registered a peak area of 7.62 at a GC pressure of 0.402 bar. As it was known the leaked sample was filled to a pressure of 1.26 bar along with three other samples that were irradiated simultaneously, the post irradiation pressures of the other three samples can be compared to identify what quantity of the sample gas has been lost. The average of the three samples post-irradiation was 0.542 bar, so dividing this pressure by the leaked pressure of 0.402 bar provides a ratio of 1.35. Multiplying the original peak area of 7.62 by 1.35 gives a corrected peak area of 10.3 – very close to the peak area of the sealed sample of 10.4. This correction is applied to a number of samples where leaks were present (typically for samples of pressure <0.5 bar) and preserved “sister” samples irradiated in equivalent conditions were available for comparison.

6.2.3.5 Water estimation/G-value uncertainty

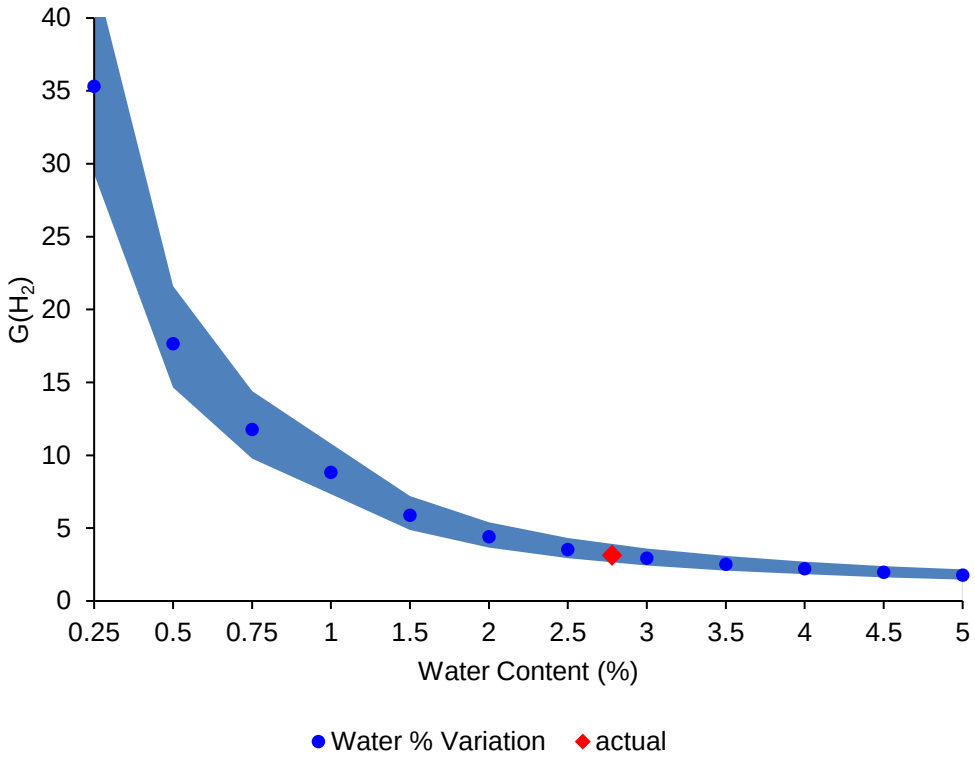

Figure 6-9. G-value sensitivity to water content – the red value is equivalent to an average of real data measured at 2.8% water content, and the blue shaded area denotes the experimental variation. The blue circles show the same data plotted at varied theoretical water contents to illustrate relative impact on water content assumptions – n.b. not real data

When establishing G-values for materials containing small quantities of water, any variation in water content can have significant effects on the output. Figure 6-9 shows the high degree of sensitivity with respect to assigning water quantities. The data is taken from four separate magnesium hydroxide irradiations (two at Row 1 and two at Row 2). The average is plotted by the blue points, with the experimental range denoted by the shaded area. The actual water content was analysed to be 2.84%, so the graph below simply shows how the resultant G-value can vary based on different estimations of water content, and not a real trend of G-value against water content. As can be expected, reducing the quantity of water increases the respective G-value based on the same quantity of hydrogen generation. The important note here is that as the assignment of water content reduces, the relative G-value increases dramatically - particularly below 1%. The effect is not hugely significant for the varied water content samples which used as-received solids, or samples with additional water, but where the water content estimation becomes more difficult this effect starts to be more significant – as in the case of the vacuum dried samples. Estimation of $G(H_2)$ for the vacuum dried samples starts to become more uncertain firstly as just discussed because of the sensitivity to small

differences in <1% water content, but additionally because the quantity of hydrogen produced is very low, it is close to the limit of detection for the setup. For most samples the hydrogen peak was visible, but with an area <1.0 where integration becomes more uncertain. Sensitivity restrictions can be improved by introducing larger sample mass quantities or by performing longer irradiations to generate larger hydrogen volumes. Neither of these options were viable during this investigation due to time limitations but could be considered for future work.

6.2.4 He^{2+} Ion beam irradiations

In addition to the γ-radiolysis of magnesium hydroxide and hydromagnesite, α-irradiation of magnesium hydroxide was undertaken. As will be discussed, these experiments were more restrictive with regard to sample preparation time and challenges, irradiation capacity limited to one sample per experiment (c.f. 8 simultaneously for γ-irradiation) and analytical complexity.

6.2.4.1 He^{2+} ion beam

The He^{2+} ions are produced by the Toroidal Volume Ion Source (TORVIS) which is coupled to a 5 MV NEC 15SDH-4 pelletron tandem accelerator, and can produce up to 100μA H^+ at 10 MeV or up to 15 μA He^{2+} ions at 15 MeV with a choice of six beam lines (illustration in Figure 6-10).[118] The beam line typically used for radiation chemistry (and enlisted in this investigation) is operated at lower currents in the 1-10 nA range. The beam targeting assembly comprises of a circular beam collimator which produces a beam area of 0.38 cm^2. The beamline is maintained at an internal high vacuum of better than 10^{-6} Torr, sealed by an 8 μm thick titanium foil window to minimise ion energy losses. The beam current corresponds to charged particles deposited into a given sample and can be detected at the beam exit window and/or sample cell.[118,124]

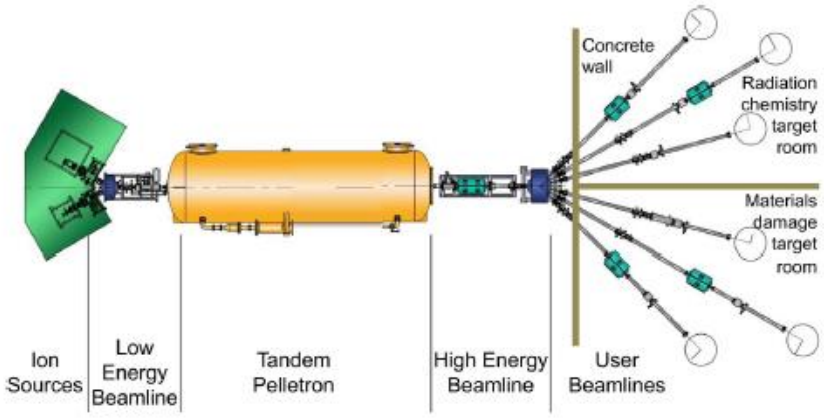

Figure 6-10. Overview of pelletron (taken from Leay et al.[118])

He^{2+} ions are produced by first feeding helium gas into the Toroidal Volume Ion Source (TORVIS), within which a current is produced from a hot filament that ionises He to He^{+}. The He^{+} ions are then passed through vaporised rubidium to charge exchange He^{+} to He^{-}, suitable for accelerating into the tandem accelerator. An Ar gas stripper is used in the central high voltage terminal to convert the He^{-} ions to He^{2+}, which then undergo a second stage of acceleration from the central terminal to the high energy beamline on the exit of the accelerator. Due to the complete stripping of the He ions to a 2+ charge state, the ions get double the acceleration in this second stage to reach an energy 3 times the terminal voltage. To generate 10 MeV He^{2+} ions therefore requires the central terminal to be run at a voltage of 3.36 MV. Instrument settings can be tuned to control the beam energy and ion quantity (i.e. current).[125]

As the sample is irradiated, it accumulates positive charge which is then balanced by transfer of electronic charge via either the ion beam window and/or sample apparatus. By electrically isolating both of these, with only one earth point available via an ammeter, the recharge current can be quantified to infer a precise irradiation ion flow current. The energy transferred to the sample can be calculated by knowing the current produced by the flow of charged ions and the charge of each ion (i.e. for He^{2+} charge is equal to +2 elementary charges, e of 1.6×10^{-19} C each) so one amp is equal to one coulomb per second. Since the ion beam current can be measured, the number of ions imparted per second is calculated by the current divided by the ion charge, 3.2×10^{-19} C (Equation 6-6). Once the irradiation rate is established, the number of ions can be multiplied by the ion energy to estimate the quantity of irradiation energy the sample has received.

$$Irrad.Rate\ (ions/sec) = \frac{Current\ (Amps)}{Charge\ (Coulombs)} \qquad \text{Equation 6-6}$$

6.2.4.2 Calculation of ion energies and losses

As radiation travels through matter, it will interact and transfer energy via the processes described in Section 2.5.3 resulting in energy loss with penetration. The software package and textbook “SRIM – The Stopping and Range of Ions in Matter” and additional program “TRIM – Transport of Ions in Matter” by Ziegler, Ziegler and Biersack allow accurate calculation of these energy losses through various media, enabling custom setup simulations.[126] From the setup employed it has been estimated that an 8.25 MeV incident He^{2+} ion will experience 4.29 MeV energy losses as it passes through the ion beam 8 µm Ti foil window, 17 mm air gap and 10 µm Al foil sample window, reaching the sample with an energy of 3.96 MeV. Initially the ion beam had been intended to irradiate with He^{2+} ions at 5.5 MeV (equivalent to that of spent nuclear fuel, as calculated by activity data derived from

FISPIN 10 provided by NNL[116]), but some energy losses from the air gap between sample and ion beam resulted in a lower final ion energy of 3.96 MeV.

During irradiation of a mixture of compounds, assessing how the energy is absorbed by the various media has an added level of complication, as each component will affect the incoming radiation differently. In this instance, the two components are solid magnesium hydroxide and adsorbed water (as illustrated in Figure 6-11), for which the stopping powers as calculated by SRIM are shown in Figure 6-12, and calculated to penetrate 13.7-15.3 µm (shown in Table 6-5 and Figure 6-12). Material stopping power is primarily determined by the interactions between electrons in the material and the incoming radiation, with a much smaller contribution from interactions with the material nuclei. Expectedly the magnesium hydroxide has greater stopping power than water, at a ratio of 1.9:1 respectively, meaning an equivalent volume of magnesium hydroxide will absorb alpha radiation to almost double the extent. The energy absorbed by the sample compositions used in this investigation are all based on this assumption and scaled proportionally to the relative water content. From this it is possible to estimate the energy absorbed by each water and solid sample component and infer a $G(H_2)$ value for the system. From particle size distribution described in Section 4.2.3.1 it was considered that 3.96 MeV alpha particle penetration may not pass through both sides of larger (>13.7 µm) particles, but it is clear from the SEM images that the solid particles are smaller when not agglomerated as in solution. Some particles are larger than 13.7 µm in diameter but the significant majority seen by SEM were on the order of only a few microns.

Table 6-5. Penetration depth of 3.96 MeV alpha He^{2+} in magnesium hydroxide/water systems (as calculated in SRIM)

Magnesium hydroxide water content	Penetration (µm)
0%	13.7
2.8%	13.9
22.8%	15.3

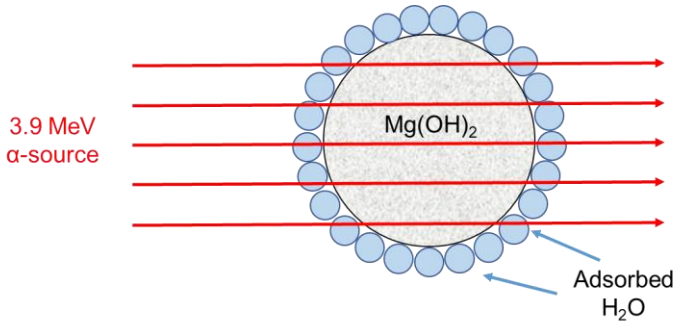

Figure 6-11. Illustration of alpha particle interaction with magnesium hydroxide/adsorbed water (not to scale)

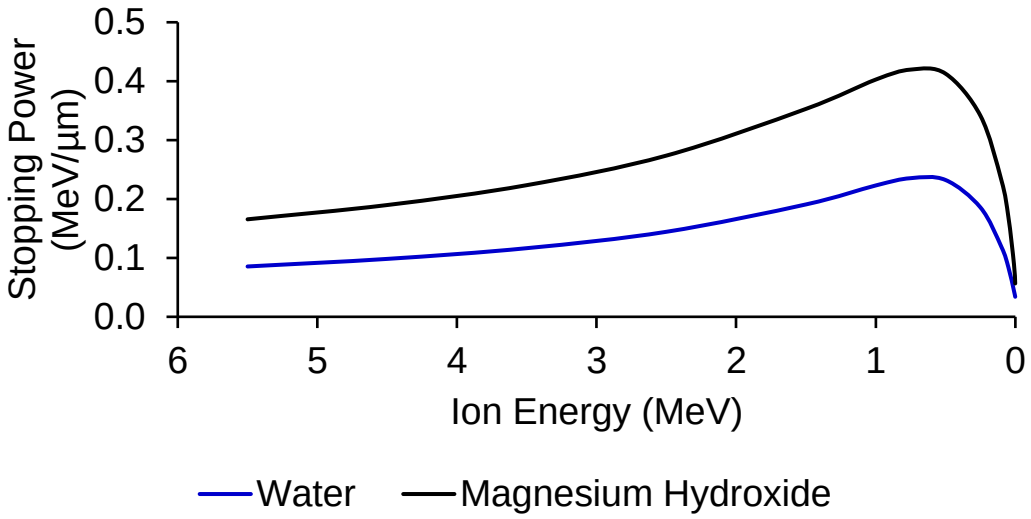

Figure 6-12. Stopping power of He^{2+} in magnesium hydroxide and water

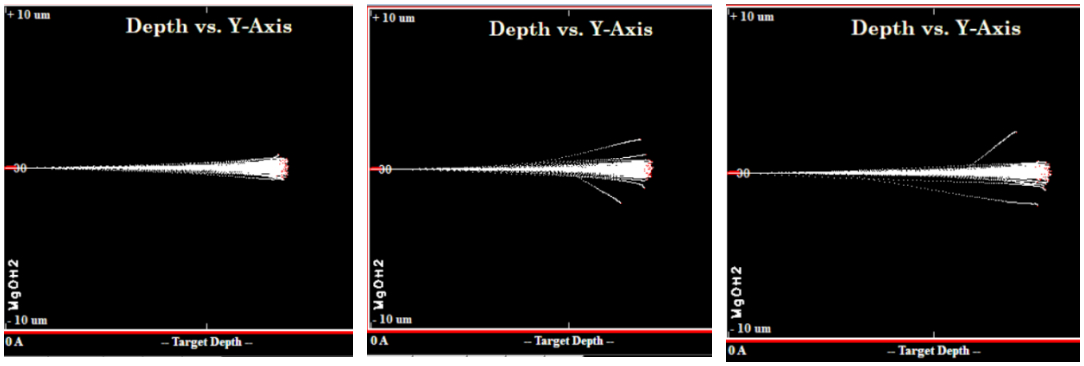

a) b) c)

Figure 6-13. TRIM ion calculation outputs a) 3.96 MeV He^{2+} in pure magnesium hydroxide, b) 3.96 MeV He^{2+} in 2.8% water/magnesium hydroxide, c) 22.8% water/magnesium hydroxide

6.2.4.3 He^{2+} ion beam sample preparation and method

The primary challenge with this experimental preparation and method is the requirement for a gas-tight sample chamber to permit hydrogen collection and detection, whilst also being transparent to incoming alpha radiation, which rules out many conventional sample holders and materials. In this instance a LewVac flange ended needle valve fitting was identified, with a thin (10 µm) aluminium sample window to seal the sample and any evolved gas (shown in Figure 6-14).

Ion beam irradiations were performed on 0.225 g magnesium hydroxide samples as-received and with 20% added water, and also on 0.65 g samples of 1 mmol/L KBr solution. Sample masses were based on the optimum quantity that could fit within the valve flange and gasket to prevent sample resting due to gravity whilst also reducing force on the aluminium window from overfilling. For all experiments this sample volume is a significant excess based on ion penetration predictions

from SRIM and TRIM, and was primarily determined by the practicalities of sample loading and handling. Preparation involved weighing the required solid (with addition of 20% water where desired), or pipetting 1 mM KBr solution and loading onto the valve end within a gasket in a horizontal orientation. Then a piece of aluminium foil was laid on the sample, and a steel ring fitting was placed onto the aluminium. Six bolts were then tightened through the steel ring and flange to seal the sample within. It was necessary to contain the sample in an inert atmosphere to avoid unwanted air reactions during irradiation, and due to the fragile nature of the aluminium foil this could not be performed by evacuation and argon backfilling. Instead, the fitting valve was opened and carefully ported into a nitrogen atmosphere glovebox, such that the sample internal and external pressure were equal and no significant pressure difference would be experienced which could rupture the foil. Once within the glovebox the fitting valve was sealed, providing the sample with an inert nitrogen atmosphere free of oxygen, which was demonstrably consistent through absence of oxygen signal in GC analysis. Once the sample was inerted it was removed from the glovebox and ready for irradiation.

a) b) c)

Figure 6-14. LewVac flanged valve fitting; a) with sample solid loaded onto foil/gasket, b) with foil seal in place on fitting, c) valve and flange in profile

6.2.4.4 Irradiation setup and method

In addition to the challenges mentioned previously with regard to preserving window integrity during preparation, this was equally relevant during irradiation and sampling. The hydrogen that accumulates in the sample valve must be accessible without rupturing the sample window, so could not be evacuated or exposed to significant pressure differences. The method that was employed is described here, with an overview of the setup in Figure 6-15.

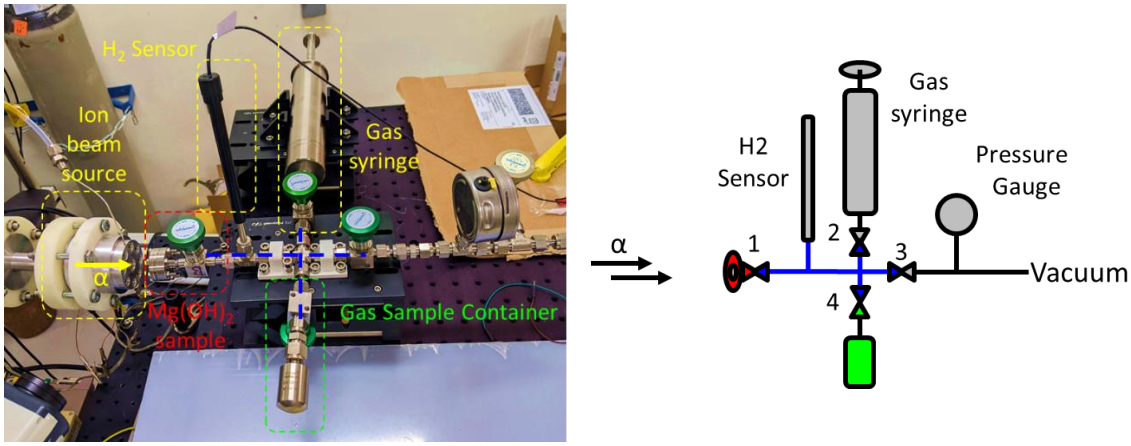

a) b)

Figure 6-15. a) photo and b) illustration of ion beam experimental setup

The sample window was placed directly in line with the end of the ion beam, with a small (17 mm) air gap that enabled sample loading and unloading but still permitted consistent placement for all tests. The setup consisted of a Unisense hydrogen sensor, a nitrogen filled gas syringe and an evacuated 10 cm^3 steel sample cylinder (the same as employed during gamma irradiation experiments). The setup was also connected to a vacuum pump and pressure gauge. Initially the hydrogen sensor had been intended to be used to quantitatively measure the hydrogen evolved during the irradiation, but the calibration procedure proved to be too time consuming. Also the sensor response was inconsistent and appeared to be affected by the ion beam irradiation. The sensor did seem to produce signals that were aligned to hydrogen generation, so the method has potential for future applications but in this instance was not used as such. Example data is shown in Appendix Figure 6-23.

During irradiation the ion beam was set to a provide a nominal current of 6-8 nA. Increasing the current (and therefore dose rate) could give rise to intertrack reactions and dose rate effects, which may interfere with the chemical processes and results, for example increasing ion flux can change reaction paths and potentially reduce H_2 yield. Additionally reducing the current helps to control the sample temperature and minimise unwanted heating. Irradiation time was predominantly determined by the need to generate sufficient hydrogen that could be detected by the GC during analysis, which was identified as 2 hours on as-received (i.e. no added water) magnesium hydroxide. Prior to irradiation, valves 1+2 (as denoted in Figure 6-15) were closed with valves 3+4 open, so the sample cylinder could be evacuated. Then 3+4 were closed and 2 was opened to repressurise the system with nitrogen from the gas syringe. Then 2 was closed and 1 was opened, which would allow the flow of any hydrogen from the sample to fill the available

system. This is the state at which the setup would remain during the irradiation, and hydrogen generated in the red sample section can collect in the red and blue sections whilst not exposing the aluminium window to any pressure differences and risk perforation or failure.

Following irradiation, Valve 1 was closed and 4 was opened, so a proportion of the gas volume could be collected inside the sample cylinder, which was then sealed and removed for GC analysis as described in Section 6.2.2.3, however due to the low sample volume and pressure, GC samples from these experiments were in the lower range of 149-165 mbar (approx. 3.5 times less than most γ-irradiations). By comparing the volume ratios of the red (sample window-Valve 1), blue (between Valves 1-4) and green (Valve 4-sample cylinder) in Figure 6-15b, the measured volume of hydrogen can be scaled to derive the total system volume of hydrogen.

6.2.4.5 Error and uncertainty in alpha irradiation

The alpha irradiation experiments have significant overlap with regard to uncertainty as the gamma irradiation experiments discussed in Section 6.2.3, with many analytical and preparative aspects being the same such as GC analysis of H_2 and estimation of water content in as-received samples.

The method proved to produce measurable hydrogen, but due to the dilution during gas sampling and low sample pressure it was necessary to irradiate for at least two hours to generate enough hydrogen for a GC response in samples without additional water. As mentioned previously it was desirable for peak areas >1.0 a.u., but this was not always possible. As a result the range of irradiation parameters (e.g. water content and irradiation time) and number of individual experiments were repeated several times but were overall restricted in terms of quantity of useable experimental data.

Section 6.2.4.2 discussed the necessity to assess the different sample component ion energy absorption, as establishing a $G(H_2)$ for water irradiation demands the water energy absorption to be known. The method for estimating this is described above, but similarly to the gamma irradiation, variation in energy absorbed or total water mass would affect the resultant G-value.

As covered in Section 6.2.4.1, measuring the beam current enables inference of the ion irradiation rate and therefore the energy transferred to the sample. Current is typically measured at the ion beam exit window and also at the sample. Detection of recharge current at the sample ammeter was inconsistent and on most occasions the sample current measurements did not register, so in most instances it was necessary to only use current measured at the ion beam exit window to infer ion irradiation rate.

6.3 Results and Discussion

6.3.1 ^{60}Co γ-Irradiation of magnesium hydroxide and hydromagnesite

6.3.1.1 γ-Irradiation of magnesium hydroxide and hydromagnesite results

Results from γ-irradiation of magnesium hydroxide and hydromagnesite are presented in Figure 6-16. The majority of irradiations were undertaken in the first irradiator row for one hour, with some irradiations undertaken in the second row for two hours (data irradiation conditions and results summarised in Table 6-12 and Table 6-13 in the Appendix). Data points are calculated by the average of each dose rate range, i.e. 1-2 hours/9-16 kGy at row 1-2 of the irradiator under argon, and 17 hours/160-270 kGy at row 1 of the irradiator under argon or air. The dose between samples varies based on the range of doses in each position from left to right and bottom or top deck of the irradiator (as covered in Section 6.2.2.7). The error bars denote the experimental range of the data collected, +/- 8.9% uncertainty from dose rate and sample cylinder volume (from Section 6.2.3).
The data in Figure 6-16a shows G-values established by considering only energy absorbed by water, at water contents of nominally 0%, 10% and 20% added water (actual 2.8%, 13.9% and 24.7% water for magnesium hydroxide, and 3.4%, 14.7% and 24.9% water for hydromagnesite). As described in Section 6.2.2.7 this dose is estimated by multiplying the dose rate (J kg^{-1} min^{-1}) as described in Figure 6-8 by estimated water mass (kg) and time (min) to calculate the total dose.

Irradiations of 0% added water magnesium hydroxide/hydromagnesite were undertaken in argon in air for 1-2 h and in air/argon for 17 h. Results measured average G(H_2) of 2.2 (162 kGy/air), 3.5 (13.9-15.0 kGy/argon) and 3.7 (269 kGy/argon) for magnesium hydroxide, and 1.2 (255 kGy/argon), 3.4 (13.3-15.8 kGy/argon) and 2.9 (166 kGy/air) for hydromagnesite.

The average G(H_2) at 10% added water for magnesium hydroxide was measured at 1.0 (13.0-16.2 kGy) and 1.21 (159 kGy), and for hydromagnesite at 0.82 (13.3-16.2 kGy) and 1.2 (171 kGy). The average G(H_2) at 20% added water for magnesium hydroxide were calculated at 0.83 (9.8-12.0 kGy) and 0.92 (226 kGy), and for hydromagnesite of 0.81 (9.4-12.2 kGy) and 1.0 (221 kGy).

The data in Figure 6-16b shows G-values from energy absorbed by both water and solid, as calculated by multiplying the dose rate (J kg^{-1} min^{-1} from Figure 6-8) by total sample mass (kg) and time (min). The average G(H_2) at 0%, 10% and 20% added water for magnesium hydroxide at 9-16 kGy dose was measured at 0.099, 0.15 and 0.22, and for hydromagnesite at 0.11, 0.13 and 0.21 respectively. Irradiations undertaken for 17 hours in argon (150-270 kGy) on 0%, 10% and 20%

added water magnesium hydroxide had a $G(H_2)$ of 0.11 0.17 and 0.21, and for hydromagnesite of 0.040, 0.19 and 0.31 respectively. 17 h irradiations of 0% added water magnesium hydroxide/hydromagnesite undertaken in air which produced average $G(H_2)$ of 0.062/0.10 respectively. It should be noted that these G-values and whole sample irradiations assume that the solid absorbs energy to the same extent as water. In reality this is likely to underestimate energy absorbed by the solid component due to higher atomic number and density than water. The error bars denote the experimental range, with an additional 8.9% dose rate and GC volume uncertainty (as described in Section 6.2.3.3).

6.3.1.2 γ-Irradiation of magnesium hydroxide and hydromagnesite discussion

The data in Figure 6-16a (energy absorbed by only water) suggest that $G(H_2)$ does show some variance with respect to the water content of the material, primarily at the lowest water contents tested (when considering energy absorbed by water component). Any differences between 10% and 20% added water are modest, and cannot be confidently assigned based on this dataset. The G-value at 0% added (actual 2.8% magnesium hydroxide, 3.4% hydromagnesite) water was higher for both magnesium hydroxide and hydromagnesite than at 10% added (actual 13.9% magnesium hydroxide, 14.7% hydromagnesite) and 20% added (actual 24.7% magnesium hydroxide, 24.9% hydromagnesite) water. Under all conditions the $G(H_2)$ was measured to be higher than the literature value of 0.45 molecules/100 eV.[69] This suggests that some energy transfer may be occurring and raising the apparent $G(H_2)$ on the magnesium hydroxide and hydromagnesite surface water, which is most evident at the lowest water content samples. Since the G-values measured here are greater than those measured for MgO,[12] which may be due to the close band gap matching and greater potential for resonant coupling between $Mg(OH)_2$ and water. $Mg(OH)_2$ has a reported band gap of 5.17-5.70 eV[80,81] and H-OH dissociation energy of 5.1 eV.[78] This fits within the 4.5-6 eV window of optimal band for greatest H_2 yield observed across the range of metal oxides investigated by Petrik et al.[12] Hydromagnesite has a band gap of 4.42 eV[127] so is on the lower end of this range. An additional factor that can improve hydrogen yield is reduced dose rate, as excess energy can go on to cause exciton side reactions and reduce availability for energy transfer to adsorbed water.[85]

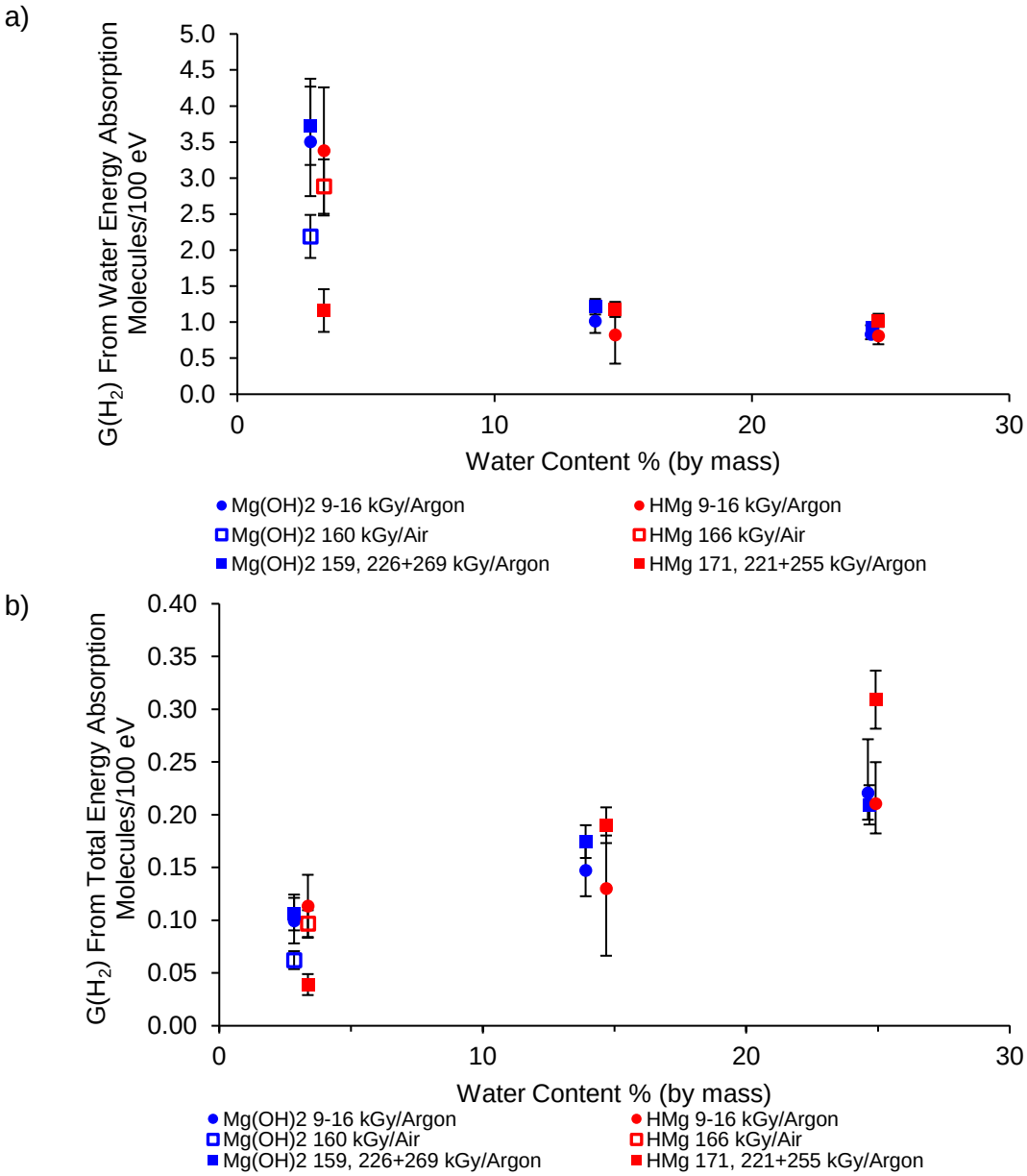

Figure 6-16. $G(H_2)$ from γ-irradiation of magnesium hydroxide and hydromagnesite (HMg) of varied water content; a) considering only energy absorbed by water, b) considering total energy absorbed by water and solid

When considering energy absorbed by the whole sample as in Figure 6-16b, decreasing water content decreases the overall amount of hydrogen produced, despite the relatively higher $G(H_2)$ observed when considering only energy absorbed by the water component. It is interesting that the surface water experiences an enhanced rate of hydrogen generation c.f. bulk water (as seen in Figure 6-16a). It is important to acknowledge that in the context of the whole system the elevated rates are only applicable to very small volumes of surface water and are not necessarily representative of gross effects. Therefore there is still demonstrable benefit to reducing water content of these materials to reduce hydrogen yield, even when considering the increased water $G(H_2)$ observed.

It is possible to estimate the number of monolayers of water adsorbed to a surface based on some fundamental water characteristics. On the basis that H_2O has a molecular mass of 18 g/mole, liquid density of 1.0 g/cm^3 and a mole is 6.02 x 10^{23} molecules, it can be calculated that 1 g of water consists of 3.35 x 10^{22} water molecules. Then given that 1 g water occupies 1 cm^3 in volume, then one water molecule has a volume of 2.99 x 10^{-29} m^3. If this molecular volume is treated as a cube, then the average molecular diameter can be estimated to be 3.1 x 10^{-10} m (3.1 Å). This is close to other literature values of 2.8 Å[128] (but close packing in bulk at this diameter this radius would be unrealistic). If it is assumed that water molecules pack as a perfect monolayer at 3.1 Å apart, the amount of molecules equates to 1.04 x 10^{19} per m^2, which is close the value quoted by Petrik et al. (~1.0 x 10^{-19} per m^2) – equivalent to 3.1 x 10^{-4} g/m^2. From this approximation the amount of adsorbed water onto the sample solids can be estimated. It is accepted that this approach is a generalisation, which makes assumptions such as close packing of water, on a flat solid surface which neglects to consider surface roughness, cracks or other features.

The Specific Surface Area (SSA) was measured by BET in Section 4.2.3.2 as 13.907 m^2/g for magnesium hydroxide, and 22.542 m^2/g for hydromagnesite. Based on calculated water content from TGA and addition of liquid water, the surface water coverage has been estimated in monolayers and is listed in Table 6-6. The SSA is shown to decrease with increasing water content as the SSA is described per gram of total sample (including water), so naturally when the water content increases per gram of samples, the available surface of solid decreases per gram accordingly. Water layer thickness assumes all water is on the material surface and not absorbed within (consistent with low porosity volume from BET analysis), and that each monolayer is closely packed and one molecule thick, so is calculated by multiplying the water layers number by 3.1 Å. This shows that even at the higher water content employed here, the average coverage is <25 nm.

Table 6-6. Layers of adsorbed water at various water content of magnesium hydroxide and hydromagnesite

	% water	SSA (m^2/g sample)	No. H_2O layers	Water layer thickness (nm)
$Mg(OH)_2$	2.84	13.51	6.8	2.1
	13.9	11.97	37.4	11.6
	24.7	10.47	76.0	23.6
Hydromagnesite	3.36	21.79	5.0	1.5
	14.7	19.23	24.6	7.6
	24.9	16.93	47.4	14.7

The data shown comparing energy absorbed by only water and both water and solid have provided interesting comparisons with respect to the overall effect and

hydrogen yield. The following discussion will now refer specifically to the energy absorbed by water only, as the relationship is equivalent (excluding the lowest water content samples) but on a different scale. For irradiations of magnesium hydroxide in argon at 0-20% added water, higher dose irradiations of >150 kGy produced higher $G(H_2)$ than those at lower doses of 9-16 kGy. The same is true for hydromagnesite except for that measured at 0% added water at 255 kGy. Inspection of this data shows that both samples experienced a degree of compromise to the gas-tight seal during analysis or irradiation, evident from the low GC pressure and molecular nitrogen/oxygen GC peak. As mentioned in Section 6.2.3.4 this can usually be corrected to some extent, but this requires intact “sister” samples of equivalent preparation conditions.

Irradiations were primarily carried out under argon as an inert atmosphere to reduce potential hydrogen consumption by additional radiolytic processes, particularly with gaseous oxygen, but some 160-170 kGy irradiations in air without added water were undertaken for comparison. For magnesium hydroxide the 269 kGy argon irradiations gave higher $G(H_2)$ of 3.7 c.f. 2.2 at 162 kGy irradiation in air. For hydromagnesite the opposite trend was observed where a higher $G(H_2)$ of 2.9 was observed for 166 kGy irradiation in air, whereas 255 kGy irradiation in argon gave a $G(H_2)$ of 1.2, but as previously described the argon sample appears to have sustained a leak. From this limited dataset the effect of irradiation in air/argon is inconclusive and would need further work to establish. Additionally in the context of this work it would be valuable to gather data in other potential dry storage gases, specifically carbon dioxide or helium.

No significant differences in $G(H_2)$ were observed between magnesium hydroxide and hydromagnesite. This suggests the water within the hydromagnesite chemical structure, may not be radiolytically released (at least at doses employed here) and does not contribute to the hydrogen generation. As mentioned by Laverne,[16] $G(H_2)$ from γ-irradiation decomposition of $Mg(OH)_2$ without adsorbed water was 0.051 molecules/100 eV, approximately an order of magnitude less than the bulk value so will be hard to identify and differentiate from that produced by adsorbed water.

6.3.1.3 Characterisation of irradiated materials

In order to further investigate potential radiolytic decomposition of the samples, thermogravimetric analysis (with mass spectrometry) was performed. Thermal decomposition of magnesium hydroxide/hydromagnesite will proceed through dehydration, and dehydroxylation (and decarbonation for hydromagnesite) to form magnesium oxide. If this has occurred radiolytically during irradiation, then it would be expected to be observable by a reduced mass loss during TGA (as some of the sample would have already undergone this transformation prior). TGA-MS of

magnesium hydroxide unirradiated, irradiated under argon, and under air is shown in Figure 6-17a (with an expanded view in Figure 6-17b and summarised in Table 6-7). The TGA data show only a marginal difference in mass loss with a final mass of 66.0% of unirradiated magnesium hydroxide, 0.4% less mass loss of 66.4% (equivalent to 1.3% reduction of theoretical step loss of 30.9%) for irradiated magnesium hydroxide in both air (162 kGy) and argon (269 kGy). XRD analysis of both irradiated sample also showed no change, notably absence of the distinctive sharp MgO peak at 2Θ 43.0° (Figure 6-18a+b).[129]

Table 6-7. TGA data for irradiated magnesium hydroxide

	Unirradiated			Argon Irradiated			Air Irradiated		
Temp. (°C)	Mass (%)	Total Mass Loss (%)	Step Mass Loss (%)	Mass (%)	Total Mass Loss (%)	Step Mass Loss (%)	Mass (%)	Total Mass Loss (%)	Step Mass Loss (%)
285	97.2	2.84	2.84	97.3	2.75	2.75	96.9	3.06	3.06
800	66.0	34.0	30.3	66.4	33.6	30.0	66.4	33.6	29.6

The same analysis was performed on unirradiated and irradiated hydromagnesite in air (166 kGy)/argon (255 kGy). TGA-MS is shown in Figure 6-17a and expanded in Figure 6-17b, with data summarised in Table 6-8. Similar to the magnesium hydroxide data, there is no significant change in mass loss for irradiated hydromagnesite c.f. unirradiated. Unirradiated hydromagnesite exhibited a final mass of 42.0%, whilst air and argon irradiated sample decomposition resulted in slightly greater mass loss, with final masses of 41.5% and 41.1% respectively. XRD of the irradiated samples are shown in Figure 6-20a+b, and also show no change or sign of MgO.

Table 6-8. TGA data for irradiated hydromagnesite

		Unirradiated			Argon Irradiated			Air Irradiated		
Temp. (°C)	Theoretical Mass Loss (%)	Mass (%)	Total mass Loss (%)	Step Mass Loss (%)	Mass (%)	Total mass Loss (%)	Step Mass Loss (%)	Mass (%)	Total mass Loss (%)	Step Mass Loss (%)
120		96.6	3.4	3.36	96.2	3.8	3.79	96.5	3.5	3.51
315	15.4	82.0	18.0	15.2	81.5	18.5	15.3	81.7	18.3	36.9
800	41.5	42.0	58.0	41.4	41.1	58.9	42.0	41.5	58.5	31.0

From this it does not appear that at the dose rates and conditions tested there was any observable or significant radiolytic degradation of the solids, and that the hydrogen observed has come from radiolysis of adsorbed water, not from chemical changes in the magnesium hydroxide/hydromagnesite. As discussed in Section 2.5.6 there are some reports in literature of structural changes from γ-irradiation of magnesium hydroxide. Shpak et. Al. report formation of magnesium carbonate under γ-irradiation, which they propose occurs via dehydroxylation to form magnesium oxide, followed by carbonation from atmospheric carbon dioxide.[15] The irradiations were undertaken in air at total doses which exceeded those employed

in this investigation, ranging from 10 to 97.5 x 10^3 kGy (and some in D_2O), where 5% dehydroxylation was observed. This dose is orders of magnitude less than that employed in the study by Shpak et al. The difference in mass from TGA suggested the potential for 1.3% radiolytic decomposition in this work, which is approximately quarter of the extent of reaction, despite only receiving 0.16-0.26% of the dose.

In this work the dehydroxylation was very similar in both unirradiated and irradiated solids, if very slightly accelerated by irradiation. In their work the irradiated magnesium hydroxide actually displayed a delayed onset of decomposition, rather than early onset. These inconsistencies and lack of definite and clear correlation between samples and solids may suggest the difference in decomposition seen here is due to experimental uncertainty and not necessarily a result of observable radiolytic decomposition. Nevertheless from these previous published observations and the work performed here there would be benefit to investigate this further, and to compare $Mg(OH)_2$ with other compounds such as hydromagnesite.

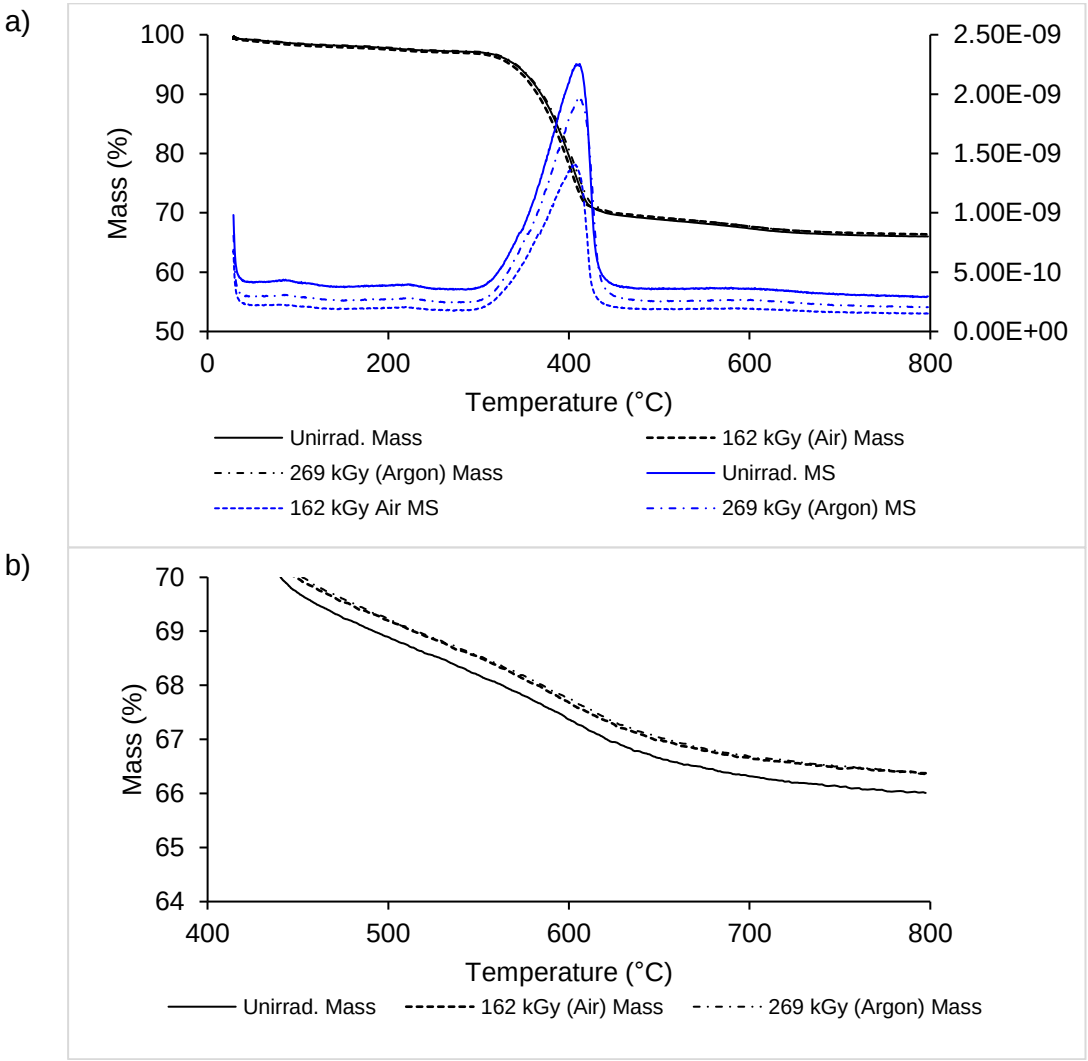

Figure 6-17. a) TGA-MS of unirradiated and irradiated magnesium hydroxide, b) TGA (enhanced) of irradiated magnesium hydroxide

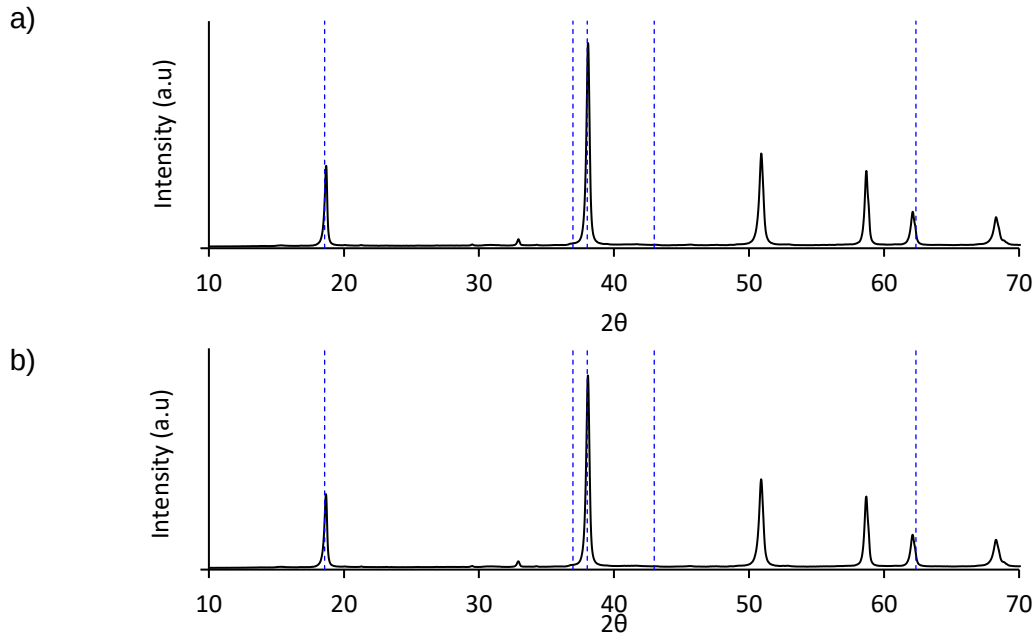

Figure 6-18. XRD for γ-irradiated $Mg(OH)_2$ (MgO peak location absence denoted by blue dash); a) 269 kGy irradiated in argon, b) 162 kGy irradiated in air

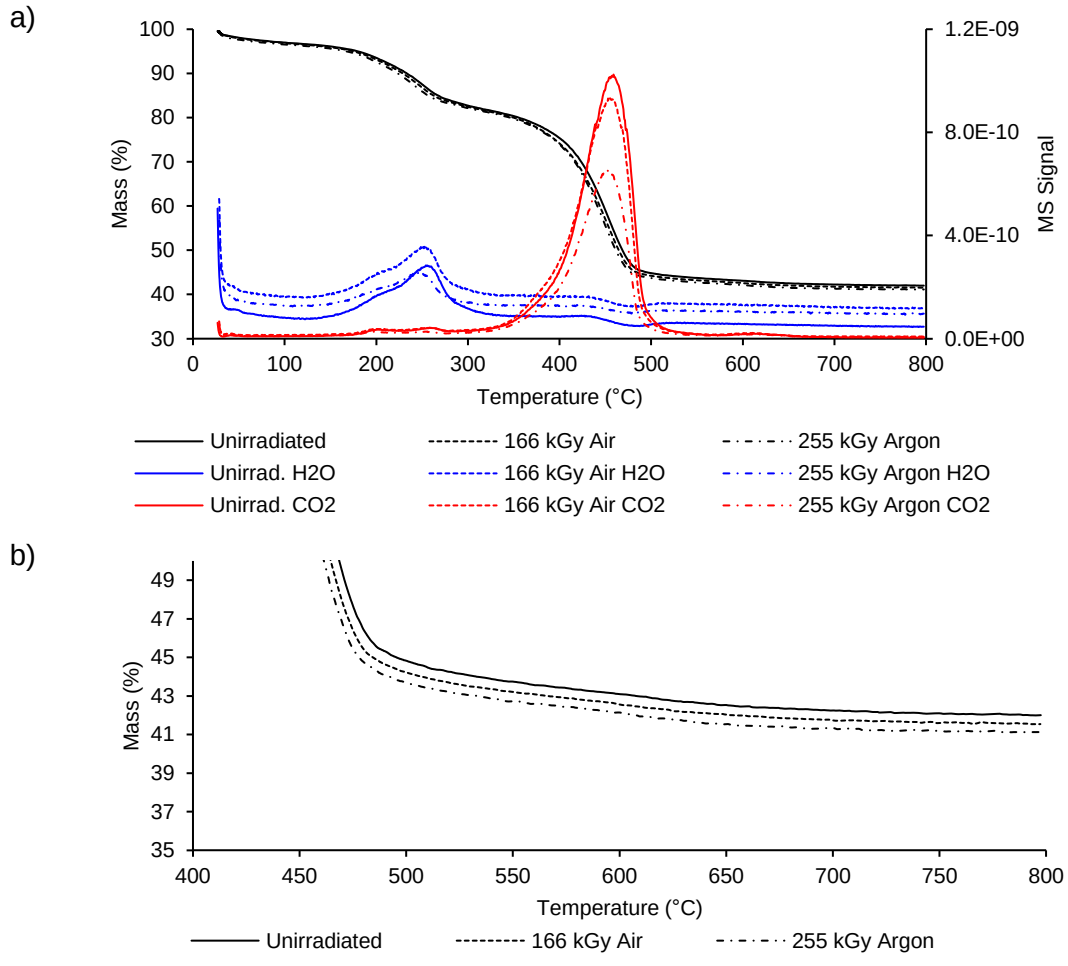

Figure 6-19. a) TGA-MS of unirradiated and irradiated hydromagnesite, b) TGA (enhanced) of irradiated hydromagnesite

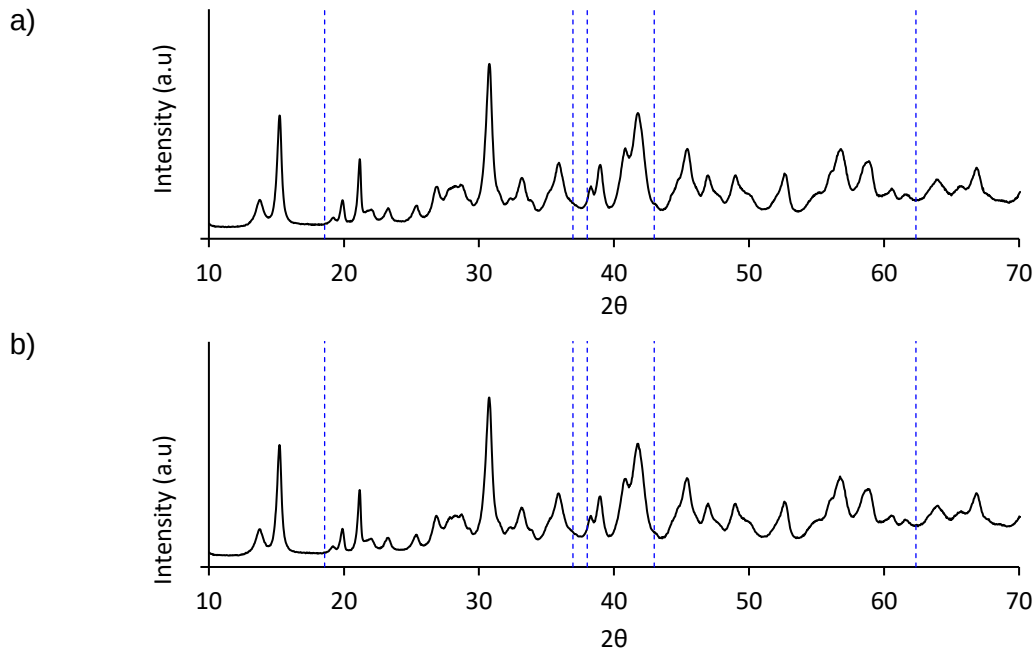

Figure 6-20. XRD for hydromagnesite γ-irradiated (MgO peak location absence denoted by blue dash); a) 255 kGy irradiated in argon, b) 166 kGy irradiated in air

6.3.2 ^{60}Co γ-Irradiation of vacuum dried magnesium hydroxide and hydromagnesite

6.3.2.1 γ-Irradiation of vacuum dried magnesium hydroxide and hydromagnesite results

In order to investigate the potential impacts of vacuum drying temperature and water carryover in to dry storage comparable to conditions observed in Chapter 5, magnesium hydroxide and hydromagnesite powders were vacuum dried at 40-200 °C prior to irradiation. This aims to quantify the real benefits of drying at elevated temperature with respect to reducing radiolytic hydrogen generation and to underpin how dry is adequate for dry storage. Magnesium hydroxide and hydromagnesite vacuum drying data are listed in Table 6-9, and show that continued mass loss was seen with elevated drying temperature up to 120 °C for both materials. Magnesium hydroxide was also dried at 200 °C but no additional mass loss was observed c.f. drying at 120 °C, and hydromagnesite begins to thermally decompose above 120 °C, so was not heated beyond this point.

Following drying, all samples were removed from the drying oven, promptly sealed and weighed to record mass losses, from which drying extent is inferred. Sealed samples were then evacuated and backfilled with argon. The prepared samples were all irradiated in the front row of the irradiator for one hour, with total dose rates from 8.9-15.7 kGy depending on position. The irradiation data are listed in Appendix Table 6-14 to Table 6-17.

Table 6-9. Vacuum dried magnesium hydroxide/hydromagnesite water loss and estimated water layer coverage

	Drying Temp. (°C)	Mass Loss (%)	Water Content (%)	SSA (m^2/g)	g/layer/m^2	No. H_2O layers	H_2O Layer Thickness (nm)
$MgOH_2$	40	0.59	2.25%	13.59	4.22E-03	5.3	1.7
	60	0.88	1.96%	13.63	4.23E-03	4.6	1.4
	90	1.15	1.69%	13.67	4.24E-03	4.0	1.2
	120	1.54	1.30%	13.73	4.26E-03	3.1	0.9
	200	1.43	1.41%	13.71	4.26E-03	3.3	1.0
Hydro-magnesite	40	1.35	2.01%	22.09	6.86E-03	2.9	0.9
	60	1.85	1.51%	22.20	6.89E-03	2.2	0.7
	90	2.29	1.07%	22.30	6.92E-03	1.5	0.5
	120	2.88	0.48%	22.43	6.96E-03	0.7	0.2

The irradiation data shown in Figure 6-21a (only considering energy absorbed by water) and Figure 6-21b (considering energy absorbed by whole sample) displays $G(H_2)$ as a function of the temperature of drying, where it should be noted the 20 °C data is undried and repeated data from the Section 6.3.1.1 for comparison. Based on energy absorbed by water, the average $G(H_2)$ from drying at 40, 60, 90, 120 and 200 °C were measured for magnesium hydroxide at; 4.2, 3.0, 3.0, 1.4 and 1.7 respectively, and for hydromagnesite at; 2.1, 4.6, 3.4 and 2.8 respectively. From energy absorbed by the combined solid and water mass, the average $G(H_2)$ after drying at 40, 60, 90, 120 and 200 °C for magnesium hydroxide was; 0.094, 0.058, 0.050, 0.018 and 0.024, and for hydromagnesite was; 0.043, 0.070, 0.036 and 0.014. Estimated monolayer coverages based on water content from vacuum drying mass loss are listed in Table 6-9, but it should be noted that estimating monolayer coverage on single monolayer (or less) is crude. At this level, water coverage will not be homogeneous,[45] but it does still provide some relative comparison between the different samples.

6.3.2.2 Discussion

When considering only energy absorbed by the water component, $G(H_2)$ trends slowly down with increasing drying temperature from 40-120 °C. If any potential energy transfer only occurs between the surface and the adsorbed molecules, it would not be expected that a significant change in G-value would be observed in the few monolayers as any removed surface water will bring about an equivalent reduction in hydrogen generation. There is no notable change between drying magnesium hydroxide at 120 °C or 200 °C, and the mass loss after drying at 120 °C was slightly greater than for 200 °C. This is not likely to indicate any loss in efficacy of drying at the more elevated temperature, and is more likely to be a slight uncertainty in the mass measurement and/or potential re-adsorption of moisture from air between drying and sealing/weighing.

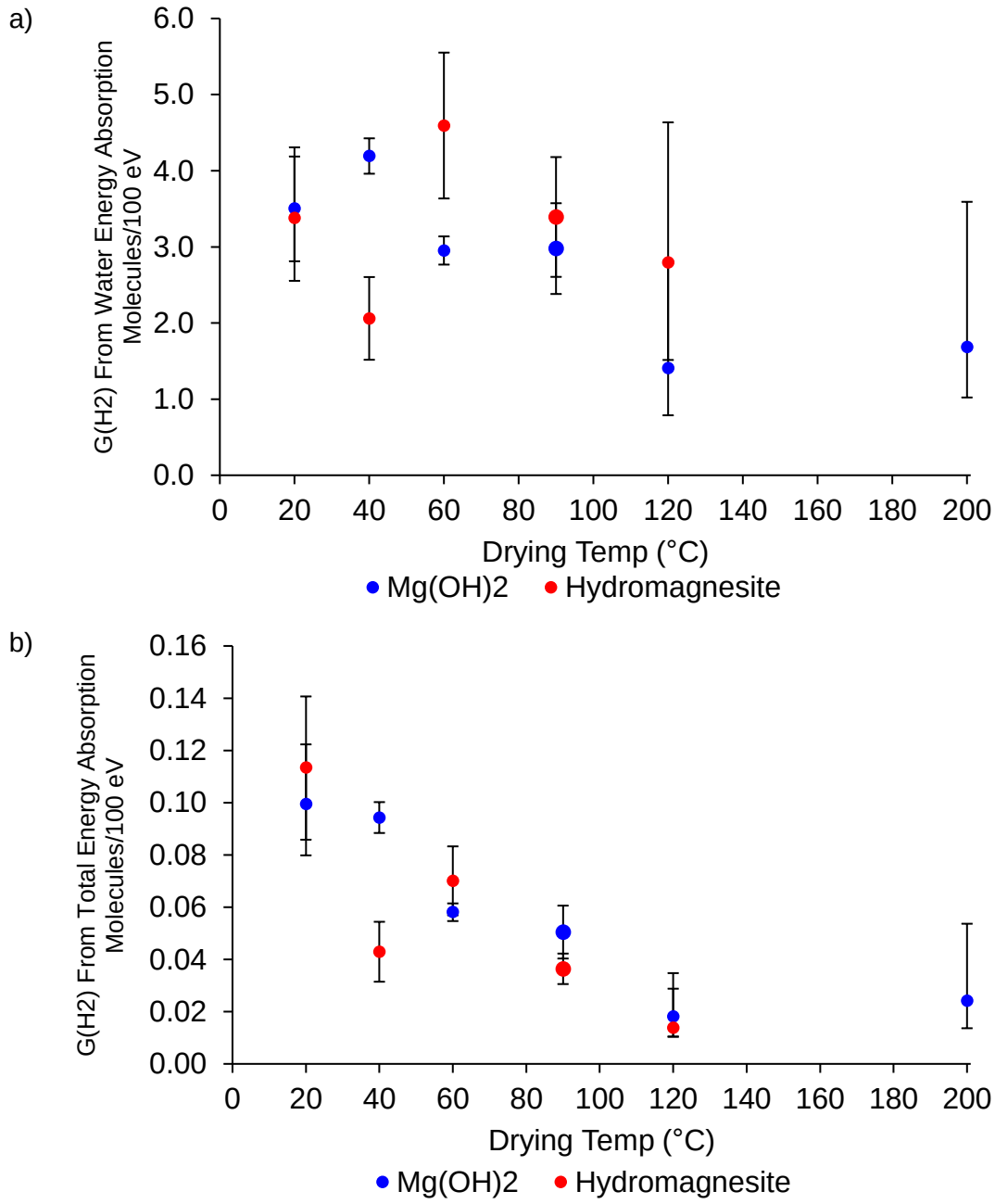

Figure 6-21. G(H_2) for undried (listed at 20 °C) and vacuum dried magnesium hydroxide and hydromagnesite powders by drying temperature assuming a) only energy absorbed by water, b) energy absorbed by both water and solid

The G-value experimental data showed relatively large experimental range variance, with an additional 8.9% dose rate and GC volume uncertainty (as described in Section 6.2.3.3) displayed by the error bars. This variance is likely to be largely associated with the high degree of sensitivity to water content assumptions by the G-value at such low amounts (as introduced in Section 6.2.3.5), and variance with small GC hydrogen signal areas. In such instances, there is additional value to comparing the energy absorbed by the whole system (water and solid) as in Figure 6-21b.

When the whole sample energy is considered, the trend with increasing drying temperature to reduced $G(H_2)$ is more clear to see for both magnesium hydroxide and hydromagnesite, as there is no necessity to infer the amount of water present. From this the $G(H_2)$ decreases steadily with increased drying temperature, and is consistent in magnitude between both solids. The data for hydromagnesite at 40 °C appears lower and is likely to be an artefact of pressure loss during analysis, despite application of H_2 peak area correction and therefore is not representative of real data. Also, for magnesium hydroxide the $G(H_2)$ at 200 °C is close to that at 120 °C, which could imply that there is little to no benefit to drying magnesium hydroxide beyond 120 °C. As mentioned previously it is possible that some small quantities of water re-adsorbed onto the solid surface after removal from the oven. Alternatively it could be from radiolytic decomposition of the solid lattice as reported by Laverne et al.[16] and Shpak et al.[15] All samples underwent the same drying and preparation procedure, so this effect should be comparable between all samples unless those that are dried at higher temperature (i.e. with least physisorbed water) re-adsorb water most rapidly and thus reach a semi-consistent state after preparation regardless of drying temperature. Whilst it would be possible to eliminate this problem, it would require access to specific facilities e.g. vacuum oven held within a gas controlled environment such as a glovebox which was not possible during this investigation.

As mentioned the $G(H_2)$ evaluation is sensitive to water content estimations, but there are other factors that can affect the data uncertainty and error. One limitation of this investigation, particularly with vacuum dried materials is that the amount of water and therefore hydrogen yield is small which makes detection sensitivity difficult. Potential ways to improve this is to increase the sample quantity irradiated or to increase the irradiation time. Also as the amount of water is inferred from mass loss, there is additional uncertainty in assessing the starting quantity of sample water which has been assigned by TGA as described in Section 4.2.1.2. Future work could look to use alternative techniques to quantify water adsorption and layers of water coverage by techniques such as FT-IR.[49,130] Additionally this is further complicated for hydromagnesite by the fact that the compound contains chemically bound water which will also be thermally liberated at temperatures >125 °C. Vacuum drying magnesium hydroxide here showed no additional mass loss above 120 °C, but during vacuum drying tests in Section 5.2.1.1 corroded Magnox Sample 1 demonstrated continued mass loss at all tested temperatures up to 180 °C. It is unclear why this is, but it could be that the magnesium hydroxide powder has all water removed at 120 °C, and that the mass loss at temperatures >120 °C seen on Sample 1 were from alternative corrosion products. If all water is

removed from magnesium hydroxide at 120 °C, then in accordance with the mass loss data from Table 6-9 the magnesium hydroxide water content may be closer to ~1.4%. If this is the case, then the magnesium hydroxide powder water content may be overestimated, and the $G(H_2)$ values (based on energy absorbed by water) will be greater than calculated. When compared to the TGA data in Figure 6-18a and water content estimates from Characterisation Chapter Section 4.2.1.2 the mass loss at 120 °C was 1.68%, and at 200 °C was 2.24%. The TGA mass loss continues to gradually decrease with a small water associated water signal response in the mass spectrometer up to 2.84% at the point of decomposition at 285 °C. There is no DSC response that suggests a chemical reaction (e.g. early dehydroxylation) is giving rise to this mass loss/water detection. TGA data from the unirradiated and two irradiated samples all showed the same gradual mass loss and mass spectrometer water response between 150-285 °C, where at the end of this period the mass loss (and therefore inferred water content) was measured at 2.75-3.06%. Either way, the overall implication of the data does not change, that being that $G(H_2)$ is disproportionately high at low water content, and that vacuum drying successfully reduces the radiolytic hydrogen yield of corroded Magnox powders.

6.3.3 Alpha irradiation of magnesium hydroxide

6.3.3.1 Alpha irradiation of magnesium hydroxide results

Results from 3.96 MeV He^{2+} irradiation of magnesium hydroxide at as-received and 20% added water, and also pure water are presented in Figure 6-22 (with full data appended in Table 6-18 to Table 6-21). Figure 6-22a shows calculated $G(H_2)$ from energy absorbed by only the water component of the sample. The G-values are calculated as 0.19, 0.21 and 0.22 for pure water, 0.10 and 0.13 for 20% added water and 2.1, 2.3 and 7.0 for as-received magnesium hydroxide. The GC data imply good sample integrity with minimal oxygen content (which would imply leaks during sample preparation an analysis).

Figure 6-22b displays the calculated $G(H_2)$ from energy absorbed by both the solid and water component. The G-values are calculated as 0.19, 0.21 and 0.22 for pure water (unchanged from previous), 0.041 and 0.030 for 20% added water, and 0.008, 0.010 and 0.029 for as-received magnesium hydroxide.

6.3.3.2 Alpha irradiation of magnesium hydroxide discussion

The data gathered from He^{2+} ion beam irradiation of magnesium hydroxide at 0% and 20% added water showed a trend between water content and $G(H_2)$, whereby when considering the energy absorbed by the water component, the G-value was

higher at the lower water content tested. This is the same observation as seen for the γ-irradiation work described previously. Again, as seen for γ-irradiation when the energy absorbed by the whole sample mass, reducing water content reduced overall hydrogen yield and $G(H_2)$, despite the relatively high hydrogen generation rate when considering only energy absorbed by water.

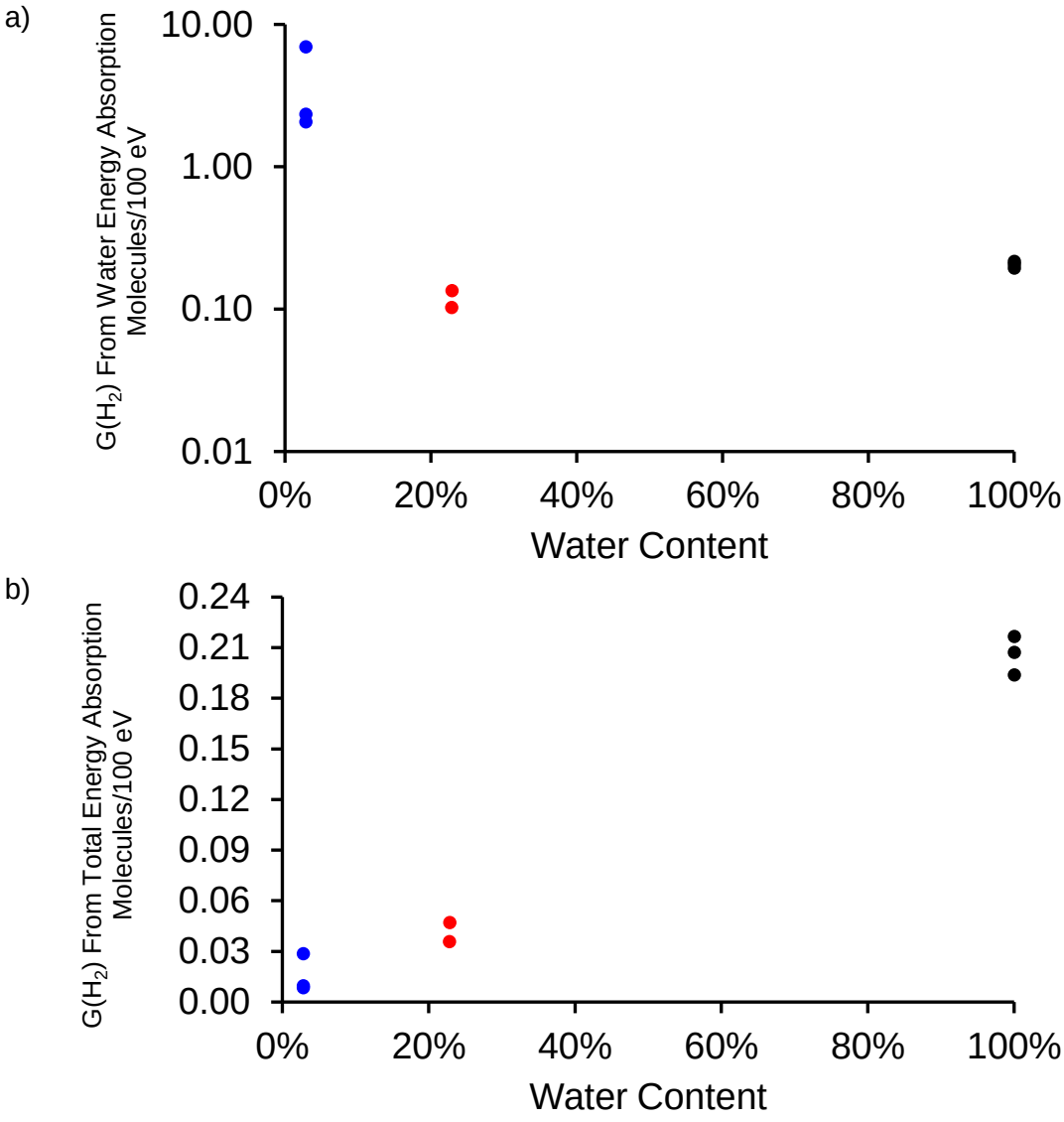

Figure 6-22. $G(H_2)$ for magnesium hydroxide powders (and pure water) based on ion flow rate from ion beam window current by water content based on a) only energy absorbed by water, b) energy absorbed by both water and solid

The following discussion will relate specifically to the data in Figure 6-22a and consider the energy absorbed by the water component. As mentioned, the $G(H_2)$ was calculated to be higher at the lowest water content tested here, suggesting some energy transfer from the solid to the adsorbed water may be taking place, but this was not observable at the 20% added water sample which had a $G(H_2)$ lower than that measured for pure water, so this effect appears to be modest. The data were generally precise and consistent, the most obvious discrepancy being the

point at $G(H_2)$ 7.0, which was measured at a considerably greater value than others for 0% added water of 2.1 and 2.3. The reason for the variation in these datapoints is not known. All three points have consistent GC pressures, with no indication of leaks from oxygen ingress so all samples appear consistent. Given that the anomalous point shows an increase in hydrogen rather than a decrease, it cannot be easily dismissed (as most experimental limitations result in loss of hydrogen) so has been included. The dataset is relatively small with three points measured at these conditions and eight over the whole set, so there is not enough data available to definitively rule one point out over any other. Therefore all these results are included and any disparity must be attributed to experimental variation. Gathering additional data would be beneficial to gain further confidence in these values, and would facilitate identification of anomalous results. Other potential limitations to the method will be discussed later in this section.

Whilst there is a trend observed with reducing water content and increasing $G(H_2)$, the G-values here are still lower than recorded literature values for bulk water of 1.2 molecules/100 eV from 5 MeV He^{2+} ions.[69] This is the case for both the adsorbed water/magnesium hydroxide samples and the pure water samples, where $G(H_2)$ was measured significantly below the literature value at 0.19-0.22 molecules/100 eV. Whilst it is uncertain how or why these values are lower than literature values, the method was performed consistently across the dataset. Therefore whilst there may be uncertainty in the potential shift in magnitude of the data, the trend should be consistent and mirrors the behaviour seen in the experimental γ-irradiation work seen here and in literature.[12,13] Some similar work is reported by Laverne and Tandon where they irradiated UO_2, CeO_2 and ZrO_2 with 5 MeV He^{2+} ions to observe G-values with varying water content up to 3.0%.[131] They report $G(H_2)$ based on total energy deposited on both water and solid in the range of 0.01 molecules/100 eV at 0.25% water up to 0.04 molecules/100 eV at 3.0% water, which is fairly consistent with the data seen here in Figure 6-22b. One point they make is that ion irradiation can displace atoms to form interstitial vacancy Frenkel pairs in the solid lattice. This is more common in ion tracks than in γ-radiolysis and can trap excitons, preventing transport to the surface water.[12,85,131]

In the work by Laverne et al.[131] they do not attempt to convert the G-value to account for the energy absorbed by water only, (however they do include this information for γ-irradiation) potentially due to the added complications and uncertainty surrounding how to estimate the energy division. The fact that their G-values are consistent with the data measured here shows some promise that this is representative and in-keeping with other work in the area. It is understandable why their work may not want to estimate G-values for the water only, as there is

uncertainty in estimation of the energy absorbed by the solid and water components from which the G-values are calculated. The basis for the estimation in this work is described previously in Section 6.2.4.2, by which the area under the stopping power curves for each material provides the proportion of energy each component absorbs per unit penetration/volume. These values have been calculated using widely used and appropriate software packages SRIM and TRIM, and are not expected to be erroneous.

The application here has to generalise with regard to how the ion energy penetrates the sample and how the energy distribution is assumed for the sake of simplicity and practicality. The energy is assumed to be split between the components based on the mass proportion of each. It also assumes that the water and magnesium hydroxide particles are evenly dispersed. There may be some limitations to these assumptions in that the alpha ion penetrations were calculated at 13.7-15.3 μm. If an alpha particle were to penetrate an $Mg(OH)_2$ particle of greater diameter than this, the majority of the energy would be transferred to the magnesium hydroxide, and proportionately little energy transferred directly to the adsorbed water.

Particle size distribution and SEM identified magnesium hydroxide particles at a range of diameters from ~1-100 μm, with approximate equal volume distributions above and below ~16 μm. Therefore a large proportion of the magnesium hydroxide is of such a scale that incoming ions are likely to pass through the adsorbed/surface water and then come to rest within the solid, depositing most of its energy within the solid volume. This may mean that the energy transferred to the adsorbed water is overestimated, which would explain why the G-values here seem to be lower than expected. Further work into more closely assessing the energy distribution across a range of particle sizes and surface water coverage would be of great interest to this question but is not included as part of this work.

A methodological reason for the low calculated G-values here (perhaps more relevant to the water sample) could be the risk for hydrogen to form and collect in a gas bubble at the top of the sample valve. If this were the case, the majority of the generated hydrogen would be unable to diffuse throughout the apparatus and would not be collected in the sample cylinder for analysis. This is perceived to be potentially likely to have occurred to some degree during this experiment, but is not expected to have been significant for the solid samples. The solids were not densely packed or pressed into the sample container, so hydrogen should have adequately unrestricted diffusion paths to mix across the apparatus, particularly as the irradiation took place over 2 hours which provides significant time for mixing to occur.

Another area for uncertainty is in the volume scaling of the captured and analysed hydrogen quantity. The apparatus is designed around protection of the integrity of the sample gas and foil, which introduces limitations in collection volume – mostly due to inability to evacuate the apparatus (or expose to a pressure difference) across foil window. This resulted in the GC analysis volume estimated to be approximately 61% of the total system gas volume, so hydrogen yields are scaled accordingly. The volumes were calculated by filling the fittings with water and weighing to assess the internal volume. These were cross checked against calculated fitting volumes from manufacturer technical drawings for consistency.

Also in relation to the sample volume is the sensitivity of the technique. As discussed it was not possible to collect all the hydrogen yielded during the irradiation. Therefore the irradiation had to be sufficient to yield measurable hydrogen by the GC. Due to the low sample pressure and volume, hydrogen signals often approached lower limits of detection (particularly for samples without added water) which limits the measurement precision. This was combated by maximising sample irradiation time/absorbed dose in order to generate the largest possible quantity of hydrogen in the available time frame. This could be improved further by increasing irradiation time and by reducing the sample apparatus internal volume. One simple way to improve on this setup in future is to remove the hydrogen sensor. Whilst it was able to provide qualitative information during irradiations, it proved too time consuming to calibrate and was unreliable so could not deliver meaningful quantitative data during this work.

This work has provided useful data, and demonstrates a viable method of He^{2+} ion material irradiation for hydrogen collection and analysis. The dataset here is modest but provides an initial indication that alpha irradiation of magnesium hydroxide can give rise to energy transfer to surface water and increase the respective water $G(H_2)$. Further validation work and energy distribution modelling would be valuable to gain more confidence in these values, particularly when the magnitude of the results does not precisely match that of reported literature values of bulk water.

6.4 Conclusions

Hydrogen generation from γ-irradiation of magnesium hydroxide and hydromagnesite at a range of water contents and following vacuum drying at 40-200 °C has been tested. Previous literature has reported that energy from γ-irradiation can be transferred from metal oxides to adsorbed water which gives rise to an increased $G(H_2)$.[12,13] $G(H_2)$ was measured for irradiated samples of magnesium hydroxide and hydromagnesite with nominally 0% added, 10% added

and 20% added water by mass (actual water contents are estimated at 2.8%, 13.9% and 24.7% water for magnesium hydroxide, and 3.4%, 14.7% and 24.9% water for hydromagnesite). The average $G(H_2)$ from energy absorbed by water at 0%, 10% and 20% added water for magnesium hydroxide at 9-16 kGy dose was measured at 3.5, 1.0 and 0.83, and for hydromagnesite at 3.4, 0.82 and 0.81 respectively. Irradiations at 150-270 kGy under argon on 0%, 10% and 20% added water magnesium hydroxide measured $G(H_2)$ of 3.7, 1.2 and 0.92, and for hydromagnesite at 1.2, 1.2 and 1.0 respectively, and for 0% added water 220 kGy irradiation in air at 2.2 for magnesium hydroxide and 2.9 for hydromagnesite. When compared to the literature $G(H_2)$ of 0.45 molecules/100 eV the values measured here are greater which suggests some element of energy transfer from the solid is occurring which gives rise to the elevated $G(H_2)$, which increases as the water content decreases. The G-values measured here are greater than those measured for MgO by Petrik et al,[12] and this may be in part due to the better band gap matching and resonant coupling between $Mg(OH)_2$ which has a reported band gap of 5.17-5.70 eV[80,81] and H-OH dissociation energy of 5.1 eV.[78] Hydromagnesite has a band gap of 4.42 eV.[127]

Whilst this data implies that lowering the water content increases the respective hydrogen generation rate, the total hydrogen yield is still lower with reduced water content. Additionally the $G(H_2)$ estimations rely on some assumptions made with regard to water content which can have a notable effect on the final value. The $G(H_2)$ consistently reduces with lower water content when the energy absorbed by the whole system is considered.

G-values were also measured from vacuum oven drying magnesium hydroxide at 40-200 °C, and hydromagnesite at 40-120 °C. At the reduced water contents following vacuum drying the average $G(H_2)$ values for energy absorbed by water were measured at between 1.4-4.2 for magnesium hydroxide and 2.1-4.6 for hydromagnesite, with a general correlation of reduction of $G(H_2)$ with increasing drying temperature but with wide variation in the data. Most of this variation is believed to be a result of the low volume of hydrogen yielded during these experiments which resulted in measurements close to apparatus detection limits and some uncertainty associated with this. Despite this, the hydrogen yield was consistently reduced with increasing vacuum drying temperature up to 120 °C which was demonstrated in the $G(H_2)$ data when considering energy absorbed by the whole sample. This suggests that there is continued benefit to increasing vacuum drying temperature up to 120 °C in the context of reducing radiolytic hydrogen yield. There was no notable difference in hydrogen yield from vacuum drying magnesium hydroxide at 120 °C and 200 °C, suggesting drying beyond

120 °C may not yield any additional benefit. No definitive evidence of water/hydrogen generation from radiolytic decomposition of magnesium hydroxide or hydromagnesite solid was observed by TGA, and the presence of the decomposition product magnesium oxide was not seen by XRD.

The main limitations of this work were low hydrogen yield/detection sensitivity for low water content materials which introduced analytical uncertainty. Without making adjustments to the analytical methods this could be improved by increasing hydrogen product volumes through longer irradiations or by irradiating larger sample quantities.

Hydrogen generation from irradiation of magnesium hydroxide by 3.96 MeV He^{2+} ions was also investigated. $G(H_2)$ was calculated at 0% added, 20% added water at 2.1-7.0 and 0.10-0.13 molecules/100 eV respectively when considering energy absorbed by only the water component. The hydrogen generation rate was greater for the as-received 0% added water samples than for 20% added and pure water. The data here show a similar trend to that seen for the γ-irradiation data where $G(H_2)$ is elevated for adsorbed surface water, where energy transfer is potentially taking place from the solid to the adsorbed water. One point to note about this data is that the measured G-values for pure water here at 0.19-0.22 molecules/100 eV are significantly lower than the reported literature values of 1.2 molecules/100 eV.[69] It is not known precisely why this is, but some possible reasons could be due to uncertainty and overestimation of energy deposition to the water, or hydrogen produced during irradiation becoming contained in the sample and not being collected for detection and analysis. Whilst there is some uncertainty with the magnitude of the data, the methods were consistent between conditions so the trends and relationships are still believed to be valid.

$G(H_2)$ values for magnesium hydroxide with 0% and 20% added water were measured at 0.008-0.029 and 0.036-0.047 molecules/100 eV respectively when considering energy absorbed by water and solid component, which is consistent with similar work in this area by Laverne and Tandon.[131] Similarly to γ-radiation data, when the energy absorbed by the whole system is considered, the $G(H_2)$ and overall hydrogen yield reduces with decreasing water content, demonstrating that lower water content does reduce the overall hydrogen yield as would be expected.

6.5 Recommendations and Future Work

From the work undertaken here, it is recommended that for corroded Magnox (magnesium hydroxide or hydromagnesite)/water systems at <25% water content, a

potential increase (compared to literature values for bulk water) in the rate of γ-radiolytic hydrogen generation is considered for estimates.

From vacuum drying magnesium hydroxide and hydromagnesite prior γ-irradiation it was seen that radiolytic hydrogen yield was consistently decreased with increasing drying temperature from 40 °C up to 120 °C. Therefore it is recommended that vacuum drying is performed at as high a temperature as practicable up to 120 °C (no benefit was observed between 120-200 °C) if hydrogen generation in storage is to be minimised. Lower drying temperatures will still viably reduce radiolytic hydrogen yield, but will be likely to generate hydrogen in potential storage conditions. This compromise between drying time/temperature and hydrogen yield should be considered when assessing risks for storage conditions. From this work, there has not been any substantial evidence of radiolytic degradation of magnesium hydroxide solid or hydromagnesite under the conditions and doses employed. Also this work has only considered water in the presence of corrosion products, since corroded magnesium has more scope for water retention.

The amount of data here is relatively modest so further data would be recommended to further underpin and refine these observations. There are many directions this could proceed in such as irradiating over increasing doses to observe $G(H_2)$ over a wider range. Additionally longer irradiations and/or irradiations of larger samples could give rise to greater hydrogen yields which could improve detection sensitivity and reduce uncertainty.

Also the experimental program was limited by time and facility availability, which resulted in highest possible dose rates being employed to achieve adequate doses over short timescales. More intense irradiations are more likely to produce dose effects that may be less representative of real world conditions. This could be more likely to give rise to competitive reaction paths that may consume hydrogen product, thereby reducing the observed $G(H_2)$ and underestimate hydrogen generation rates. It would be valuable to compare equivalent doses at a range of dose rates to gain more understanding of dose rate effects.

Water content was calculated from mass loss from TGA and bench top analysis, but further quantification by other techniques such as FTIR or precise mass measurements/Quartz Crystal Microbalance (QCM)[49,130] would provide additional benefit for accurately and confidently assigning water layer coverage and efficacy of drying conditions. This could also be enlisted to produce a more precise calculation of monolayer coverage, and if coupled with improved hydrogen detection sensitivity could produce valuable data to observe a correlation and precise quantification of energy transfer from $Mg(OH)_2$ to adsorbed water.

For α-irradiations of magnesium hydroxide, this work has demonstrated a viable method for He^{2+} ion beam irradiation, hydrogen collection and analysis, but more data is required to deduce hydrogen generation rates and G-values. Similar to the γ-irradiation data, a variation in $G(H_2)$ was seen with water content, which should be taken in to consideration, particularly for low (<~5%) water content solids. The data here shows some discrepancy in magnitude when compared to literature values for bulk water. The cause for this has not been identified, so it is not recommended that the G-values calculated here are directly applied to other work without further work. Overall the penetration of α-radiation is very small. Even if doses and radiolytic hydrogen generation rates are relatively high the actual physical quantity of the affected material is minimal (<20 μm penetration) so this should be taken in to consideration in the context of the whole system.

Hydrogen peaks were small and hard to detect by this method, largely due to the low penetration of alpha particles and therefore small amount of irradiated material. In order to improve this data, it would be beneficial to undertake many more irradiations, preferably whilst improving the sensitivity or measurable hydrogen quantity through greater irradiation doses. Also in the context of dry storage, it would be of interest to irradiate vacuum dried materials to observe the effects of various drying conditions. From the work undertaken here, due to the small proportion of each sample that was irradiated, no characterisation of the irradiated material was undertaken to attempt to identify any physical or chemical changes. It may be of interest to see if the magnesium hydroxide did undergo physical degradation or change from exposure to the α-radiation, and whether this can undergo dehydroxylation/water liberation and contribute to $G(H_2)$.

One of the largest analytical challenges with this work was quantifying the energy transferred to the solid and water components of the mixtures to calculate the $G(H_2)$. This method generalises energy absorption and does not consider variation in particle size or water coverage. Further work is recommended to model this system and consider how particle size/water coverage can affect energy distribution, particularly when ion penetration is less than a proportion of particle the particle size distribution. Another aspect that has not been investigated here is β-radiation, which is another potential source of radiolytic hydrogen. A method similar to that employed here for α-irradiation could be directly applicable to this line of investigation.

6.6 Appendix

6.6.1 ^{60}Co γ-Irradiation of vacuum dried magnesium hydroxide and hydromagnesite tabulated data

*Low pressure – sample/GC leak suspected and correction applied
#Undertaken in air – all others irradiated under argon

Table 6-10. Sample and GC data for magnesium hydroxide γ-irradiation

Sample ID	Sample Mass (g)	Water Mass (g)	Water %	Sample Press (mbar)	GC Press. (bar)	Peak Area (H_2)	Adjusted Peak Area (H_2)	Peak Area (O_2)	Peak Area (N_2)	H_2 qty (moles)
0MaF	2.273	0.065	2.84	1245	0.553	3.54	3.54	0.63	2.11	3.3E-07
0MbF	2.26	0.064	2.84	1265	0.566	3.89	3.89	0.11	0.52	3.6E-07
0MaM	0.989	0.028	2.84	1215	0.547	1.82	1.82	0.27	0.37	1.7E-07
0MbM	2.261	0.064	2.84	1256	0.554	2.79	2.79	0.33	0.38	2.6E-07
0MaFArg	2.266	0.064	2.84	1346	0.604	81.49	81.5	0.13	0.23	7.6E-06
0MbFArg	2.2591	0.064	2.84	1362	0.444*	62.04	62.0	0.32	1.65	5.8E-06
#0MaFAir	2.248	0.064	2.84	1013	0.435	22.08	22.1	71	246	2.6E-06
#0MbFAir	2.2425	0.064	2.84	1013	0.198*	12.89	28.33	30	109	2.1E-06
10MaF	2.499	0.36	13.9	1276	0.559	6.15	6.15	0.11	0.95	5.6E-07
10MbF	2.534	0.36	13.9	1265	0.559	4.83	4.83	0.00	0.34	4.4E-07
10MaM	2.474	0.36	13.9	1303	0.604	6.54	6.54	0.27	0.53	6.0E-07
10MbM	2.519	0.36	13.9	1254	0.556	5.76	5.76	0.00	0.19	5.3E-07
10MaF	2.532	0.36	13.9	1346	0.600	79.39	79.4	0.21	0.33	7.3E-06
20MaF	1.249	0.33	24.7	1245	0.461*	2.40	2.94	0.77	31	2.8E-07
20MbF	1.162	0.33	24.7	1265	0.436*	2.50	3.35	0.59	1.74	3.2E-07
20MaM	1.28	0.33	24.5	1215	0.551	3.34	3.34	0.19	0.64	3.1E-07
20MbM	1.287	0.33	24.6	1256	0.571	3.40	3.40	0.40	0.60	3.2E-07
20MaF	1.442	0.33	24.7	1388	0.637	75.26	75.3	0.00	0.46	7.1E-06

Table 6-11. Sample and GC data for hydromagnesite γ-irradiation

Sample ID	Sample Mass (g)	Water Mass (g)	Water %	Sample Press. (mbar)	GC Press. (bar)	Peak Area (H_2)	Adjusted Peak Area (H_2)	Peak Area (O_2)	Peak Area (N_2)	H_2 qty (moles)
0HaF	1.639	0.06	3.36	1245	0.551	2.5	2.5	0.3	2.1	2.3E-07
0HbF	1.651	0.06	3.36	1265	0.605	3.4	3.4	0	0.3	3.2E-07
0HaM	0.859	0.03	3.36	1215	0.546	1.6	1.6	0.81	1.0	1.6E-07
0HbM	1.808	0.06	3.36	1254	0.591	3.0	3.0	0.33	0.93	2.8E-07
0HaFArg	1.637	0.06	3.36	1346	0.520	22	22	1.8	17	2.1E-06
0HbFArg	1.5945	0.05	3.36	1362	0.396*	12	13	31	108	1.3E-06
#0HaFAir	1.803	0.06	3.36	1013	0.434	28	28	74	238	2.7E-06
#0HbFAir	1.83	0.06	3.36	1013	0.442	37	37	77	244	3.4E-06
10HaF	1.933	0.31	14.7	1276	0.393*	3.4	5.1	4.4	14	4.7E-07
10HbF	2.012	0.31	14.7	1265	0.582	4.9	4.9	0.32	0.47	4.6E-07
10HaM	1.981	0.31	14.7	1303	0.443*	1.9	2.6	46	143	2.4E-07
10HbM	1.937	0.31	14.7	1256	0.397*	2.9	4.2	5.3	17	3.9E-07
10HaF	1.923	0.31	14.7	1361	0.611	70	70	0.34	1.1	6.5E-06
20HaF	1.314	0.33	24.9	1276	0.592	3.3	3.3	0.59	1.1	3.1E-07
20HbF	1.27	0.33	25.0	1265	0.574	2.6	2.6	0.21	0.13	2.4E-07
20HaM	1.244	0.33	24.7	1215	0.524	3.2	3.2	0.56	2.5	3.0E-07
20HbM	1.288	0.33	24.9	1254	0.559	3.8	3.8	0.30	1.3	3.6E-07
20HaF	1.1068	0.33	24.9	1388	0.630	83	83	0.89	1.3	7.8E-06

Table 6-12. Magnesium hydroxide γ-irradiation data

Sample ID	Added Water (%)	Irradiator Row	Irradiator Deck	Irradiator Position	Irradiation Time (h)	Total Dose (kGy)	$G(H_2)$ Water Only	$G(H_2)$ Water + Solid
0MaF	0	1	Bottom	3	1	15.0	3.3	0.09
0MbF	0	1	Bottom	3	1	15.0	3.6	0.10
0MaM	0	2	Bottom	3	2	13.9	4.3	0.12
0MbM	0	2	Bottom	3	2	13.9	2.8	0.08
0MaFArg	0	1	Bottom	2	17	269	4.2	0.12
0MbFArg	0	1	Bottom	2	17	269	3.2	0.09
#0MaFAir	0	1	Bottom	1	17	162	2.5	0.07
#0MbFAir	0	1	Bottom	1	17	162	1.9	0.05
10MaF	10	1	Top	3	1	13.0	1.1	0.18
10MbF	10	1	Top	3	1	13.0	0.90	0.14
10MaM	10	2	Top	3	2	14.0	1.1	0.18
10MbM	10	2	Top	2	2	16.2	0.86	0.13
10MaF	10	1	Top	1	17	159	1.2	0.18
20MaF	20	1	Bottom	4	1	9.8	0.83	0.23
20MbF	20	1	Bottom	4	1	9.8	0.95	0.28
20MaM	20	2	Bottom	4	2	12.0	0.77	0.21
20MbM	20	2	Bottom	4	2	12.0	0.78	0.21
20MaF	20	1	Top	2	17	226	0.92	0.22

Table 6-13. Hydromagnesite γ-irradiation data

Sample ID	Added Water (%)	Irradiator Row	Irradiator Deck	Irradiator Position	Irradiation Time (h)	Total Dose (kGy)	G(H_2) Water Only	G(H_2) Water + Solid
0HaF	0	1	Bottom	2	1	15.8	2.6	0.09
0HbF	0	1	Top	2	1	13.3	4.2	0.14
0HaM	0	2	Bottom	2	2	14.4	3.6	0.12
0HbM	0	2	Top	3	2	14.0	3.2	0.11
0HaFArg	0	1	Bottom	3	17	255	1.4	0.05
0HbFArg	0	1	Bottom	3	17	255	0.89	0.03
#0HaFAir	0	1	Bottom	4	17	166	2.5	0.09
#0HbFAir	0	1	Bottom	4	17	166	3.2	0.11
10HaF	10	1	Top	2	1	13.3	1.1	0.18
10HbF	10	1	Bottom	2	1	15.8	0.89	0.14
10HaM	10	2	Top	2	2	16.2	0.46	0.07
10HbM	10	2	Bottom	2	2	14.4	0.84	0.13
10HaF	10	1	Top	4	17	171	1.2	0.19
20HaF	20	1	Top	1	1	9.4	0.97	0.25
20HbF	20	1	Top	4	1	10.0	0.70	0.18
20HaM	20	2	Top	1	2	12.2	0.71	0.19
20HbM	20	2	Top	1	2	12.2	0.85	0.22
20HaF	20	1	Top	3	17	221	1.0	0.31

Table 6-14. Sample and GC data for vacuum dried magnesium hydroxide γ-irradiation

Sample ID	Vac Dry Temp (°C)	Pre-Drying Sample Mass (g)	Drying Mass Loss (g)	Drying Mass Loss (%)	Post-Drying Water (%)	Sample Pressure (mbar)	GC Press. (bar)	Peak Area (H_2)	Adjusted Peak Area (H_2)	Peak Area (O_2)	Peak Area (N_2)	H_2 qty (moles)
VD40MeF	40	2.259	0.013	0.60	2.2	1265	0.565	1.86	1.860	0.2	0.5	2.0E-07
VD40MfF	40	2.250	0.013	0.58	2.2	1265	0.557	2.14	2.140	0.11	0.5	2.3E-07
VD60MaF	60	2.249	0.020	0.87	1.9	1280	0.599	1.11	1.110	0.3	0.9	1.2E-07
VD60MbF	60	2.248	0.020	0.89	1.9	1280	0.564	1.38	1.380	0	0.2	1.4E-07
VD90MaF	90	2.252	0.026	1.15	1.7	1270	0.532	0.949	0.949	0.1	3.2	8.9E-08
VD90MbF	90	2.260	0.026	1.15	1.7	1270	0.542	1.406	1.406	0.1	0.9	1.4E-07
VD120MaF	120	2.249	0.036	1.59	1.2	1272	0.547	0.65	0.650	90	270	6.1E-08
VD120MbF	120	2.250	0.034	1.50	1.3	1272	0.559	0.503	0.503	90	270	4.7E-08
VD120McF	120	2.254	0.034	1.53	1.3	1272	0.587	0.361	0.361	94	277	3.4E-08
VD120MdF	120	2.220	0.005	0.24	1.2	1267	0.530	0.783	0.783	0	0.6	7.2E-08
VD120MeF	120	2.222	0.005	0.24	1.3	1267	0.535	0.537	0.537	0	0.6	4.8E-08
VD120MfF	120	2.227	0.004	0.20	1.3	1264	0.576	0.34	0.340	0	5.2	3.1E-08
VD200MaF	200	2.248	0.034	1.49	1.3	1272	0.550	0.379	0.379	86	258	3.4E-08
VD200MbF	200	2.250	0.031	1.37	1.4	1272	0.579	1.11	1.110	94	286	1.2E-07
VD200McF	200	2.213	0.000	0.0	1.3	1267	0.538	0.366	0.366	0	0	3.2E-08
VD200MdF	200	2.218	0.001	0.03	1.4	1267	0.566	0.384	0.384	0	0	3.5E-08

Table 6-15. Sample and GC data for vacuum dried hydromagnesite γ-irradiation

Sample ID	Vac Dry Temp (°C)	Pre-Drying Sample Mass (g)	Drying Mass Loss (g)	Drying Mass Loss (%)	Post-Drying Water (%)	Sample Press. (mbar)	GC Press. (bar)	Peak Area (H_2)	Adjusted Peak Area (H_2)	Peak Area (O_2)	Peak Area (N_2)	H_2 qty (moles)
VD40HeF	40	1.799	0.024	1.34	2.0	1265	0.429	1.12	1.464	9	29	1.5E-07
VD40HfF	40	1.796	0.025	1.37	2.0	1265	0.384	0.6	0.877	20	63	8.7E-08
VD60HaF	60	1.803	0.033	1.82	1.5	1280	0.569	1.36	1.360	0.25	0.7	1.4E-07
VD60HbF	60	1.795	0.034	1.88	1.5	1280	0.440	1.37	1.799	2.4	8.6	2.0E-07
VD90HaF	90	1.806	0.040	2.21	1.1	1270	0.428	0.632	0.799	6.8	24	7.6E-08
VD90HbF	90	1.801	0.042	2.36	1.0	1270	0.550	1.011	1.011	0.3	1.2	1.0E-07
VD120HaF	120	1.795	0.049	2.74	0.6	1287	0.568	0.199	0.199	0.3	2.6	1.7E-08
VD120HbF	120	1.799	0.054	3.00	0.4	1287	0.317	0	0.000	4.4	15	0.0E+00
VD120HcF	120	1.800	0.052	2.91	0.4	1287	0.459	0.316	0.391	1.9	7.1	3.6E-08
VD120HaF	120	1.673	0.012	0.72	0.6	1264	0.497	0.435	0.483	0.8	4.3	4.5E-08
VD120HbF	120	1.750	0.011	0.62	0.4	1264	0.350	0.23	0.363	11.5	37	3.3E-08
VD120HcF	120	1.753	0.010	0.55	0.4	1264	0.415	0.18	0.240	17	55	2.1E-08

Table 6-16. Vacuum dried magnesium hydroxide γ-irradiation data

Sample ID	Vac Dry Temp. (°C)	Irrad. Row	Irrad. Deck	Irrad. Position	Irrad. Time (h)	Total Dose (kGy)	G (H_2) Water Only	Ave.	G (H_2) Water +Solid	Ave.
VD40MeF	40	1	Bottom	1	1	9.5	4.0		0.089	
VD40MfF	40	1	Bottom	4	1	9.8	4.4	4.19	0.100	0.094
VD60MaF	60	1	Top	1	1	9.4	2.8		0.055	
VD60MbF	60	1	Top	4	1	10.0	3.1	2.95	0.061	0.058
VD90MaF	90	1	Top	1	1	9.4	2.4		0.041	
VD90MbF	90	1	Top	4	1	10.0	3.5	2.98	0.060	0.050
VD120MaF	120	1	Bottom	2	1	15.8	1.3		0.017	
VD120MbF	120	1	Bottom	3	1	15.0	1.0		0.014	
VD120McF	120	1	Top	2	1	13.3	0.8	1.05	0.011	0.014
VD120MdF	120	1	Bottom	2	1	9.4	2.7		0.033	
VD120MeF	120	1	Bottom	3	1	10.0	1.6		0.021	
VD120MfF	120	1	Top	2	1	10.0	1.0	1.41	0.014	0.018
VD200MaF	200	1	Bottom	1	1	9.5	1.1		0.015	
VD200MbF	200	1	Bottom	4	1	9.8	3.4	2.28	0.051	0.033
VD200McF	200	1	Bottom	1	1	9.5	1.1		0.015	
VD200MdF	200	1	Bottom	4	1	9.8	1.1	1.68	0.016	0.024

Table 6-17. Vacuum dried hydromagnesite γ-irradiation data

Sample ID	Vac Dry Temp (°C)	Irrad. Row	Irrad. Deck	Irrad. Position	Irrad. Time (h)	Total Dose (kGy)	G (H_2) Water Only	Average	G (H_2) Water +Solid	Average
VD40HeF	40	1	Bottom	2	1	15.8	2.6		0.053	
VD40HfF	40	1	Bottom	3	1	15.0	1.6	2.1	0.032	0.043
VD60HaF	60	1	Top	2	1	13.3	3.7		0.058	
VD60HbF	60	1	Top	3	1	13.0	5.5	4.6	0.082	0.070
VD90HaF	90	1	Top	2	1	13.3	2.7		0.031	
VD90HbF	90	1	Top	3	1	13.0	4.1	3.4	0.042	0.036
VD120HaF	120	1	Top	1	1	9.4	1.6		0.011	
VD120HbF	120	1	Top	3	1	13.0	0.0		0.00	
VD120HcF	120	1	Top	4	1	10.0	4.3	3.0	0.020	0.015
VD120HaF	120	1	Top	1	1	9.4	4.5		0.028	
VD120HbF	120	1	Top	3	1	13.0	3.9		0.014	
VD120HcF	120	1	Top	4	1	10.0	2.5	2.8	0.011	0.014

6.6.2 He^{2+} ion irradiation of magnesium hydroxide tabulated data

Table 6-18. Sample preparation and GC data for He^{2+} ion beam irradiation

Sample ID	Solid Mass (g)	Water Mass (g)	Total Water %	Irrad. Water mass (g)	GC Press. (bar)	Peak Area (H_2)	Peak Area (O_2)	Peak Area (N_2)	H_2 Yield (moles)	Volume Ratio Scaled Yield (moles)
20MHe2h2	0.225	0.04514	22.9%	2.09E-04	0.1529	3.42	4.69	101	3.3E-07	5.3E-07
20MHe2h3	0.225	0.045	22.8%	2.09E-04	0.1652	2.348	3.81	107	2.2E-07	3.7E-07
0MHe2h2	0.225	0	2.84%	2.60E-05	0.1536	0.694	2.2	102	6.6E-08	1.1E-07
0MHe2h5	0.218	0	2.84%	2.60E-05	0.1491	0.517	2.08	101	4.9E-08	8.2E-08
0MHe2h6	0.225	0	2.84%	2.60E-05	0.1575	1.983	0.54	109	1.9E-07	3.1E-07
BHe30min1	0	0.65	100%	7.52E-04	0.160	3.286	0.596	111	3.1E-07	4.5E-07
BHe30min2	0	0.65	100%	7.52E-04	0.1624	3.738	0.62	114	3.6E-07	5.1E-07
BHe30min3	0	0.65	100%	7.52E-04	0.161	3.65	0.3	108	3.5E-07	5.0E-07

Table 6-19. Magnesium hydroxide ion beam irradiation parameters

Sample ID	Sample Ave Current (nA)	Window Ave Current (nA)	Total Ave Current (nA)	Irrad. Time (min)	Irrad. Rate (ions/s)
20MHe2h2		7.69	7.69	120	2.40E+10
20MHe2h3	4.49	6.94	1.14	120	2.17E+10
0MHe2h2		7.69	7.69	120	2.40E+10
0MHe2h5		6.51	6.51	120	2.03E+10
0MHe2h6	4.95	7.39	1.23	120	2.31E+10
BHe30min1	6.21	6.31	1.25	30	1.97E+10
BHe30min2		6.42	6.42	30	2.01E+10
BHe30min3		6.56	6.56	30	2.05E+10

Table 6-20. Magnesium hydroxide ion beam irradiation data (G-value established only from energy absorbed by water)

		Molecular Water System Only			
Sample ID	Total Ions	Water Energy Ratio	$Mg(OH)_2$ Energy Ratio	Total Energy (100 eV)	$G(H_2)$ (molec./100 eV)
20MHe2h2	1.73E+14	0.348	0.652	2.39E+18	0.13
20MHe2h3	1.56E+14	0.348	0.652	2.16E+18	0.10
0MHe2h2	1.73E+14	0.004	0.996	2.82E+16	2.34
0MHe2h5	1.46E+14	0.004	0.996	2.39E+16	2.06
0MHe2h6	1.66E+14	0.004	0.996	2.71E+16	6.97
BHe30min1	3.55E+13	1.00		1.41E+18	0.19
BHe30min2	3.61E+13	1.00		1.43E+18	0.22
BHe30min3	3.69E+13	1.00		1.46E+18	0.21

Table 6-21. Magnesium hydroxide ion beam irradiation data (G-value established from energy absorbed by solid+water)

Sample ID	Total Ions	Total Energy (100 eV)	G Value (molec./100 eV)
20MHe2h2	1.73E+14	6.85E+18	0.047
20MHe2h3	1.56E+14	6.18E+18	0.036
0MHe2h2	1.73E+14	6.85E+18	0.010
0MHe2h5	1.46E+14	5.80E+18	0.008
0MHe2h6	1.66E+14	6.58E+18	0.029
BHe30min1	3.55E+13	1.41E+18	0.194
BHe30min2	3.61E+13	1.43E+18	0.217
BHe30min3	3.69E+13	1.46E+18	0.207

6.6.3 He^{2+} ion irradiation of magnesium hydroxide hydrogen sensor data

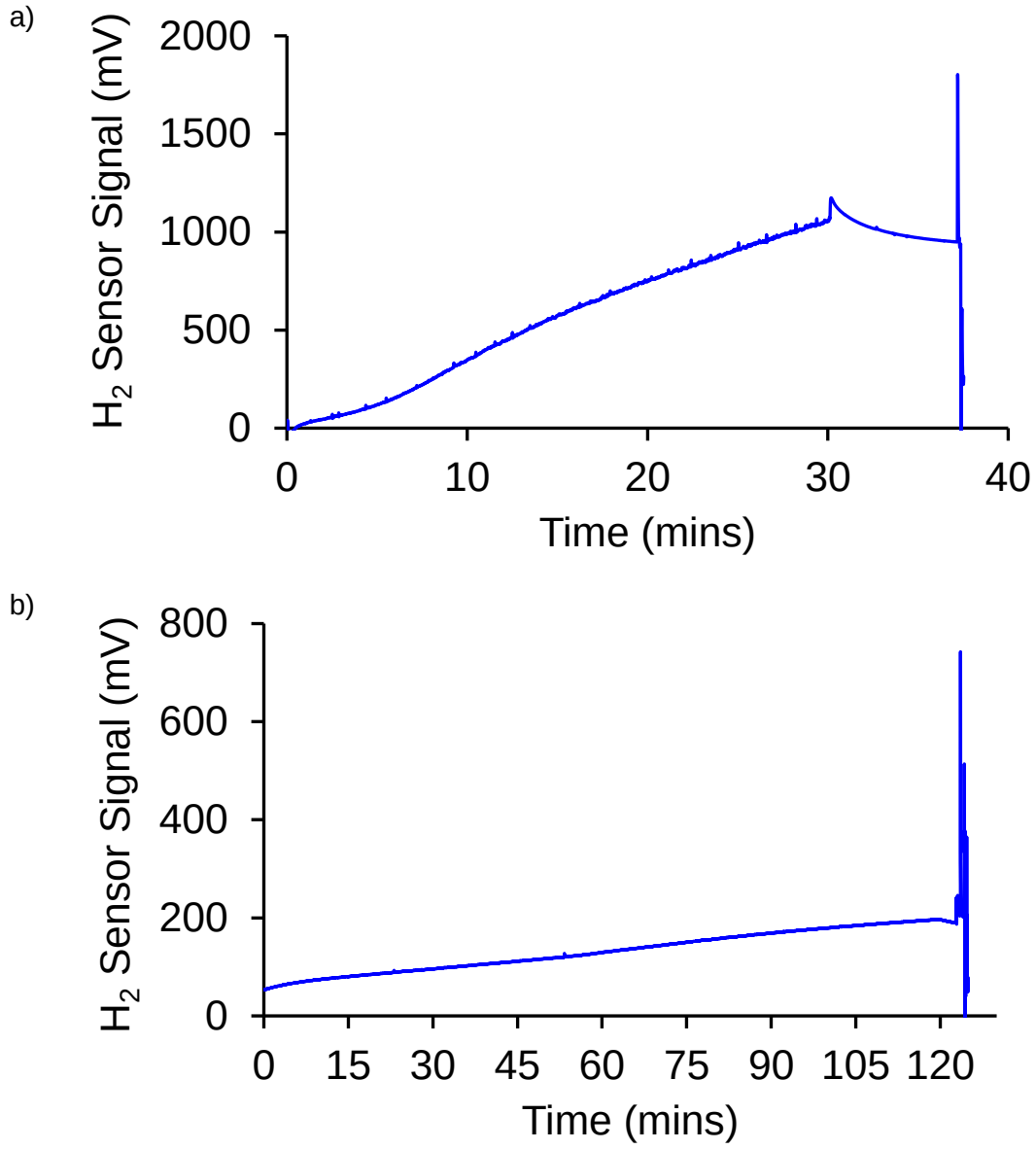

Figure 6-23. H_2 sensor response during He^{2+} irradiations for a) water irradiated for 30 mins, b) magnesium hydroxide w/ 20% added water irradiated for 2 hours

Chapter 7 Thesis Conclusions

This thesis has investigated whether wet and corroded Magnox spent fuel cladding can be adequately dried to prevent degradation during dry interim storage prior to eventual future disposal. This was approached by initially undertaking a review of the existing literature and research relevant to this work, as discussed in Chapter 2. This chapter discussed the current position of the UK and potential limitations of the existing strategy of wet storage. Previous research has been covered to describe the potential corrosion products that are likely to form during wet storage of Magnox cladding and how that may impact a drying process. This was then further considered with regard to how such materials may interact with or retain water if a drying process were deployed. Previous work on drying corroded uranium metal fuel at Hanford[56] and existing vacuum drying practices have been established,[43] with some vacuum drying technologies being considered for Magnox in the UK.[62,63]

From the discussion of water retention and vacuum drying, further study was undertaken to consider what the implications of water carryover into dry storage, particularly with regard to hazards from hydrogen generation via radiolysis. Radiolytic production of hydrogen from water is a well-studied effect, but through this research it was also observed that a number of metal oxides can significantly enhance radiolytic hydrogen rates at the surface,[12,13] which has particular relevance to many heterogeneous systems which include water, and in this case the radiolysis of water adsorbed onto the surface of Magnox fuel cladding. The work by Petrik observed a correlation between metal oxide band gap and hydrogen generation rate,[12] and the reported band gap of magnesium hydroxide of 5.17-5.70 eV[80,81] fits within the resonant range discussed, so may suggest greater radiolysis to be expected for adsorbed water.

From this work the approach was structured to investigate and consider the condition of wet stored/corroded Magnox cladding, required drying conditions (predominantly under vacuum, at a range of temperatures, timeframes and samples) and active investigation of radiolytic hydrogen generation from adsorbed water on Magnox corrosion products.

From the characterisation work in Chapter 4 on simulant unirradiated corroded Magnox cladding, XRD and TGA showed the presence of magnesium hydroxide, as well as Mg-hydroxycarbonates such as hydromagnesite and potentially artinite also. This is interesting as it provides a route for chemically bound water to be retained within the chemical structure of the Mg-hydroxycarbonates. In addition to that the potential for physical trapping of water within void spaces was explored by x-ray µ-CT where the void space was estimated at 3% by volume for the sample analysed.

The surfaces of corroded Magnox samples were observed by optical and scanning electron microscopy, showing uneven surfaces with rod-like, platelet and rosette morphologies, with many cracks and areas for water contact. This characterisation work showed that the nature of corroded Magnox has a variety of ways to retain water which should be considered and overcome to get most effective drying.

The investigation then went on to test a vacuum drying process on two of the corroded Magnox cladding samples. Temperatures from 40-120 °C were investigated and showed that increasing the temperature not only increased the rate of drying but increased the extent of dryness achieved also. For Sample 1 no drying benefit was observed (via mass loss) beyond 90 °C which was unexplained, since drying at increasing temperature (over tested range 40-120 °C) consistently increased mass loss for Sample 2. Further tests were undertaken on Sample 1 which suggested the sample had reacted over the test campaign which affected later results at higher temperatures, and that this effect was not indicative of any reduction in drying efficacy >90 °C. Therefore this work concluded that vacuum drying corroded Magnox at increasing temperatures beyond that of 40-120 °C not only increases the drying rate, but also removes more water from the sample. This is unsurprising given that Mg-hydroxycarbonates are reported to dehydrate at temperatures >120 °C.[106] For any potential implementation industrially this work suggests that unless fairly intense drying regimes are employed, some water carryover following drying is inevitable, and leads to query what the implications of this could be.

In order to investigate one avenue of how dry is adequate for dry storage, from the perspective of reducing hydrogen generation in a radioactive environment from water radiolysis, active testing of corroded Magnox compounds was undertaken. This was carried out with the use of the Dalton Cumbrian Facility γ-irradiator and He^{2+} ion beam. Samples of magnesium hydroxide and hydromagnesite were irradiated with varying water content from 2.8-3.4% (as-received) up to 25%, and a variation of radiolytic hydrogen yield was seen. Samples with lower water contents demonstrated relative increases in observed $G(H_2)$ which could be due to the energy transfer effect described by Petrik[12] and Le Caer.[13] Despite this effect the overall hydrogen yield does reduce with decreasing water content. This was further investigated by vacuum drying as-received powders at 40-120 °C and irradiating, which demonstrated the benefits of drying with regard to hydrogen yield. This work showed continuous reduction in hydrogen yield with increasing drying temperature from 40-120 °C. No observable benefit was seen with drying >120 °C within the sensitivities of this experiment. A similar observation of relative G-value increase at

lower water content was seen from He^{2+} ion irradiation of magnesium hydroxide at water content 2.8-25%.

In summary from this thesis, the main conclusions are that corroded Magnox fuel is likely to contain chemically and physically bound water, which can require prolonged drying to achievement of the best extent of dryness. Increasing temperature continues to give increasing drying extent over all temperatures tested up to and above 120 °C. Water carryover is likely to be inevitable on some level, but with regard to hydrogen generation from radiolysis of water carryover (within the sensitivities achievable by the methods employed here), there was no observed reduction in hydrogen generation from vacuum drying at 200 °C c.f. 120 °C.

Chapter 8 Bibliography

1. Hinton, C. Calder Hall. *J. Nucl. Energy* **4**, 1–3 (1957).
2. Department for Business Energy and Industrial Strategy. *UK Energy in Brief 2018*. (2018).
3. Nuclear Decommissioning Authority. *NDA Business Plan 2022 to 2025*. (2022).
4. Pöyry Energy Limited & Amec Foster Wheeler plc. *Radioactive Waste Inventory: Radioactive wastes and materials not reported in the 2016 Waste Inventory*. (2017).
5. IAEA. *Spent Fuel Performance Assessment and Research: Final Report of a Coordinated Research Project (SPAR-II)*. (2012).
6. Morris, J. E., Richardson, P. J. & Wickham, S. M. *Magnox Spent Fuel Contingency: Review of Options for Drying, Packaging and Storage of Magnox Fuel (Unpublished)*. **44**, (2009).
7. Plys, M. G., Epstein, M., Lee, S. J. & Apthorpe, R. A. ICEM2011-59114. 1–9 (2011).
8. Goode, J., Hanson, B. & Harbottle, D. Transitioning of Spent AGR Fuel from Wet to Dry Storage. (University Of Leeds, 2017).
9. Goode, J. B., Harbottle, D. & Hanson, B. C. Vacuum drying of advanced gas reactor fuel. *Prog. Nucl. Energy* **109**, 145–158 (2018).
10. Goode, J. B., Hambley, D. I. & Hanson, B. C. End point determination for spent nuclear fuel drying operations. *Prog. Nucl. Energy* **116**, 108–114 (2019).
11. Yun, L. *et al.* Drying kinetics of magnesium hydroxide of different morphological micro nanostructures. *Dry. Technol.* **27**, 523–528 (2009).
12. Petrik, N. G., Alexandrov, A. B. & Vall, A. I. Interracial energy transfer during gamma radiolysis of water on the surface of ZrO2 and some other oxides. *J. Phys. Chem. B* **105**, 5935–5944 (2001).
13. Caër, S. Le. Water radiolysis: Influence of oxide surfaces on H2 production under ionizing radiation. *Water (Switzerland)* **3**, 235–253 (2011).
14. Donoclift, T. The Radiolytic Steady-State and Factors Controlling H2 Production. (University of Manchester, 2016).
15. Shpak, A. P. *et al.* The effect of γ-irradiation on the structure and subsequent thermal decomposition of brucite. *Phys. Chem. Miner.* **30**, 59–68 (2003).
16. Laverne, J. A. & Tandon, L. H 2 and Cl 2 Production in the Radiolysis of Calcium and Magnesium Chlorides and Hydroxides. (2005). doi:10.1021/jp044166o
17. Jensen, S. E. & Nonbol, E. *Description of the Magnox Type of Gas Cooled Reactor (MAGNOX), NKS-2 ISBN 87-7893-050-2*. (1998).
18. Nuclear Decommissioning Authority. *The Magnox Operating Programme 9 (MOP 9)*. (2012).
19. World Nuclear News. Sellafield starts controlled shutdown of Magnox facility : Covid-19 - World Nuclear News. Available at: https://world-nuclear-news.org/Articles/Sellafield-starts-controlled-shutdown-of-Magnox-fa. (Accessed: 2nd September 2020)

20. GOV.UK. Green light to restart Magnox Reprocessing - GOV.UK. Available at: https://www.gov.uk/government/news/green-light-to-restart-magnox-reprocessing. (Accessed: 2nd September 2020)

21. Nuclear Decommissioning Authority. Operations to end at Sellafield's Magnox Reprocessing Plant. Available at: https://www.gov.uk/government/news/operations-to-end-at-sellafields-magnox-reprocessing-plant.

22. Office for Nuclear Regulation. *Review of Magnox Reprocessing Separation Plant Regulatory Strategy - ONR-SEL-PAR-15-004*. (2015).

23. Würger, T., Feiler, C., Vonbun-Feldbauer, G. B., Zheludkevich, M. L. & Meißner, R. H. A first-principles analysis of the charge transfer in magnesium corrosion. *Sci. Rep.* **10**, 1–11 (2020).

24. Friskney, C. A. *et al. The corrosion of Magnox Al-80 alloy in aqueous and moist environments*.

25. Parry, S. A. *et al.* Plutonium Behaviour in Nuclear Fuel Storage Pond Effluents. *Energy Environ. Sci.* **4**, 1457 (2011).

26. van Veelen, A. *et al.* Uranium uptake onto Magnox sludge minerals studied using EXAFS. *Mineral. Mag.* **76**, 3095–3104 (2012).

27. Gregson, C. R., Goddard, D. T., Sarsfield, M. J. & Taylor, R. J. Combined electron microscopy and vibrational spectroscopy study of corroded Magnox sludge from a legacy spent nuclear fuel storage pond. *J. Nucl. Mater.* **412**, 145–156 (2011).

28. Aluminium Federation. *UK Aluminium Industry Fact Sheet 2 : Aluminium and Corrosion*.

29. Gregson, C. R., Goddard, D. T., Sarsfield, M. J. & Taylor, R. J. Combined Electron Microscopy and Vibrational Spectroscopy Study of Corroded Magnox Sludge from a Legacy Spent Nuclear Fuel Storage Pond. *J. Nucl. Mater.* **412**, 145–156 (2011).

30. Hallam, K. R., Minshall, P. C., Heard, P. J. & Flewitt, P. E. Corrosion of the alloys Magnox AL80, Magnox ZR55 and pure magnesium in air containing water vapour. *Corros. Sci.* **112**, 347–363 (2016).

31. Lindström, R., Johansson, L.-G., Thompson, G. E., Skeldon, P. & Svensson, J.-E. Corrosion of magnesium in humid air. *Corros. Sci.* **46**, 1141–1158 (2004).

32. Fotea, C., Callaway, J. & Alexander, M. R. Characterisation of the surface chemistry of magnesium exposed to the ambient atmosphere. *Surf. Interface Anal.* **38**, 1363–1371 (2006).

33. White, W. B. Thermodynamic equilibrium, kinetics, activation barriers, and reaction mechanisms for chemical reactions in Karst Terrains. *Environ. Geol.* **30**, 46–58 (1997).

34. Nogalska, A., Zukowska, A. & Garcia-Valls, R. Atmospheric CO2 capture for the artificial photosynthetic system. *Sci. Total Environ.* **621**, 186–192 (2018).

35. Delegard, C. H. & Schmidt, A. J. *Uranium Metal Reaction Behavior in Water, Sludge, and Grout Matrices*. (2008).

36. Orr, R. *et al.* Formation and physical properties of uranium hydride under conditions relevant to metallic fuel and nuclear waste storage. *J. Nucl. Mater.* **477**, 236–245 (2016).

37. Orr, R. *et al.* Kinetics of the reaction between water and uranium hydride

prepared under conditions relevant to uranium storage. *J. Alloys Compd.* **695**, 3727–3735 (2017).

38. Hilton, B. A. *Argonne National Laboratory Review of Oxidation Rates of DOE Spent Nuclear Fuel: Part 1: Metallic Fuel*.

39. Mujumdar, A. S. *Handbook of Industrial Drying*. *Handbook of Industrial Drying* (2006). doi:10.1201/9780429289774

40. Atkins, P. W. (Peter W. & De Paula, J. *Atkins' Physical chemistry*. (Oxford University Press, 2010).

41. Gatley, D. P. *Understanding Psychrometrics*. (2013).

42. Williams-Gardner, A. *Industrial Drying*. (Leonard Hill, 1971).

43. ASTM C1553-16, Standard Guide for Drying Behavior of Spent Nuclear Fuel. in *Astm* 1–19 (ASTM International, 2016). doi:10.1520/C1553-08.2

44. Ewing, G. E., Foster, M., Cantrell, W. & Sadtchenko, V. Thin Film Water on Insulator Surfaces. in *Water in Confining Geometries* 179–211 (Springer-Verlag Berlin Heidelberg, 2003).

45. Ewing, G. E. Ambient thin film water on insulator surfaces. *Chem. Rev.* **106**, 1511–1526 (2006).

46. Thommes, M. *et al. Physisorption of gases, with special reference to the evaluation of surface area and pore size distribution (IUPAC Technical Report)*. *Pure and Applied Chemistry* **87**, (2015).

47. Yeşilbaş, M. & Boily, J. F. Particle Size Controls on Water Adsorption and Condensation Regimes at Mineral Surfaces. *Sci. Rep.* **6**, 1–10 (2016).

48. Ewing, G. E. Feature - Article Feature - Article. *J. Phys. Chem. B* **108**, 15953–15961 (2004).

49. Foster, M., Furse, M. & Passno, D. An FTIR study of water thin films on magnesium oxide. *Surf. Sci.* **502**–**503**, 102–108 (2002).

50. Foster, M., Passno, D. & Rudberg, J. Fourier transform infrared study of methanol, water, and acetic acid on MgO(100). *J. Vac. Sci. Technol. A Vacuum, Surfaces, Film.* **22**, 1640–1646 (2004).

51. Keey, R. B. *Introduction to Industrial Drying Operations*. (1978).

52. Berk, Z. *Food Process Engineering and Technology*. (Pergamon Press, 2009). doi:10.1007/978-3-642-33335-4_40374

53. Morris, J., Wickham, S., Richardson, P., Rhodes, C. & Newland, M. Contingency Options for the Drying, Conditioning and Packaging of Magnox Spent Fuel in the UK, ICEM2009-16331. *12th Int. Conf. ICEM2009 Environ. Remediat. Radioact. Waste Manag.* 1–7

54. Patterson, C., Garzarolli, F., Adamson, R., Coleman, K. & Rudling, P. *Dry Storage Handbook Performance of Spent Nuclear Fuel during Dry Storage*. (Advanced Nuclear Technology International, 2015).

55. Huang, F. . Container materials in environments of corroded spent nuclear fuel. *J. Nucl. Mater.* **231**, 74–82 (1996).

56. Culley, G. E., Gerber, E. W., Fulton, J. C. & Hansen, C. A. *Hanford's Progress Toward Dry Interim Storage of K Basins Spent Fuel*. (1996).

57. Rutherford, W. W. & Holgado, H. O. Accelerated Closure of the Spent Nuclear Fuel Project. in *WM'01 Conference, February 25-March 1, 2001, Tucson, AZ* (2001).

58. U.S. Department of Energy. *Independent Oversight Review of K Basin and Cold Vacuum Drying Facility Found Fuel Multi-Canister Overpack Operations*. (2012).

59. Mccracken, K. J. *Hanford Spent Nuclear Fuel Cold Vacuum Drying Proof of Performance Test Procedure*. (1998).

60. Nuclear Decommissioning Authority. *Magnox Fuel Strategy Contingency Options*. (2014).

61. Sellafield Ltd. Dry Storage of Spent Fuels. (2019). Available at: https://www.nwtrb.gov/docs/default-source/meetings/2019/november/standring.pdf?sfvrsn=4.

62. Nuclear Decommissioning Authority. Cutting-edge kit set for dry run. (2017). Available at: https://www.gov.uk/government/news/cutting-edge-kit-set-for-dry-run.

63. Nuclear Decommissioning Authority. One more pond to drain. (2020). Available at: https://nda.blog.gov.uk/2020/08/10/one-more-pond-to-drain/.

64. O'Donnell, J. H. & Sangster, D. F. *Principles of Radiation Chemistry*. (1970).

65. Lieser, K. H. *Nuclear and Radiochemistry Fundamentals and Applications*. *Nuclear and Radiochemistry* (John Wiley & Sons, Ltd, 2001). doi:10.1002/9783527612758.FMATTER

66. Svensk Kärnbränslehantering AB. *Deep Repository For Spent Nuclear Fuel SR 97 – Post-Closure Safety*. **1**, (1999).

67. Hedin, A. *Spent Nuclear Fuel - How Dangerous Is It? IAEA Technical Report 97-13* (1997).

68. Choppin, G. R., Liljenzin, J.-O., Rydberg, J. & Ekberg, C. *Radiochemistry and Nuclear Chemistry*. *Applied Radiation and Isotopes* (2013). doi:10.1016/0969-8043(95)90023-3

69. Hunter, F., Adeogun, A., Dawson, J., LaVerne, J. & Watson, S. Determination of G-values for use in SMOGG gas generation calculations. 1–77 (2015).

70. C, F. & Jay-Gerin, J.-P. The Effect Of pH On Water Radiolysis: A Still Open Question - A Minireview. *Res. Chem. Intermed* **26**, 549–565 (2000).

71. Dainton, F. S. & Watt, W. S. The Effect of pH on the Radical Yields in the y-Radiolysis of Aqueous Systems. *Nature* **195**, 1294–1296 (1962).

72. Draganic, I. G. & Draganic, Z. D. *The Radiation Chemistry of Water*. (1971). doi:10.1016/b978-0-12-221650-3.50002-9

73. Pastina, B., Laverne, J. A. & Pimblott, S. M. Dependence of Molecular Hydrogen Formation in Water on Scavengers of the Precursor to the Hydrated Electron. *J. Phys. Chem. A* **103**, 5841–5846 (1999).

74. Laverne, J. A. & Pimblott, S. M. New mechanism for H2 formation in water. *J. Phys. Chem. A* **104**, 9820–9822 (2000).

75. Rabe, J. G., Rabe, B. & Allen, A. O. Radiolysis in the Adsorbed State. *Trans. Faraday Soc* **62**, 2203 (1961).

76. Rabe, J. G., Rabe, B. & Allen, A. O. *Radiolysis and Energy Transfer in the Adsorbed State*. *J. Am. Chem. Soc* **83**, (UTC, 1961).

77. Marci, G. & Palmisano, L. *Heterogeneous Photocatalysis Relationships with Heterogeneous Catalysis and Perspectives*. (Elsevier, 2019).

78. Haynes, W. M. *CRC Handbook of Chemistry and Physics*. *Journal of the American Pharmaceutical Association* (CRC, 2015).

79. Ryabchuk, V. Photophysical processes related to photoadsorption and photocatalysis on wide band gap solids: A review. *Int. J. Photoenergy* **6**, 95–113 (2004).

80. Wu, S., Senevirathna, H. L., Weerasinghe, P. V. T. & Wu, P. Engineering electronic structure and band alignment of 2d Mg(OH)2 via anion doping for photocatalytic applications. *Materials (Basel).* **14**, (2021).

81. Ichimura, M. Impurity doping in Mg(OH)2 for n-type and p-type conductivity control. *Materials (Basel).* **13**, 1–10 (2020).

82. Strehlow, W. H. & Cook, E. L. Compilation of Energy Band Gaps in Elemental and Binary Compound Semiconductors and Insulators. *J. Phys. Chem. Ref. Data* **2**, 163–200 (1973).

83. Laverne, J. A. & Tonnies, S. E. H2 production in the radiolysis of aqueous SiO2 suspensions and slurries. *J. Phys. Chem. B* **107**, 7277–7280 (2003).

84. Brodie-Linder, N., Le Caër, S., Alam, M. S., Renault, J. P. & Alba-Simionesco, C. H2 formation by electron irradiation of SBA-15 materials and the effect of CuII grafting. *Phys. Chem. Chem. Phys.* **12**, 14188–14195 (2010).

85. Le Caër, S. *et al.* Radiolysis of confined water: Hydrogen production at a high dose rate. *ChemPhysChem* **6**, 2585–2596 (2005).

86. Nguyen, T. V. A., Tolochko, B. P., Mikhailenko, M. A., Gerasimov, K. B. & Sharafutdinov, M. R. Studying the effects of electron beam irradiation on thermal properties and particle size distribution of magnesium hydroxide. *AIP Conf. Proc.* **2299**, (2020).

87. Dhaouadi, H., Chaabane, H. & Touati, F. Mg(OH)2 nanorods synthesized by a facile hydrothermal method in the presence of CTAB. *Nano-Micro Lett.* **3**, 153–159 (2011).

88. Martin Marietta Magnesia Specialties. Versamag® Magnesium Hydroxide Powder Data Sheet.

89. Housecroft, C. E. & Sharpe, A. G. *Inorganic Chemistry*. (2008).

90. Carmignato, S., Dewulf, W. & Leach, R. *Industrial X-Ray Computed Tomography*. (Springer International Publishing, 2018).

91. Brunauer, S., Emmett, P. H. & Teller, E. Adsorption of Gases in Multimolecular Layers. *J. Am.Chem.Soc.* **60**, 309–319 (1938).

92. Tamari, S. & Aguilar-Chávez, A. Optimum design of gas pycnometers for determining the volume of solid particles. *J. Test. Eval.* **33**, 135–138 (2005).

93. Guo, X. Z. Experimental study of the electrical conductivity of hydrous minerals in the crust and the mantle under high pressure and high temperature. *Sci. China Earth Sci.* **59**, 696–706 (2016).

94. Guo, X., Yoshino, T., Okuchi, T. & Tomioka, N. Crossroads in Earth and Planetary Materials: H-D interdiffusion in brucite at pressures up to 15 GPa. *Am. Mineral.* **98**, 1919–1929 (2013).

95. Bowles, J. F. W. *Encyclopedia of Geology*. *Encyclopedia of Geology* (Academic Press, 2021). doi:10.1016/B978-0-08-102908-4.00162-4

96. Unluer, C. & Al-tabbaa, A. Characterization of Light and Heavy Hydrated Magnesium Carbonates Using Thermal Analysis. *J. Therm. Anal. Calorim.*

115, 595–607 (2014).

97. The RRUFF Project. Available at: https://rruff.info/Artinite/R060166. (Accessed: 12th December 2022)

98. L'vov, B. V., Novichikhin, A. V. & Dyakov, A. O. Mechanism of thermal decomposition of magnesium hydroxide. *Thermochim. Acta* **315**, 135–143 (1998).

99. Anderson, P. J. & Horlock, R. F. Thermal Decomposition of Magnesium Hydroxide. (1962).

100. van der Merwe, E. M. & Strydom, C. A. Quantitative Thermogravimetric Analysis Of Binary Mixtures. *J. Therm. Anal. Calorim.* **76**, 149–156 (2004).

101. Molefe, D. M., Labuschagne, J., Focke, W. W., Van Der Westhuizen, I. & Ofosu, O. The effect of magnesium hydroxide, hydromagnesite and layered double hydroxide on the heat stability and fire performance of plasticized poly(vinyl chloride). *J. Fire Sci.* **33**, 493–510 (2015).

102. Hartman, M., Trnka, O. & Veselý, V. Thermal dehydration of magnesium hydroxide and sintering of nascent magnesium oxide. *AIChE J.* **40**, 536–542 (1994).

103. Chen, Y. *et al.* A novel preparation of nano-sized hexagonal Mg(OH)2. *Procedia Eng.* **102**, 388–394 (2015).

104. Rothon, R. N. & Hornsby, P. R. Flame retardant effects of magnesium hydroxide. *Polym. Degrad. Stab.* **54**, 383–385 (1996).

105. Liu, C., Liu, T. & Wang, D. Non-isothermal kinetics study on the thermal decomposition of brucite by thermogravimetry. *J. Therm. Anal. Calorim.* **134**, 2339–2347 (2018).

106. Hollingbery, L. A. & Hull, T. R. The thermal decomposition of natural mixtures of huntite and hydromagnesite. *Thermochim. Acta* **528**, 45–52 (2012).

107. Padeste, C., Oswald, H. R. & Reller, A. The Thermal Behaviour Of Pure And Nickel-Doped Hydromagnesite In Different Atmospheres. *Mat. Res. Bull* **26**, 1263–1268 (1991).

108. Hollingbery, L. A. & Hull, T. R. The thermal decomposition of huntite and hydromagnesite-A review. *Thermochimica Acta* **509**, 1–11 (2010).

109. Sawada, Y., Uematsu, K., Mizutani, N. & Kato, M. Thermal decomposition of hydromagnesite 4MgCO3·Mg(OH)2·4H2O. *J. Inorg. Nucl. Chem.* **40**, 979–982 (1978).

110. Sawada, Y. *et al.* Isothermal differential scanning calorimetry on an exothermic phenomenon during thermal decomposition of hydromagnesite 4 MgCO3 · Mg(OH)2 · 4 H2O. *Thermochim. Acta* **34**, 233–237 (1979).

111. Sawada, Y. *et al.* Thermogravimetric study on the decomposition of hydromagnesite 4 MgCO3 · Mg(OH)2 · 4 H2O. *Thermochim. Acta* **33**, 127–140 (1979).

112. Paraskevoulakos, C., Hallam, K. R., Adamska, A. & Scott, T. B. Monitoring uranium corrosion in Magnox sludge using X-ray computed tomography: A direct analogue to "legacy" fuel storage ponds. *Corros. Sci.* **168**, 108551 (2020).

113. Davenport, A. J. *et al.* Synchrotron X-ray microtomography study of the role of y in corrosion of magnesium alloy WE43. *Electrochem. Solid-State Lett.* **10**, (2007).

114. Esmaily, M. *et al.* Fundamentals and advances in magnesium alloy corrosion. *Prog. Mater. Sci.* **89**, 92–193 (2017).

115. Rogers, G. F. C. & Mayhew, Y. R. *Thermodynamic and transport properties of fluids : SI units*. (B. Blackwell, 1995).

116. Goode, J. Personal Memo - Activity Inventory of Generic Spent Magnox Fuel. 1–6 (2022).

117. Morris, J., Wickham, S., Richardson, P., Rhodes, C. & Newland, M. Icem2009-16330 Contingency Options for the Dry Storage of. 1–6 (2009).

118. Leay, L. *et al.* Development of irradiation capabilities to address the challenges of the nuclear industry. *Nucl. Instruments Methods Phys. Res. Sect. B Beam Interact. with Mater. Atoms* **343**, 62–69 (2015).

119. Starovoitova, V. Radioisotopes (the Kirk-Othmer Encyclopedia). in (John Wiley & Sons, Inc, 2017). doi:10.1002/0471238961.1801040908051213.a01.pub3

120. Preoteasa, E., Preoteasa, E. & Suciu, I. *Atomic and Nuclear Surface Analysis Methods: a Novel Perspective for the Characterization of Dental Composites*. (Nova Science Publishers, Inc., 2012).

121. SRI. SRI Tech Support Multiple Gas#5 GC Configuration. 1–23 (2018).

122. Spinks, J. W. T. & Woods, R. J. *An Introduction to Radiation Chemistry*. *International Journal of Radiation Biology* (1990). doi:10.1080/09553007614551181

123. LaVerne, J. A., Ryan, M. R. & Mu, T. Hydrogen production in the radiolysis of bromide solutions. *Radiat. Phys. Chem.* **78**, 1148–1152 (2009).

124. National Electrostatics Corporation. National Electrostatics Toroidal Volume Ion Source (TORVIS).

125. Southworth, J. S., Koehler, S. P. K. & Pimblott, S. M. Investigation of Anomalous Hydrogen Production from Water Adsorbed on Metal Oxide Surfaces. (2019).

126. Ziegler, J. F., Ziegler, M. D. & Biersack, J. P. SRIM - The stopping and range of ions in matter (2010). *Nucl. Instruments Methods Phys. Res. Sect. B Beam Interact. with Mater. Atoms* **268**, 1818–1823 (2010).

127. Lu, S., Yan, P., Gao, Y. & Zhang, C. Theoretical Investigation of the Energies , Structures , and Growth Properties of Hydromagnesite Surfaces. *Cryst. Growth Des.* **20**, (2020).

128. Israelachvili, J. N. *Intermolecular and Surface Forces*. *Industrial & Engineering Chemistry* **46**, (Academic Press, 2011).

129. Aramendía, M. A. *et al.* Characterization of Various Magnesium Oxides by XRD and1H MAS NMR Spectroscopy. *J. Solid State Chem.* **144**, 25–29 (1999).

130. Tang, M., Cziczo, D. J. & Grassian, V. H. Interactions of Water with Mineral Dust Aerosol: Water Adsorption, Hygroscopicity, Cloud Condensation, and Ice Nucleation. *Chem. Rev.* **116**, 4205–4259 (2016).

131. La Verne, J. A. & Tandon, L. H2 production in the radiolysis of water on UO2 and other oxides. *J. Phys. Chem. B* **107**, 13623–13628 (2003).